

AN INVESTIGATION OF THE MOTION OF LIQUID  
SHORT CHAIN MOLECULES USING  
RAYLEIGH-BRILLOUIN SPECTROSCOPY

A thesis submitted for the Degree of Doctor of Philosophy by

RALPH PETER TATAM

in partial fulfillment of the requirements of the Council for  
National Academic Awards.

Department of Physics  
Sir John Cass Faculty of Physical Sciences and Technology  
City of London Polytechnic  
31 Jewry Street  
London EC3N 2EY

**City of London Polytechnic**  
**Tower Hill Library**

January 1986

<u>CONTENTS</u>	<u>Page</u>
TITLE	
ABSTRACT	1
ACKNOWLEDGEMENTS	2
CHAPTER 1 - INTRODUCTION	3
CHAPTER 2 - REVIEW OF THEORY	8
2.1 Introduction to light scattering in molecular liquids	9
2.2 Polarised Rayleigh-Brillouin scattering	14
2.2.1 Low viscosity liquids	14
2.2.2 Viscoelastic liquids	17
2.3 Depolarised Rayleigh-Brillouin scattering	18
2.3.1 Low frequency region of the spectrum	19
2.3.2 Collision induced light scattering	33
2.4 Analysis of molecular correlation times	36
2.4.1 The Stokes-Einstein-Debye relation	36
2.4.2 ' <i>Stick-Slip</i> ' boundary conditions	38
2.4.3 Orientational correlation parameters	42
2.4.4 Computer simulations	44
CHAPTER 3 - EXPERIMENTAL TECHNIQUES AND DATA ANALYSIS	52
3.1 Experimental techniques	53
3.1.1 Description of the light scattering spectrometer	53
3.1.2 Measurement of the Free Spectral Range	58
3.1.3 Alignment of the Fabry-Perot Interferometer	58
3.1.4 Sample cell holder	60
3.1.5 Thermostatting of the sample	60
3.2 Sample preparation and ancilliary measurements	63
3.2.1 Filtration techniques	64
3.2.2 Measurement of kinematic viscosity	65
3.2.3 Measurement of density	65
3.2.4 Measurement of refractive index	66
3.3 Analysis of the spectral data	67
3.3.1 Description of the analysis program	67
3.3.2 Statistical analysis of the experimental data	70

	<u>Page</u>
CHAPTER 4 - OLEIC ACID RESULTS AND DISCUSSION	74
4.1 Introduction	75
4.2 Experimental considerations	79
4.3 Results	80
4.3.1 Kinematic shear viscosity	80
4.3.2 Density	80
4.3.3 Refractive index	80
4.3.4 Polarised Rayleigh-Brillouin scattering	84
4.4 Statistical analysis of the results	90
4.5 Discussion	96
4.5.1 Kinematic viscosity	96
4.5.2 Density	97
4.5.3 Refractive index	99
4.5.4 Polarised Rayleigh-Brillouin scattering	99
4.6 Conclusions	101
CHAPTER 5 - RESULTS AND ANALYSIS OF DEPOLARISED RAYLEIGH-BRILLOUIN SCATTERING FROM THE ALKANES $C_5H_{12}$ TO $C_8H_{18}$	104
5.1 Introduction	105
5.2 Results	108
5.2.1 Isomers of $C_8H_{18}$	108
5.2.2 Isomers of $C_7H_{16}$	116
5.2.3 Isomers of $C_6H_{14}$	125
5.2.4 Isomers of $C_5H_{12}$	134
5.3 Analysis of the spectral data	138
5.3.1 The Stokes-Einstein-Debye relation	138
5.3.2 Molecular self-diffusion	158
5.3.3 Origin of the second Lorentzian	163
5.3.4 Comparison of experimental molecular correlation times with results from computer simulations	165
CHAPTER 6 - SUMMARY OF CONCLUSIONS AND SUGGESTIONS FOR FUTURE INVESTIGATIONS	170
6.1 Summary of conclusions	171
6.2 Suggestions for future investigations	174
List of Figures	176
List of Tables	178
References	179

	<u>Page</u>
APPENDIX 1 - DEVELOPMENT OF A DATA ANALYSIS PROGRAM	i
A1.1 Weighting of the data points	ii
A1.2 Initial estimates of the fitting parameters	ii
A1.3 Linearisation of the data points	v
A1.4 Construction of the fitting functions	vi
A1.4.1 Fitting functions for polarised Rayleigh-Brillouin spectra	vi
A1.4.2 Fitting functions for depolarised Rayleigh-Brillouin spectra	ix
A1.5 Deconvolution of instrumental broadening	xii
APPENDIX 2 - STATISTICAL TESTS	xvi
A2.1 The chi-square test	xvii
A2.2 The One-Sample Runs test	xxi
A2.3 The linear correlation test	xxiv

## ABSTRACT

"An investigation of the motion of liquid short chain molecules using Rayleigh-Brillouin spectroscopy."

RALPH P TATAM

Dynamic laser light scattering spectroscopy is used to study the motion of short chain flexible molecules in the liquid state.

Depolarised Rayleigh-Brillouin scattering is used to investigate the isomers of the homologous alkane series n-pentane to n-octane. In addition to the low frequency Lorentzian component, associated with molecular reorientation, a second Lorentzian component is found in the spectra from the liquids 2,2,4-trimethylpentane, 2-methylhexane, 3-methylhexane, 2,2-dimethylpentane, 2,3-dimethylpentane, 2,2,3-trimethylbutane, 2-methylpentane, 3-methylpentane, 2,2-dimethylbutane, n-pentane and 2-methylbutane. The contribution to the spectra of this second Lorentzian, which is broader than the Lorentzian associated with molecular reorientation and distinct from the interaction induced component, reduces as the molecules become more anisotropic and flexible. The origin of this component is associated with local translational order.

The correlation times obtained from molecular reorientation are analysed in terms of a modified Stokes-Einstein-Debye relation. The Stokes-Einstein-Debye volumes obtained are interpreted as the quantity  $(g_2/J_2)\alpha PV$ , where  $(g_2/J_2)$  is associated with molecular correlation,  $P$  and  $\alpha$  with molecular shape and  $V$  is the molecular volume.

Values of  $\alpha$ , the *stick-slip* coefficient, obtained for the n-alkanes indicate that the average molecular conformation is approximately midway between a sphere and an extended chain. For all the isomers  $\alpha$  is found to decrease as the molecule becomes more rigid and more spherical.

The liquid 2,2-dimethylbutane is analysed in terms of the theory of Madden [Mol Phys, 36, 365 (1978)]; dipole-induced dipole interactions between pairs of density fluctuations cause intermolecular optical anisotropy. The results indicate that molecular reorientation may not be the predominant relaxation mechanism.

Oleic acid was investigated using polarised Rayleigh-Brillouin spectroscopy. The temperature gradient of the hypersonic frequency shift and elastic modulus show anomalous behaviour in the range 14 - 18 °C. This suggests that oleic acid undergoes a change of phase to form a locally nematic structure about 5 °C above the melting point. Complementary measurements of viscosity, density and refractive index support this interpretation.

## ACKNOWLEDGEMENTS

I am grateful to the City of London Polytechnic for the award of a Research Assistantship, thus making this work possible, and to my colleagues in the Physics Department for many stimulating discussions. I would especially like to thank Dr J F Crilly, Dr G H Meeten and my supervisor Dr J V Champion.

I would also like to thank Mr D C L Wiffen for his expert technical assistance.

Finally, I also wish to record my gratitude to my parents who have encouraged me throughout the course of this work.

CHAPTER 1 - INTRODUCTION

## Introduction

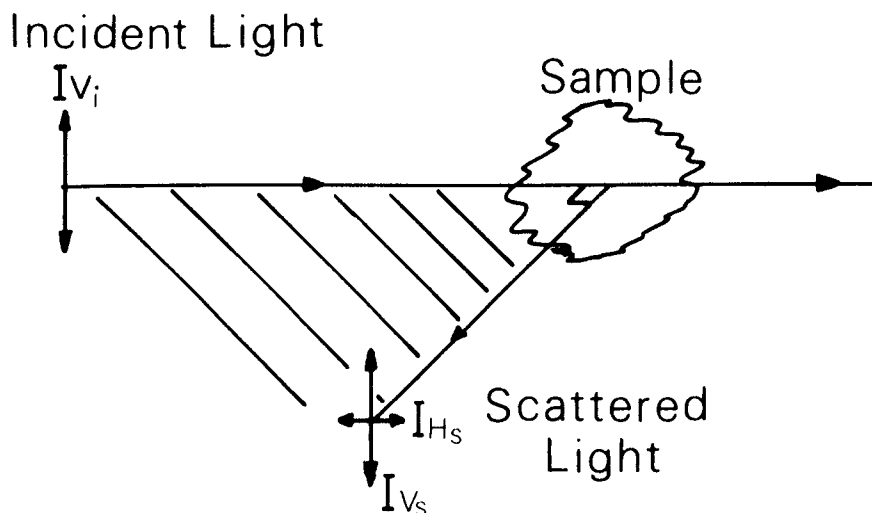
In recent years a number of authors have attempted to gain a greater understanding of the dynamics of short chain polymer molecules from experimental<sup>[1,2,3]</sup> and theoretical<sup>[4]</sup> studies. Computer simulation studies have concentrated on the smaller molecules with characteristic relaxation times in the picosecond region as these molecules have the simplest structures and are therefore the easiest to 'model' for the simulations. Conversely, most experimental studies have been performed on longer chain molecules, predominantly the n-alkanes. These molecules are more anisotropic, therefore scattering more light, and are consequently more easily studied experimentally. The n-alkanes have relaxation times greater than two picoseconds.

The purpose of this work was to examine the intermediate regime between small rigid molecules and short chain flexible molecules in order to provide high quality experimental data. This data can be compared to both computer simulations and simple theoretical models thus providing further insight into the structure and dynamics of molecular behaviour in the liquid state.

The technique used to investigate the molecular behaviour in this regime was that of Rayleigh-Brillouin spectroscopy; light scattering from molecular liquids arises from local variations in the dielectric constant caused by density and orientational fluctuations of the molecules, hence the spectrum of the scattered light contains structural and dynamical information about the relative positions and orientations of the molecules.

This technique is shown schematically in Figure 1.1.

Figure 1.1 Schematic diagram of light scattering geometry



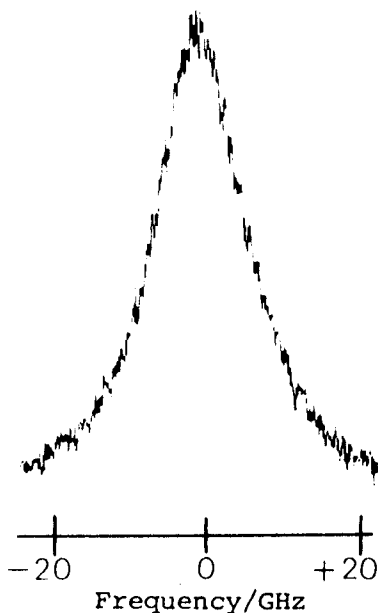
Collimated linearly polarised light is incident vertically ( $I_{V_i}$ ) upon the sample. The light scattered at  $90^\circ$  with respect to the incident beam is detected and resolved into two components, one vertically polarised ( $I_{V_s}$ ) and the other horizontally polarised ( $I_{H_s}$ ). The vertically polarised component is that due to polarised Rayleigh-Brillouin scattering (Figure 1.2) from which information about the macroscopic quantities associated with the liquid is obtained, for example, the ratio of the specific heat capacities  $C_p/C_v$ , liquid viscosity and the hypersonic velocity of sound in the liquid.

Figure 1.2 Polarised Rayleigh-Brillouin spectrum of n-octane at  $30^\circ\text{C}$



The horizontally polarised, or depolarised component, (Figure 1.3) reflects the dynamics of optical anisotropy fluctuations, that is, the microscopic properties of the liquid.

Figure 1.3 Depolarised Rayleigh-Brillouin spectrum of n-octane at 30 °C



For rigid symmetric top molecules these fluctuations arise from reorientational motions of the symmetry axis of the molecule. However for flexible molecules, for example the n-alkanes, there will be many motions which lead to anisotropy fluctuations and hence there will be a distribution of relaxation times which will determine the spectrum. For the lower n-alkanes conformational changes are slow compared to overall molecular reorientation and molecular reorientation will therefore be the predominant mechanism. However, as the chain length increases, a limiting value of  $n > 28$  is reached, where  $n$  is the number of atoms in the carbon chain, at which intramolecular conformational changes dominate the spectrum<sup>[5]</sup>.

At present, theoretical descriptions and computer simulations in the intermediate region between rigid and short chain flexible molecules

are not available and the experimental data is extremely limited<sup>[1]</sup>. In this thesis the liquids chosen to investigate this regime were the isomers of the homologous alkane series n-pentane to n-octane; the flexibility decreases as the branching increases for each alkane homologue.

In addition, to study the effect of decreasing the flexibility of a longer chain molecule, the properties of cis-9-octadecenoic (oleic) acid were investigated. This molecule has less flexibility than the saturated form of the acid, stearic acid, imposed by the presence of a carbon-carbon double bond midway along the backbone chain. Oleic acid was also chosen because of its vital importance in biological systems<sup>[6,7]</sup>.

A review of depolarised light scattering theories is presented in Chapter 2 and the limitations of present theories are also discussed. Chapter 3 describes the experimental techniques and the implementation of the data analysis schemes. In Chapter 4 the results and discussion from the oleic acid experiments are presented. The depolarised light scattering results from the homologous alkane series are presented and discussed in Chapter 5. Finally in Chapter 6 a summary of the results and conclusions are presented and outlines for future experimental investigations are suggested.

## CHAPTER 2 - REVIEW OF THEORY

### Contents

- 2.1 Introduction to Light Scattering in Molecular Liquids
  
- 2.2 Polarised Rayleigh-Brillouin Scattering
  - 2.2.1 Low Viscosity Liquids
  - 2.2.2 Viscoelastic Liquids
  
- 2.3 Depolarised Rayleigh-Brillouin Scattering
  - 2.3.1 Low Frequency Region of the Spectrum
  - 2.3.2 Collision Induced Light Scattering
  
- 2.4 Analysis of Molecular Correlation Times
  - 2.4.1 The Stokes-Einstein-Debye Relation
  - 2.4.2 *Stick-Slip* Boundary Conditions
  - 2.4.3 Orientational Correlation Parameters
  - 2.4.4 Computer Simulations

## 2.1 Introduction to Light Scattering in Molecular Liquids

Light scattering in simple liquids may be considered to be due to local fluctuations in the dielectric constant<sup>[8]</sup>. In Fig 2.1.1 light of frequency  $\omega_0$  and wavevector  $\underline{q}_i$  is incident on the sample. The light is scattered at an angle  $\theta$  with wavevector  $\underline{q}_s$  and frequency distribution  $I(\underline{q}, \omega)$ . The scattering vector characterising the fluctuations is defined as

$$\underline{q} = \underline{q}_s - \underline{q}_i \quad (2.1.1)$$

where  $|\underline{q}_i|$  and  $|\underline{q}_s|$  are equal to  $2\pi n/\lambda_i$  and  $2\pi n/\lambda_s$  respectively.  $\lambda_i$  and  $\lambda_s$  are the free space wavelengths of the incident and scattered light and  $n$  is the refractive index of the medium. In the case of Rayleigh-Brillouin scattering the frequency shifts, of the order  $10^8 - 10^{11}$  Hz, are small compared to the incident frequency  $\omega_0$  (approximately  $5 \times 10^{14}$  Hz). Hence,  $|\underline{q}_i| \approx |\underline{q}_s|$  and

$$q = |\underline{q}_s - \underline{q}_i| = \frac{4\pi n}{\lambda_i} \sin(\theta/2) \quad (2.1.2)$$

This is the Bragg condition. It specifies the wave vector component of the dielectric constant fluctuation that gives rise to scattering at an angle  $\theta$ .

The scattering geometry is shown in Fig 2.1.2. Light polarised vertically with respect to the scattering plane, defined by the X and Z axes, is scattered at  $90^\circ$  to the incident wavevector. The scattered light can be resolved into two polarisation states, one vertically polarised (VV) and the other horizontally polarised (VH).  $I_{VV}$  is called the "polarised" component and  $I_{VH}$  is called the "depolarised" component.

Fig 2.1.1 Scattering diagram for Rayleigh-Brillouin spectroscopy:  
wave vector representation

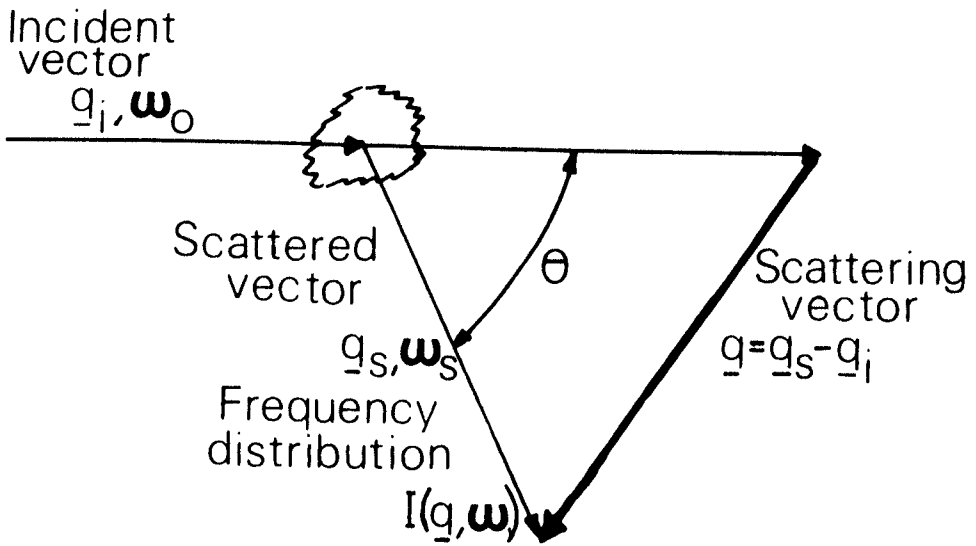
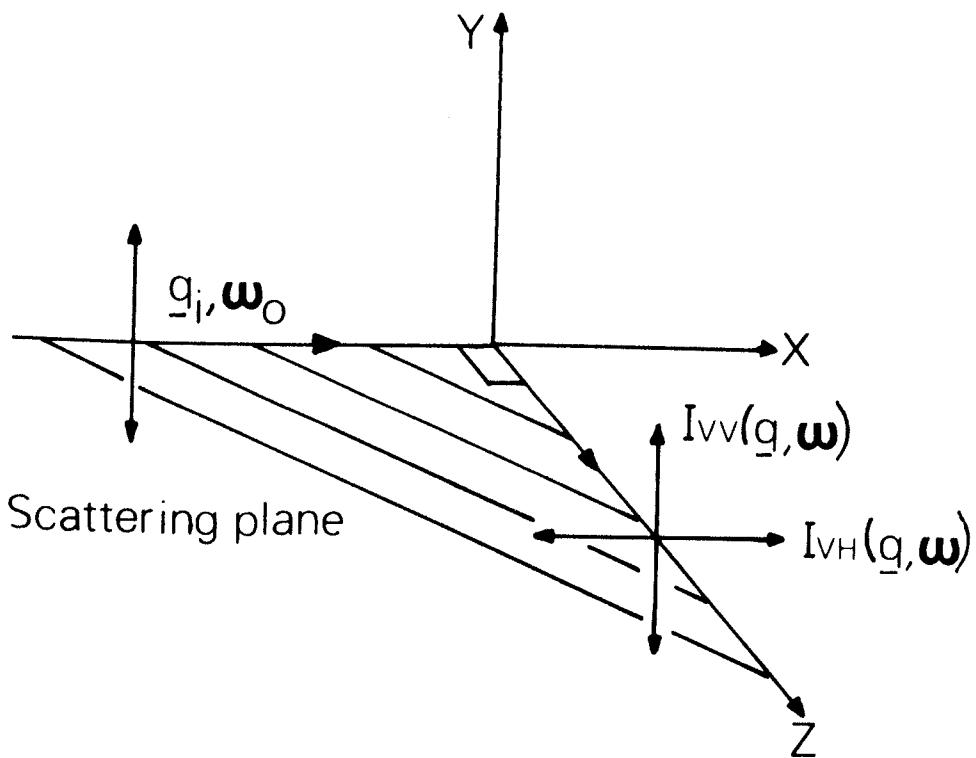


Fig 2.1.2 Scattering geometry



All theoretical formulations of light scattering spectra require the calculation of a time-dependent autocorrelation function of the dielectric constant fluctuation. This is related to the power spectral density, via the Wiener-Khinchine theorem<sup>[9]</sup>, by time Fourier transform of the autocorrelation function,

$$I(\underline{q}, \omega) \propto \int_{-\infty}^{\infty} \exp(-i\omega t) \langle \Delta\epsilon(\underline{q}, 0) \Delta\epsilon^*(\underline{q}, t) \rangle dt \quad (2.1.3)$$

where  $\Delta\epsilon$  is the dielectric constant fluctuation and the angular brackets denote an ensemble average.

From the scattering geometry (Fig 2.1.2) the specific components of the dielectric fluctuations that give rise to the spectra components are given by<sup>[10]</sup>:

(1) In the polarised case

$$\Delta\epsilon_{VV}(\underline{q}, t) = \Delta\epsilon_{YY}(\underline{q}, t) \quad (2.1.4)$$

Substituting (2.1.4) into (2.1.3) leads to

$$I_{VV}(\underline{q}, \omega) \propto \int_{-\infty}^{\infty} \exp(-i\omega t) \langle \Delta\epsilon_{YY}(\underline{q}, 0) \Delta\epsilon_{YY}^*(\underline{q}, t) \rangle dt \quad (2.1.5)$$

The average dielectric tensor for an isotropic amorphous medium is a scalar, and it is longitudinal density fluctuations that couple to the dielectric tensor and lead to polarised light scattering<sup>[12]</sup>.

Equation (2.1.5) can then be written

$$I_{VV}(\underline{q}, \omega) \propto \int_{-\infty}^{\infty} dt \exp(-i\omega t) \langle \Delta\rho(\underline{q}, 0) \Delta\rho^*(\underline{q}, t) \rangle \quad (2.1.6)$$

The density autocorrelation function has been calculated<sup>[9,10,12]</sup> and the results are presented in Section 2.2.

(2) In the depolarised case

$$\Delta\epsilon_{VH}(\underline{q},t) = \Delta\epsilon_{YX}(\underline{q},t) \sin(\theta/2) - \Delta\epsilon_{YZ}(\underline{q},t) \cos(\theta/2) \quad (2.1.7)$$

Substituting equation (2.1.7) into equation (2.1.3) leads to

$$I_{VH}(\underline{q},\omega) \propto \int_{-\infty}^{\infty} dt \exp(-i\omega t) \left[ \langle \Delta\epsilon_{YX}(\underline{q},0) \Delta\epsilon_{YX}^*(\underline{q},t) \rangle \sin^2(\theta/2) + \langle \Delta\epsilon_{YZ}(\underline{q},0) \Delta\epsilon_{YZ}^*(\underline{q},t) \rangle \cos^2(\theta/2) \right] \quad (2.1.8)$$

where the cross correlation terms, for example

$$\langle \Delta\epsilon_{YZ}(\underline{q},0) \Delta\epsilon_{YX}(\underline{q},t) \rangle, \text{ are zero}^{[10]}.$$

The depolarised Rayleigh-Brillouin scattering spectrum is also due to light being scattered from fluctuations in the local dielectric tensor. However, in this case the spectrum arises from fluctuations of the polarisability anisotropy. Equation (2.1.8) then becomes

$$I_{VH}(\underline{q},\omega) \propto \int_{-\infty}^{\infty} dt \exp(-i\omega t) \left[ \langle \Delta\alpha_{YX}(\underline{q},0) \Delta\alpha_{YX}^*(\underline{q},t) \rangle \sin^2(\theta/2) + \langle \Delta\alpha_{YZ}(\underline{q},0) \Delta\alpha_{YZ}^*(\underline{q},t) \rangle \cos^2(\theta/2) \right] \quad (2.1.9)$$

where  $\Delta\alpha_{ij}(\underline{q},t)$  is the fluctuation in the  $ij$  component of the polarisability tensor with wavevector  $\underline{q}$  at time  $t$ . Equation (2.1.9) can be written<sup>[10,13]</sup>

$$I_{VH}(\underline{q},\omega) = I_{YX}(\underline{q},\omega) \sin^2(\theta/2) + I_{YZ}(\underline{q},\omega) \cos^2(\theta/2) \quad (2.1.10)$$

Thus there are two independent but related dynamical problems to be solved: one for  $I_{\underline{YX}}(\underline{q},\omega)$  and one for  $I_{\underline{YZ}}(\underline{q},\omega)$ . Section 2.3 reviews the various theories that have been developed to describe the experimentally observed spectra.

## 2.2 Polarised Rayleigh-Brillouin Scattering

### 2.2.1 Low Viscosity Liquids

The polarised Rayleigh-Brillouin spectrum arises from localised density fluctuations in the liquid; thermally induced density fluctuations give rise to propagating longitudinal modes, that is the longitudinal phonons (sound waves), from which inelastic light scattering occurs. Entropy, or heat fluctuations, give rise to the elastically scattered Rayleigh component. A typical polarised Rayleigh-Brillouin spectrum is shown in Fig 2.2.1<sup>[11]</sup>. The Brillouin doublet, shifted in frequency by  $\omega_L$  and disposed symmetrically about the Rayleigh line, is due to the inelastic scattering from the longitudinal phonons. In supercooled liquids the transverse thermal phonons can also propagate and give rise to transverse Brillouin peaks. The Rayleigh-Brillouin spectrum of supercooled toluene<sup>[14]</sup> is shown in Fig 2.2.2. The longitudinal and transverse Brillouin peaks are not at the same frequencies. Light scattering from transverse shear modes is discussed in Section 2.3.1.

The light scattering spectrum arising from density fluctuations from a simple purely viscous liquid has been calculated using the linearised hydrodynamic equations of irreversible thermodynamics<sup>[9,10,12]</sup>. The details of the spectrum are now well understood<sup>[17]</sup>. The central Rayleigh line has a half width at half maximum height given by  $D_T q^2$ , where  $D_T$  is the thermal diffusivity. In liquids observed at  $90^\circ$   $D_T q^2$  is too narrow (10 - 40 MHz) to be resolved with a Fabry-Perot interferometer but is accessible using photon correlation techniques. The widths of the observed Rayleigh peaks in this work are therefore entirely due to instrumental effects (discussed in Section 3.1.1). The velocity of the longitudinal phonons ( $V_L$ ) is

Fig 2.2.1 Polarised Rayleigh-Brillouin spectra of octamethylnonane [11]

- (a)  $T = 100\text{ }^\circ\text{C}$
- (b)  $T = 23\text{ }^\circ\text{C}$

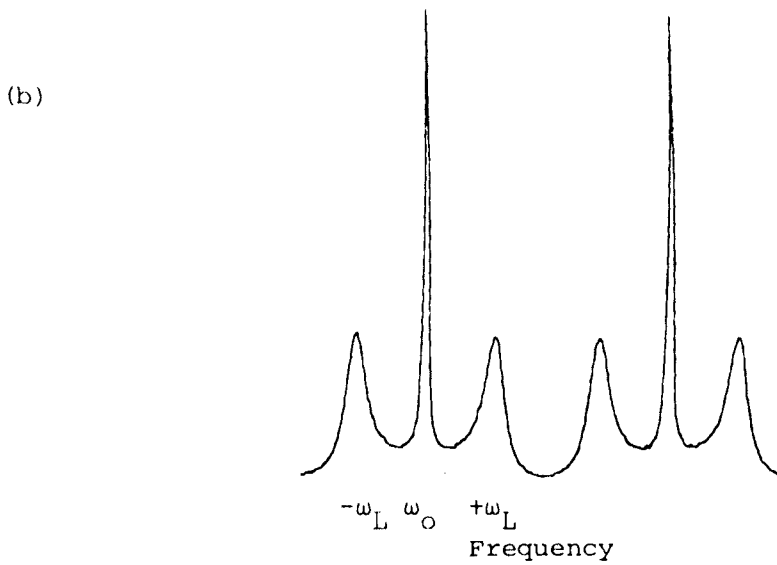
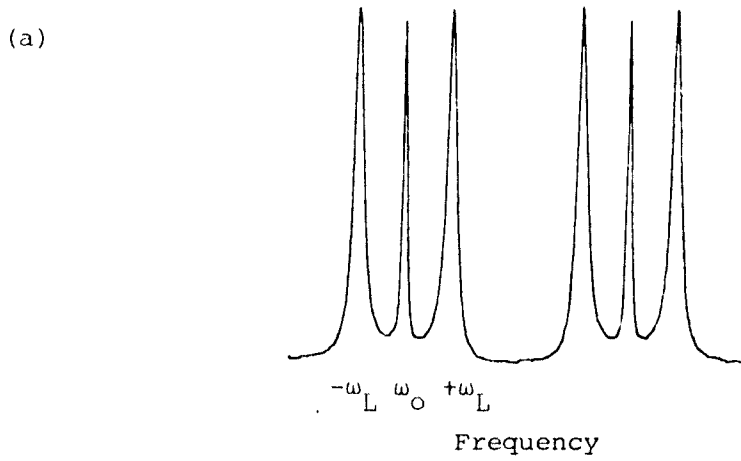
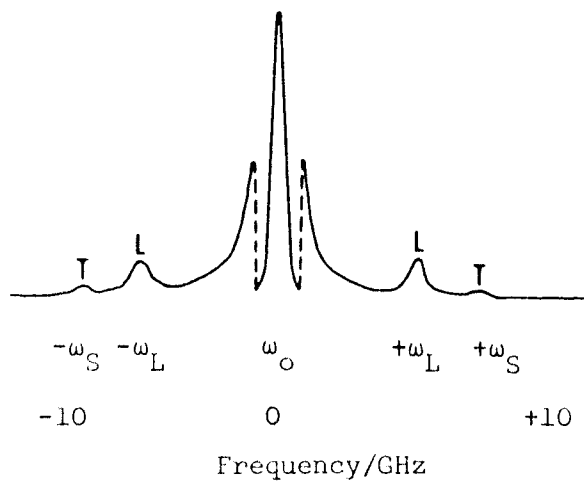


Fig 2.2.2 Total Rayleigh-Brillouin spectrum of supercooled toluene showing both transverse ( $\omega_S$ ) and longitudinal Brillouin ( $\omega_L$ ) [14]



proportional to the frequency shift ( $\omega_L$ ), typically in the range 0 - 10 GHz for 90° scattering, and may be determined from the expression

$$v_L = \omega_L \lambda_i / (2n \sin(\theta/2)) \quad (2.2.1)$$

where  $\lambda_i$  is the incident laser wavelength,  $\theta$  the scattering angle and  $n$  the liquid refractive index. Because the sound waves are damped the shifted peaks, which are Lorentzian in shape, have a width given by:

$$\Gamma_L = \alpha_L v_L \quad (2.2.2)$$

where  $\alpha_L$  is the attenuation coefficient for the phonons. The velocity of the longitudinal acoustic phonons is determined by the longitudinal modulus ( $M$ )

$$M = K + 4/3 G \quad (2.2.3)$$

where  $K$  is the modulus of compression and  $G$  is the shear modulus<sup>[15]</sup>. The sound velocity depends on the real part of  $M$  evaluated at the frequency of the Brillouin shift

$$v_L(\omega_L) = \left[ \frac{M'(\omega_L)}{\rho} \right]^{1/2} \quad (2.2.4)$$

where  $M'$  is the real part of the longitudinal modulus and  $\rho$  is the density.

### 2.2.2 Viscoelastic Liquids

In a liquid the relaxing molecular internal degrees of freedom may couple to the translational motion. When the time scale of these relaxations is of the order  $10^{-10}$  seconds the liquid exhibits significant viscoelasticity<sup>[17]</sup>. In this case an additional feature appears in the spectrum. This line, first predicted by Mountain<sup>[16]</sup> and called the "Mountain line", is centred on the Rayleigh line and has a spectral shape given by<sup>[17]</sup>

$$S_M(\omega) = \int_0^{\infty} \frac{\rho(\tau)\tau d\tau}{1 + (\omega\tau)^2} \quad (2.2.5)$$

where  $\rho(\tau)$  is the distribution of relaxation strengths for the relaxation processes. The shape of the Mountain peak is independent of  $q$ . Equation (2.2.5) represents a distribution of Lorentzian functions which when combined do not produce a single Lorentzian lineshape. However, in practice, as the temperature rises one relaxation mechanism dominates and the spectrum shown in Fig 2.2.1(b) can be fitted to a sum of two central Lorentzian peaks and two shifted Brillouin peaks<sup>[17]</sup>. In a recent publication Carroll and Patterson<sup>[18]</sup> examined the shape of the Mountain line over a range of temperatures down to near the glass transition for a series of highly branched alkanes. They found that a distribution of relaxation times was needed to describe the observed Mountain peak in the high viscosity regime.

To summarise, the polarised Rayleigh-Brillouin spectrum for a purely viscous liquid is well described by three Lorentzians; one centred at the incident frequency and two shifted by  $\pm \omega_L$ . An additional peak, the Mountain line, that can be represented by a Lorentzian centred on the Rayleigh line is present in the viscoelastic regime.

### 2.3 Depolarised Rayleigh-Brillouin Scattering

The depolarised Rayleigh-Brillouin scattering spectrum is caused by anisotropy in the molecular polarisability tensor. The low frequency region of this spectrum is associated predominantly with the reorientational motion of the molecules causing local variations in this tensor, while the high frequency region, often called the "Rayleigh wing", is associated with collisional effects.

In the simple case where molecular reorientation gives rise to anisotropic fluctuations, the spectrum is a single Lorentzian centred at the exciting frequency. The width of this line is inversely proportional to the collective reorientational correlation time. The single-particle orientational correlation function also decays exponentially and can be related to the collective reorientational correlation function<sup>[13]</sup>

$$(2\pi \Gamma)^{-1} = \tau_{LS} = (g_2/J_2) \tau_S \quad (2.3.1)$$

where

$\Gamma$  is the half width of the Lorentzian

$\tau_{LS}$  is the light scattering correlation time

$\tau_S$  is the single-particle correlation time

$g_2$  is the static orientational correlation parameter

$J_2$  is the dynamical orientational correlation parameter

The orientational correlation parameters,  $g_2$  and  $J_2$ , are discussed in Section 2.4.3.

The correlation times obtained may be related to simple models of molecular reorientation based on rotational diffusion. However, when coupling between molecular reorientation in microscopic terms (or the fluctuations in the stress tensor in macroscopic terms) and

the hydrodynamic shear modes occur, new features appear in the spectra. These are discussed in Section 2.3.1. In addition, when interaction induced contributions to the polarisability fluctuations are considered, the spectrum becomes yet more complex. The effects of these contributions are discussed briefly in Section 2.3.2.

### 2.3.1 Low Frequency Region of the Spectrum

The depolarised doublet, Fig 2.3.1(b), found in the light scattering spectrum of a system of optically anisotropic molecules was first predicted by Leontovich<sup>[19]</sup> on the basis of a hydrodynamic theory. Rytov<sup>[20]</sup> presented a more general approach to the same analysis. Fundamentally, the Leontovich and Rytov theories assumed that the light scattering spectra were due to fluctuations in the stress tensor and that the doublet arises due to coupling of the stress tensor to low frequency shear waves. However, Rytov's phenomenological theory was not found to be in quantitative agreement with experimental results<sup>[21,22,23]</sup>.

Numerous theories have been developed using both the simple viscoelastic theory<sup>[24,25]</sup> and several microscopic approaches<sup>[13,26-29]</sup> based on the Mori formalism<sup>[30]</sup>. The Mori formalism is essentially a statistical mechanical approach to generalised hydrodynamics; a set of "primary" variables is chosen, generally an orientation or polarisability tensor, which couple directly to the local dielectric constants. Additional "secondary" variables, generally a momentum density tensor, are also chosen. These are not directly related to the dielectric fluctuation but are coupled to the primary variable through linear transport equations.

The various theories are discussed by Tsay and Kivelson<sup>[31]</sup>, who examined the merits of the early theories and by Searby et al<sup>[32]</sup>

who compared and contrasted results predicted by the theories under different physical conditions. The number of variables in each theory and their physical interpretation differ from author to author. However, all the two-variable theories predict the same general spectral distribution in the region of low viscosity. Using, as an example, the notation of Andersen and Pecora<sup>[28]</sup> the depolarised (VH) spectrum from a liquid composed of rigid symmetric top molecules is given by

$$I_{VH}(\underline{q}, \omega) \propto \frac{\Gamma}{\Gamma^2 + \omega^2} \sin^2(\theta/2) + \frac{\Gamma[\omega^2 + \beta^2\Gamma^2(1-R)]\cos^2(\theta/2)}{(\omega^2 - \beta\Gamma^2)^2 + \omega^2(\Gamma + \Gamma\beta(1-R))^2} \quad (2.3.2)$$

where

$$\beta = q^2 \eta_s / \Gamma$$

$\eta_s \equiv \eta/\rho$ , is the kinematic shear viscosity:  $\eta$  is the shear viscosity and  $\rho$  the density  
 $q$  is the scattering vector (equation(2.1.2))

$\Gamma$  is the reciprocal of the molecular reorientation time

$R$  is the dynamic coupling parameter.

The first term in equation (2.3.2) describes a 'sharp' Lorentzian line with half width at half maximum height of  $\Gamma$ , which arises from molecular reorientation. The second term arises from the coupling of shear modes to the molecular reorientation.  $R$ , which lies in the range  $0 < R < 1$ , is a dimensionless coupling parameter which represents the strength of the coupling between molecular reorientation and the shear modes, that is,  $R$  measures the ability of a system under shear to relieve the shear by molecular reorientation.

Equation (2.3.2) can be analysed in terms of the parameter  $\beta$ .

Four characteristic regions can be defined<sup>[32]</sup>

(1)  $\beta \ll 1$

(2)  $\beta < 1$

(3)  $\beta > 1$

(4)  $\beta \gg 1$

Region (1) ( $\beta \ll 1$ ) corresponds to that of liquids composed of small simple molecules, which have very short reorientation times (a picoseconds) and low viscosity.

In this limit equation (2.3.2) reduces to

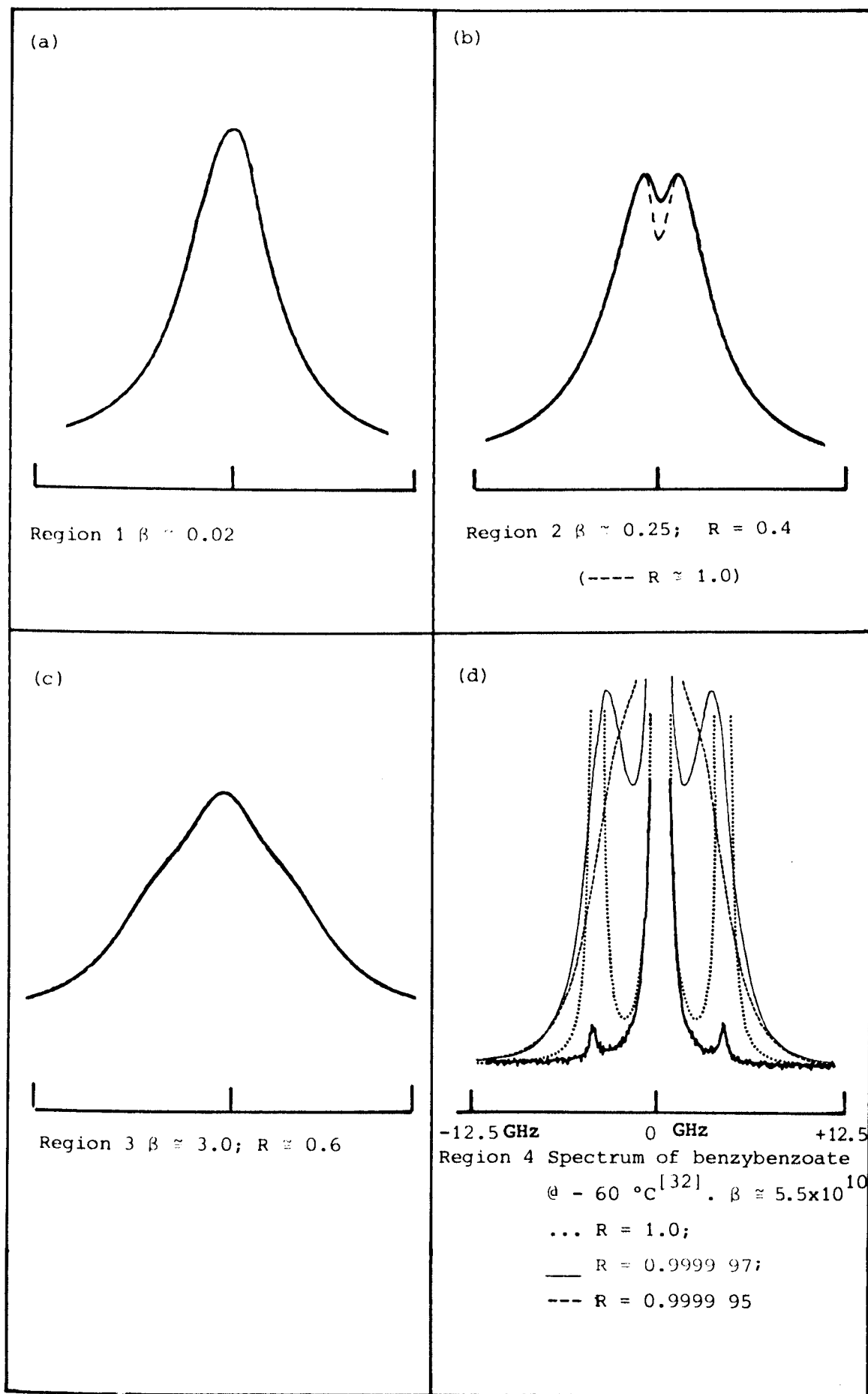
$$I_{\text{VH}}(q, \omega) \propto \frac{\Gamma}{\Gamma^2 + \omega^2} - \frac{R\beta^2 (\Gamma\beta \cos^2(\theta/2))}{(\omega^2 + (\beta\Gamma)^2)^2} \quad (2.3.3)$$

In this regime the central dip is not observed since the half width of the dip, given by  $q^2 \eta_s$ , is too small to be resolved experimentally. The spectrum approximates to a single Lorentzian of half width  $\Gamma$  (Fig 2.3.1(a)).

Region (2) ( $\beta < 1$ ). The central dip is clearly observed in the spectrum (Fig 2.3.1(b)). R parameters are readily obtained from fits to the spectra and lie in the range 0.2 to 0.7. In this region R represents a measure of the depth of the dip relative to the main Lorentzian line.

Region (3) ( $\beta > 1$ ) is characteristic of viscous liquids. The dip disappears and the spectrum is highly non-Lorentzian becoming more triangular in shape (Fig 2.3.1(c)).

Fig 2.3.1 Depolarised VH lineshapes predicted by equation (2.3.2) for four characteristic regions of  $\beta$



Region (4) ( $\beta \gg 1$ ) corresponds typically to supercooled liquids close to the glass transition temperature. In this regime the shear waves become propagative and give rise to well separated doublets, centred upon a sharp depolarised unshifted component. These doublets are analogous to the longitudinal Brillouin spectrum but are not at the Brillouin frequencies (see Fig 2.2.2 in Section 2.2.1). Bezot et al<sup>[33]</sup> observed the doublets in ethylbenzoate and salol. Enright and Stoicheff<sup>[34]</sup> also observed the splitting in liquid salol.

The early two-variable theories predict the spectra fairly well in liquids of low and moderate viscosity. However, although equation (2.3.1) predicts an oscillating doublet at low temperature, when  $\beta \gg 1$  the theory fails to reproduce the experimental intensity. It can be shown that for  $90^\circ$  scattering the integrated intensity of the two shifted terms ( $2I_s$ ) is exactly equal to the intensity ( $I_c$ ) of the central term<sup>[32,33,35]</sup>. This is contrary to experimental results in which the intensity of the central peak is found to be much greater than that of the shifted side band<sup>[33,34,36]</sup>. For example, Bezot et al<sup>[33]</sup> find the ratio  $I_c/2I_s = 90$  for ethylbenzoate at  $-110^\circ\text{C}$  ( $\beta \gg 1$ ) (Fig 2.3.1(d)).

In an attempt to explain the much smaller intensities observed in the side bands, several theories have been proposed. Chappell et al<sup>[37]</sup> derived a three-variable theory that described the observed spectra of triphenylphosphite (TPP) over the range  $-27.7$  to  $87.5^\circ\text{C}$  ( $5000 > \beta > 0.1$ ).

In the supercooled state, that is, at a temperature where the shear wave doublets can be resolved, their theory predicts: (a) the central peak is  $q$  dependent and consists of two Lorentzians with two greatly varying rate constants: (b) the frequency  $\omega_s$  of the shear

peak (analogous to the Brillouin splitting  $\omega_L$  equation (2.2.1)) is proportional to  $q(\Gamma\eta)^{\frac{1}{2}}$ . According to the Stokes-Einstein-Debye relation (discussed in Section 2.4),  $\Gamma$  varies as  $T/\eta$  (this follows from equations (2.3.1) and (2.4.5)) and therefore  $\omega_s$  varies as  $qT^{\frac{1}{2}}$ ; and (c) the width of the shear peak is independent of  $q$ . Using photon correlation spectroscopy Wang et al have shown that prediction (a) is in disagreement with the experimental results obtained for  $\alpha$ -phenyl *o*-cresol<sup>[38]</sup> and for *o*-terphenyl<sup>[39]</sup> in which the shape of the central peak is found to be  $q$  independent and cannot be represented by two Lorentzians. In addition, the frequency of the shear peak is found to be directly proportional to the temperature for the liquids dibutylphthalate<sup>[40]</sup> and 3-phenyl-propanol<sup>[41]</sup>. This conflicts with prediction (b). Prediction (c) does not agree with the results of the angular dependence studies of  $\alpha$ -phenyl *o*-cresol<sup>[42]</sup> and *o*-terphenyl<sup>[43]</sup> in which the shear wave linewidths are found to be proportional to  $q^2$ . In a subsequent paper, Chappell and Kivelson<sup>[44]</sup> also found that their three-variable theory was in disagreement with their experimental results for TPP when studied at three scattering angles ( $60^\circ$ ,  $90^\circ$  and  $120^\circ$ ) at one temperature. This led them to modify their three-variable theory by introducing an additional variable, whose physical meaning was not specified, thus making it a four-variable theory. This modified theory contains eight parameters therefore making it difficult to access the physical parameters and hence to assess the value of the theory.

An alternative three-variable theory has been developed by Wang<sup>[35]</sup>. This theory associates the two weak symmetrically displaced side peaks with the propagating shear phonon. The main advantage of this theory is that only four parameters are needed to describe

the spectra; the collective molecular reorientation rate ( $\Gamma$ ), the shear wave oscillating frequency ( $\Omega$ ), the shear wave relaxation rate ( $\eta_r$ ), and the dynamic coupling coefficient between the polarisability anisotropy and the shear wave ( $\delta$ ). The spectral form obtained by Wang is given by

$$I_{\text{VH}}(\underline{q}, \omega) \propto \frac{\eta_r \omega_s^2 \omega^2 + \Gamma(\omega^2 - \Omega^2)^2}{\omega^2 (-\omega^2 + (\omega_s^2 + \Omega^2))^2 + (\omega^2 \Gamma_s - \Gamma \Omega^2)^2} \text{Cos}^2(\theta/2) + \frac{\Gamma}{\omega^2 + \Gamma^2} \text{Sin}^2(\theta/2) \quad (2.3.4)$$

where  $\Gamma_s = \Gamma + \eta_r$  is the overall relaxation rate of the polarisability correlation function and  $\omega_s^2 = \eta_r \Gamma + \delta$ .

The form of equation (2.3.4) differs from that of equation (2.3.2) by the presence of the quantity  $\Omega$ , which is associated with the oscillation frequency of the shear wave. This is important in viscoelastic systems because the shear wave frequency has both a real and imaginary (relaxation) component. If the real component is neglected the result is an incorrect description of the light scattering data in the viscoelastic regime. Conversely, at high temperature the elastic component of the system decreases and  $\Omega$  vanishes. In this case the shear motion is diffusive and equation (2.3.4) is reduced to the form of equation (2.3.2), that is, the Andersen and Pecora expression.

In a later publication<sup>[42]</sup> this theory was used to analyse the low temperature VH spectrum of  $\alpha$ -phenyl *o*-cresol at various scattering angles. Experimentally the shear wave frequency was observed to decrease linearly with increasing temperature and vanished at a temperature at which the linewidth of the longitudinal Brillouin

spectrum was a maximum. In addition, the shear wave frequency ( $\Omega$ ) was found to be proportional to  $q$  and the linewidth to be proportional to  $q^2$ . The results are in accordance with Wang's theory but the  $q$  dependence of the shear wave frequency and the  $q^2$  dependence of the linewidth are in disagreement with the predictions of Chappell et al<sup>[37]</sup>.

Quentrec<sup>[45,46,53]</sup> has derived a three-variable theory where local order of the centres of gravity of molecules and local orientational order were added to the stress tensor of the fluid. This theory predicts the  $q$  dependence of the shear wave frequency and the  $q^2$  dependence of the sidepeak linewidth. While this is consistent with Wang's theory, Quentrec's theory also predicts that the central peak is strongly  $q$  dependent. Such a prediction has not been observed experimentally<sup>[38,39]</sup>.

Recently, MacPhail and Kivelson<sup>[47]</sup> have presented a generalised hydrodynamic theory of viscoelasticity. In this paper they discuss two-, three- and four-variable theories in an attempt to describe the dynamic behaviour of transverse phenomena (VH depolarised light scattering, flow birefringence, transverse shear waves and viscous flow) in a liquid. They find that a four-variable theory is necessary to fit the VH light scattering data on a supercooled liquid composed of symmetric top molecules (TPP). They find their results are consistent with viscous flow and flow birefringence experiments. However, two of the four variables used in the theory do not have clear physical interpretations.

It would appear that at present the three-variable theory of Wang represents the best model to describe the shear-rotational coupling in the low frequency high viscosity regime. However, as pointed out by Wang et al<sup>[42]</sup>, the comparison of theory with experiment has

only been made with respect to the  $q$  dependence. The proportionality constants were not evaluated, and much work is still needed to ascertain the validity of this theory.

Equation (2.3.2) describes the experimentally observed spectra in the limits  $\beta \ll 1$  and  $\beta < 1$ . However, it only applies for frequency shifts of approximately 15 GHz ( $0.5 \text{ cm}^{-1}$ ) [28]. Several authors have reported a broader Lorentzian background with a width of the order 60 - 200 GHz [48 - 51]. (This is not equivalent to the high frequency spectral wing, discussed in section 2.3.2, which generally occurs at frequencies greater than 900 GHz and is approximately exponential in shape.)

Viovy et al [48,49], making use of a formalism developed by de Gennes [52] and extended by Quentrec [45,53], have shown that the second broad Lorentzian line is due to a second variable describing local anisotropy. In this three-variable theory the two variables linked to the local anisotropy are the density of molecular re-orientation,  $\underline{I}$ , and the anisotropy in the distribution of the centres of gravity,  $\underline{G}$ .  $\underline{G}$  is effectively a measure of local translational order.

Viovy et al [49] consider three alternatives; (i) in the most general case where  $\underline{G}$  and  $\underline{I}$  are mutually coupled primary variables they show [48] that the depolarised spectrum depends on more unknown parameters than there are measurable quantities. Therefore it is not possible to obtain a unique set of values for the unknown parameters, (ii)  $\underline{G}$  is a secondary variable coupled to both  $\underline{I}$  and the velocity gradient (ie shear modes). This case has also been considered by Andersen and Pecora [28], who use the stress tensor and an orientation density as local variables, and Quentrec [45] who uses  $\underline{G}$  and  $\underline{I}$  as local ordering parameters. The results are very similar, identical in the limit of small  $q$  and low frequency, and the VH depolarised

spectrum is the sum of five different Lorentzians. The three-variable theory of Chappel and Kivelson<sup>[37]</sup> also predicts a five Lorentzian spectrum in the high temperature region. In their theory the two  $I_{YZ}(\underline{q}, \omega)$  Lorentzians are predicted to be indistinguishable from the two positive  $I_{YX}(\underline{q}, \omega)$  Lorentzian. This results in a spectrum that can be described by a Lorentzian plus a sharp negative Lorentzian and an additional positive Lorentzians. However, this theory has more undetermined variables and fails to predict the observed spectra in more ways than that of Quentrec's, (iii)  $\underline{G}$  is a primary variable coupled to the velocity gradient but not to  $\underline{I}$ , which is also a primary variable. By generalising Quentrec's results to the case of two primary variables and taking the limit  $q^2 \eta_s / \Gamma_A, q^2 \eta_s / \Gamma_B \ll 1$ , where  $\Gamma_A$  and  $\Gamma_B$  are the widths of the two positive Lorentzians, they obtain a spectrum that contains two wide positive Lorentzians plus one negative narrow Lorentzian.

By combining the experimental results of depolarised light scattering and flow birefringence on the liquids benzene, pyridine, cyanopropyne, 2-butyne, carbon tetrachloride and iodopropyne they propose that  $\underline{G}$  is probably a primary variable (case iii). However, the experimental precision was not sufficient to enable them to be conclusive. With  $\underline{G}$  as a primary variable the depolarised spectrum is given by

$$I_{VH}(\underline{q}, \omega) \propto \left[ \frac{v_A \Gamma_A}{\omega^2 + \Gamma_A^2} + \frac{v_B \Gamma_B}{\omega^2 + \Gamma_B^2} - \frac{q^2 \eta_s}{\omega^2 + (q^2 \eta_s)^2} \cos^2(\theta/2) \left( \frac{v_A R_A}{\Gamma_A} + \frac{v_B R_B}{\Gamma_B} \right) \right] \quad (2.3.5)$$

where

$\Gamma_A, \Gamma_B$  are the halfwidths of the two positive Lorentzians,  
 $v_A$  represents the fraction of the depolarised light scattered by molecular reorientation alone and  $v_B$  the fraction scattered by the translational order.

$R_A$  and  $R_B$  are the coupling parameters between the velocity gradient and  $\underline{I}$  and  $\underline{G}$  respectively.

The relative intensity of the negative Lorentzian now depends on two coupling parameters. Under certain conditions the two positive Lorentzians are of comparable intensity, but typically the second Lorentzian B contains between 10% and 30% of the total depolarised intensity. If the Lorentzian B is disregarded, the remaining terms are formally equivalent to equation (2.3.2) with the following relationship between the parameters:

$$\Gamma = \Gamma_A, R = R_A + \frac{v_B \Gamma_A}{v_A \Gamma_B} R_B$$

In the above theoretical development Viovy et al make the assumption that all fast processes, for example collisions and vibrations, are not coupled to the slow variables and are contained in a tensor  $\underline{F}$ . This assumption, which is inherent in all the theories discussed in this section, is only valid if a time scale separation of the fast and slow processes can be achieved. For many liquids composed of anisotropic molecules a separation is possible and the resulting spectrum consists of the low frequency region, containing one or two Lorentzians and fine structure, superimposed on a broad high frequency background due to intermolecular interactions. Conversely, if there is no time scale separation, then there are contributions to the spectrum due to cross-correlations between the intrinsic and interaction induced polarisability fluctuations.

Viovy et al<sup>[49]</sup> find that the separation of time scales gives good agreement between their theory and experimental results in the range  $\pm 600$  GHz. However, they also argue that  $\underline{I}$  and  $\underline{G}$  cannot relax exponentially at times comparable with the time between molecular

collisions. In this case  $\underline{F}$  contains the short-time behaviour of both  $\underline{G}$  and  $\underline{I}$ . A separation of the variables is extremely complicated and has not yet been achieved. Indeed, as indicated by Chappell and Kivelson<sup>[44]</sup>, as one moves to the higher frequency regime the number of dynamical variables needed to describe the spectra proliferates rapidly and the theory becomes unwieldy.

The theories discussed so far all assume that the molecules are anisotropic in shape. Madden<sup>[54]</sup> has calculated the depolarised Rayleigh spectrum from a system of isotropically polarisable molecules. Scattering is due to dipole-induced-dipole interactions between pairs of density fluctuations. The full spectrum is complicated, extending to frequencies of approximately 3000 GHz ( $100 \text{ cm}^{-1}$ ). However, in the central region, out to approximately 600 GHz, the spectrum is Lorentzian with a linewidth given by:

$$\Gamma \propto 2Dq_0^2 \quad (2.3.6)$$

where

$D$  is the translational self diffusion coefficient,  
 $q_0$  is the magnitude of the scattering vector at the maximum  
in the centre of mass structure factor.

Qualitative agreement has been obtained using this theory to describe the experimentally observed central Lorentzian in liquid argon<sup>[55]</sup>.

This translational self diffusion central Lorentzian is present for all liquids but its intensity may be very small in comparison to the scattering from the intrinsic molecular anisotropy. Patterson and Carroll<sup>[1]</sup> examined the depolarised light scattering spectrum of the alkanes n-pentane to n-nonane and several branched isomers. They reasoned that since the intrinsic molecular anisotropy decreases

with decreasing molecular size and increasing branching, the Lorentzian component of the spectra of the small almost spherical alkanes may be due to interaction induced effects.

However, Patterson and Carroll's approach assumed that the proportionality constant in equation (2.3.6) was equal to unity, that is, they calculated the theoretical halfwidth and compared it to that determined experimentally. The linewidths were found to be equal and hence Patterson and Carroll concluded that Madden's theory was appropriate. The above assumption is not necessarily valid for molecular liquids and hence the results for the highly branched alkanes are open to interpretation. Nevertheless, it is possible that translational diffusion and light scattering from intermolecular pair anisotropy could play an important role in the highly branched pseudo-globular alkanes.

To summarise, it would appear that a complete theory that quantitatively describes the experimentally observed VH depolarised light scattering spectrum over the entire viscosity regime  $1 \ll \beta \ll 1$  is not available at present. Although Wang's theory seems to be the most appropriate in the limit  $\beta \gg 1$  it does not predict a two Lorentzian spectrum in the region  $\beta \ll 1$ . In fact it reduces to the two-variable theory of Andersen and Pecora (equation 2.3.2).

At this time the theory of Quentrec is probably the most appropriate over the complete viscosity range. In the high viscosity region the inconsistency is that the theory predicts a strongly angularly dependent central peak that has not been observed experimentally. However, only a limited number of experiments have been performed which examine this dependence<sup>[38,39,56]</sup> and more data is needed, not only to analyse this effect but also to quantify the proportionality constants in Wang's theory<sup>[35]</sup>.

Each theory must be assessed on its ability to describe the experimentally observed data using parameters that can be related to physical properties of the liquid. However, at the present time a single theory is not available to describe the observed data over the complete viscosity range,  $1 \ll \beta \ll 1$ , even for rigid symmetric top molecules. The situation is far more complex when flexible molecules with time varying conformations are considered. It is hoped that the experimental data presented in this thesis can aid future theoretical considerations of the nature of the liquid state.

### 2.3.2 Collision Induced Light Scattering

For liquids composed of isotropic molecules depolarised light scattering arises exclusively from intermolecular interactions causing polarisability fluctuations.

For anisotropic molecular liquids the interaction induced phenomena contribute to the depolarised light scattering spectrum, in addition to the polarisability fluctuations associated with the intrinsic molecular anisotropy. Keyes et al<sup>[57]</sup> developed a theory relating depolarised light scattering spectra to two separate processes, one being molecular reorientation, a relatively slow process, and the other being a fast intermolecular interaction. As discussed in the previous section, if there is no time scale separation then there will be contributions in the spectrum from cross correlations between the intrinsic and interaction induced polarisability fluctuations. All the theoretical calculations assume that there is such a time scale separation. However, this simple spectral form, in which the interaction induced and intrinsic anisotropy fluctuations are separable is only likely to hold for liquids over a limited range of temperatures, if at all.

The interaction induced contribution dominates the depolarised spectrum in the high frequency regime,  $> 900$  GHz, and the lineshape appears to be a piecewise exponential. The experimental and theoretical progress<sup>[58]</sup> has been reviewed by Gelbart<sup>[58]</sup> and more recently by Tabisz<sup>[59]</sup>.

In general, when two molecules collide they suffer distortions in their electronic charge distributions. These distributions persist for the time it takes a molecule to cross the effective range of the intermolecular potential, approximately  $10^{-13}$  seconds. Thus equation (2.1.9) will not account for the short time phenomena.

There are three mechanisms thought to be mainly responsible for the time evolving properties of the polarisability fluctuations: (i) the dipole-induced-dipole (DID), (ii) electron overlap (EO), and (iii) frame distortion interactions.

(i) In the DID model the incident field induces a moment on a molecule. A neighbouring molecule, which is in the field of the first dipole, has induced on it an additional small moment, in general not in the direction of the incident field. This model accounts for relatively long range effects of the collisional process, that is, moderate separations of the two molecules, and varies as  $x^{-3}$  where  $x$  is the intermolecular distance.

(ii) In the EO model the anisotropy fluctuations arise from the overlap and subsequent distortion of the electron clouds. This effect has a much stronger dependence on the intermolecular separation,  $x^{-9}$ , than DID effects.

(iii) Molecular frame distortion is a very short range collisional distortion that occurs in molecular liquids. An  $x^{-13}$  dependence has been proposed<sup>[60]</sup>.

In the liquid (dense) state all three effects are likely to be present and it may be that it is impossible to separate them. However, it would seem likely that for molecular liquids the high frequency portion of the collisional spectrum is due to the short range intermolecular interaction and hence is determined mainly by EO processes. Bucaro and Litovitz<sup>[60]</sup> derived an expression for the line profile of isotropic liquids at high frequencies using a binary collision EO model.

$$I(\omega) \propto \omega^{2(m-7)/7} \exp(-\omega/\omega_0); \quad \omega > \omega_0 \quad (2.3.7)$$

where the induced polarisability is taken to vary as  $x^{-m}$  and  $\omega_0$  is related to the mean frequency of collision. They propose that  $m = 13$ , that is, that the polarisability fluctuations are due to molecular frame distortion. However, equation (2.3.7) assumes a zero impact parameter which is physically unrealistic. When this limitation is removed the pre-exponential factor reduces to  $\omega^0$ . Therefore

$$I(\omega) \propto \exp(-\omega/\omega_0) \quad (2.3.8)$$

The quantity  $\omega_0$  is related to the mass ( $m$ ) of the colliding unit by

$$\frac{1}{\omega_0} = 2\pi \times \left[ \frac{m}{k_B T} \right]^{1/2} \quad (2.3.9)$$

The calculations of the theoretical interaction induced spectrum from anisotropic molecular liquids is much more complicated than the above model, which assumes isotropically polarisable molecules undergoing binary collisions, because of the added complexity of molecular reorientation and flexible molecules.

## 2.4 Analysis of Molecular Correlation Times

### 2.4.1 The Stokes-Einstein-Debye Relation

Pecora<sup>[61]</sup> has calculated the depolarised light scattering spectrum from a system of rigid anisotropic molecules. He assumes that reorientation takes place by rotational diffusion and neglects orientational correlations and the coupling with hydrodynamic modes. The spectrum is the weighted sum of five Lorentzians. If the molecules have cylindrical symmetry, that is, are symmetric tops, and are undergoing independent translational and rotational diffusion with respective diffusion coefficients  $D$  and  $\theta_T$ , the spectrum decomposes to one Lorentzian of linewidth  $(q^2 D + 6\theta_T)$ . For small molecules  $q^2 D \ll 6\theta_T$  and the single particle reorientation time is given by

$$\tau_s = \frac{1}{6\theta_T} \quad (2.4.1)$$

For a spherical hydrodynamic particle, that is one in which the rotating particle is much larger than the continuum particles, the rotational diffusion coefficient is related to the viscosity ( $\eta$ ) of the fluid by the Stokes-Einstein-Debye relation<sup>[62]</sup>

$$\theta_T = \frac{k_B T}{f_R} \quad (2.4.2)$$

where  $f_R$ , the friction coefficient, is given by

$$f_R = 8\pi\eta a^3 \quad (2.4.3)$$

and  $a$  is the particle radius. Equation (2.4.1) then becomes

$$\tau_s = \frac{4\pi a^3 \eta}{3k_B T} \quad (2.4.4)$$

This can be written in terms of the molecular volume  $V$  as

$$\tau_s = \frac{V\eta}{k_B T} \quad (2.4.5)$$

This linear relationship between the macroscopic liquid viscosity and the single particle reorientational time has been found to hold for many liquids and solutions<sup>[63,64,67]</sup>. In many cases however, the straight line fit to equation (2.4.5) produces a non-zero intercept<sup>[64-66]</sup>. To take account of the non-zero intercept, equation (2.4.5) is written

$$\tau_s = \frac{V\eta}{k_B T} + \tau_0 \quad (2.4.6)$$

where  $\tau_0$  is the zero viscosity intercept. The origin of  $\tau_0$  is uncertain but it has been associated with inertial rotation<sup>[64]</sup>, that is, the free rotor time in the limit of zero viscosity.

$$\tau_0 = \frac{2\pi}{9} \left[ \frac{I}{k_B T} \right]^{\frac{1}{2}} \quad (2.4.7)$$

However, free rotor reorientation is not consistent with the rotational diffusion model used in the derivation of the Stokes-Einstein-Debye model. In this model  $\tau_0$  is zero.

Equation (2.4.5) and (2.4.6) apply only to spherical particles. For ellipsoidal particles the theory is more complicated. Perrin<sup>[68]</sup> has derived expressions for  $f_R$  in terms of the particle dimensions and the liquid viscosity.

For a prolate ellipsoid

$$f_R = \left[ \frac{4V\eta}{r^2} \right] \left[ \frac{1 - r^4}{(2 - r^2)G(r) - 1} \right] \quad (2.4.8)$$

where  $r$  is the ratio of the minor semiaxis to the major semiaxis of the ellipsoid and  $G(r)$  has the form

$$G(r) = (1 - r^2)^{-\frac{1}{2}} \ln \left[ \frac{1 + (1 - r^2)^{\frac{1}{2}}}{r} \right]; \quad r < 1 \quad (2.4.9)$$

For an oblate ellipsoid  $f_R$  is described by equation (2.4.8) but with  $G(r)$  now given by

$$G(r) = (r^2 - 1)^{-\frac{1}{2}} \tan^{-1} (r^2 - 1)^{\frac{1}{2}}; \quad r > 1 \quad (2.4.10)$$

Equation (2.4.6) can now be written

$$\tau_s = \frac{PV\eta}{k_B T} + \tau_0 \quad (2.4.11)$$

where  $P$  is the Perrin factor

$$P = \frac{2(1 - r^4)}{3r^2((2 - r^2)G(r) - 1)} \quad (2.4.12)$$

The Perrin expression, which is simply the spherical formula multiplied by functions of the axial ratio, shows that the rotational diffusion coefficient for an ellipsoidal particle is smaller than for a spherical particle of the same volume.

#### 2.4.2 Stick-Slip Boundary Conditions

The Stokes-Einstein-Debye relation and the Perrin model of rotational diffusion both assume hydrodynamic conditions, that is, the particles can be treated as being immersed in a continuum fluid. This is a good approximation for a macromolecule immersed in a solvent of small molecules but not for a particle undergoing rotational diffusion in a liquid composed of similar molecules. Further-

more, both models assume *stick* boundary conditions, which stipulate that at the surface of the particle the fluid velocity is zero relative to the particle velocity<sup>[69]</sup>, that is, the continuum rotates with the particle.

It has been shown<sup>[69-72]</sup> that the reorientation of small molecules is usually better described using *slip* boundary conditions. In the case of perfect *slip* there are not tangential forces on the surface of the rotating molecule and only non-spherical molecules are subject to a hydrodynamic drag. The process of rotational diffusion in the perfect *slip* limit can be envisaged as the molecule reorientating within its own cavity without disturbing the surrounding molecules.

The Stokes-Einstein-Debye equation can be modified to take into account the *stick-slip* behaviour. Equation (2.4.11) becomes

$$\tau_s = \frac{\alpha PV\eta}{k_B T} + \tau_0 \quad (2.4.13)$$

where  $\alpha = 1$  for *stick* conditions and  $\alpha = \phi$  ( $0 < \phi < 1$ ) for *slip* conditions.  $\phi$  is a geometric factor; it is 0 for a sphere and 1 for a long rod.

The degree of *slip* depends on the departure of the molecule from spherical symmetry. Hu and Zwanig<sup>[69]</sup> have performed hydrodynamic calculations of the rotational friction coefficients of prolate and oblate ellipsoids as a function of the axial ratio ( $r$ ) using *slip* boundary conditions. In the disc limit (oblate ellipsoid) and the needle limit (prolate ellipsoid) the value of  $\alpha(\text{SLIP})/\alpha(\text{STICK})$  was found to be equal to one. In the limit of a sphere  $\alpha(\text{SLIP})/\alpha(\text{STICK})$  is equal to zero. The results of Hu and Zwanig have been applied to the experimental results of Bauer et al<sup>[73]</sup>

who studied the reorientational relaxation times of a wide variety of small molecules in organic solvents. The experimental results were found to be in general agreement with theoretical predictions using *slip* boundary conditions, whilst the theoretical predictions using *stick* boundary conditions were much too large.

However, complex molecular shapes cannot always be well represented by a spheroid. Youngren and Acrivos<sup>[70]</sup> obtained frictional coefficients for ellipsoids rotating about their principal axes using a curvilinear coordinate system. In the special cases of oblate and prolate ellipsoids their results agree with those of Hu and Zwanig. Youngren and Acrivos were also able to obtain a frictional coefficient for benzene. They modelled the molecular shape as six hemispheres (hydrogen atoms) placed symmetrically on a base (carbon ring). Their results were within 10% of the experimental results of Alms et al<sup>[64]</sup>. This compares to a difference of 40% when benzene was modelled as an oblate spheroid.

The question has arisen as to why macroscopic particles obey *stick* boundary conditions while the slipping boundary condition seems to be more appropriate for molecular motion in liquids. One possible reconciliation of these observations was proposed by Richardson<sup>[74]</sup>. He argued that *slip* on a rough surface is asymptotically equivalent to *stick* on the smooth surface which approximates the actual rough surface. However, Richardson's treatment does not answer the question of how large a particle must be, relative to the scale of surface roughness, for the sticking boundary condition to be correct. Zwanig<sup>[75]</sup> extended Richardson's method to treat the rotation of a "bumpy" infinite cylinder. In the region of bumps or cusps very large fluid velocity gradients cause a large dissipation of energy and the tangential flow along the surface is slowed down. Zwanig found that in the limit of a large particle (500-1000 Å) with a molecularly rough surface, *stick* and *slip* boundary conditions give the same result for the frictional coefficient. Therefore a macroscopic particle appears to exhibit *stick* boundary conditions because the energy

dissipation due to the molecularly rough surface causes the *slip* boundary condition to appear identical to *stick* conditions on the averaged surface.

From the above discussion it is evident that energy dissipation is an important factor when considering the appropriate choice of boundary conditions. However, a molecule does not have a rigid structure or a well defined surface and therefore there are difficulties in assigning boundary conditions to a molecular surface. An approach adopted by Peralta-Fabi and Zwanig<sup>[76]</sup> describes the interaction of the molecule with the fluid by an intermolecular potential. The boundary conditions are replaced by the actual intermolecular force field between the molecule and its surrounding fluid. When a molecule moves it pushes fluid out of its path and sets up velocity gradients. These cause viscous energy dissipation and consequently a viscous drag on the moving molecule. The drag forces were modelled using two simple interaction potentials; a step potential and a ramp potential. Only translational motion was investigated in this study and the results showed that it is possible to calculate the hydrodynamic drag exerted by the fluid on the molecule without imposing boundary conditions. The frictional coefficient calculated was found to be a strong function of the shape of the potential, approaching one as the potential approached infinity. This type of calculation for the hydrodynamic drag on a molecule probably represents the best method of obtaining theoretical values of the molecular friction coefficients since it does not involve any assumptions about boundary conditions. However, the models used were very simple and only apply to translational drag. Until this method is further developed to include more complex potentials and rotational drag, the method of Youngren and Acrivos represents the best approach to obtaining theoretical frictional coefficients.

### 2.4.3 Orientational Correlation Parameters

In a molecular fluid atoms can be strongly bound to others by intramolecular interactions thus producing molecules. These forces tend to constrain the configuration space available to the atoms, and it is these constraints that produce orientational pair correlations between the molecules.

Equation (2.4.13) may be applied to single-particle correlation times measured, for example from Raman scattering and NMR spin-lattice relaxation experiments.

$$\tau_s = \frac{\alpha PV\eta}{k_B T} + \tau_0 \quad (2.4.13)$$

However, depolarised light scattering is a coherent process and it is the collective reorientational relaxation time that is measured<sup>[77]</sup>. Recalling equation (2.3.1)

$$\tau_{LS} = (g_2/J_2)\tau_s \quad (2.3.1)$$

the modified Stokes-Einstein-Debye equation for depolarised light scattering is obtained

$$\tau_{LS} = \left[ \frac{g_2}{J_2} \right] \left[ \frac{\alpha PV\eta}{k_B T} + \tau_0 \right] \quad (2.4.14)$$

The factor  $(g_2/J_2)$  may be written as  $(1 + fN)/(1 + gN)$  where the factors  $fN$  and  $gN$  measure the strength of the static (equilibrium) and dynamic orientational pair correlations respectively.

Kivelson and Madden<sup>[71]</sup> in a review of light scattering in molecular liquids point out that equation (2.4.14) holds to a high degree of accuracy. In the limit of zero viscosity  $\tau_s$  is equal to

the purely inertial rotation time  $\tau_0$ , equation (2.4.7), and is therefore not dependent upon  $(g_2/J_2)$ . Hence equation (2.4.14) becomes

$$\tau_{LS} = (g_2/J_2) \left[ \frac{\alpha PV\eta}{k_B T} \right] + \tau_0 \quad (2.4.15)$$

In most circumstances the difference between equation (2.4.14) and (2.4.15) are negligible.  $\tau_0$  is usually much smaller than  $\tau_{LS}$  and values of  $(g_2/J_2)$  are of the order of one. However, in systems in which  $\tau_0$  is of the same magnitude as  $\tau_{LS}$  the difference between the two equations can cause significant inconsistencies in the interpretation of the data.

The influence on the correlation time of the dynamic correlation factor  $J_2$  has been discussed by Gierke<sup>[78]</sup> for symmetric top molecules. He concluded from symmetry considerations that this factor does not affect the depolarised Rayleigh profile, that is,  $J_2$  is equal to 1 in equation (2.4.14). However according to Wolynes and Deutch<sup>[79]</sup> this result is incorrect if hydrodynamic behaviour is an important component of orientational dynamics. Their calculations were performed with a many particle model in which rotational and translational diffusion were coupled. They also assumed a particle immersed in a continuum which, as already discussed in section 2.4.2, is not necessarily a valid assumption for molecular liquids. Evans et al<sup>[97]</sup> in a computer simulation, discussed in more detail in Section 2.4.4, do not find any evidence for  $J_2 > 1$ . In practice  $J_2$  has been found to be close to 1<sup>[71]</sup>.

The static correlation factor  $g_2$  is given by<sup>[80,81]</sup>

$$g_2 = 1 + \frac{1}{2} \left\langle \sum_{i \neq j}^N 3 \cos^2 \theta_{ij} - 1 \right\rangle \quad (2.4.16)$$

where  $\theta_{ij}$  is the angle between the molecular axes of the  $ij$  pair of molecules and the summation is over a system of  $N$  molecules.

When there is no correlation between pairs of molecules, the ideal gas case,  $g_2 = 1$ . In liquids however, values of  $g_2$  ranging from 1.0 to  $> 2.0$  have been reported<sup>[71]</sup>. It has been shown by de Gennes<sup>[52]</sup> that for liquids in the isotropic phase  $g_2$  follows the relation

$$g_2 = \frac{T}{(T - T_0)} \quad (2.4.17)$$

where  $T_0$  is a temperature just below the observed isotropic-nematic transition. Patterson et al<sup>[82]</sup> obtain results consistent with equation (2.4.17) for the n-alkanes and  $T_0$  was calculated to be  $> 100$  °C below the melting point.

In conclusion the Stokes-Einstein-Debye equation represents a useful method of relating molecular correlation times obtained from depolarised light scattering experiments to the macroscopic viscosity of the liquid. By fitting experimental data to equation (2.4.15) information can be extracted about the dynamical behaviour of molecules in the liquid state.

#### 2.4.4 Models and Computer Simulations

The discussion presented in Sections 2.3.1 to 2.4.3 is based on the model of a rigid symmetric top molecule. However, the experimental work presented in this thesis describes light scattering from flexible non-symmetric molecules. In this section an attempt is made to bridge this gap by examining models and computer simulations of alkane chains.

The conclusion of the previous section is that the molecular reorientational correlation time can be directly related to the line-width of the Lorentzian component of the depolarised Rayleigh spectrum.

By combining equation (2.3.1) and equation (2.4.1) this can be written

$$\tau_{LS} = (g_2/J_2)\tau_S = (g_2/J_2)\frac{1}{6\theta_T} \quad (2.4.18)$$

All the terms are as previously defined. As discussed in Section 2.4.1  $\tau_S$  is only equal to  $(1/6\theta_T)$  in the limit of a rigid symmetric top molecule. For an asymmetric rigid molecule Pecora<sup>[61]</sup> has calculated the depolarised Rayleigh spectrum to be composed of five Lorentzians corresponding to rotational diffusion about the different axes. Each Lorentzian is weighted according to the optical anisotropy about the corresponding reorientational axis. In general the linewidths are comparable and the individual components are not separable in the spectra. Alms et al<sup>[67]</sup> discuss the circumstances under which the various components are separable, the conclusion being that this is only possible if the Lorentzian linewidths are significantly different, the intensities comparable, and the signal to noise ratio very high. There have not been any light scattering measurements in which the individual Lorentzian components due to rotation about the different molecular axes have been separated. However, there have been NMR relaxation experiments in which a successful separation of the individual reorientational components has been achieved<sup>[83]</sup>.

For flexible molecules such as the alkanes the situation is even more complex as any single molecule can take up a number of different conformations. Each conformation will have a different characteristic reorientation time about its separate axes. The observed depolarised Rayleigh spectrum will be the sum of up to five separate Lorentzians for each conformation, with each weighted

according to the anisotropy of each conformation about the axis concerned. The optical anisotropy of the alkanes is a strong function of chain conformation being a maximum for the all-*trans* state and a minimum for the most globular state. In addition, further complications arise because the population of the individual conformations are constantly changing and molecules continuously undergo transitions between them. The rate of the transition is important. If the transition time between conformational states is longer than the characteristic reorientational time the spectra could be analysed, theoretically at least, in terms of individual conformation contributions. Conversely, if the transition time is of the same order, or less than the reorientational time, the observed spectra could be analysed in terms of the reorientation of a molecule in an average conformational state.

As already mentioned in preceding sections (Section 2.3.1 and Section 2.3.2) if two processes proceed on comparable time scales then there is the possibility of coupling between them. In the above case where the reorientational and conformational rates are comparable extra features, due to coupling interactions, could appear in the spectrum. Further, the time scale of the conformational changes will be related to the collisional processes in the liquid. This allows for the additional possibility of coupling between reorientational motion and collisional processes.

From the above discussion it is apparent that flexible anisotropic molecules can appreciably complicate the theoretical formulations discussed in Section 2.3.1 and Section 2.3.2. Therefore a knowledge of the dynamics of chain molecules is required before a complete analysis and hence understanding of the observed depolarised Rayleigh light scattering spectrum can be accomplished.

Computer simulations of liquid systems at the molecular level are the primary source of non-experimental information about their structure and dynamical properties. The original calculations were based on Monte Carlo (MC) methods<sup>[86]</sup>. From such simulations only the static properties are available although a limited amount of dynamical information may be derived from the static properties.

A more direct way of obtaining information about the dynamical properties of chain motion is the technique of molecular dynamics (MD)<sup>[84]</sup>. In general for the n-alkanes the model consists of rigid carbon-carbon bonds, that are free to rotate, with a common length of 1.53 Å and the angles between adjacent bonds fixed at 109° 28' (the tetrahedral bond angle). The barrier to rotation of two parts of a chain adjacent to a carbon-carbon bond are modelled with a potential energy function. In most cases the hydrogen atoms are not explicitly included. The simulations are performed by setting a number of molecules, of the order of a hundred, in a volume such that the number of molecules per unit volume matches the density in the thermodynamic state being simulated. The interactions between adjacent CH<sub>2</sub> and CH<sub>3</sub> groups are described by means of Lennard-Jones potentials which are generally truncated to prevent an atom interacting more than once with any other atom. From molecular dynamics calculations a variety of thermodynamic information is obtained, for example, *trans/gauche* ratios, pair distribution functions and internal chain transition times.

The main problem with any molecular dynamics simulation involves the choice of realistic potential functions to represent the model system under consideration. Stochastic dynamics (SD)<sup>[95]</sup> simulations have been used to circumvent this limitation. The simplest form of SD is called Brownian dynamics (BD)<sup>[95]</sup> in which one molecule in vacuo

is considered. The influence of neighbouring molecules is represented by a potential that includes the average interaction with the surrounding molecules. In addition, a randomly fluctuating force having stochastic properties that are determined by the liquid considered is used to represent the deviation of the real force from the mean force exerted by the molecular environment. These are the basic simulation techniques that have been applied to the n-alkanes. A discussion of the results and limitations of some of these simulation is now presented.

Ryckaert and Bellemans<sup>[84]</sup> applied one of the first molecular dynamics simulation to short n-alkane chain liquids. They studied the liquids n-butane and n-decane. An important result for the interpretation of spectra is that the average time between conformational changes for each of the nine carbon-carbon bonds in n-decane at 480 K is approximately 2 ps. Thus for the n-decane molecule the average time between conformational changes is approximately 0.22 ps.

Rebertus et al<sup>[85]</sup> examined n-butane in a variety of non-polar solvents using molecular dynamics simulations. These "exact" results were compared with Monte Carlo calculations of Pratt et al<sup>[86,87]</sup> where n-butane was modelled as two cavities. Qualitative agreement was found but the approximate two-cavity theory was found to overestimate the solvent effect on the conformational equilibrium.

Weber<sup>[88,89]</sup> has performed molecular dynamics calculations of n-butane and n-octane using a realistic model incorporating bond stretch and bend potentials, rotational potentials and Lennard-Jones fluid interactions. The additional flexibility of this model, that is, the bond stretch and bend potentials, resulted in good agreement between available experimental and simulation data for n-butane. In

the case of n-octane Weber obtains rotational diffusion constants for the middle bond vector of  $0.28 \text{ ps}^{-1}$  to  $0.57 \text{ ps}^{-1}$  over the temperature range 300 K to 600 K. This corresponds to reorientational frequencies, of the middle bond vector, of 270 GHz and 545 GHz. However, Weber does not discuss how the reorientational diffusion coefficient of the middle bond vector relates to that for the whole molecule.

In a series of papers Evans and Knauss<sup>[90,91,92]</sup> simulated the reorientational motion of alkane chains, up to six carbon-carbon bonds, using a statistical theory where bond lengths and nearest neighbour bond angles were held constant. The correlation times obtained sampled overall tumbling of the molecule investigated in addition to the internal torsional dynamics. In a later publication<sup>[4]</sup> they compare the results of the statistical theory with results from a Brownian dynamics simulation of the alkanes n-pentane to n-undecane. Similar approximations are made in this simulation: rigidly constrained bond lengths and bond angles. In addition *trans* and *gauche* minima are treated equally. Evans and Knauss identify the  $Q = 1$  mode, first harmonic correlation time, as the closest to molecular reorientation. Comparing their simulation results with correlation times obtained from dielectric relaxation measurements<sup>[93]</sup> on a series of 1-bromoalkanes they conclude that the appropriate potential is the  $U/k_B T = 5$ ;  $U/k_B T = 0$  and  $U/k_B T = \infty$  are the freely rotating chain and rigid body potentials respectively. The  $U/k_B T = 5$  potential was chosen by interpolating between results for  $U/k_B T = 4$  and  $U/k_B T = 8$ .

In Section 5.3.4 the simulation results of Evans and Knauss are compared to the experimental results obtained from depolarised light scattering presented in this thesis.

As already mentioned the conformational transition rate will depend on the intermolecular collision frequency. Montgomery et al<sup>[94]</sup>, using stochastic molecular dynamics calculations, examine the collision frequencies for n-butane, n-pentane and n-decane. A comparison of results obtained for different collisional rates, that is, the average frequency at which the velocity of a particular mass on the chain is randomised, with results from molecular dynamics simulation gives the closest (< 10%) agreement when the collisional rate is approximately  $2.0 \times 10^{12}$  Hz. The average time between *trans-gauche* (t-g) transitions for n-butane is calculated to be 24 ps. This is approximately ten times longer than that calculated by Ryckaert and Bellemans.

In a review of stochastic dynamics Gunsteren et al<sup>[95]</sup> discuss how various approximations can be incorporated into the simulation to produce a variety of stochastic dynamics models. They compare a simple stochastic dynamics simulation (Brownian dynamics) with the molecular dynamics simulation of Ryckaert and Bellemans for n-butane and n-decane. They find that the results from the two simulations are essentially the same: an average time between *gauche* and *trans* states of 15 ps and 3 ps for n-butane and n-decane respectively.

Evans et al<sup>[96]</sup> using an Enskog type kinetic theory calculate the collective and single-particle orientation correlation times for ellipsoids in a bath of spheres. Both the ellipsoids and spheres are assumed to be smooth and hard. They find that the particle shape anisotropy plays the role of the roughness parameter used in hard sphere calculations. Comparison of their theory with experimental results indicates that the kinetic theory consistently neglects part of the frictional drag since in all cases studied the

calculated times were a factor of 2 to 4 below the experimental values. They conclude that the rotational relaxation problem requires a more comprehensive treatment of the dynamics of the bath. From their calculations they find no evidence that the dynamic orientational correlation parameter  $J_2 > 1$ . In recent publications the same authors<sup>[97,98]</sup> have used the kinetic theory to calculate the coupling parameter (R) for a neat fluid of hard smooth ellipsoids. They find that the theory predicts that R is insensitive to molecular shape, the density of the liquid and to the temperature, as borne out by experiment. The calculated values of R ranged from 0.5 to 0.65 as compared to the experimental values of approximately 0.4 for a variety of symmetric top molecules.

From the results of the simulations an average value of the collisional rate for the n-alkanes would be  $\omega_{\text{COLL}} = 2 \times 10^{12}$  Hz and an average time between conformational changes would be  $\tau_{\text{t-g}} = 1-4$  ps for n-decane and  $\tau_{\text{t-g}} = 10-30$  ps for n-butane.

As already discussed the reorientational times depend upon these timescales; if a timescale separation does not exist between the collisional and reorientational motion then extra features may be observed in the spectrum due to rotational-collisional coupling.

## CHAPTER 3 - EXPERIMENTAL TECHNIQUES AND DATA ANALYSIS

### Contents

- 3.1 Experimental Techniques
  - 3.1.1 Description of the Light Scattering Spectrometer
  - 3.1.2 Measurement of the Free Spectral Range
  - 3.1.3 Alignment of the Fabry-Perot Interferometer
  - 3.1.4 Sample Cell Holder
  - 3.1.5 Thermostatting of the Sample
  
- 3.2 Sample Preparation and Ancilliary Measurements
  - 3.2.1 Filtration Techniques
  - 3.2.2 Measurement of Kinematic Viscosity
  - 3.2.3 Measurement of Density
  - 3.2.4 Measurement of Refractive Index
  
- 3.3 Analysis of the Spectral Data
  - 3.3.1 Description of the Analysis Program
  - 3.3.2 Statistical Analysis of the Experimental Data

### 3.1 Experimental Techniques

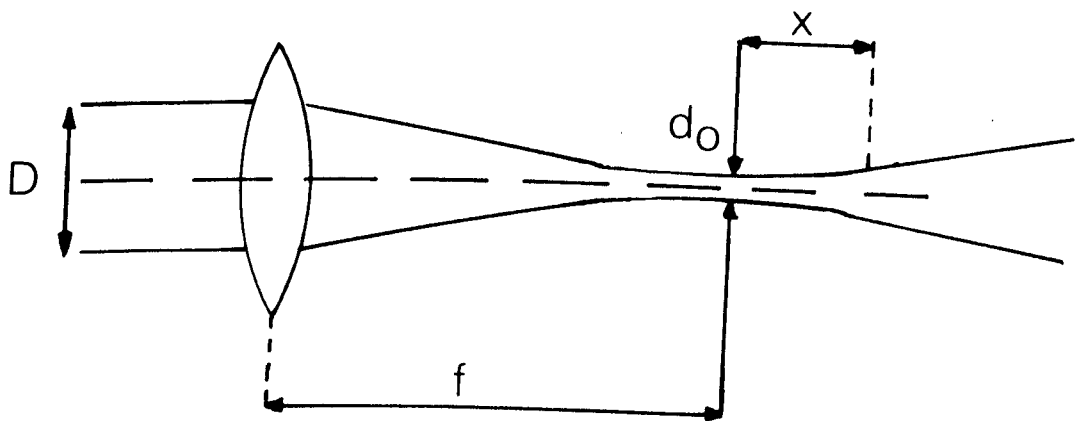
#### 3.1.1 Description of the Light Scattering Spectrometer

Measurements of the depolarised (VH) and polarised (VV) Rayleigh-Brillouin spectra were made using the light scattering arrangement shown in Fig 3.1.1. A Spectra-Physics model 165 argon ion laser operating in a single longitudinal mode was used as a source. Single mode operation was attained by the inclusion of an intra-cavity air spaced etalon (Spectra Physics Model 589).

The power of the focused beam passing through the sample was < 300 mW for the work on the oleic acid and octanoic acid solutions. For the measurements on the small branched alkanes laser powers up to 700 mW were used. A uniform low divergence distribution of the power density within the scattering volume was attained by using the Gaussian line shape of the laser mode combined with a lens of 16 cm focal length.

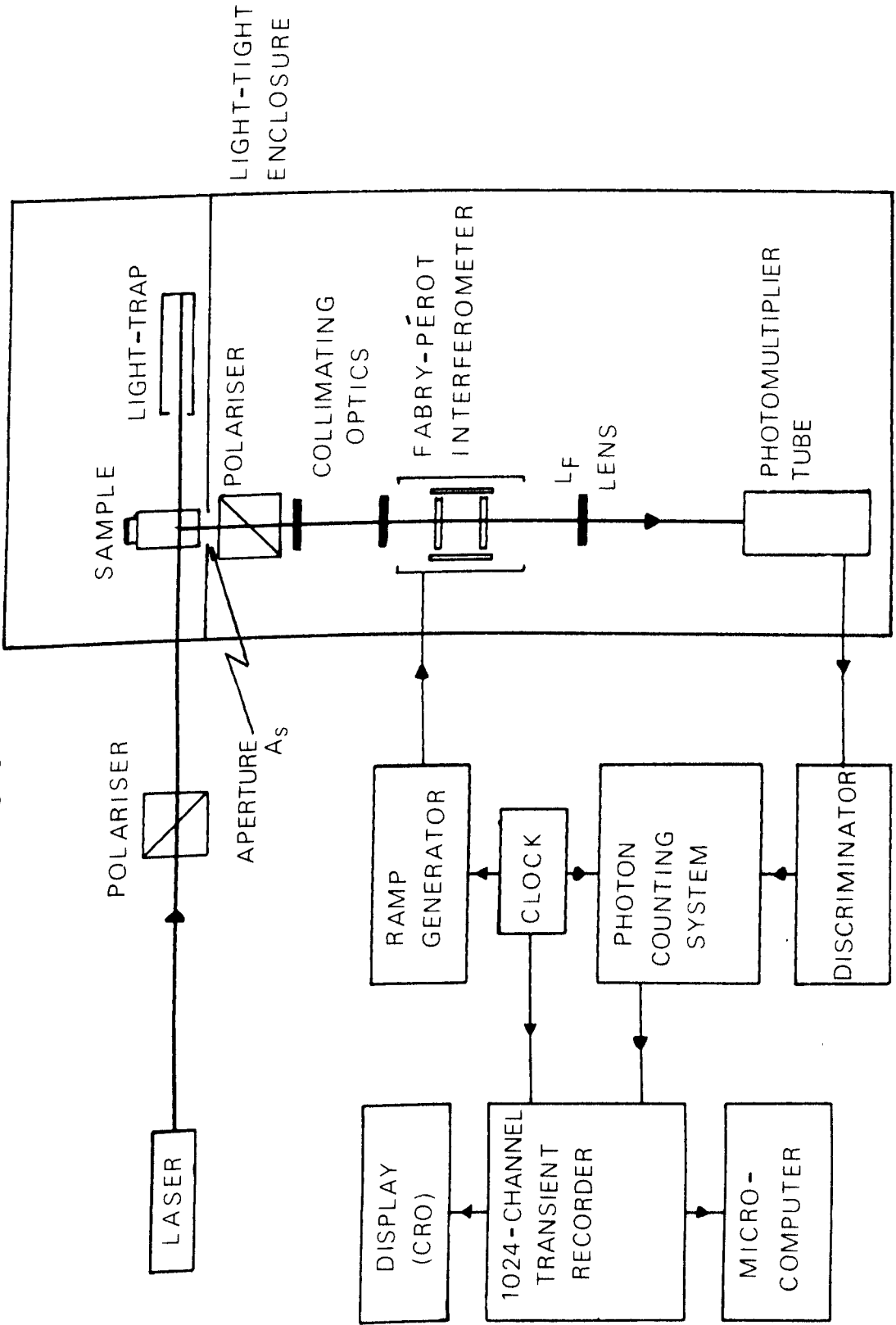
The divergence of the beam within the scattering volume was calculated from the equation of Kogelnik and Li [99] (Fig 3.1.2)

Fig 3.1.2 Focusing of the collimated laser beam



$$X = \frac{\pi d_0^2}{12\lambda} \quad (3.1.1)$$

Fig. 3.1.1. Schematic diagram of the light scattering spectrometer



where:  $d_0 = 4\lambda f/\pi D$  is the diameter of the focused beam  
 $\lambda$  = incident laser wavelength  
 $f$  = focal length of the lens  
 $D$  = diameter of the unfocused laser beam  
 $X$  = distance over which the power density is reduced  
by 10%

The laser beam diameter  $D$ , the diameter at which the laser beam intensity falls to  $1/e^2$  of the peak on-axis value, was measured by scanning with a photodiode and computer fitting the resulting profile to a Gaussian lineshape. The values calculated from equation (3.1.1) are  $d_0 \approx 7.7 \times 10^{-2}$  mm and  $X \approx 6$  mm, that is, the beam divergence was less than 10% over 6 mm.

The scattered light was monitored at  $90^\circ \pm 0.2^\circ$  [101] by a piezo-electrically scanned Fabry-Perot interferometer. The interference pattern produced by the interferometer was focused onto an EMI 9789B photomultiplier tube, chosen for its spectral response, sensitivity and low noise, using a lens ( $L_F$  in Fig 3.1.1) of 1.33 m focal length. The output of the photomultiplier tube was fed to a photon counting system via a discriminator. The analogue output from the photon counting system was input to a 1024 channel transient recorder which had a resolution of 1 part in 256.

A clock was used to simultaneously control the rate meter of the photon counting system, the increment rate of the transient recorder channel and a 300 V staircase ramp, applied to the Fabry-Perot scanning pads.

A spectrum was obtained by scanning over three Fabry-Perot orders at the end of which the transient recorder was triggered and the information retained in the recorder. Scan times varied between 5 and 30 minutes.

The transient recorder was interfaced to a BBC microcomputer via the 'user' port. The data was stored on floppy disc and subsequently transferred to a mainframe computer for analysis.

The choice of mirrors used in the Fabry-Perot was made so as to obtain spectra with a good signal to noise ratio and scan times shorter than the time taken for the interferometer to go out of adjustment due to thermal and mechanical fluctuations, typically about 30 minutes. The mirrors used for polarised Brillouin spectra were 25 mm in diameter and had reflectivities of 98.4%. However the light scattering levels involved in depolarised Rayleigh scattering from the n-alkanes and branched isomers was very low. For example, the optical anisotropy of n-octane is approximately  $6.6 \times 10^{-48} \text{ cm}^6$  whilst that of benzene is  $43.5 \times 10^{-48} \text{ cm}^6$ . The optical anisotropy of the branched isomers decreases with increasing branching, that is as the molecule becomes more globular in shape, and is much lower than that of the n-alkanes; experimentally 2,2,4-trimethylpentane was found to have approximately 0.1 times the light scattering level of n-octane.

These very low light levels required very careful alignment of the optical components to produce spectra with a reasonable signal to noise ratio. Mirrors of 50 mm diameter and with reflectivities of 93.5% were used to maximise the light transmission whilst still maintaining adequate resolution with a maximum obtainable finesse of 47.

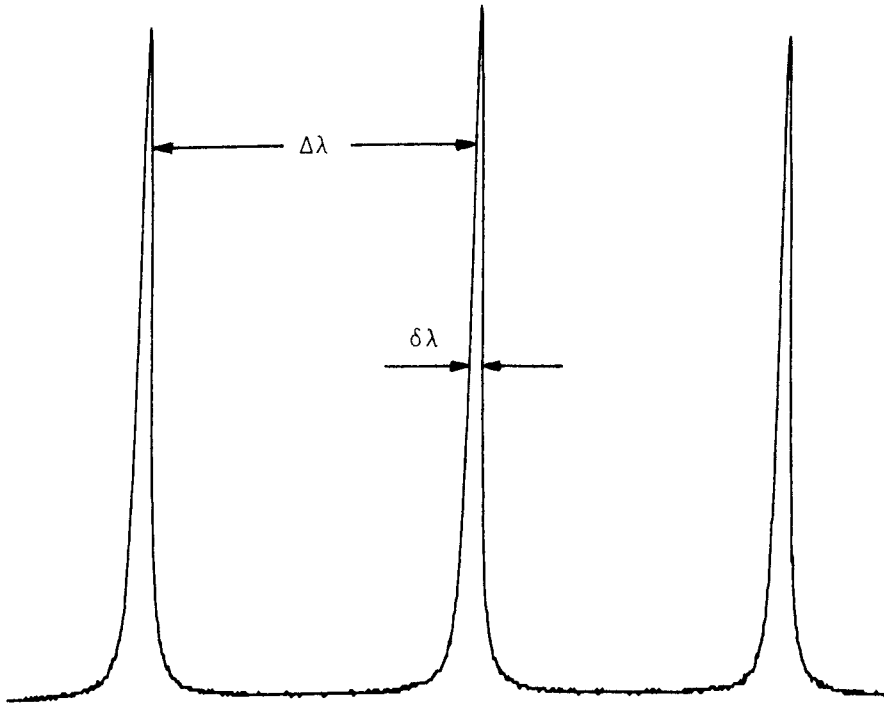


Fig 3.1.3 Instrumental function: finesse =  $\Delta\lambda/\delta\lambda$

The overall finesse of the system, defined as  $\Delta\lambda/\delta\lambda$  in Fig 3.1.3, is determined by the reflectivity, optical flatness, inhomogeneity and alignment of the mirrors in addition to diffraction effects at the pinholes [9]. In practice the limiting finesse is the reflectivity finesse which is given by [10]:

$$F_R = \frac{\pi (R_p)^{\frac{1}{2}}}{(1 - R_p)} \quad (3.1.2)$$

where  $R_p$  is the reflectivity of the plates.

$F_R$  was maximised by careful mirror alignment. An overall finesse of approximately 30 at an incident laser wavelength of 514.5 nm was used for the depolarised spectra, whilst a finesse of at least 45 at an incident wavelength of 488.0 nm was used for polarised spectra.

### 3.1.2 Measurement of the Free Spectral Range

For the polarised spectra and the depolarised spectra from the longer chain alkanes, the mirror separation was measured to within  $\pm 0.01$  mm using a travelling microscope and vernier scale. However the depolarised spectra of the more globular branched alkanes studied required mirror spacings as close as 0.05 mm. These very small mirror spacings were measured using a calibrated graticule in the eye-piece of the travelling microscope.

The error in measuring the free spectral range (FSR) ranged from  $\pm 0.1\%$  for an FSR  $< 15$  GHz, to  $\pm 20\%$  for the largest FSR used of approximately 3300 GHz.

The FSR was then calculated from the relation

$$\text{FSR} = c/2d \quad (3.1.3)$$

where  $c$  = velocity of light

$d$  = mirror separation.

An FSR of approximately 15 GHz was used for the polarised spectra, whilst that used for the depolarised spectra ranged from 100 GHz to 3300 GHz.

### 3.1.3 Adjustment of the Fabry-Perot Interferometer

A telescope, focused on infinity, replaced lens  $L_F$  and was used to view the scattering volume and interference pattern produced from a colloid sample. The circular fringes were arranged so as to evolve symmetrically about the scattering volume. However, when mirror separations  $< 0.2$  mm were used this procedure was found to be inadequate because the fringe pattern was composed of rings more widely spaced than the telescope field of view. The adopted proce-

dure was to reflect the incident laser beam down through the detection optics and project the interference pattern onto a screen placed in front of the photomultiplier tube pinhole. The interference pattern was then symmetrically aligned about the undeviated incident beam.

Before a spectrum could be recorded the finesse of the Fabry-Perot had to be maximised. This was accomplished by monitoring the polarised spectrum of a colloid whilst scanning at the maximum rate. The voltage across each scanning pad was varied until the narrowest peak was obtained; the spectrum from a colloid is too narrow (<1MHz) to be resolved with a Fabry-Perot and hence the width of the peaks are due entirely to instrumental effects.

A refinement was introduced that allowed fine tuning of the Fabry-Perot without removal of the sample or heating block. One end of a fibre optic bundle was positioned in the laser beam and the other end was incident into a cell containing a colloid. This cell could be lowered into position in front of the detection aperture  $A_s$  (Fig 3.1.1) without opening the enclosure. The illuminated colloid was then used to maximise the finesse as previously described. This technique has the advantage that once positioned the sample is left undisturbed for data collection over the complete temperature range to be studied, thus avoiding thermal currents causing condensation on the cell walls when the sample is below ambient temperature.

To ensure equal intensity peaks in the spectrum and to maximise the signal to noise ratio the spectral distribution pattern must be centred on the photomultiplier tube pinhole. This was attained by fast scanning a Brillouin spectrum from an alkane sample and traversing the interference pattern vertically across the pinhole using lens  $L_F$ . In addition, to ensure equal intensity of successive

orders and, in the case of a Brillouin spectrum, equal intensity of the Stokes and anti-Stokes lines, the interference pattern was centred horizontally on the pinhole using lens  $L_F$ .

A Glan-Thomson polariser with an extinction ratio greater than 1 in  $10^6$  was used as an analyser for the depolarised spectra. The polariser was set to within  $\pm 0.1^\circ$ , horizontally polarised with respect to the scattering plane (Fig 2.1.1), by minimising the polarised Brillouin spectrum from carbon tetrachloride.

#### 3.1.4 Sample Cell Holder

To minimise the effects of parasitic light scattering, for example, from the sample cell walls and reflections inside the heating block, the sample cell was held in place by the brass cell holder shown in Fig 3.1.4. The rectangular ports restrict the scattering volume to 7 mm. This effectively removes parasitic scattering from the entrance and exit faces of the light scattering cell.

The cylindrical tube mounted on the top of the cell holder serves two functions. Firstly, it allows positioning of the cell relative to the incoming laser beam and secondly, it permits passage of the thermocouple probe down the inside of the tube to the top of the sample cell.

#### 3.1.5 Thermostating of the Sample

The sample cell and cell holder were held in a thermostatically controlled brass block. The block has a four-port configuration to enable precise positioning of the sample cell with respect to the incident laser beam and the detection optics. Thermostating of the sample was provided in two ways: (i) electrical heating was supplied by a wire coil wound around the centre of the

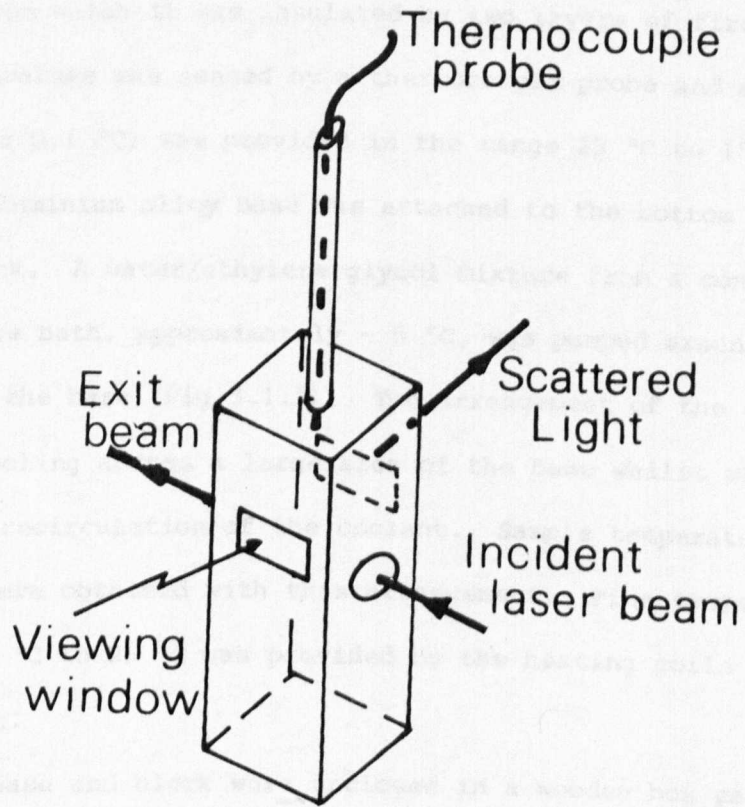
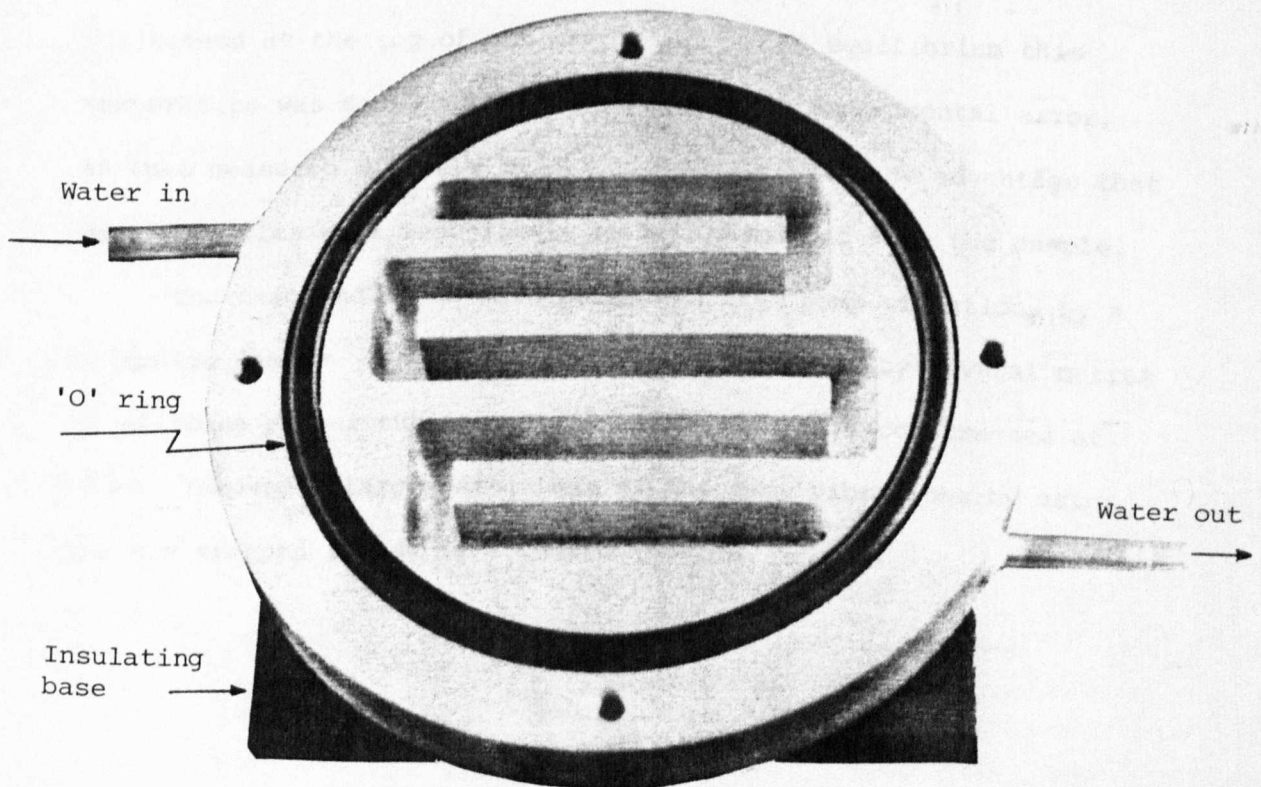


Fig 3.1.5 Photograph of cooling block



block, from which it was insulated by two layers of fire cement. The temperature was sensed by a thermocouple probe and accurate control ( $\pm 0.1$  °C) was provided in the range 25 °C to 150 °C, (ii) an aluminium alloy base was attached to the bottom of the brass block. A water/ethylene glycol mixture from a constant temperature bath, approximately - 5 °C, was pumped around the channels milled in the base (Fig 3.1.5). The arrangement of the channels allowed cooling across a large area of the base whilst maintaining efficient recirculation of the coolant. Sample temperatures down to - 2.0 °C were obtained with this arrangement. Fine temperature control from 0 °C to 25 °C was provided by the heating coils inside the brass block.

The base and block were enclosed in a wooden box packed with insulating wool and mounted on an insulating slab. This prevented condensation forming on the cell walls and reduced temperature fluctuations to  $\pm 0.05$  °C in the range 0 °C to 120 °C.

The temperature was monitored with a thermocouple probe positioned at the top of the sample cell. At equilibrium this temperature was found to be the same, within experimental error, as that measured directly in the liquid but with the advantage that dust particles were less likely to be introduced into the sample.

The base and block were protected from pump vibrations by a hydraulic damper in the pump line and by several metres of silicone rubber tubing. The hydraulic damper, constructed of glass, removed a large percentage of the pump vibrations by using the air trapped inside as a damping medium.

### 3.2 Sample Preparation and Ancilliary Measurements

The liquids studied are listed in Table 3.2.1. All the samples were used without further purification.

TABLE 3.2.1

Liquid	Supplier	% Purity by Assay	Bpt/°C
n-Octane	F	>99.5	125
2-Methylheptane	A	99	116
3-Methylheptane	F	>98	115
2,5-Dimethylhexane	A	99	108
2,2,4-Trimethylpentane	F	>99.5	99
2,3,4-Trimethylpentane	F	95	113
n-Heptane	A	99	98
2-Methylhexane	A	99	90
3-Methylhexane	A	99	91
2,2-Dimethylpentane	A	>99	78
2,3-Dimethylpentane	A	95	90
2,2,3-Trimethylbutane	F	>99	80
n-Hexane	BDH	puriss	69
2-Methylpentane	A	>99	62
3-Methylpentane	F	>99	64
2,2-Dimethylbutane	A	98	50
n-Pentane	KL	spectrosol	36
2-Methylbutane	A	>99	28
<i>cis</i> -9-Octadecenoic Acid (Oleic Acid)	BDH	>92	220
n-Octanoic Acid	BDH	>97.5	237
Carbon-Tetrachloride	BDH	spectrosco- pic grade	77

Supplier abbreviations: F - Fluka-Fluorochem Ltd, BDH - BDH Chemicals Ltd  
 KL - Koch-Light Laboratories Ltd, A - Aldrich Chemical Co Ltd.

### 3.2.1 Filtration Techniques

To obtain good quality light scattering spectra the liquid samples must be as free from dust as possible. Dust in the samples causes large increases in the intensity of the polarised and depolarised Rayleigh peak. This leads to large errors in the measured widths and can hide any fine structure present in the depolarised spectrum.

All samples were filtered using Millipore filtration units and Millipore filters. The filtration unit and syringe, used to force the sample through the filter, were thoroughly cleaned before use. Firstly they were washed with distilled water followed by methanol, propan-2-ol and finally rinsed in chloroform. To minimise dust contamination all the components were dried in a stream of filtered air and placed in a clean air cabinet for assembly.

The alkanes were filtered using 0.025  $\mu\text{m}$  filters. A few mls of the liquid were filtered and discarded before a sample was collected. This removed any remaining dust and any loose fragments on the filter. A few of the samples required a 0.05  $\mu\text{m}$  filter in addition to the 0.025  $\mu\text{m}$  filter to produce a clean sample after one filtration. This was especially important for some of the liquids, for example 3-Methylheptane, of which only 10 ml was available due to the high cost involved. For these samples only 4-5 drops could be filtered through before a sample was collected.

The oleic acid solution was filtered with a 0.22  $\mu\text{m}$  filter and the octanoic acid solution with a 0.05  $\mu\text{m}$  filter.

The sample being prepared was filtered directly into a Helmar fused-quartz light scattering cell. The cell had been thoroughly cleaned using the procedure previously described. The prepared sample was placed in the laser beam and examined for dust particles.

These appear as bright scintillations passing through the beam. With some of the more viscous samples scintillations were observed when examined immediately after filtration. However, if the sample was allowed to stand for 24 hours the scintillations were found to have disappeared. Therefore, the scintillations were thought to arise from small air bubbles introduced at the filtration stage.

The samples which were prepared in this way were judged to be of a very high quality.

### 3.2.2 Viscosity Measurements

For all the liquids investigated viscosity measurements were made using Ubbelohde viscometers. The viscometers were immersed in a thermostatically controlled water bath. The water bath was insulated enabling temperature control to within  $\pm 0.1$  °C over the temperature range 4 °C to 95 °C.

The viscometers were calibrated using liquids of known viscosities and the accuracy of the calibration was  $\pm 1\%$ .

Several flow times were measured at each temperature and the average value taken. The data obtained in this way were fitted to the Arrhenius expression

$$\eta_s = \eta_o \exp (-A/T) \quad (3.2.1)$$

A typical standard deviation on the fitted slope was 2% and the maximum extrapolation made was 10 °C.

### 3.2.3 Density Measurements

Density measurements for all the liquids examined were made using a Paar DMA 40 digital density meter.

The instrument was calibrated over the temperature range 5 °C to 80 °C using water and air. Thermostatting of the system was provided by circulating a water/ethylene glycol mixture around a water jacket. The water jacket surrounded a thin glass U-tube containing the sample. The temperature of the sample was monitored with a thermocouple probe positioned in the liquid at the end of the U-tube. Thermal stability was  $\pm 0.05$  °C over the range 5 °C to 90 °C. The individual points were measured with an accuracy of  $0.0001 \text{ g cm}^{-3}$ . Density values for the alkanes were calculated from linear fits to the data. Typical standard deviations on the fitted slope were 2%.

The variation of density with temperature for the oleic acid solution was found to be non-linear. This is discussed in detail in Chapter 4.

#### 3.2.4 Refractive Index Measurements

Refractive index measurements were made on oleic acid and octanoic acid solutions using a Bellingham and Stanley Abbe refractometer thermostatically controlled to  $\pm 0.1$  °C in the temperature range 5 °C to 60 °C. All measurements were made using the laser wavelength of 488.0 nm and the measurement precision was estimated to be  $5 \times 10^{-3}$ %.

### 3.3 Analysis of the Spectral Data

#### 3.3.1 Description of the Analysis Program

In order that a full spectral decomposition could be performed, a comprehensive data analysis program was developed. This incorporated a non-linear least-squares fitting procedure to account for multiple overlapping of the Fabry-Perot orders and non-linearity of the piezo-electric scan, together with rigorous statistical tests designed to compare the experimental data with the theoretical model under investigation.

A detailed description of the operations performed by the computer program is given in Appendix 1. Shown in Fig 3.3.1 is a flow diagram of the operations performed by the analysis program.

The peak positions as a function of channel number are located. From these the data are linearised and initial estimates of the fitting parameters calculated. A theoretical spectrum is then generated and compared with the experimentally observed spectrum. The program then uses the minimisation routine EO4GAF to adjust the fitting parameters so as to minimise the chi-square (Appendix 2 (A.2.1)).

Finally, the fitted values of the input parameters are returned together with the results of the statistical analysis.

Shown in Fig 3.3.2(a) is the polarised Rayleigh-Brillouin spectrum of n-octane at 23.5 °C. Every fourth data point is represented by a dot and the solid line represents the fitted curve using equation (A1.4.1). Fig 3.3.2(b) shows the depolarised (VH) Rayleigh-Brillouin spectrum of n-octane at 23.5 °C. Every fourth data point is represented by a cross and the solid line represents the fitted curve using equation (A1.4.3). It is evident in both cases that the experimental data is well represented by the fitting function employed.

Fig 3.3.1 Flow diagram showing operations performed by the computer program

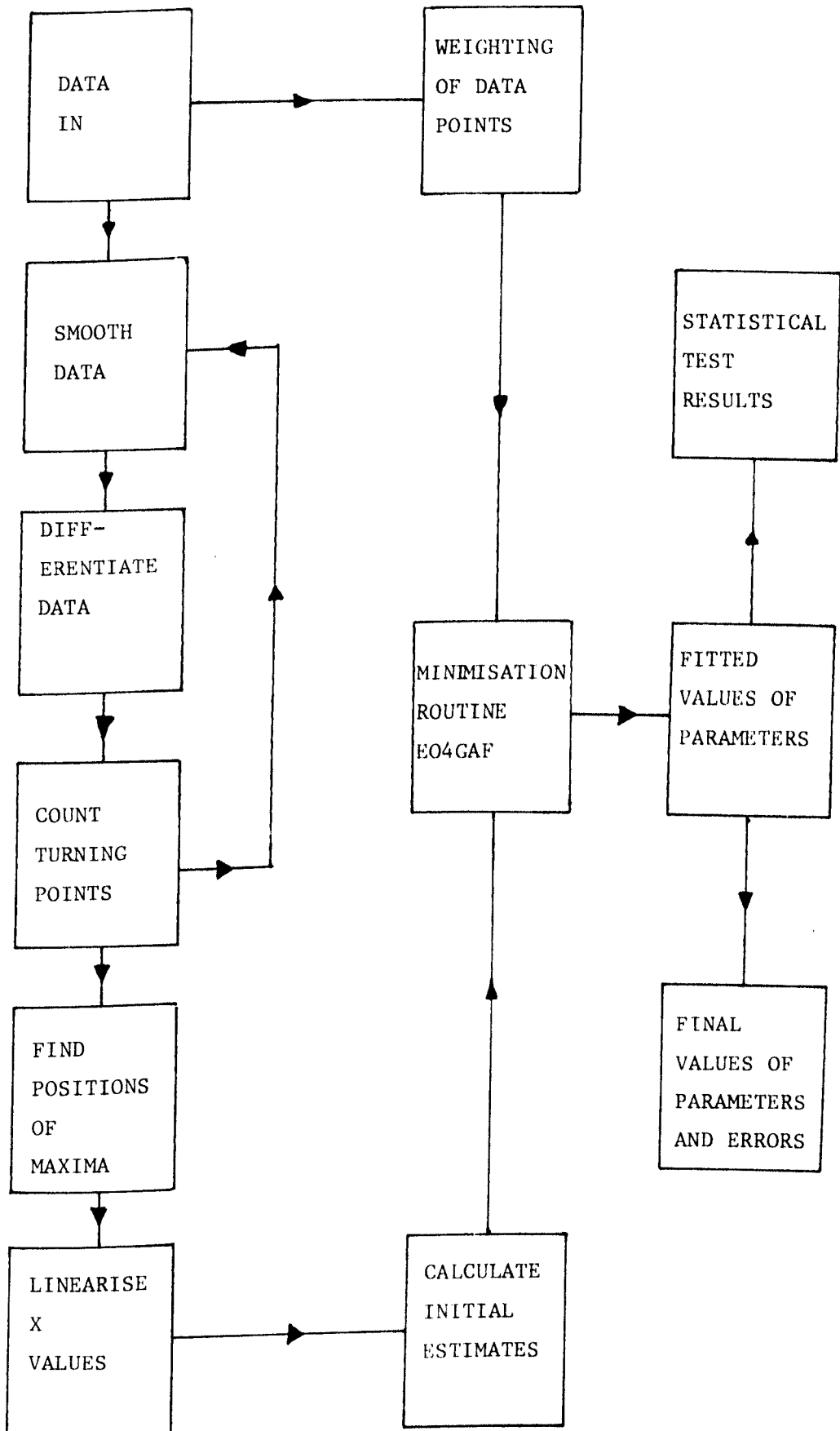
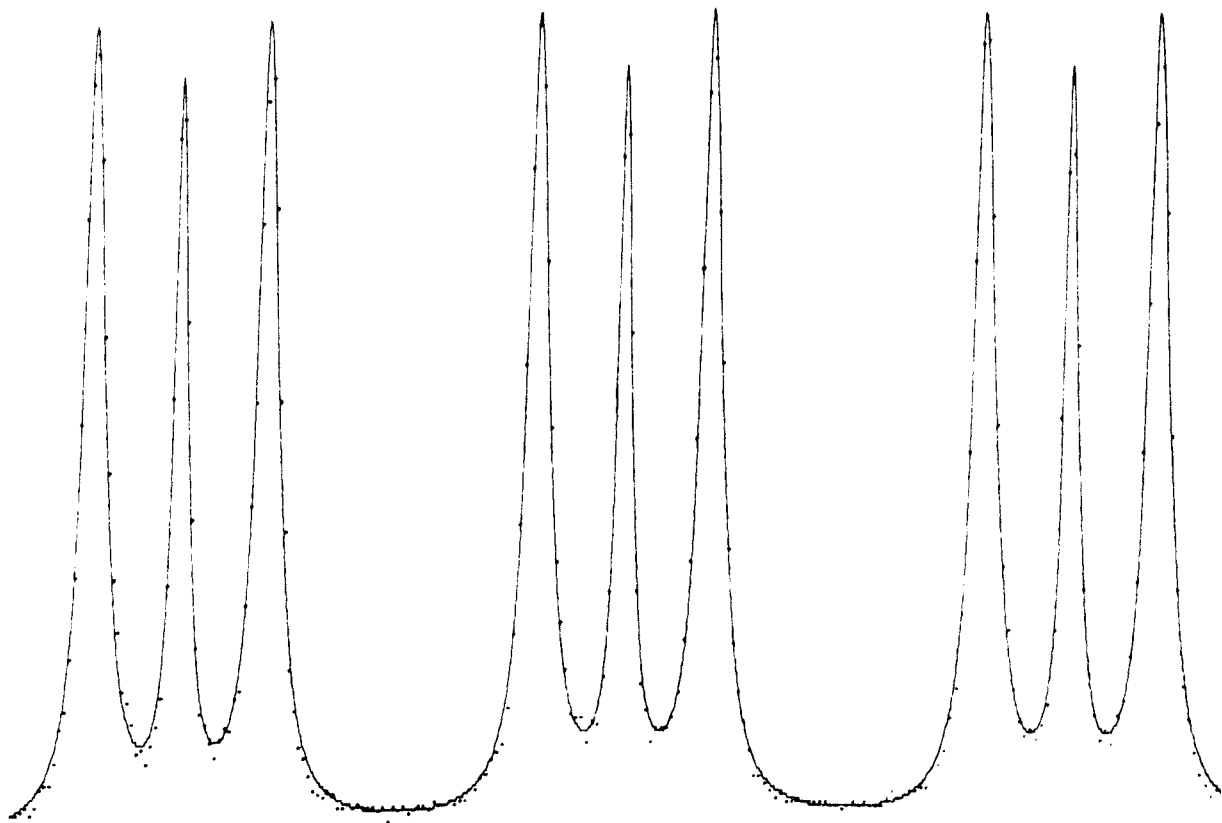
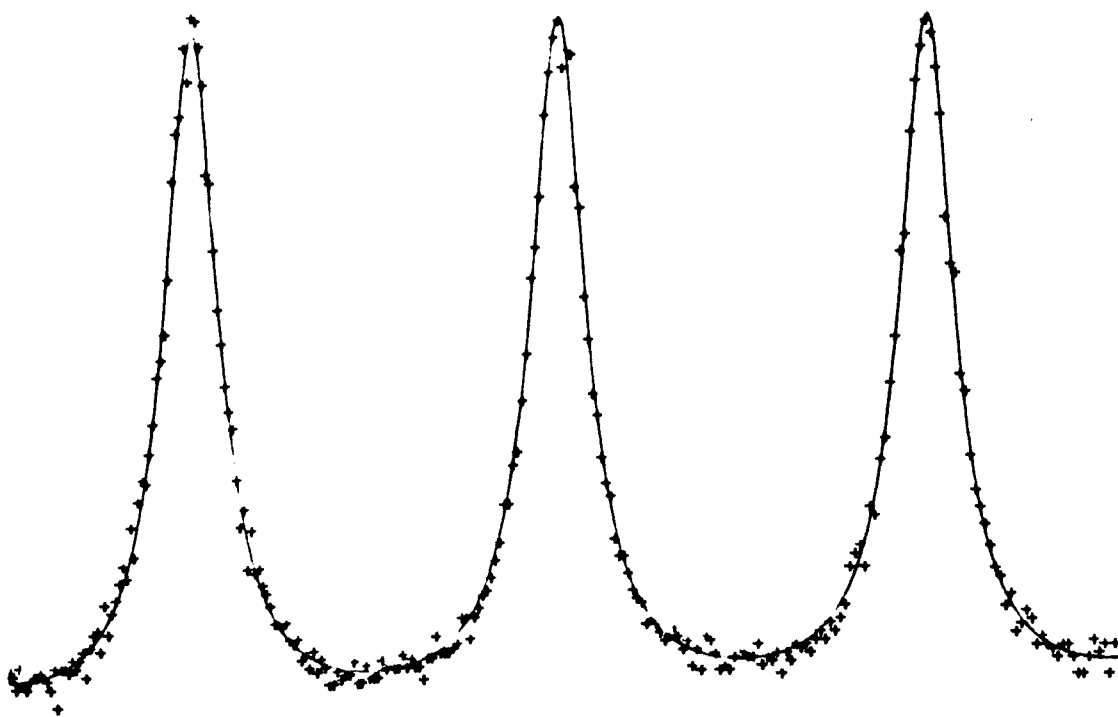


Fig 3.3.2 (a) Polarised Rayleigh-Brillouin spectrum of n-octane.  
 $T = 23.5 \text{ }^\circ\text{C}$ ; FSR = 15 GHz. Every fourth data point  
is represented by a dot.



(b) Depolarised Rayleigh-Brillouin spectrum of n-octane.  
 $T = 23.5 \text{ }^\circ\text{C}$ ; FSR = 110 GHz. Every fourth data point  
is represented by a cross.



### 3.3.2 Statistical Analysis of the Experimental Data

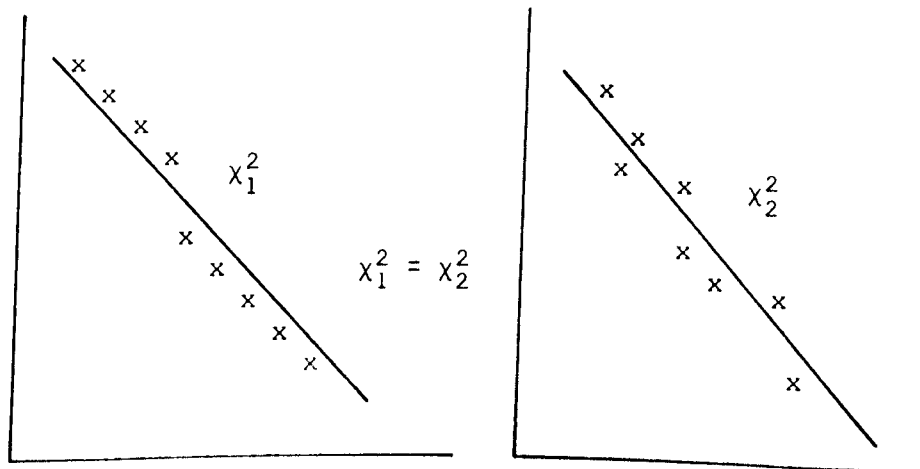
A full discussion of the statistical tests and definitions of the terms used is given in Appendix 2. Three independent statistical tests were used to: (i) test quantitatively that the data and fitting function were compatible, and (ii) to test for lack of independence in the residuals.

The three tests are:

- (a) Chi-Square ( $\chi^2$ ) test, which is a "goodness-of-fit" type - type (i).
- (b) The One-Sample Runs Test, which indicates the randomness of a sample from the order or sequence in which the residuals occur - type (ii).
- (c) The Linear Correlation Test, which is very sensitive to any long range systematic deviation of the residuals from the fitting function - type (ii).

The Chi-Square test gives a reliable indication of the match between the data and the fitting function but it can be misleading in that it does not take account of the order of the residuals (Fig 3.3.3). For this reason tests (b) and (c) are also used.

Fig 3.3.3 Example of misleading interpretation of the chi-square test.



The One-Sample Runs test and Linear Correlation test are complementary; the One-Sample Runs test does not give a quantitative estimate of the lack of independence when the number of runs obtained is low, whereas the Linear Correlation test returns a quantitative value for the non-randomness of the residuals for both a low and high number of runs.

The significance level for tests (b) and (c) was taken to be 5%, that is, the residuals were not considered to be random if there was less than one chance in 20 of obtaining the given set of residuals purely by chance.

The statistical tests were used to examine the applicability of the theoretical function chosen to describe the experimental data. Three important results were found when the tests were applied to the light scattering data.

- (i) It was not always possible to use the integral chi-square probability as a test of the validity of the choice of fitting function. The reason for this is discussed in Appendix A2.1 and results in the use of the reduced chi-square as an indication of the optimum choice of objective function.
- (ii) The One-Sample Runs test was found to return values for the probability when the number of runs obtained was in the range  $300 < \text{number of runs} < 520$  (for a mean  $(\mu_r) \cong 512$  and standard deviation  $(\sigma_r) \cong 16$ ). Hence both the number of runs obtained and the Runs test probability were used as indication of the validity of the objective function.
- (iii) The Linear Correlation test probability was found to return values ranging from 0.0 to 1.0 for both appropriate and inappropriate choices of objective function. This was, therefore, the least useful of the of the statistical tests.

A possible reason for obtaining a probability  $< 0.05$ , when the other tests indicated an optimum choice of fitting function, was an asymmetry of the Fabry-Pérot orders (discussed in Section 3.1.3) causing a systematic deviation from the fitting function.

An example to illustrate the three points discussed above is shown in Table 3.3.1.

Table 3.3.1 Results of the Statistical Tests for the Experimental Data Fitted to Two Different Objective Functions.

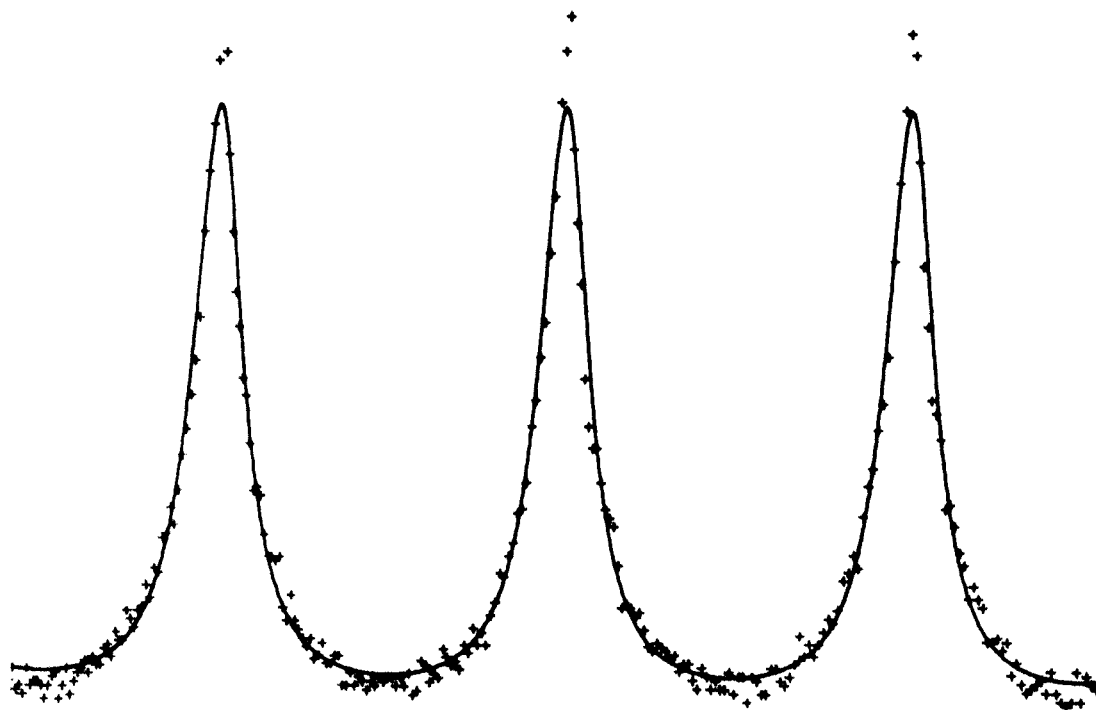
Objective Function	Integral $\chi^2$ Probability	Reduced $\chi^2$	One-Sample Runs Test Probability	Number of Runs Obtained	Linear Correlation Test Probability
(i) One Lorentzian and Flat Base	0.0	2.24	$3.0 \times 10^{-26}$	342	$4.1 \times 10^{-2}$
(ii) Two Lorentzians and Flat Base	$2.5 \times 10^{-3}$	1.07	1.0	514	$3.0 \times 10^{-2}$

It is evident that function (ii) best describes the experimental data. This is displayed pictorially in Fig 3.3.4. The crosses represent every fourth data point and the solid line represents the fitted curve. Clearly, the lower curve matches the data points most closely, in agreement with the statistical analysis.

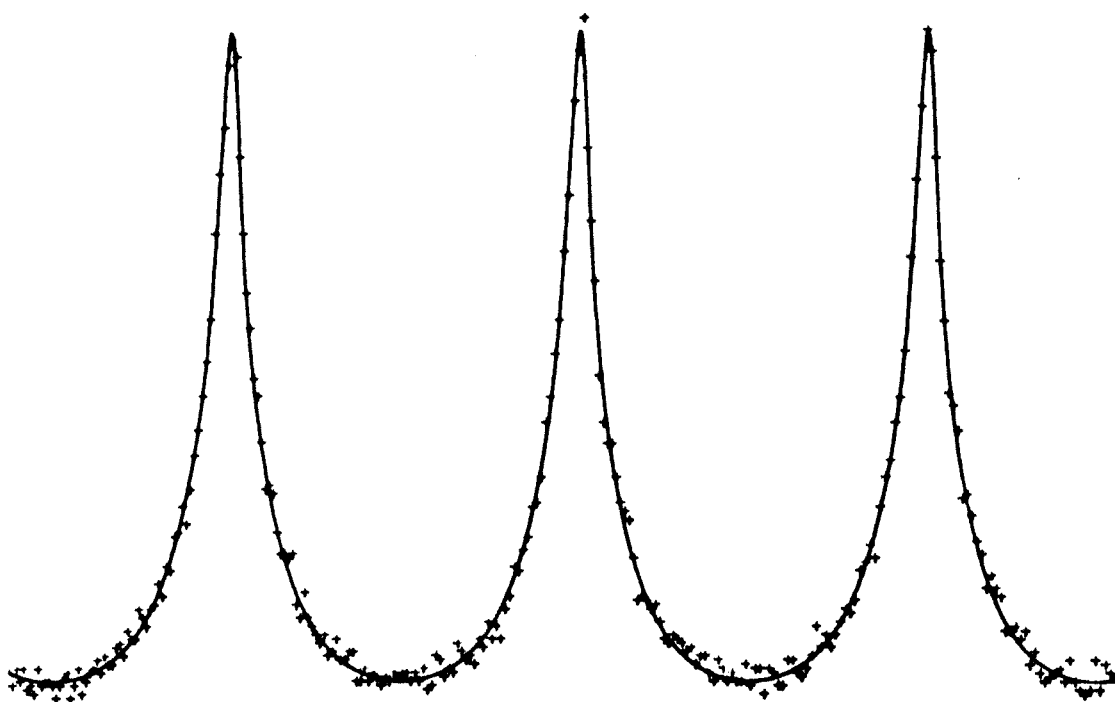
Fig 3.3.4 Depolarised Rayleigh-Brillouin spectrum of 2,2,4-trimethylpentane

Every fourth data point is represented by a cross.

(a) Single Lorentzian fit to data.



(b) Two Lorentzian fit to data.



Contents

4.1 Introduction

4.2 Experimental Considerations

4.3 Results

4.3.1 Kinematic Shear Viscosity

4.3.2 Density

4.3.3 Refractive Index

4.3.4 Polarised Rayleigh-Brillouin Scattering

4.4 Statistical Analysis of the Results

4.5 Discussion

4.5.1 Kinematic Viscosity

4.5.2 Density

4.5.3 Refractive Index

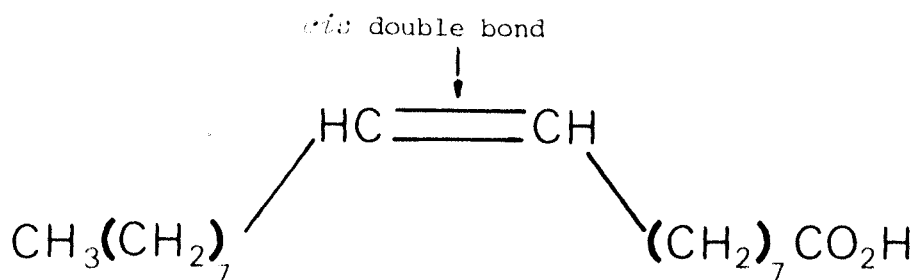
4.5.4 Polarised Rayleigh-Brillouin Scattering

4.6 Conclusions

#### 4.1 Introduction

Presented in this chapter is the experimental evidence that suggests that oleic acid (*cis*-9-octadecanoic acid) undergoes a thermotropic phase transformation approximately 5 °C above the melting point.

Fig 4.1.1 Oleic (*cis*-9-octadecanoic) acid



The *cis* double bond causes a rigid kink in the hydrocarbon chain. The rigidity is contributed by the nonrotating double bond. The kink in the molecule reduces the packing efficiency compared to the *all-trans* form (elaidic acid) and hence reduces the melting point from 45 °C for elaidic acid to approximately 13 °C for oleic acid. This is a very important effect of *cis* unsaturation of fatty acids and consequently these structures are biologically very significant, particularly in membranes [6,7].

The reasons for studying oleic acid are now discussed.

Recent Brillouin Spectroscopy experiments have provided considerable evidence for the existence of a phase transformation in the melts of various n-alkanes [102,103]. It is believed that the transition involves the formation of a mesomorphic structure in the melt, occurring at a particular temperature. This temperature is

above the melting point and depends on the molecular weight of the alkane homologue. As this transition is characterised by a change in the hypersonic attenuation properties it has become known as the  $T_u$  phenomenon. A variety of experimental techniques including densitometry, viscometry and ultrasonic attenuation measurements have corroborated the results of the Brillouin work. In spite of much convincing experimental work the very existence of the phenomenon in the higher n-alkanes continues to be the subject of considerable controversy<sup>[104]</sup>.

Previous authors have associated the  $T_u$  phenomenon with the isotropic-nematic transition of low molecular weight liquid crystals<sup>[52,102]</sup>. Unfortunately Brillouin scattering measurements on liquid crystals close to the transition temperature have been rather inconclusive<sup>[102]</sup>. It is pertinent therefore to investigate substances other than the n-alkanes which are known to have definite liquid crystalline properties at accessible temperatures.

Whilst the work of Kruger et al concentrates on the n-alkane melts many substances, such as lipids or fatty acids, comprise hydrocarbon chains in their molecular structure. It is known that some of these do not undergo a direct thermal transition from an isotropic liquids phase to the gel or crystalline state. An intermediate or mesomorphic state exists below a well defined characteristic transition temperature. The lipids of some biomembranes show this thermotropic behaviour. The nature of lipid transitions has been the object of intensive research over the past 20 years<sup>[105]</sup>. Extensive experimental and theoretical research has shown that the transition has its origin in the conformational changes in the lipid alkyl chain<sup>[106-108]</sup>. In membranes the effect is cooperative and

consequently influences the intramolecular forces leading to a change in the macroscopic properties of the system<sup>[106]</sup>. The idea of mesophases resulting from changes in the configuration of saturated hydrocarbon chains of lipids is clearly relevant to the thermotropic behaviour of n-alkanes<sup>[107,109]</sup>.

Oleic (*cis*-9-octadecenoic) acid is an important structural component of certain biopolymers, for example sphingomyelin. It occurs in most natural fats in the form of the glyceride and it is believed that lipids with oleyl chains are preferentially synthesized in biomembranes to maintain fluidity below physiological temperatures. There is some evidence for the existence of a thermotropic mesophase in the melt of oleic acid; prior to freezing at approximately 13 °C colourless needles form in the melt and become visually observable below about 14 °C. The appearance of such structures suggests that oleic acid in the higher temperature liquid state has some degree of short range order which increases as the temperature tends to the melting point. Above a certain intermediate temperature the melt may be considered an isotropic liquid. Moreover, the discrepancy in the published value of its melting point suggests that oleic acid freezes continuously over the range 13.6 °C to 16.4 °C<sup>[110,111]</sup>. This gives tentative support to the idea of an intermediate phase between the isotropic liquid and solid.

Light scattering<sup>[112,113]</sup> and other measurements<sup>[114,115]</sup> on membranes composed of the monoglyceride ester of oleic acid (glycerol monooleate) have provided evidence of a thermotropic structural transformation within the range 15 °C to 18 °C. There is clearly some overlap between this temperature range and that of the freezing point of oleic acid. The structural similarity, that is the oleyl chain, between these substances implies a concomitance possible in their thermotropic behaviour.

In order to ascertain the importance of the *cis* double bond configuration a control solution was also studied. This solution was chosen so as to model oleic acid on a molecular level but with the double bond removed. The saturated form of octadecenoic acid, stearic acid, and the all-*trans* form were not chosen because of their relatively high melting points, 45 °C and 72 °C respectively. The solution chosen consisted of n-octane and n-octanoic acid.

To summarise, oleic acid was investigated because of the recent interest in alkane chain conformation and the relationship between this and biological membranes.

Presented in this chapter are the results of polarised Rayleigh-Brillouin scattering experiments on oleic acid and octanoic acid solutions complemented by measurements of density, kinematic shear viscosity and refractive index.

## 4.2 Experimental Considerations

At room temperature oleic acid is an oily liquid and freezes to a white opaque wax at approximately 13 °C. To separate the localised one dimensional ordering transition from the melting process a small quantity of a non-perturbing (inert) solvent was added to the oleic acid. This depressed the freezing point and thus assisted in the elucidation of the pre-freezing transition. The solvent, carbon tetrachloride, was added to oleic acid to obtain a 10% solution by volume. The quantity of carbon tetrachloride added was such that the system was perturbed as little as possible to separate the transitions. The freezing point of this solution was 9 °C.

The solution chosen to molecularly model the oleic acid solution consisted of 45.6% n-octane, 44.4% n-octanoic acid and 10% carbon tetrachloride by volume. On a molecular level this exactly models the oleic acid solution but with the -CH = CH- group removed. The freezing point of this solution was also approximately 9 °C. All experimental data was collected above this temperature.

## 4.3 Results

### 4.3.1 Kinematic Shear Viscosity

The kinematic shear viscosity measurements are shown in Fig 4.3.1. The results are presented in the form of an Arrhenius plot. In the case of the oleic acid solution there is a well defined discontinuous change in slope which occurs at a temperature of 18.5 °C. For the octanoic acid solution a linear plot is obtained which does not exhibit a discontinuous change at any unique temperature.

### 4.3.2 Density

The results of the density measurements for the oleic acid solution are shown in Fig 4.3.2(a) and those for the octanoic acid solution in Fig 4.3.2(b). It is apparent that the dependence of density on temperature for the oleic acid solution is nearly linear except for a distinct change in gradient in the range 17 °C to 14 °C. The variation of density with temperature for the octanoic acid solution is also nearly linear apart from a small change in gradient in the range 18 °C to 14 °C. This change in slope is smaller than that for the oleic acid solution and appears to be more gradual.

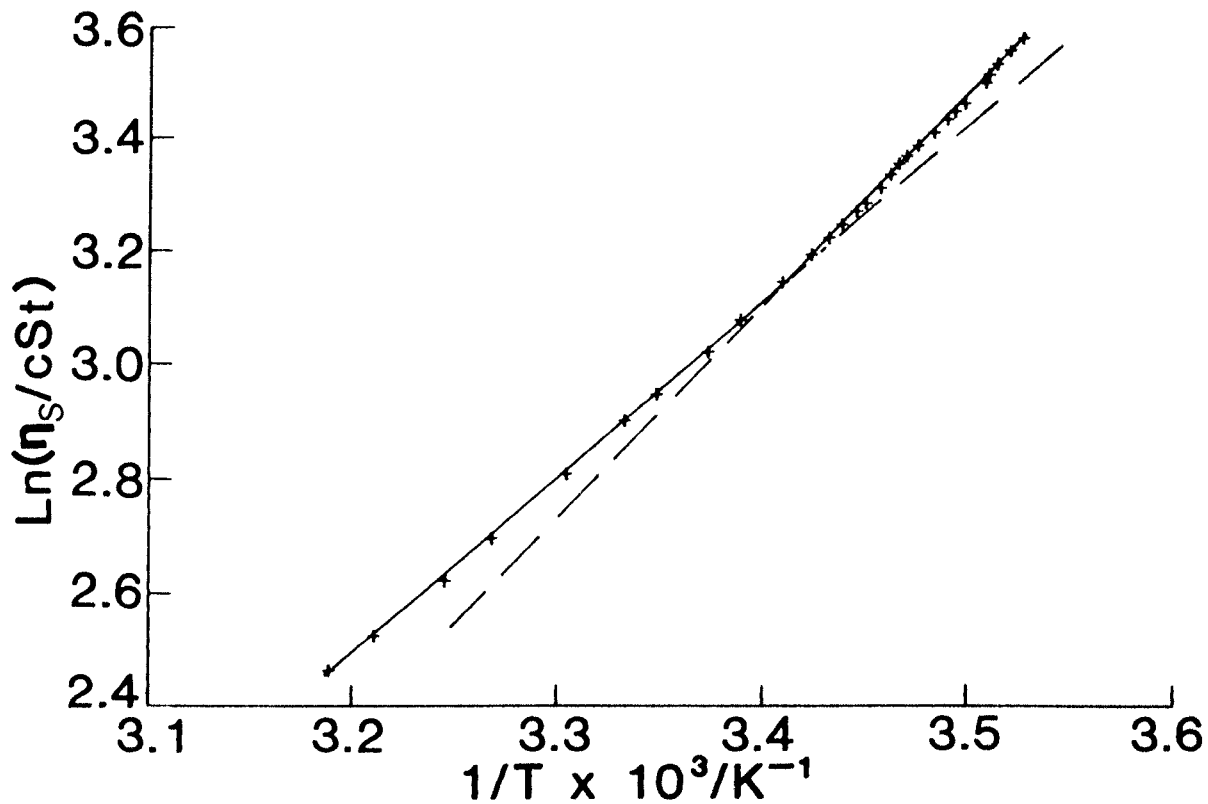
### 4.3.3 Refractive Index

The results of the refractive index measurements for the oleic acid solution are shown in Fig 4.3.3(a). Clearly a point of inflexion occurs at approximately 16.5 °C. The low temperature state has a steeper gradient than the high temperature state.

The refractive index results for the octanoic acid solution are shown in Fig 4.3.3(b). There is no clear discontinuity in the data although the spread on the data points is larger than for the oleic acid solution. This was possibly due to the differential

Fig 4.3.1 Arrhenius plot of the kinematic shear viscosity:

(a) Oleic acid solution showing the two best fit straight lines



(b) Octanoic acid solution showing the single best fit straight line

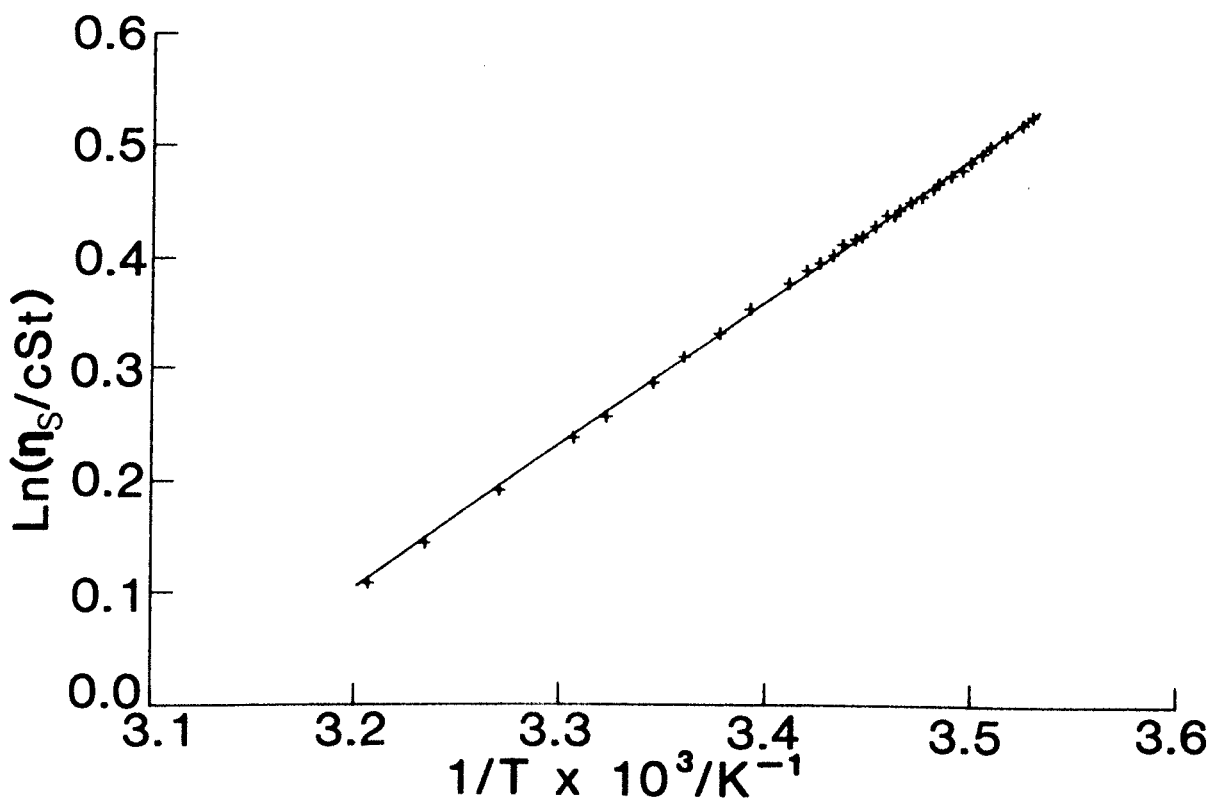
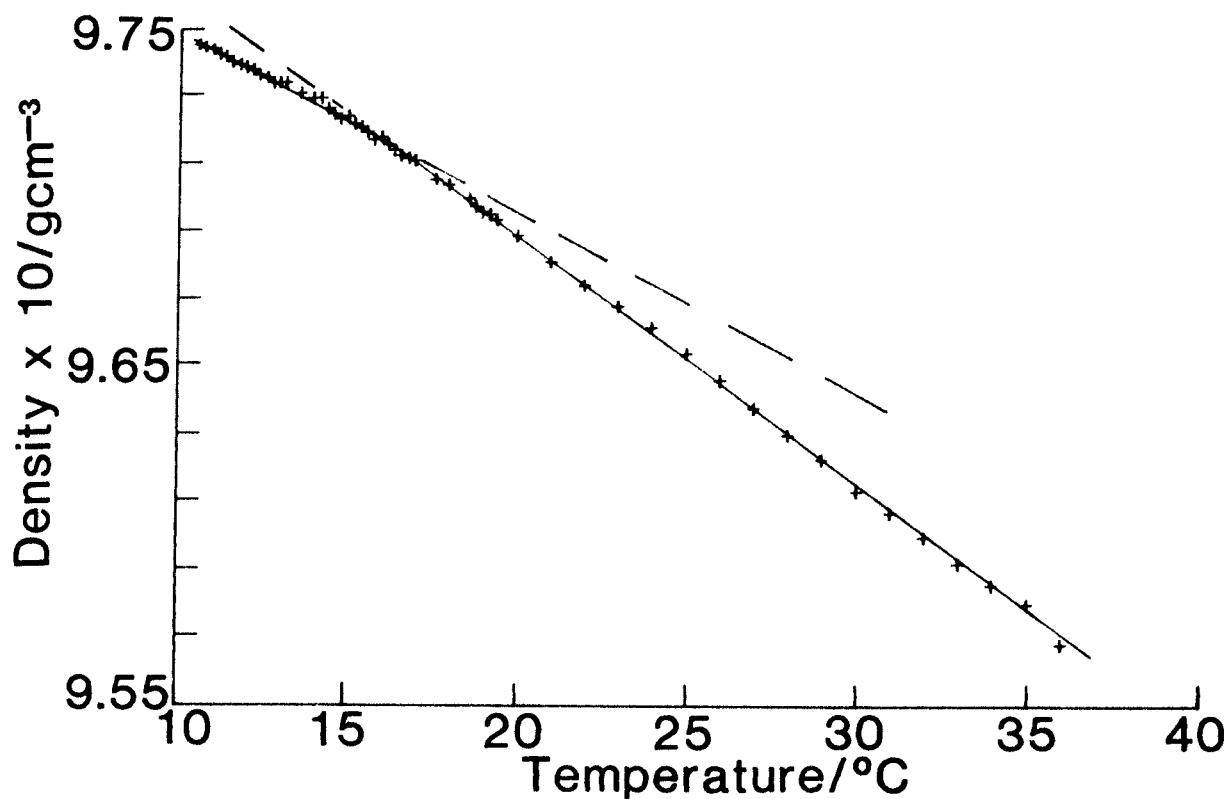


Fig 4.3.2 Density measurements

(a) Oleic acid solution showing the two best fit straight lines



(b) Octanoic acid solution showing single straight line fit

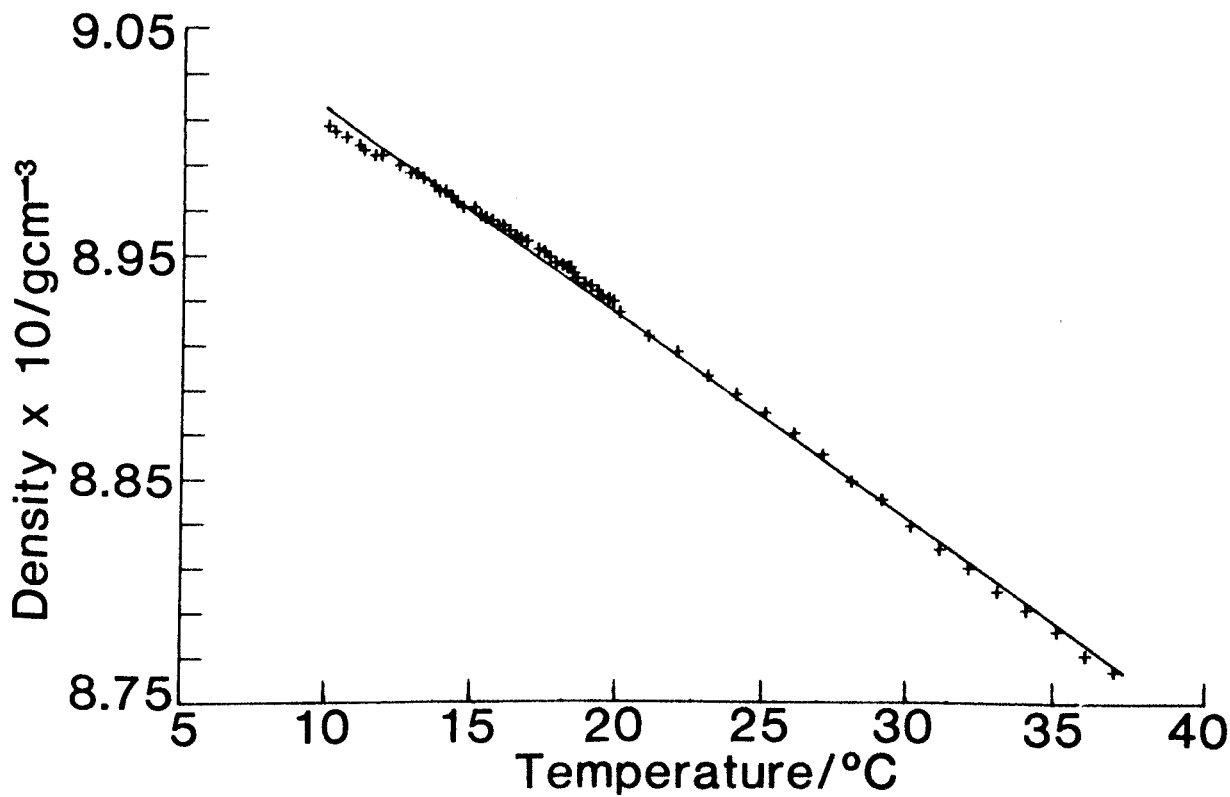
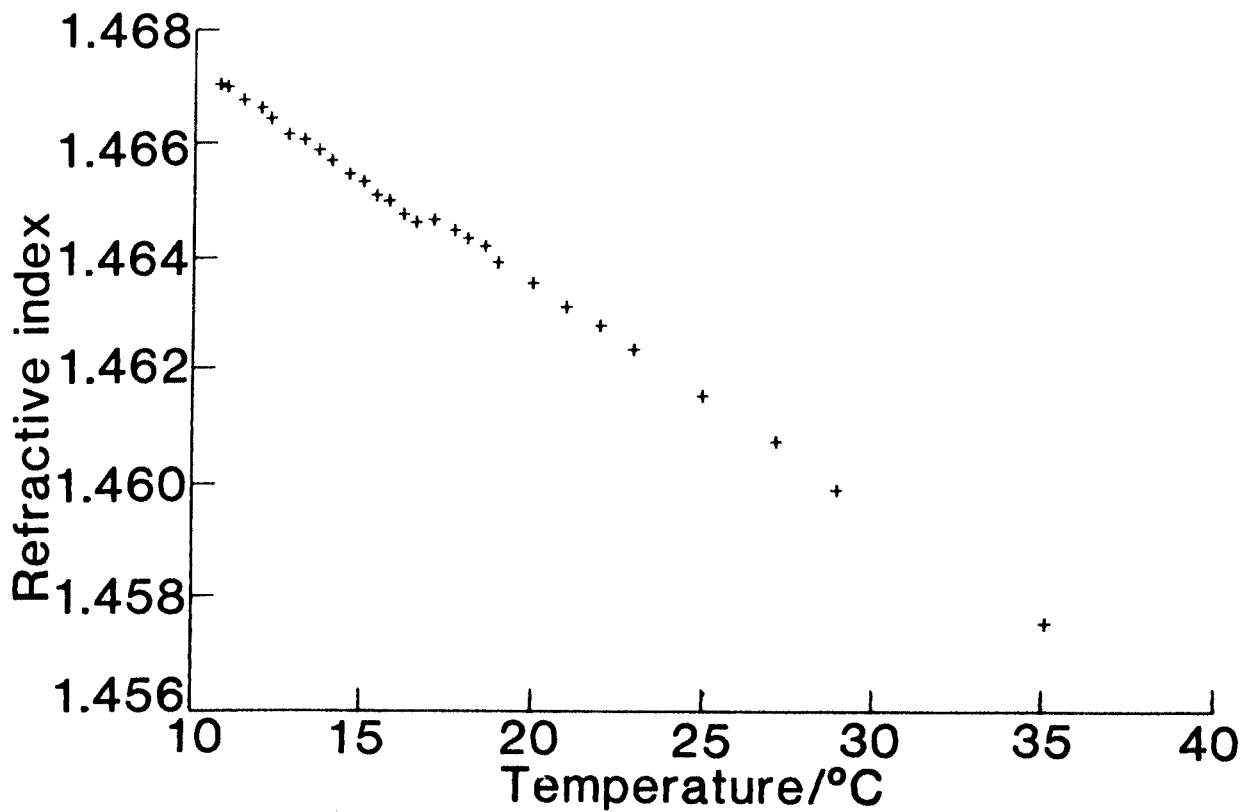
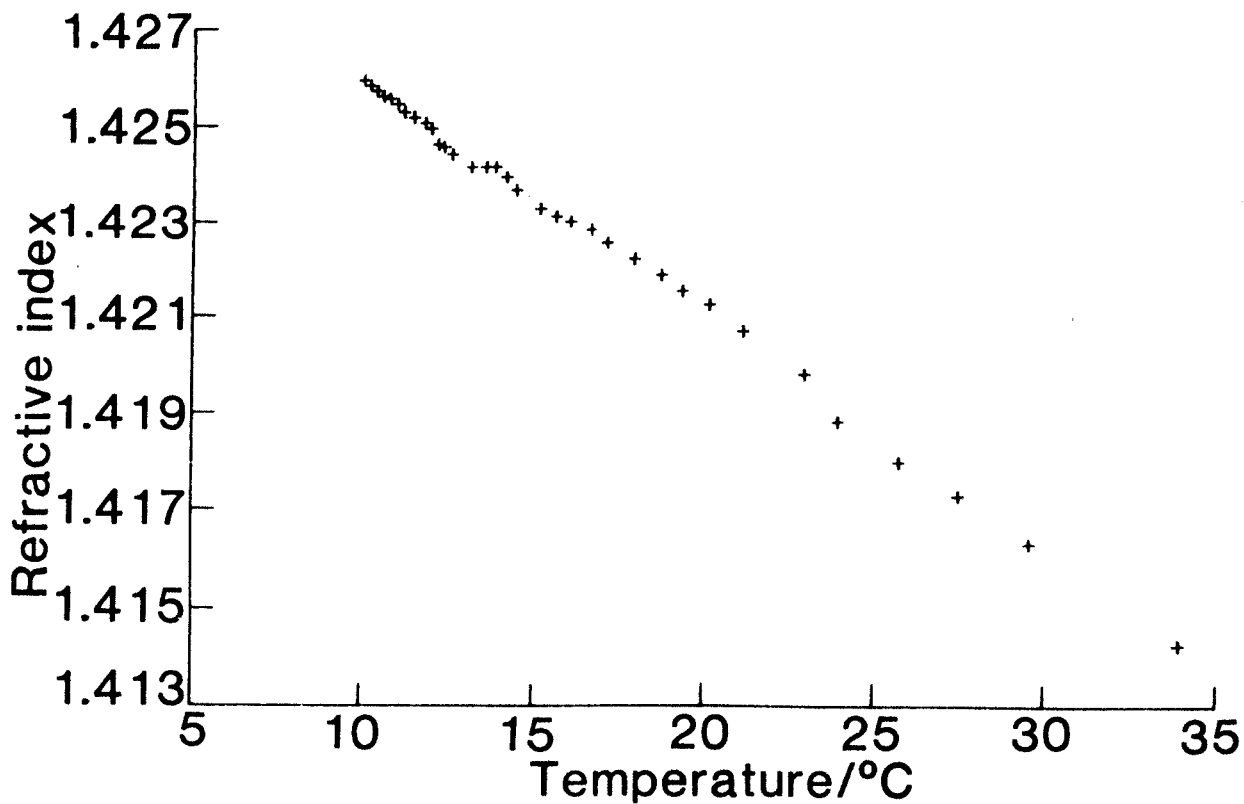


Fig 4.3.3 Refractive index measurements.  $\lambda = 488.0\text{nm}$

(a) Oleic acid solution



(b) Octanoic acid solution



evaporation of n-octane whilst measurements were in progress. Loss of carbon tetrachloride from the oleic acid solution may also have taken place. However, this would have been rather less noticeable as the refractive indices of oleic acid and carbon tetrachloride are almost exactly matched; 1.458 and 1.460 respectively at 20 °C and 589.6 nm. It is highly unlikely that the inflexion point in Figure 4.3.3(a) could have resulted from a gradual loss of carbon tetrachloride from the oleic acid solution.

#### 4.3.4 Polarised Rayleigh-Brillouin Scattering

The polarised Rayleigh-Brillouin spectra for both solutions were fitted with the objective functions described in Section A1.4.1. The results of the statistical analysis (Section 3.3.2) for the oleic acid solution were found to be improved when a Mountain line was included in the fitting function (Equation A1.4.2)) implying that the oleic acid solution was in its viscoelastic regime. A Mountain line was not detected in the octanoic acid solution spectra and hence Equation (A1.4.1) was used to fit the data. Figure 4.3.4 shows a polarised spectrum of the oleic acid solution at 12 °C.

The Brillouin frequency shift as a function of temperature for the oleic acid solution is shown in Figure 4.3.5(a). This quantity appears to vary linearly with temperature outside a narrow range centred on 16.5 °C. The real part of the longitudinal modulus,  $M'$ , was calculated from Equation (2.2.4).

$$V_L(\omega_L) = \left[ \frac{M'(\omega_L)}{\rho} \right]^{\frac{1}{2}} \quad (2.2.4)$$

The results are plotted in Figure 4.3.5(b) and show a similar variation to the frequency shift indicating that the anomaly is not only a consequence of density. The linear dependence of Brillouin shift

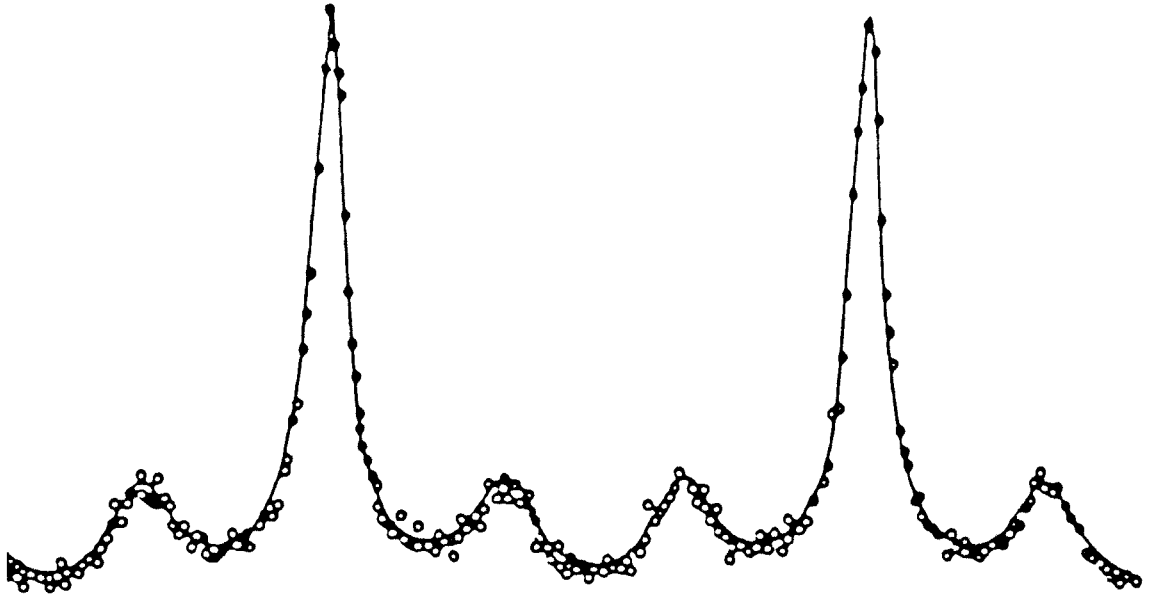
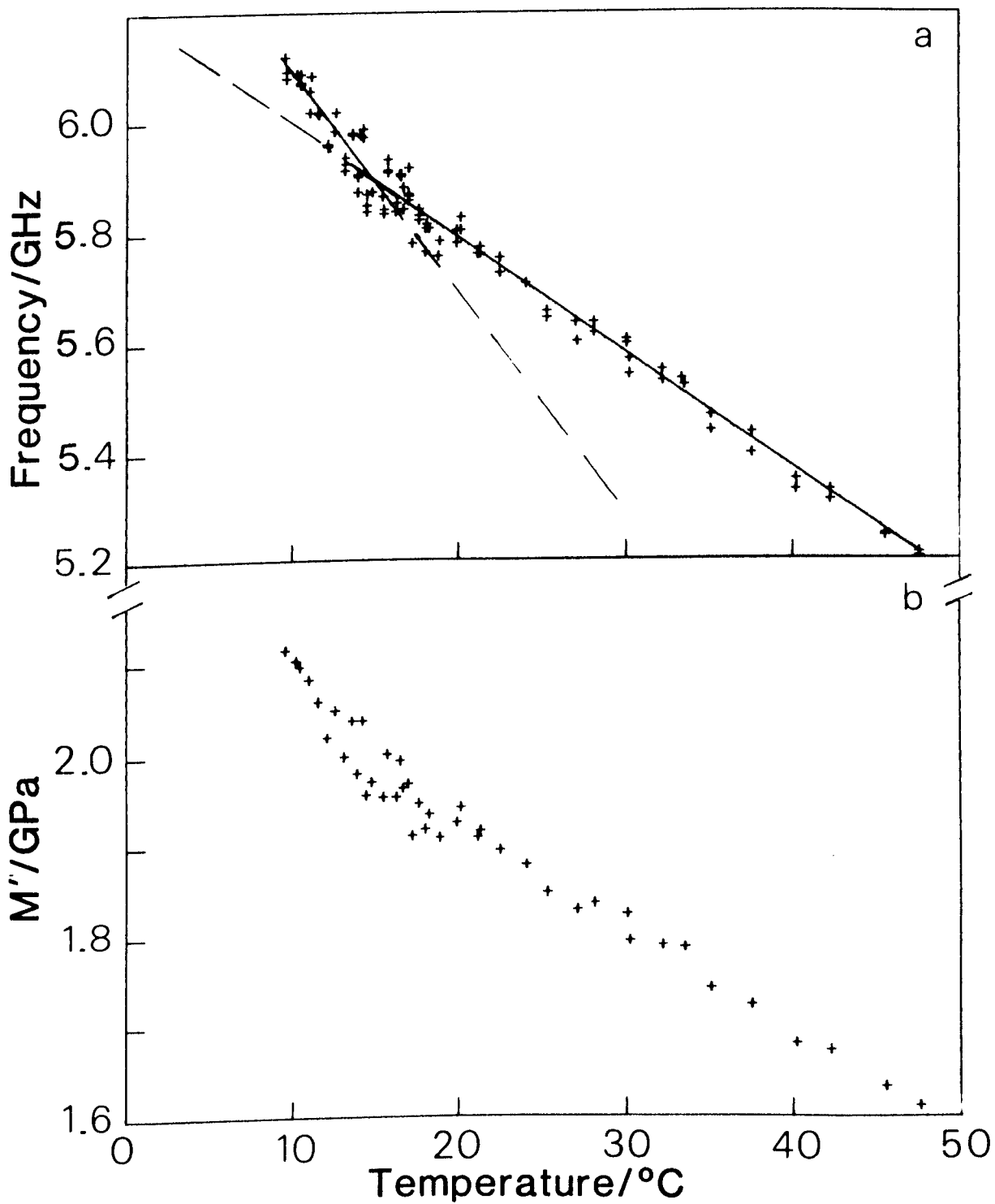
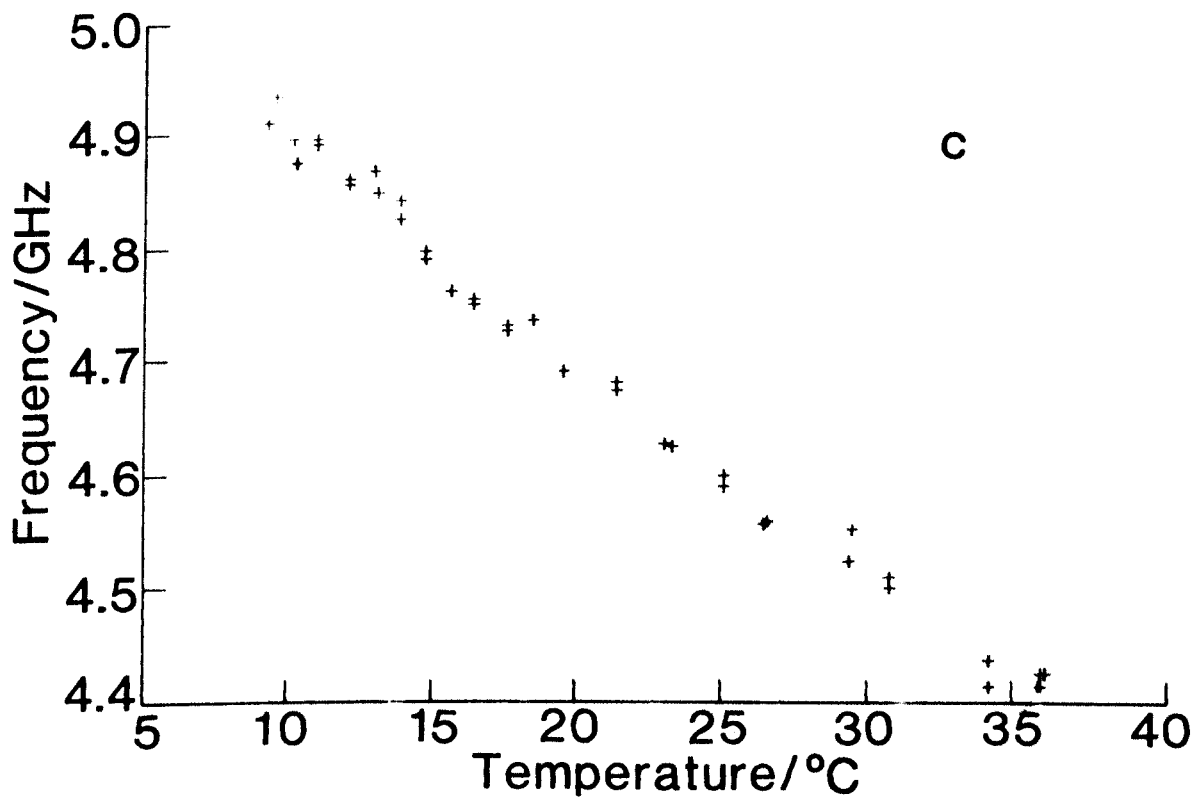


Fig 4.3.4 Experimental polarised Rayleigh-Brillouin spectrum of oleic acid at 12 °C showing two Fabry-Perot orders. The solid line indicates the theoretical fit incorporating a Mountain line (equation A1.4.2) and every fourth data point by a circle.

Fig 4.3.5 Oleic acid results

- (a) Measured Brillouin shifts plotted against temperature
- (b) Calculated hypersonic elastic modulus plotted against temperature





Octanoic acid solution

(c) Measured Brillouin shifts plotted against temperature

on temperature is typical and has been found for a wide range of polymer melts<sup>[116]</sup>. It is evident that there is considerably more spread on the data within the transition region than outside it.

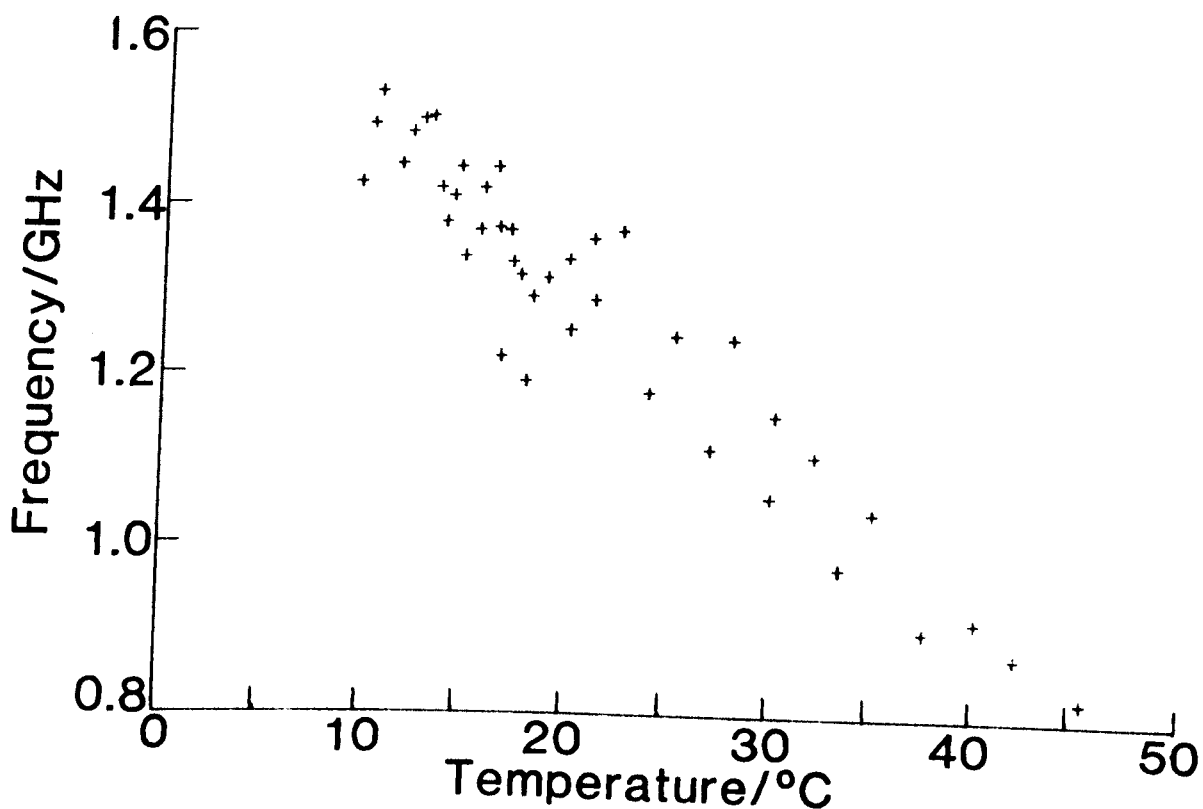
The variation of frequency shift with temperature for the octanoic acid solution is very slightly exponential (Fig 4.3.5(c)) with no evident discontinuity. The small deviation from linearity is probably due to different temperature coefficients for n-octane and n-octanoic acid. The spread on the data points appears to be constant across the entire temperature range.

The difference in spread on the data points between the two solutions is significant and is discussed in Section 4.5.4.

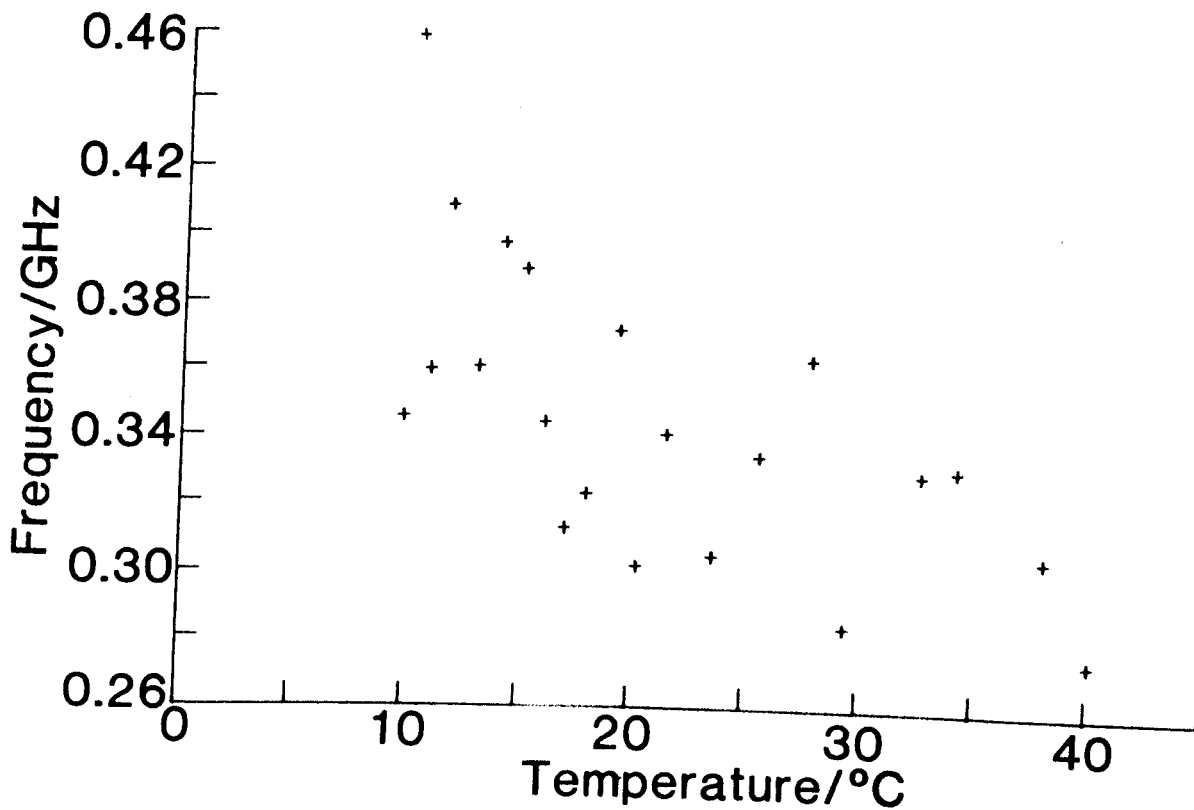
The Full-Width at Half-Maximum Height (FWHM) of the Brillouin linewidth for both solutions show no discernible anomaly in their variation with temperature (Fig 4.3.6). The scatter on the linewidth data is considerably larger than that of the shift measurements. A discontinuity in the Brillouin linewidth variation with temperature may indeed exist, but even if this is the case it is smaller than that for the shift and masked by the large scatter on the original data. However, the FWHM tends to increase with decreasing temperature for both solutions.

Fig 4.3.6 Measured deconvoluted Brillouin linewidths plotted against temperature:

(a) Oleic acid solution



(b) Octanoic acid solution



#### 4.4 Statistical Analysis of the Results

Three independent statistical methods were employed to ascertain the optimum choice of fitting function for the results. In addition to the usual least squares criteria a Linear Correlation test and the One-Sample Runs test were used. (A full description of these tests is given in Section 3.3.2 and Appendix 2.)

The results were fitted to two straight lines and for comparison a single straight line and an exponential.

For the case of two straight lines it was necessary to determine a statistically significant break point between the high and low temperature regions. This was achieved by making the break point a variable parameter of the fitting procedure. The optimum value of the break point ( $T_B$ ) was that which corresponded to a global minimum in the sum of squares and maximised the One-Sample Runs test probability.

The statistical analysis of the data from the oleic acid solution is shown in Table 4.4.1. It is apparent that two straight lines intersecting at a unique temperature best describe the viscosity data of Fig 4.3.3 and the density data of Fig 4.3.1. On the basis of the One-Sample Runs test two straight lines were found to be preferable to the other functions because the systematic deviations on the fitted variables are lower. The results of the statistical analysis for the Brillouin measurements are also presented in Table 4.4.1. As with the previous results the variation of frequency shift with temperature is best described by two straight lines with a marked change in slope of approximately 50% between the high and low temperature regions. The results for the FWHH of the Brillouin lines indicate that there is no preferred functional description. This is not surprising in view of the characteristically large scatter on the data.

Table 4.4.1 Results of Statistical Analysis: Oleic Acid Solution

FITTING FUNCTION	EXPERIMENTAL RESULTS	SUM OF SQUARES	ONE-SAMPLE RUNS TEST PROBABILITY	LINEAR CORRELATION TEST PROBABILITY	LINE 1 ( $T \leq T_B$ )		LINE 2 ( $T > T_B$ )	
					A (1) (S.D)	A (2) (S.D)	A (1) (S.D)	A (2) (S.D)
One Straight Line	(a) $v_B$	$1.4 \times 10^{-3}$	0.1	1.0	6.25 (0.05)	-0.022 (0.002)		
	(b) FWHH	$3.5 \times 10^{-3}$	0.1	1.0	1.69 (0.10)	-0.019 (0.004)		
	(c) $\eta_s$	$2.0 \times 10^{-4}$	$5.5 \times 10^{-6}$	1.0	-8.19 (0.36)	3.33 (0.11)		
	(d) $\rho$	$8.2 \times 10^{-8}$	$1.0 \times 10^{-10}$	1.0	0.9827 (0.0028)	-0.0007 (0.0001)		
Two Straight Lines	(a) $v_B$	$4.9 \times 10^{-4}$	1.0	1.0	6.49 (0.13)	-0.040 (0.009)	6.21 (0.04)	-0.021 (0.001)
	(b) FWHH	$3.1 \times 10^{-3}$	1.0	1.0	1.82 (0.24)	-0.029 (0.017)	1.71 (0.127)	-0.020 (0.004)
	(c) $\eta_s$	$2.0 \times 10^{-5}$	$2.1 \times 10^{-2}$	1.0	-7.53 (0.18)	3.13 (0.05)	-9.63 (0.32)	3.75 (0.09)
	(d) $\rho$	$8.5 \times 10^{-9}$	$1.3 \times 10^{-2}$	1.0	0.9804 (0.0004)	-0.0005 (0.0000)	0.9836 (0.0039)	-0.0007 (0.0002)
One Exponential Curve	(a) $v_B$	$3.5 \times 10^{-5}$	$9.1 \times 10^{-2}$	1.0	6.28 (0.01)	-0.004 (0.000)		
	(b) FWHH	$2.2 \times 10^{-3}$	1.0	1.0	1.81 (0.08)	-0.017 (0.003)		
	(c) $\eta_s$	$2.4 \times 10^{-6}$	$2.4 \times 10^{-3}$	1.0	0.07 (0.04)	1.10 (0.01)		
	(d) $\rho$	$2.0 \times 10^{-6}$	$8.2 \times 10^{-8}$	1.0	0.9831 (0.0030)	-0.0007 (0.0001)		

Table 4.4.2 Results of Statistical Analysis: Octanoic Acid Solution

FITTING FUNCTION	EXPERIMENTAL RESULTS	SUM OF SQUARES	ONE-SAMPLE RUNS TEST PROBABILITY	LINEAR CORRELATION TEST PROBABILITY	LINE 1 ( $T \leq T_B$ )		LINE 2 ( $T > T_B$ )	
					A (1) (S.D)	A (2) (S.D)	A (1) (S.D)	A (2) (S.D)
One Straight Line	(a) $\nu_B$	$2.1 \times 10^{-4}$	$1.3 \times 10^{-2}$	1.0	5.05 (0.03)	-0.014 (0.001)		
	(b) FWHH	$4.3 \times 10^{-2}$	$8.4 \times 10^{-2}$	1.0	0.49 (0.07)	-0.003 (0.003)		
	(c) $\eta_s$	$5.4 \times 10^{-6}$	$5.9 \times 10^{-6}$	1.0	-4.02 (0.07)	1.29 (0.02)		
	(d) $\rho$	$1.9 \times 10^{-6}$	$6.5 \times 10^{-11}$	1.0	0.9103 (0.0028)	-0.0009 (0.0001)		
Two Straight Lines	(a) $\nu_B$	$1.1 \times 10^{-4}$	1.0	1.0	5.04 (0.05)	-0.013 (0.004)	5.01 (0.03)	-0.013 (0.001)
	(b) FWHH	$3.6 \times 10^{-2}$	1.0	1.0	0.43 (0.19)	0.002 (0.186)	0.44 (0.09)	-0.002 (0.003)
	(c) $\eta_s$	$2.1 \times 10^{-6}$	$5.8 \times 10^{-2}$	1.0	-4.12 (0.05)	1.32 (0.02)	-3.86 (0.13)	1.25 (0.04)
	(d) $\rho$	$1.5 \times 10^{-6}$	$9.6 \times 10^{-3}$	1.0	0.972 (0.0083)	-0.0007 (0.0006)	0.9121 (0.0003)	-0.0010 (0.0000)
One Exponential Curve	(a) $\nu_B$	$1.2 \times 10^{-5}$	$3.7 \times 10^{-3}$	1.0	5.06 (0.010)	-0.004 (0.0003)		
	(b) FWHH	$3.5 \times 10^{-1}$	$8.4 \times 10^{-2}$	1.0	0.49 (0.20)	-0.009 (0.009)		
	(c) $\eta_s$	$6.2 \times 10^{-3}$	$2.0 \times 10^{-5}$	1.0				
	(d) $\rho$	$2.3 \times 10^{-6}$	$4.1 \times 10^{-11}$	1.0	0.9105 (0.0030)	-0.0010 (0.0002)		

For comparison the results of the statistical analysis for the n-octanoic acid solution are shown in Table 4.4.2. Although the results of the Brillouin shift against temperature visually display an anomaly the statistical analysis of the data indicates that there is no preferred fitting function; the fitted values of the two straight-line fit overlap when the associated standard deviations are considered, that is, the two lines are indistinguishable. Similar arguments apply to the Brillouin linewidths, the density and the viscosity results.

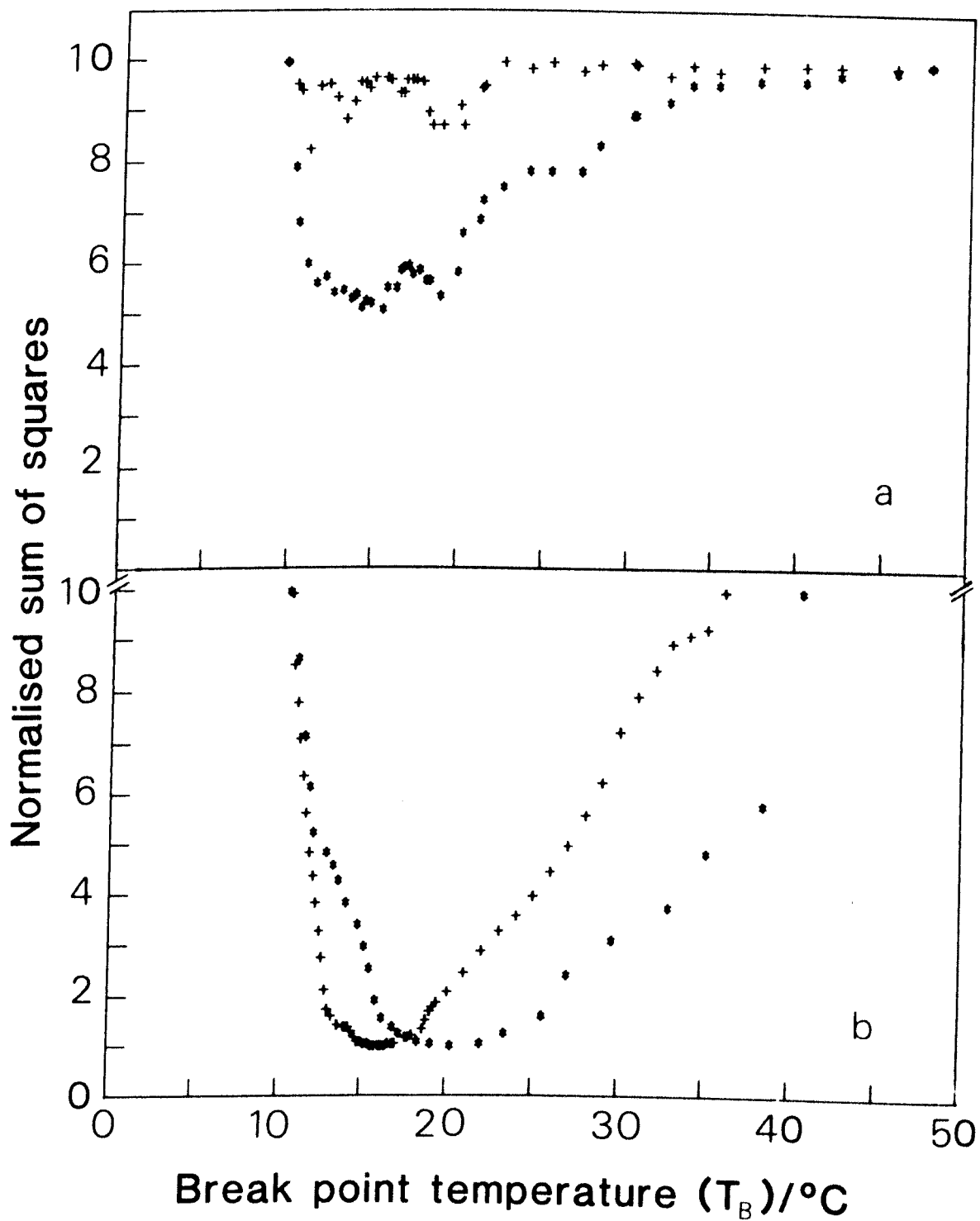
In Fig 4.4.1 the sum of squares corresponding to each selected break point for the oleic acid solution results are depicted. The sum of squares is normalised such that a single straight line fit is equal to 10. In all cases, except that of the Brillouin linewidths, there is a clear optimum range of values over which the sum of squares varies little from its minimum value. This was also found to be the case for the One-Sample Runs test probability. The Linear Correlation test returned a value of 1.0 for all the functional forms investigated, indicating that none of the functions investigated was preferred. This test was therefore not useful in distinguishing the appropriate function.

The transition temperatures found for each experimental set are shown in Table 4.4.3. The ranges shown are those for which the transition temperature is nearly equiprobable.

Fig 4.4.1 Normalised sum of squares plotted against break point temperature  $T_B$  for the oleic acid solution.

(a) Brillouin linewidths (+); Brillouin shifts (\*).

(b) Density (+); Kinematic shear viscosity (\*).



Experiment	Transition Temperature $T_B/^\circ\text{C}$	Temperature Range for $T_B/^\circ\text{C}$
Brillouin Shift	16.2	14.0 - 18.0
Brillouin FWHH	18.0	14.5 - 20.0
Kinematic Viscosity	18.5	18.0 - 20.0
Density	16.0	15.4 - 17.6

Table 4.4.3 Transition temperature ( $T_B$ ) and range of  $T_B$  from each experiment: Oleic Acid Solution

The general concurrence of the statistical analysis demonstrates that in all cases, except that of the Brillouin linewidths, the oleic acid solution data are best represented by two intersecting straight lines. However, the statistical analysis of the data for the *n*-octanoic acid solution indicates that there are no preferred functional forms.

## 4.5 Discussion

### 4.5.1 Kinematic Shear Viscosity

The viscosity of the solutions can be described by the Arrhenius-Frenkel-Eyring equation<sup>[117]</sup>.

$$\eta = \left[ \frac{hN}{V} \exp\left(-\frac{\Delta S^*}{R}\right) \right] \exp\left[\frac{\Delta H^*}{RT}\right] \quad (4.5.1)$$

where  $h$  is Planck's constant;  $N$  is the Avogadro number;  $V$  is the molar volume;  $\Delta S^*$  and  $\Delta H^*$  are, respectively, the entropy and heat of activation of the process of viscous flow;  $R$  is the gas constant;  $T$  is the absolute temperature.

The corresponding kinematic shear viscosity is given by

$$\eta_s = \eta/\rho = \left[ \frac{h}{M} \exp\left(-\frac{\Delta S^*}{R}\right) \right] \exp\left[\frac{\Delta H^*}{RT}\right] \quad (4.5.2)$$

where  $M$  is the molar mass and  $\rho$  the density. According to equation (4.5.2) a change in slope is indicative of a change in the activation energy associated with viscous flow between the high and low temperature ranges.

The results for the temperature dependence kinematic viscosity of the oleic acid solution agree with those found by other experimenters for a variety of polymer melts<sup>[102]</sup>. The Arrhenius plot consists of two straight lines with a break point occurring in this case at 18.5 °C. The slope in the  $T < 18.5$  °C range is greater than that in the  $T > 18.5$  °C, the converse is true for the corresponding intercepts.

The activation energy ( $\Delta H^*$ ) increases from the high temperature to the low temperature state from 26.0 kJmol<sup>-1</sup> to 32.2 kJmol<sup>-1</sup>, a

change of  $5.2 \text{ kJmol}^{-1}$ , that is, the low temperature state has a higher activation energy for the process of viscous flow. The intercept for the high temperature state exceeds that for the low temperature state indicating a change in entropy at the transition temperature, that is, an increase in the entropy change required for the process of viscous flow from the high to the low temperature state.

Using the Boltzmann relation,

$$S = k_B \ln W \quad (4.5.3)$$

where  $k_B$  is the Boltzmann constant and  $W$  is the number of molecular arrangements, in conjunction with equation (4.5.2) the ratio  $W_h/W_l$  is calculated to be approximately 3. The subscripts refer to the high (h) and low (l) temperature states. This implies that there are nearly 3 times as many molecular arrangements in the high temperature state as in the low temperature state.

Both the increase in activation energy and the increase in the entropy in going from the high to the low temperature state imply that the transition involves an increase in the local order of the liquid.

#### 4.5.2 Density

The density variation with temperature of the oleic acid solution shows a discontinuity in the region  $14^\circ\text{C}$  to  $17^\circ\text{C}$ .

The volume expansion coefficient,  $\gamma$ , is given by

$$\gamma = \frac{1}{V_0} \left[ \frac{\partial V}{\partial T} \right]_p \quad (4.5.4)$$

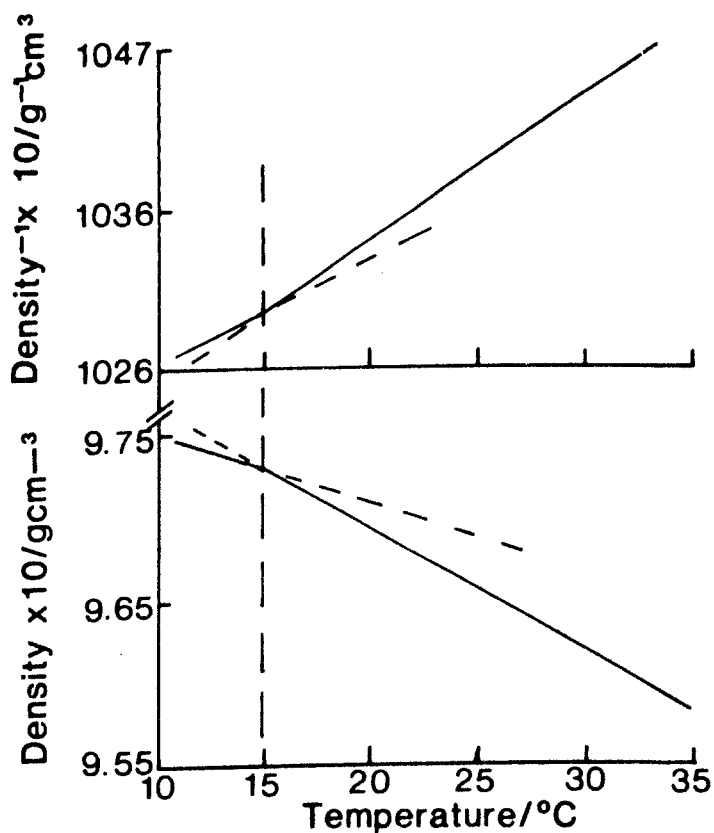
this can be written as

$$\gamma \propto \frac{1}{(1/\rho_0)} \left[ \frac{\partial \left[ \frac{1}{\rho} \right]}{\partial T} \right]_P \quad (4.5.5)$$

The variation of  $\frac{\partial \rho}{\partial T}$  and  $\frac{\partial \left[ \frac{1}{\rho} \right]}{\partial T}$  are shown in Fig 4.5.1. Clearly, the low temperature state has a smaller expansion coefficient. This result implies an increase in the local order of the liquid consistent with the viscosity result. The value of  $\gamma$  in the low temperature region is  $5.65 \times 10^{-4} \text{ K}^{-1}$  compared to  $7.87 \times 10^{-4} \text{ K}^{-1}$  above the transition region.

Fig 4.5.1 Oleic acid solution

- (a) Variation of thermal expansion coefficient
- (b) Variation of density with temperature



#### 4.5.3 Refractive Index

The temperature variation of refractive index is greater below 16.5 °C than above. This result is closely connected to the density result through the Lorentz-Lorenz equation<sup>[118]</sup>

$$\frac{(n^2 - 1)}{(n^2 + 2)} \propto \rho \alpha_0 \quad (4.5.6)$$

where  $n$  is the refractive index,  $\alpha_0$  is the molecular polarisability and  $\rho$  is the density.

According to equation (4.5.6) a decrease in the slope of density against temperature should be accompanied by a proportionately smaller decrease in the temperature gradient of the refractive index. This is not found experimentally. Fig 4.3.3(a) shows an increase in the refractive index gradient. This implies that the average molecular polarisability has increased. This is consistent with an increase in local ordering to produce a locally nematic phase.

#### 4.5.4 Polarised Rayleigh-Brillouin Scattering

The longitudinal hypersonic modulus evaluated from the Brillouin measurements also reflects the change in structure; two straight lines, intersecting at a temperature of 16.2 °C with a change of slope of approximately 50%, describe this behaviour most closely. This large change in gradient must be associated with a change in the local structure of the liquid to form a more ordered phase.

As mentioned in Section 4.3.4 there is an increase in scatter on the data points within the transition region. This transition region involves a change of phase analogous to that of the glass-to-rubber transition that occurs in amorphous polymers. This glass-to-

rubber transition has been found to be rate dependent<sup>[119]</sup>. It is likely therefore, that the ordering phenomenon in oleic acid is also a rate dependent process, thus accounting for the increased spread on the data within the transition region. This was not found in the octanoic acid solution.

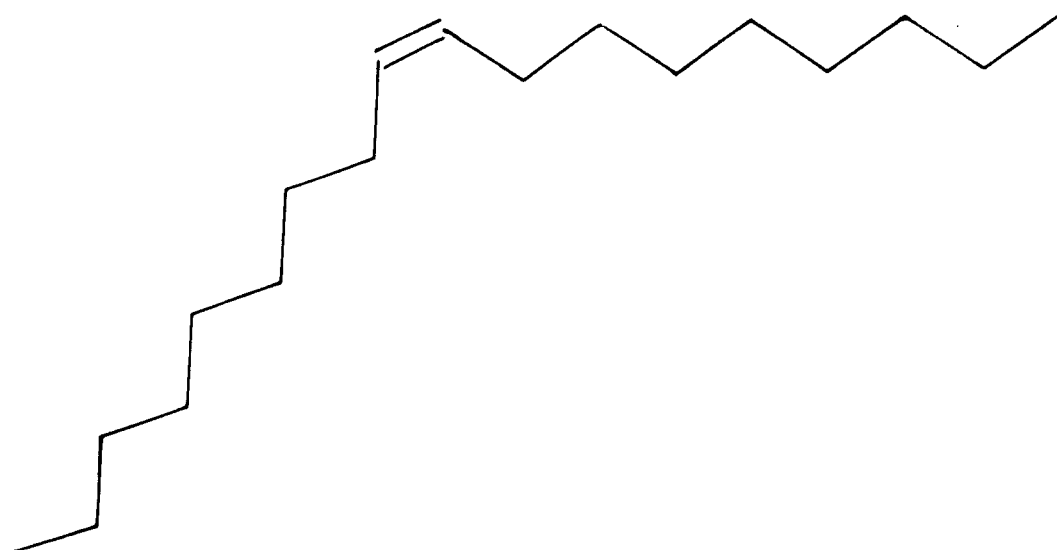
#### 4.6 Conclusions

From the various measurements described above, it appears that oleic acid exhibits anomalous behaviour in the temperature variation of the physical properties investigated. The important fact that different physical properties of oleic acid show anomalous behaviour within the same narrow temperature range, 14 °C to 18 °C, implicates a change of structure.

It is highly probable that the ordering of the liquid is caused by a transisomerisation of the alkyl chains to form a locally nematic structure, that is, alignment of the molecules can take place far more easily if the alkyl chains take up an all-*trans* configuration, the lowest energy conformation, about the *cis*-double bond (Fig 4.6.1).

This conclusion is supported by the fact that the physical properties of the octanoic acid solution show no discernible anomaly over the same temperature range. This solution was chosen to molecularly model the oleic acid solution but with the *cis*-double bond absent thus removing the anchoring effect of the double bond about which the transisomerisation can take place.

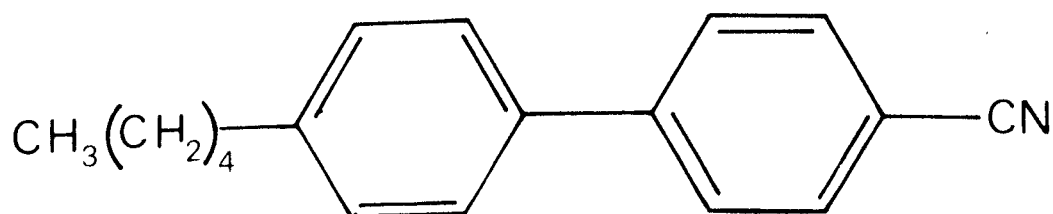
Fig 4.6.1 All-*trans* configuration of oleic acid



The temperature range over which the anomalous behaviour occurs is similar to that found in some biological membranes, containing fatty acid alkyl chains, of which oleic acid is a fundamental constituent, for example, glycerol monooleate. This suggests that the thermotropic phase transformation seen in these systems can be associated with the  $T_u$  phenomenon occurring in the oleyl chain.

Depolarised Raleigh-Brillouin scattering can be used to study molecular motion in liquids (Section 2.3). The depolarised spectrum monitors fluctuations in the anisotropy tensor associated with molecular reorientation. This spectrum would be very sensitive to any mesomorphic ordering in the liquid. The depolarised (VH) spectrum of the oleic acid solution was examined but the line width obtained was found to be too narrow to resolve with the Fabry-Perot interferometer. This implies that the multiparticle correlation time is very long and that there is large scale cooperative motion in the liquid. A similar effect was found when the depolarised spectrum of the liquid crystal 4-cyano-4'-n-pentylbiphenyl (Fig 4.6.2) was examined.

Fig 4.6.2 Molecular Structure of the Liquid Crystal 4-cyano-4'-n-pentylbiphenyl



The width of the depolarised spectrum could be resolved only above approximately 45 °C. At 80 °C the half-width was approximately 120 MHz, implying large scale cooperative motion even in the isotropic phase. Hence, the behaviour exhibited by oleic acid resembles that of a liquid crystal; the high temperature region equivalent to the

isotropic phase and the low temperature region equivalent to the nematic phase.

CHAPTER 5 - RESULTS AND ANALYSIS OF DEPOLARISED RAYLEIGH-BRILLOUIN  
SCATTERING FROM THE ALKANES  $C_5H_{12}$  to  $C_8H_{18}$

Contents

5.1 Introduction

5.2 Results

5.2.1 Isomers of  $C_8H_{18}$

5.2.2 Isomers of  $C_7H_{16}$

5.2.3 Isomers of  $C_6H_{14}$

5.2.4 Isomers of  $C_5H_{12}$

5.3 Analysis of the Spectral Data

5.3.1 The Stokes-Einstein-Debye Relation

5.3.2 Molecular Self-Diffusion

5.3.3 Origin of the Second Lorentzian

5.3.4 Comparison of Experimental Molecular Correlation Times  
with Results from Computer Simulations

## 5.1 Introduction

Presented in this chapter are the depolarised light scattering results from the alkanes n-pentane to n-octane and some isomers of the homologous series. The liquids, listed in Table 3.2.1, were studied over a temperature range of 0 °C to within 25 °C of their boiling points.

Three to four spectra were consecutively obtained at a particular temperature. The values obtained for the peak half widths were averaged thus reducing the scatter on the final results. To optimise the error in the data analysis the FSR's used were such that the ratio of the peak half width to the FSR was approximately 0.1.

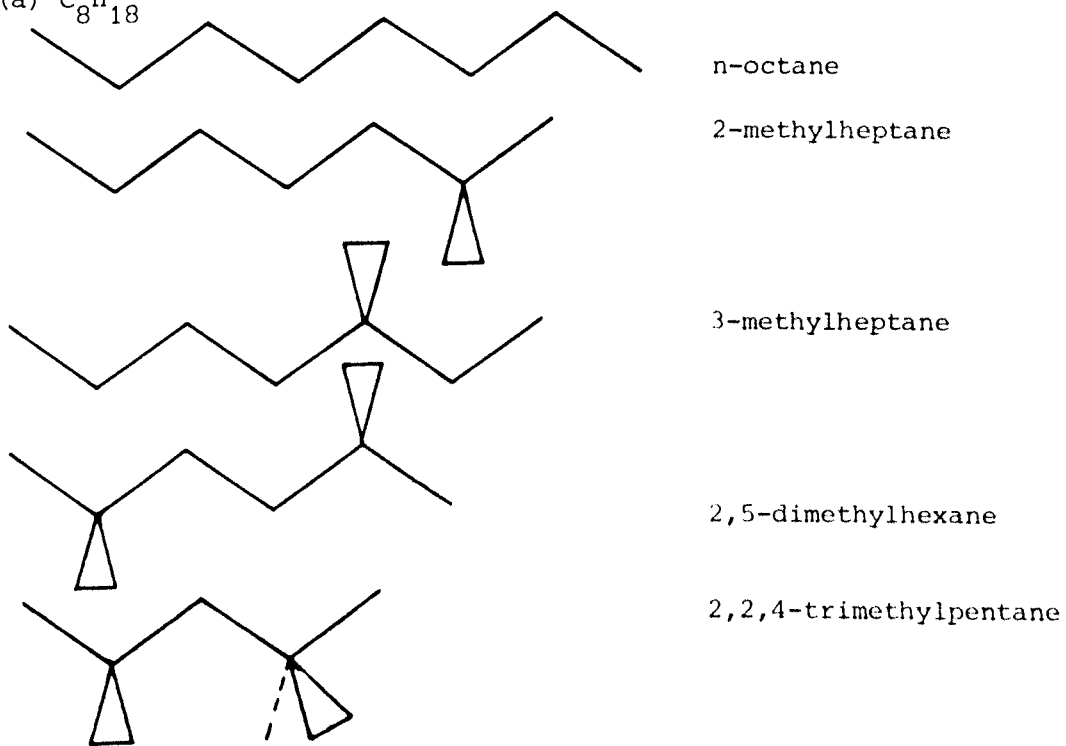
Since coupling between shear modes and molecular reorientation may occur, the depolarised Rayleigh-Brillouin spectrum can potentially be very complex. This coupling manifests itself as a dip in the VH spectra, Section 2.3, and such a dip has been observed for longer chain n-alkanes [3,104,120]. However, for all the alkanes studied in this thesis the dip was too narrow and too small to be resolved.

In Fig 5.1.1 to Fig 5.1.4 the all-*trans* structure of each of the liquids investigated is depicted. Each line represents a carbon-carbon bond and the hydrogen atoms have been omitted for clarity. From these diagrams it is clear that the molecules become more spherical and have more restricted conformational degrees of freedom as the branching increases.

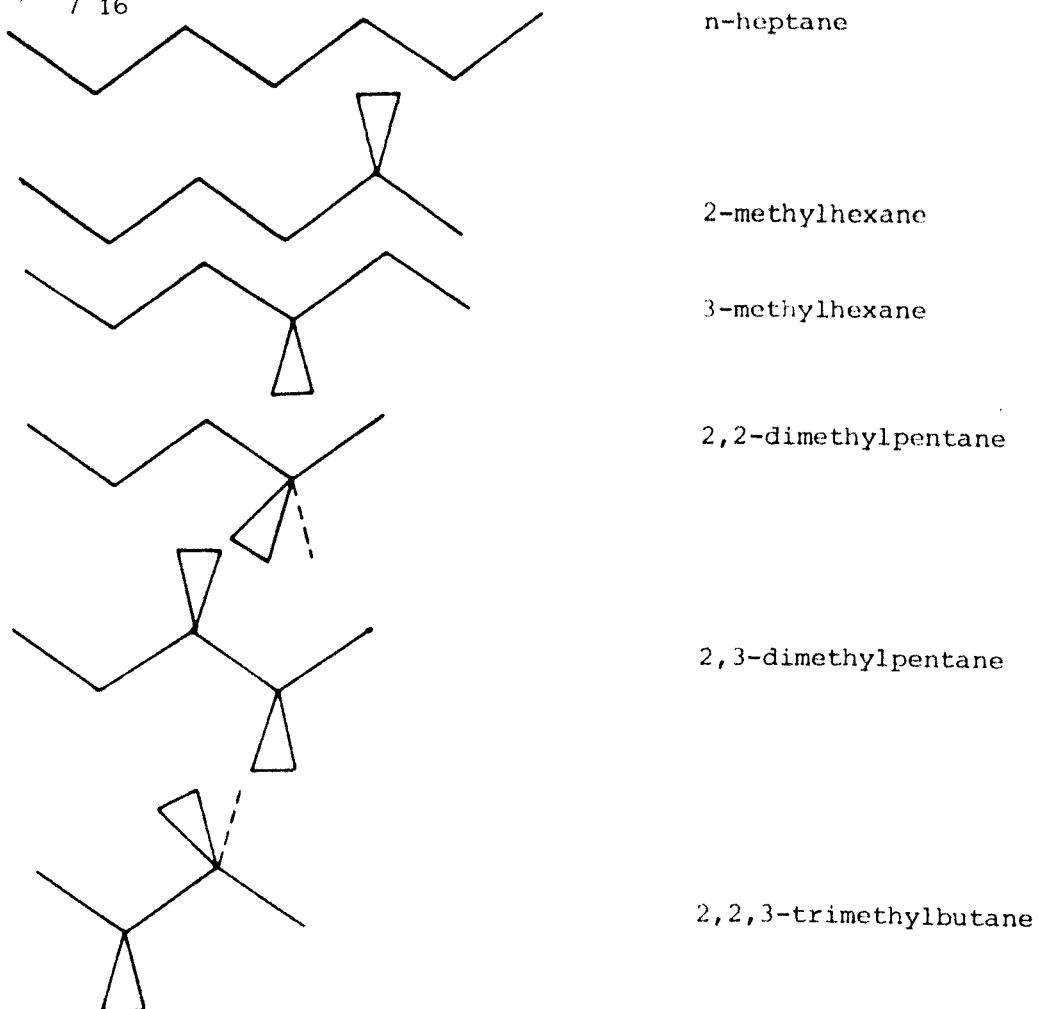
The results obtained for each group of isomers, that is,  $C_8H_{18}$ ,  $C_7H_{16}$ ,  $C_6H_{14}$  and  $C_5H_{12}$  are presented. The molecular correlation times are then analysed in terms of the Stokes-Einstein-Debye relation discussed in Section 2.4.

Fig 5.1.1 Schematic all-*trans* representation of the isomers

(a)  $C_8H_{18}$



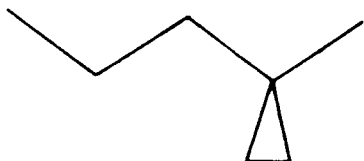
(b)  $C_7H_{16}$



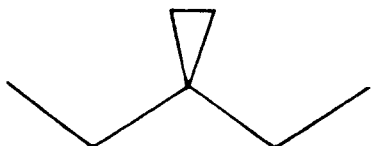
(c)  $C_6H_{14}$



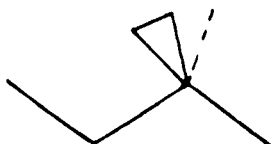
n-hexane



2-methylpentane



3-methylpentane

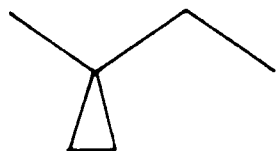


2,2-dimethylbutane

(d)  $C_5H_{12}$



n-pentane



2-methylbutane



carbon-carbon bond in the plane of the paper



carbon-carbon bond into the plane of the paper



carbon-carbon bond out of the plane of the paper

## 5.2 Results

### 5.2.1 Isomers of C<sub>8</sub>H<sub>18</sub>

The results for the peak half width as a function of temperature are presented in Fig 5.2.1 to Fig 5.2.5. Clearly the reorientational frequency increases with increasing temperature for all the isomers.

For the isomers n-octane, 2-methylheptane, 3-methylheptane and 2,5-dimethylhexane the spectra were all successfully fitted to a single Lorentzian superimposed on a flat base (equation (A1.4.3) for the entire range of FSR's used. The flat base arises from the multiple overlapping of the broad collisional background. The standard deviation on each individual peak half width measured was of the order 12%. However, the peak half widths were found to be reproducible to within  $\pm 5\%$ . Table 5.2.1 shows examples of the statistical analysis of a single Lorentzian fit to the spectra for each of the isomers discussed above. For these isomers the peak half widths measured at different FSR's were found to agree within experimental error. However, when the isomer 2,2,4-trimethylpentane was investigated at FSR's of 685 GHz and 1500 GHz the results for the peak half widths as a function of temperature did not agree - Fig 5.2.5. The values measured at an FSR of 1500 GHz are approximately 50% larger than those measured at an FSR of 685 GHz. The implication of these results is that the spectra are not single Lorentzian.

The cause of this discrepancy was investigated in some detail and is discussed below. As already discussed in Chapter 2, in order to obtain spectra that are composed of single Lorentzian lineshapes superimposed on a flat background, there must be a timescale separation between the rotational and the collisional motion. With the large FSR's used to examine the spectra from 2,2,4-trimethylpentane the first possibility that arises is that the background is no longer

Fig 5.2.1 n-octane. Single Lorentzian fit to data: FSR = 110 - 170 GHz

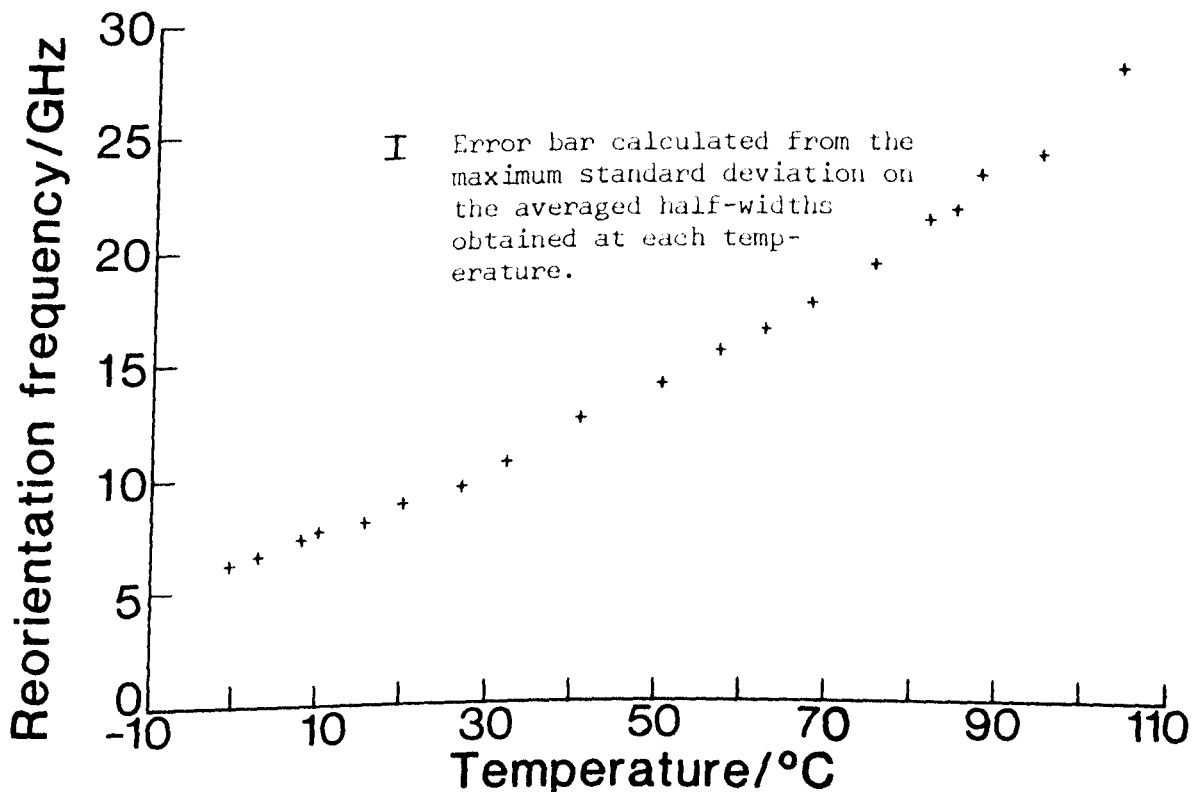


Fig 5.2.2 2-methylheptane. Single Lorentzian fit to data: FSR = 170 - 270 GHz

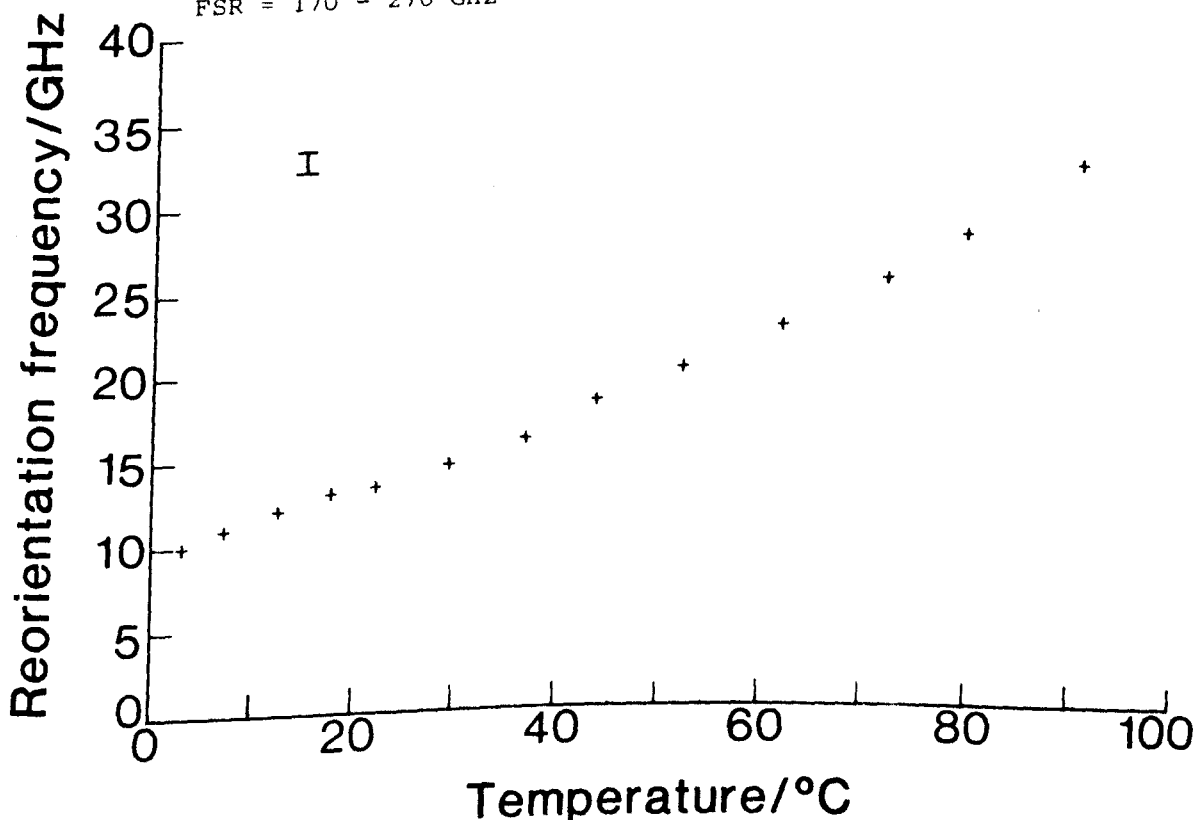


Fig 5.2.3 3-methylheptane. Single Lorentzian fit to data:  
FSR = 170 - 370 GHz

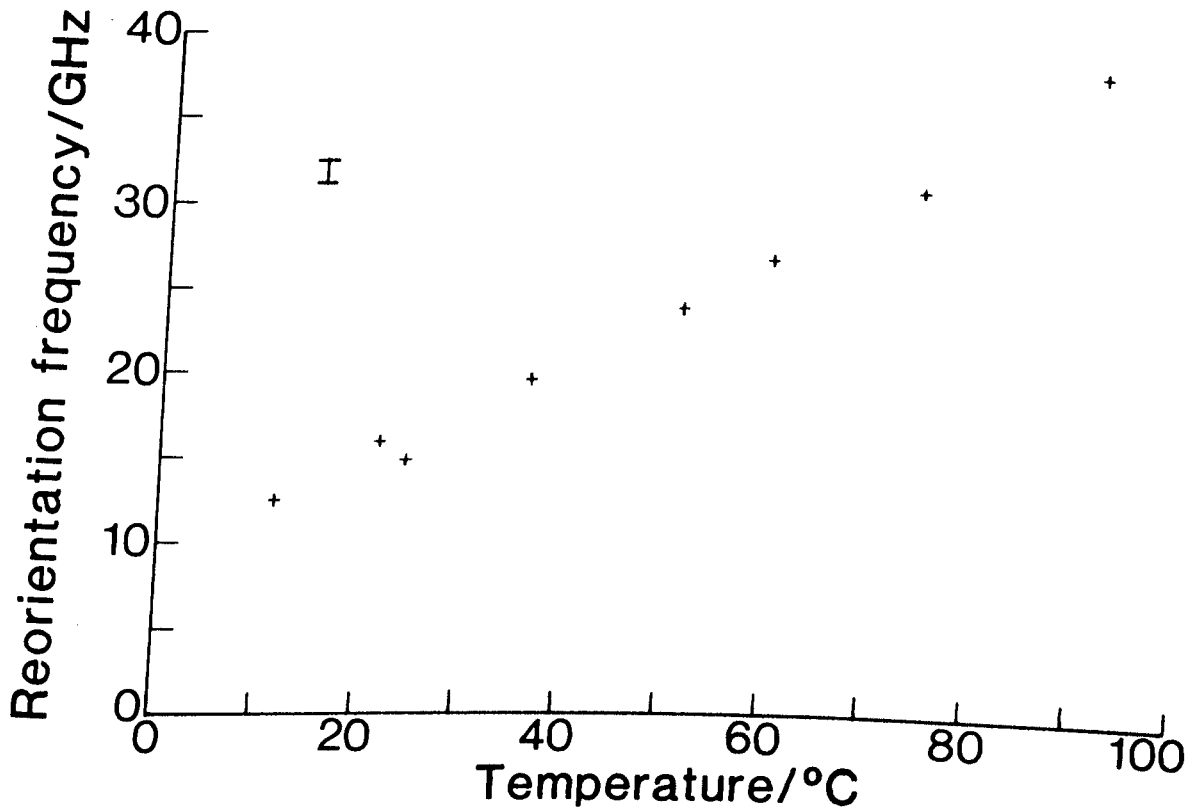


Fig 5.2.4 2,5-dimethylhexane. Single Lorentzian fit to data:  
FSR = 260 - 420 GHz

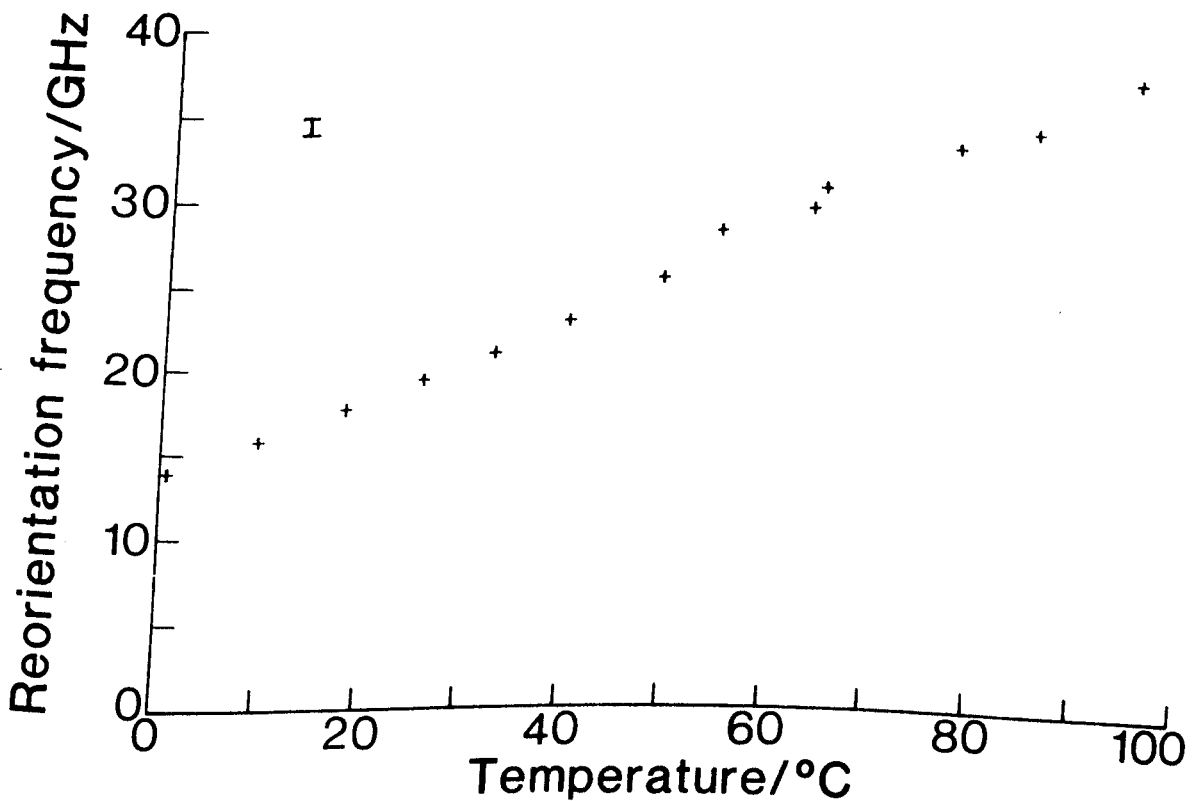


Fig 5.2.5 2,2,4-trimethylpentane.

- (a) Single Lorentzian fit to data: FSR = 1500 GHz
- (b) Single Lorentzian fit to data: FSR = 685 GHz
- (c) Two Lorentzian fit to data: FSR = 685 GHz (+)  
FSR = 1500 GHz (\*)

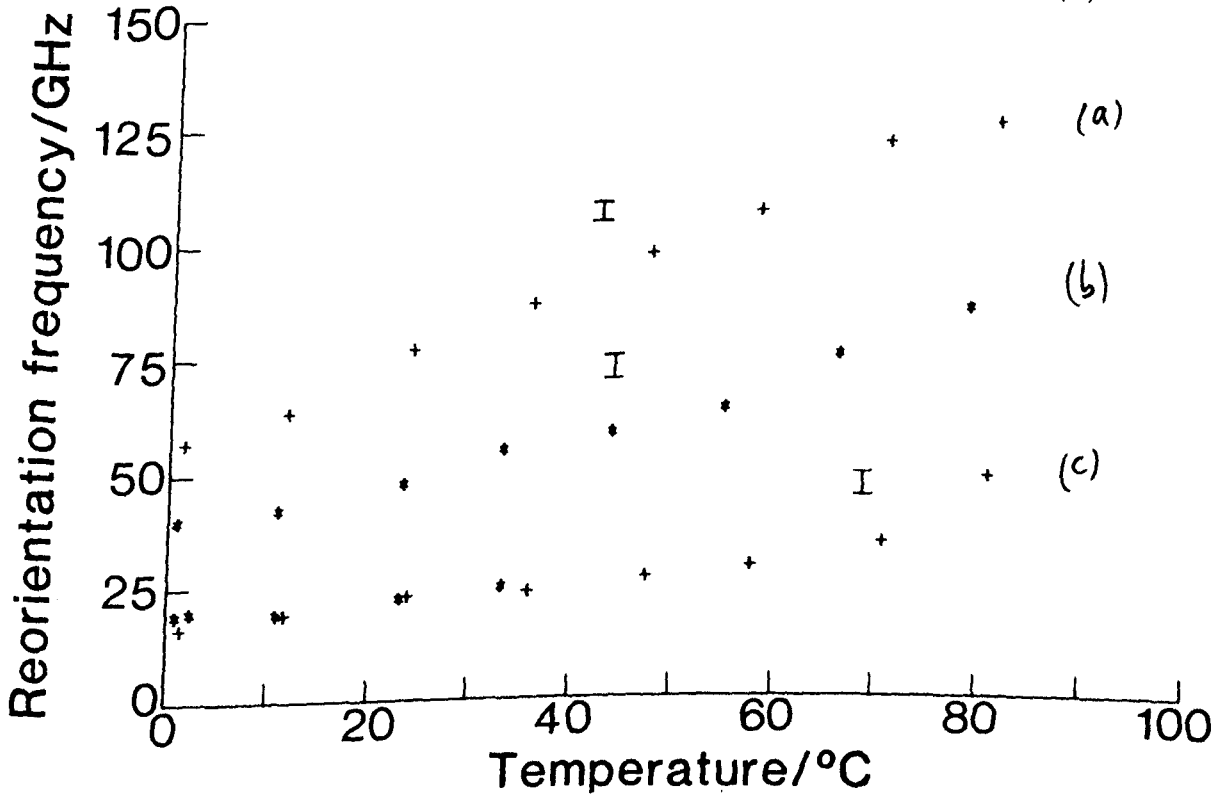


Fig 5.2.6 2,2,4-trimethylpentane. Variation of the second Lorentzian peak half width with temperature. FSR = 1500 GHz

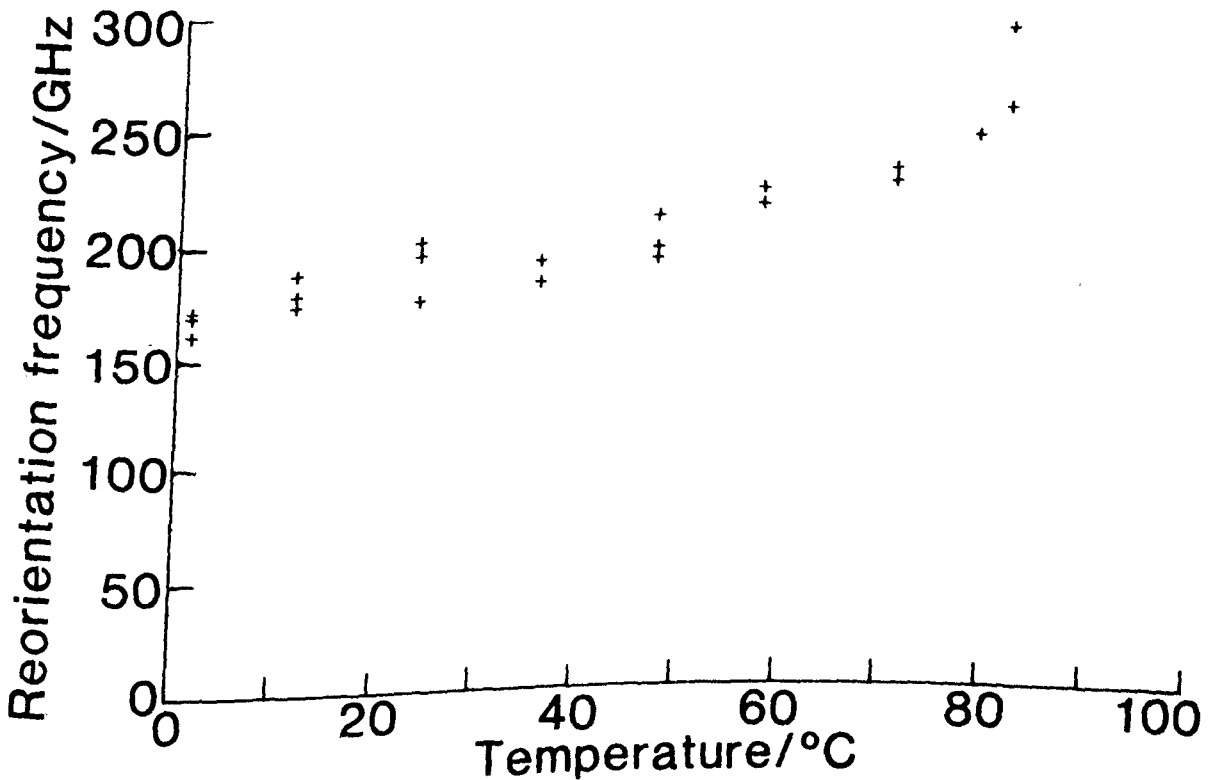


Table 5.2.1 EXAMPLES OF THE STATISTICAL ANALYSIS OF THE SPECTRA OBTAINED FOR THE ISOMERS OF  $C_8H_{18}$ . THE FITTING FUNCTION WAS A SINGLE LORENTZIAN PLUS A FLAT BASE.

Liquid	Reduced $\chi^2$	Integral $\chi^2$ Probability	Linear Correlation Test: Probability	One Sample Runs Test	
				Number of Runs ( $n_r$ ) $\mu_r = 512$ $\sigma_r = 16$	Probability of Exceeding $ n_r $
n-octane T = 68 °C FSR = 112 GHz	0.98	0.43	0.32	514	1.0
2-methylheptane T = 41 °C FSR = 170 GHz	0.95	0.24	0.64	510	1.0
3-methylheptane T = 11.5 °C FSR = 170 GHz	1.02	0.41	0.10	506	1.0
2,5-dimethylhexane T = 40 °C FSR = 270 GHz	1.05	0.12	0.36	508	1.0

flat. Instead, due to the Fabry-Perot resolving part of the collisional motion, the base is better represented as exponential. The spectra were then analysed using a fitting function of a Lorentzian superimposed on an exponential base (equation (A1.4.4)). A comparison of the statistical analysis of the two objective functions, Table 5.2.2, indicated that the exponential base did not significantly improve the fit.

The second possibility investigated was that the spectra were composed of two Lorentzians, both centred at the incident frequency, superimposed on a flat base (equation (A1.4.5)). This fitting function was chosen on the basis of the results of Viogy et al<sup>[49]</sup>, discussed in Section 2.3.1, where a second broad Lorentzian component was found superimposed on a collisional background for several small 'rigid' symmetric and spherical top molecules. Since 2,2,4-trimethylpentane has far less flexibility than n-octane and is essentially globular in structure it is conceivable that similar effects could be influencing the spectra. The data were re-examined using the two Lorentzian fitting functions and the resulting fit found to be significantly improved. Indeed, the statistical analysis of the fit (Table 5.2.2) indicates that this is an appropriate choice of fitting function.

Fig 5.2.5 shows the variation of peak half widths, with temperature for the different fitting functions and different FSR's. Up to temperatures of approximately 40 °C a two Lorentzian fit to the data at both FSR's gives values for the reorientational frequency that are the same within experimental error. This is another indication of the validity of the choice of fitting function. At higher temperatures the values obtained at an FSR of 1500 GHz increase whilst those obtained at 685 GHz FSR start to decrease. This decrease is due to:

Table 5.2.2 A COMPARISON OF THE STATISTICAL ANALYSIS OF VARIOUS FITTING FUNCTIONS FOR 2,2,4-TRIMETHYLPENTANE:  
 FSR = 1500 GHz, T = 71 °C

Fitting Function	Reduced $\chi^2$	Integral $\chi^2$ Probability	Linear Correlation Test: Probability	One Sample Runs Test	
				Number of Runs ( $n_r$ ) $\mu_r = 512$ $\sigma_r = 16$	Probability of Exceeding $ n_r $
Single Lorentzian plus flat base	1.96	0.0	0.41	355	$1.4 \times 10^{-22}$
Single Lorentzian plus exponential base	2.14	0.0	0.18	373	$5.4 \times 10^{-17}$
Two Lorentzians plus flat base	1.03	0.196	0.49	505	1.0

- (i) the decrease in signal-to-noise ratio of the spectra, and
- (ii) the increase in the peak half width of the broad lower intensity second Lorentzian.

The combination of these two effects results in inadequate resolution of the two components and hence the computer program is unable to effect a separation of the two Lorentzian features.

Alms et al<sup>[67]</sup> discuss the situation under which a separation of two Lorentzians from a spectrum is possible. They conclude that it is necessary for the noise level to be significantly smaller than the maximum error and that a high signal-to-noise ratio is required to observe a low intensity broad Lorentzian under a strong narrow Lorentzian. The experimental considerations are realised at an FSR of 1500 GHz, and over a limited range of temperatures at 685 GHz FSR, by careful alignment of the optical components. However, above 40 °C at an FSR of 685 GHz exactly the opposite effects are seen thus causing the erroneous result of a decrease of peak half width with increasing temperature. Fig 5.2.6 depicts the variation of peak half width for the second Lorentzian component. All the values are presented to illustrate that the spread on the fitted values is much larger for the broad low intensity Lorentzian. This is to be expected from the previous discussion. However, the trend is an increase of peak half width with increasing temperature. In addition to 2,2,4-trimethylpentane, the isomer 2,3,4-trimethylpentane was examined but the results were not of sufficient reproducibility, due to a poor quality sample, to be included. However the results indicated very similar trends to those of 2,2,4-trimethylpentane.

### 5.2.2 Isomers of C<sub>7</sub>H<sub>16</sub>

The variation of the reorientational frequency with temperature for the isomers of C<sub>7</sub>H<sub>16</sub> investigated are shown in Fig 5.2.7 to Fig 5.2.12. The peak half width increases with increasing temperature for all the isomers.

The spectra obtained from n-heptane over the complete range of FSR's used were all successfully fitted to a single Lorentzian superimposed on a flat base. However, the fits to the spectra from the isomers 2-methylhexane, 3-methylhexane, 2,2-dimethylpentane, 2,3-dimethylpentane and 2,2,3-trimethylbutane were all found to be significantly improved when fitted to two Lorentzians superimposed on a flat base. An improvement was not found when the spectra were fitted to a single Lorentzian plus an exponential base. These observations are similar to those made for 2,2,4-trimethylpentane. A comparison of the statistical analysis of the various fitting functions for the isomers of C<sub>7</sub>H<sub>16</sub> is given in Table 5.2.3.

The liquids 2-methylpentane, 2,2-dimethylpentane and 2,2,3-trimethylbutane were only examined over a single FSR because in general a significantly different FSR gave very poor signal-to-noise ratios on the spectra and consequently very unreliable fits to the data. In addition difficulties were encountered in containing liquids of high vapour pressure.

The reorientational frequencies obtained from a two Lorentzian fit to the spectra from 3-methylhexane at lower FSR's were found to exhibit large scatter and are not shown. This scatter is due to the multiple overlapping of adjacent orders and hence the second Lorentzian appears as a portion of the background.

Fig 5.2.7 n-heptane. Single Lorentzian fit to data.  
FSR = 170 - 350 GHz

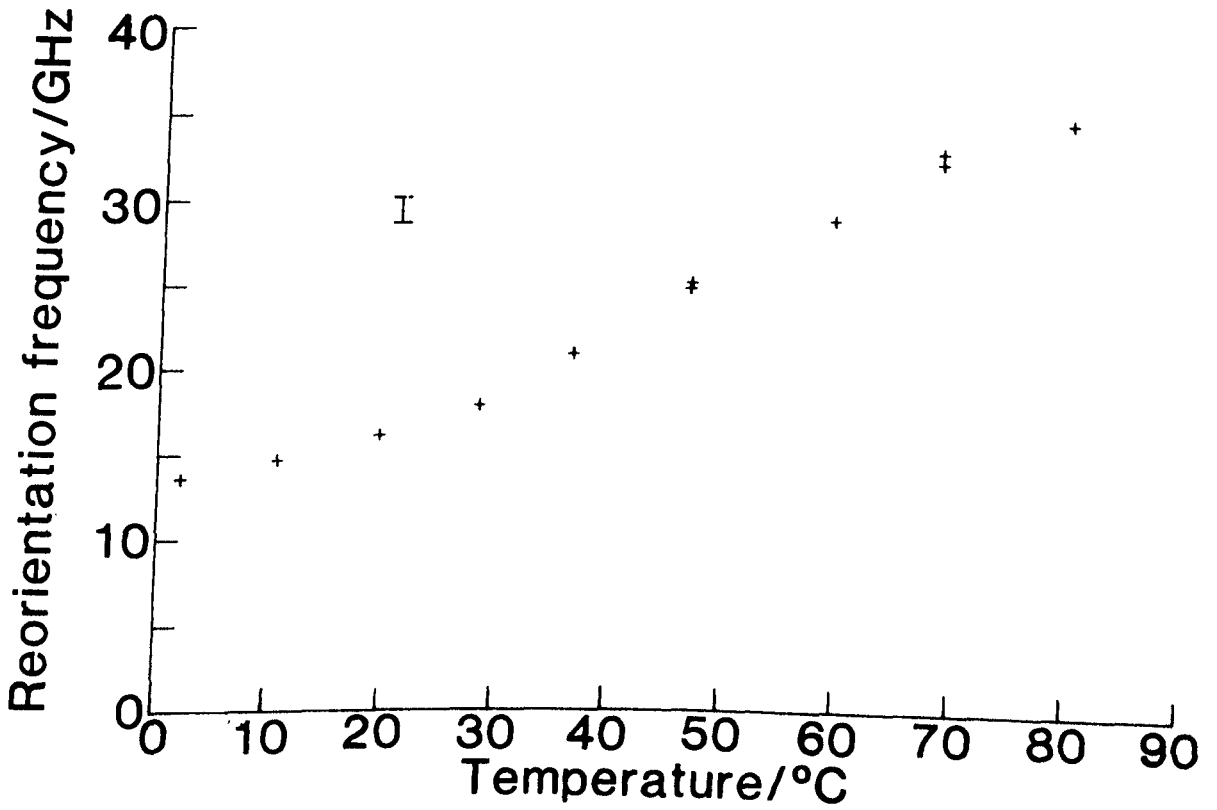


Fig 5.2.8 2-methylhexane. FSR = 450 GHz  
(a) Single Lorentzian fit to data  
(b) Two Lorentzian fit to data

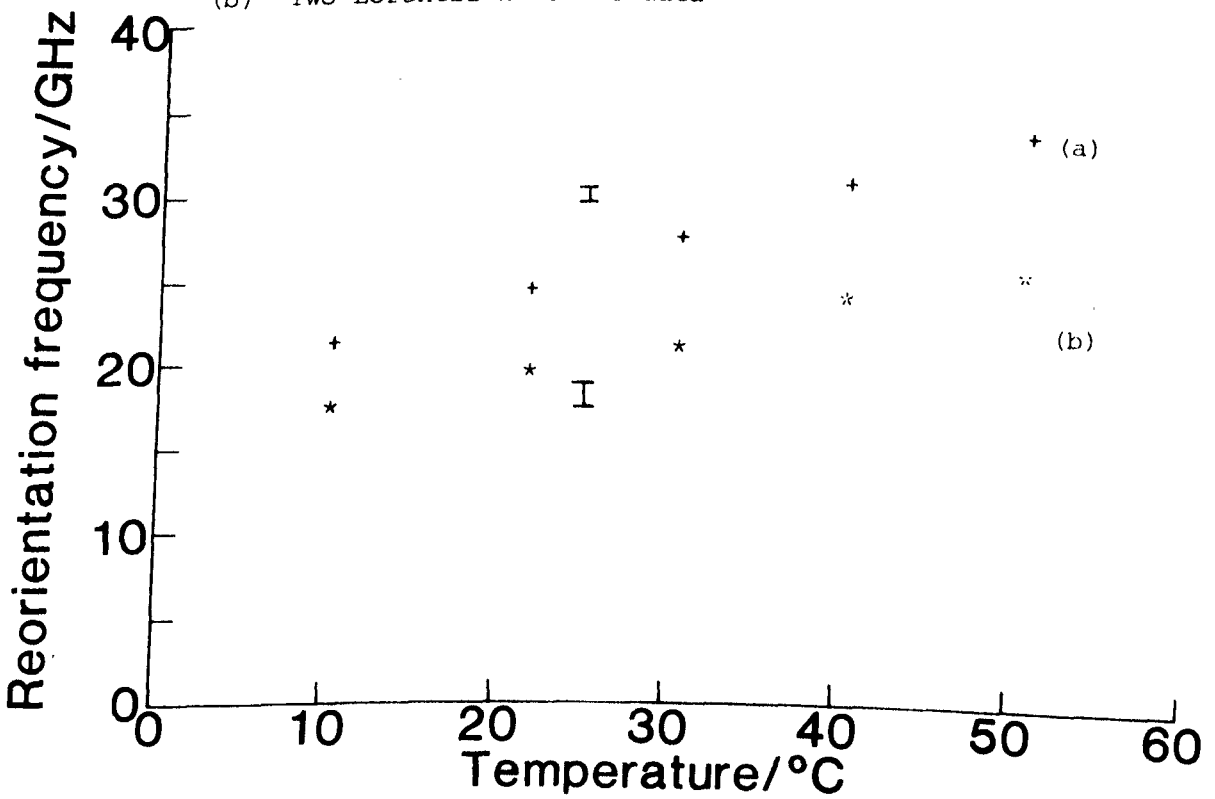


Fig 5.2.9 3-methylhexane.

- (a) Single Lorentzian fit to data. FSR = 1250 GHz
- (b) Single Lorentzian fit to data. FSR = 400-600 GHz
- (c) Two Lorentzian fit to data. FSR = 1250 GHz

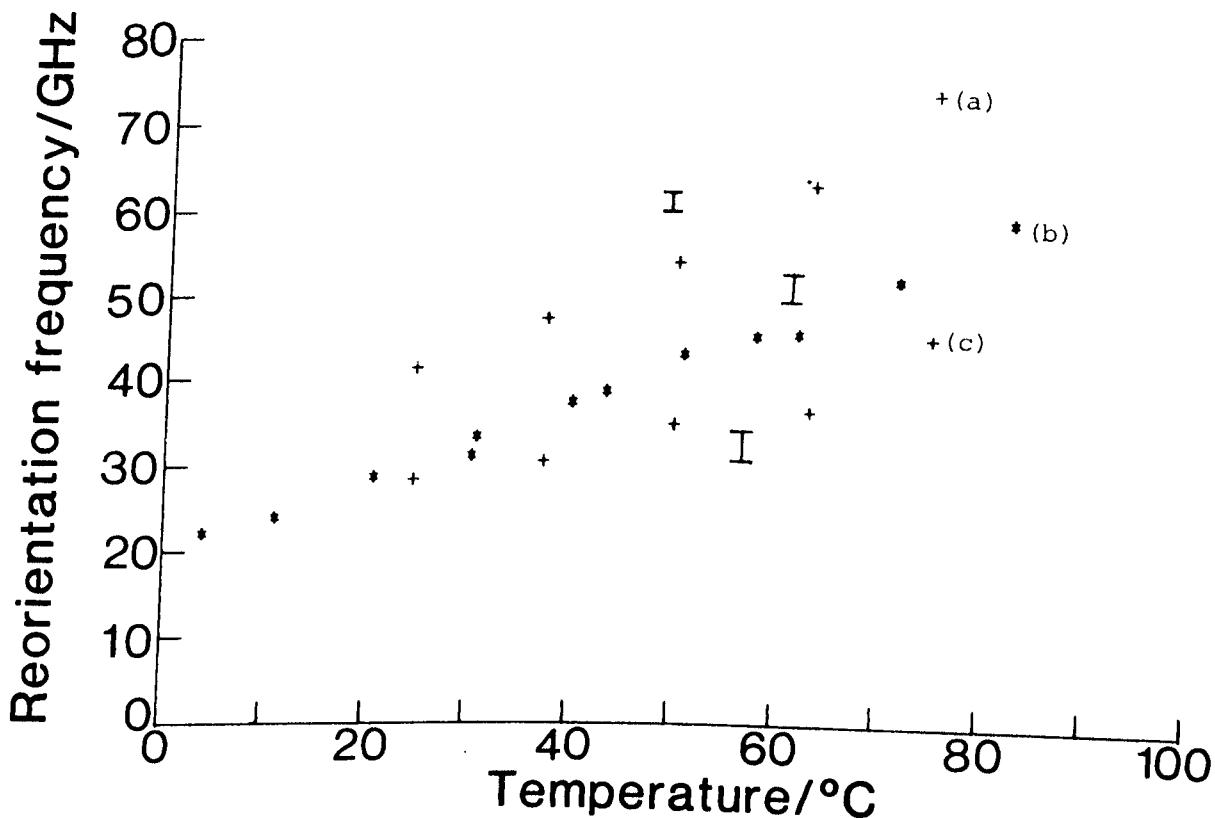


Fig 5.2.10 2,2-dimethylpentane: FSR = 1000 GHz

- (a) Single Lorentzian fit to data
- (b) Two Lorentzian fit to data

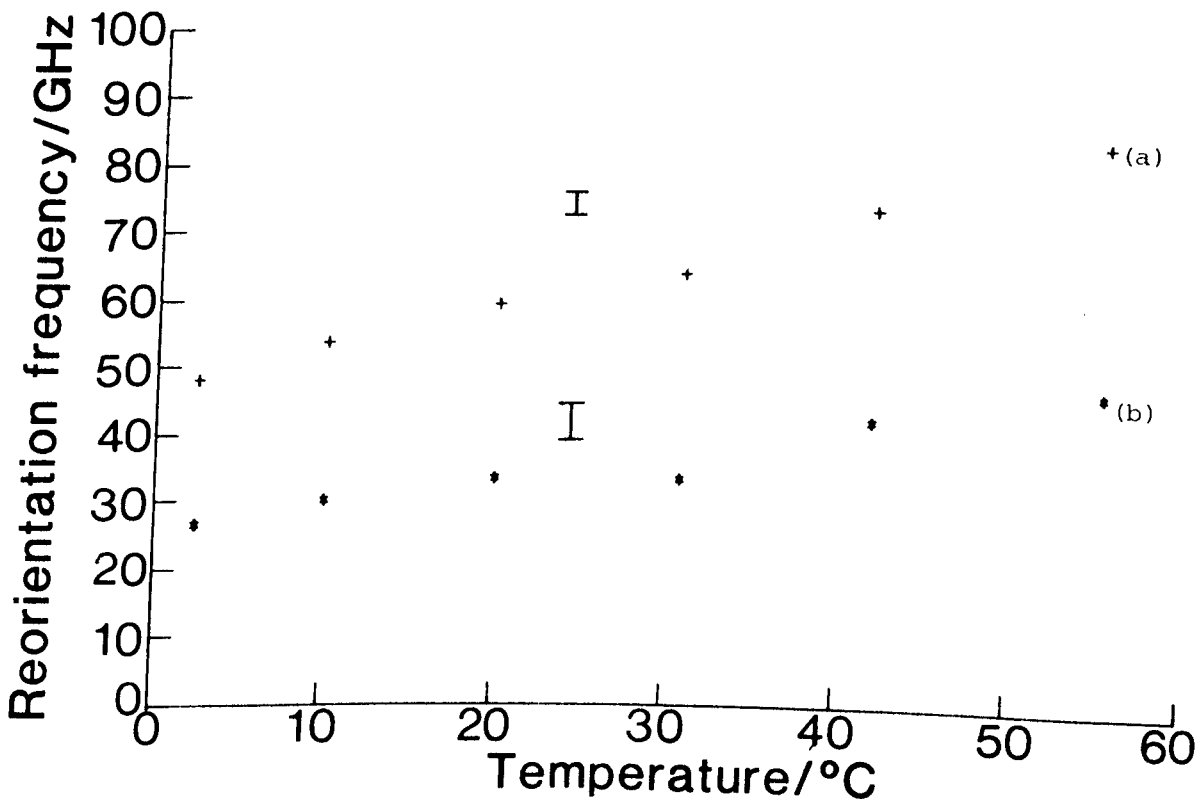


Fig 5.2.11 2,3-dimethylpentane

- (a) Single Lorentzian fit to data: FSR = 2000 GHz
- (b) Single Lorentzian fit to data: FSR = 950 GHz
- (c) Two Lorentzian fit to data: FSR = 2000 GHz
- (d) Two Lorentzian fit to data: FSR = 950 GHz

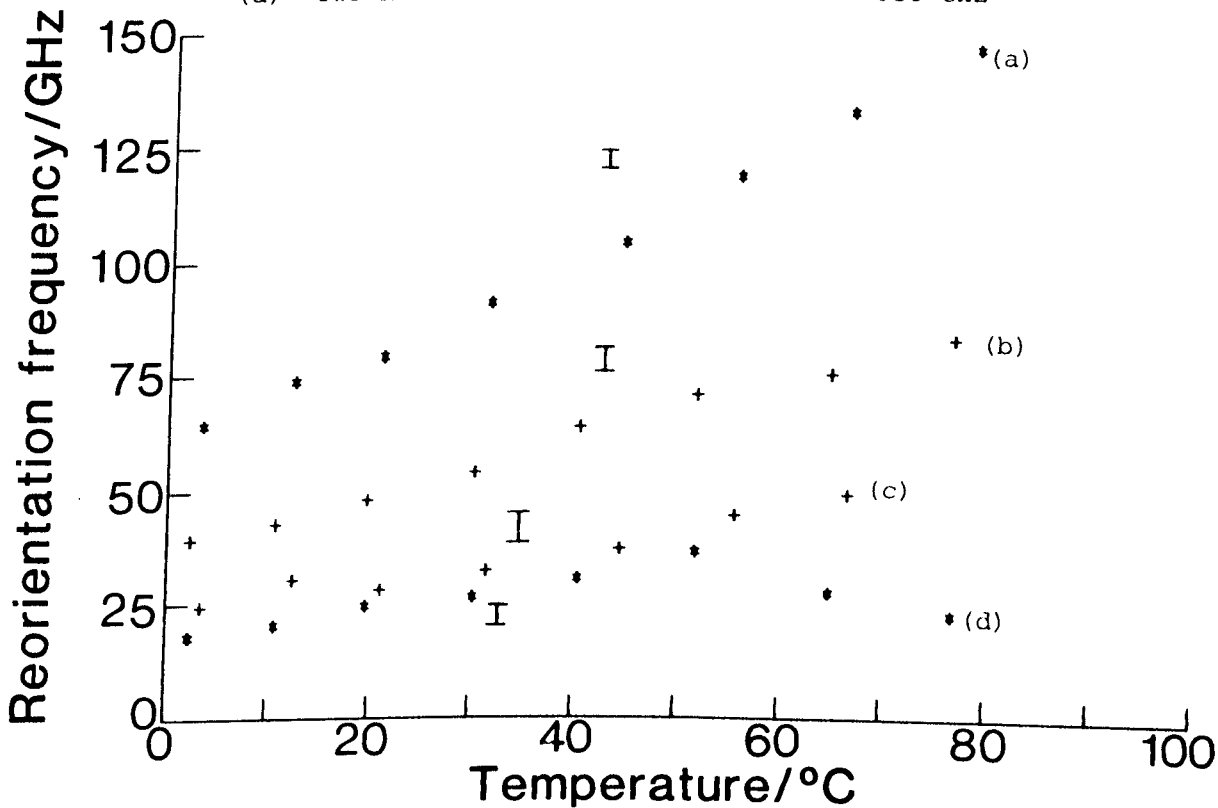


Fig 5.2.12 2,2,3-trimethylbutane: FSR = 2000 GHz

- (a) Single Lorentzian fit to data
- (b) Two Lorentzian fit to data

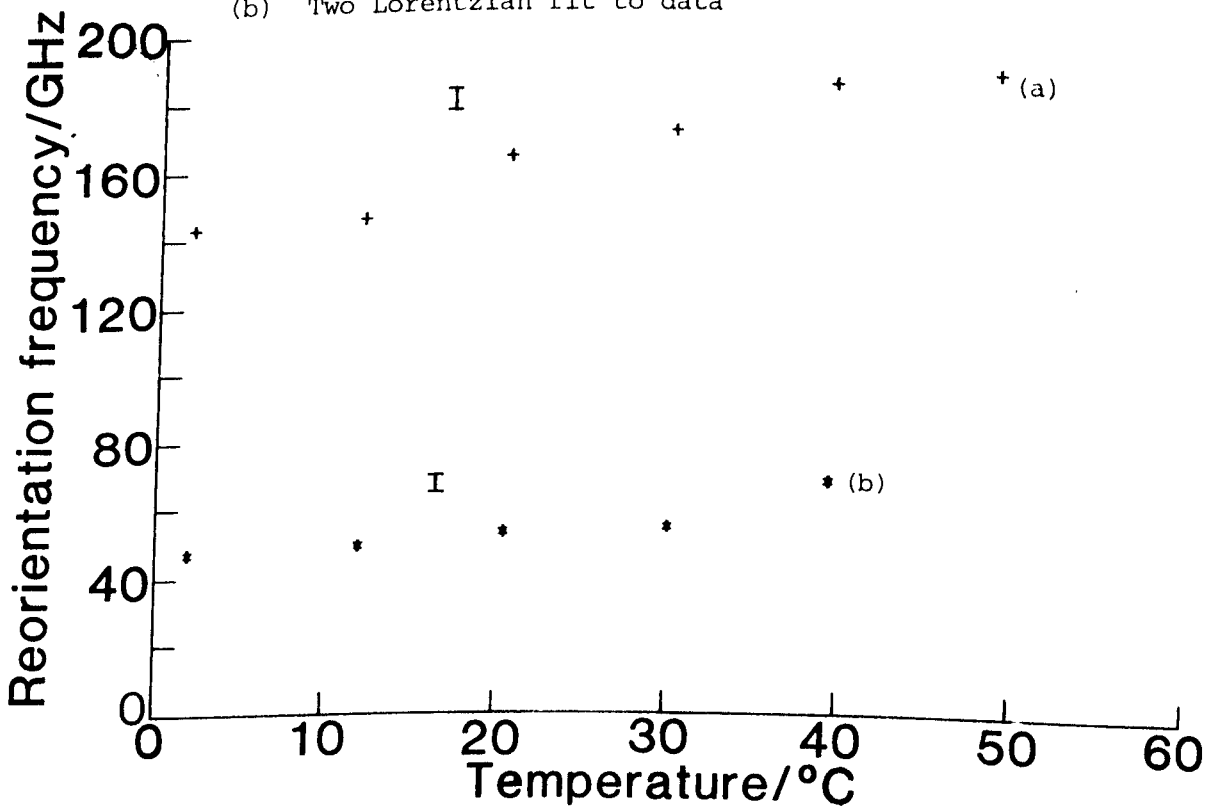


Table 5.2.3 A COMPARISON OF THE STATISTICAL ANALYSIS OF THE FITTING FUNCTIONS FOR THE ISOMERS OF C<sub>7</sub>H<sub>16</sub>

Liquid	Fitting Function	Reduced $\chi^2$	Integral $\chi^2$ Probability	Linear Correlation Test: Probability	One Sample Runs Test	
					Number of Runs ( $n_r$ ) $\mu_r = 512$ $\sigma_r = 16$	Probability of Exceeding $ n_r $
n-heptane T = 3 °C FSR = 250 GHz	(i)	1.10	$1.0 \times 10^{-4}$	$5.8 \times 10^{-3}$	498	1.0
2-methylhexane T = 30.6 °C FSR = 455 GHz	(i)	1.30	0.0	0.85	461	$1.4 \times 10^{-3}$
	(ii)	1.30	0.0	0.70	455	$3.5 \times 10^{-4}$
	(iii)	1.10	$1.0 \times 10^{-4}$	0.62	502	1.0
3-methylhexane T = 75.0 °C FSR = 1250 GHz	(i)	1.80	0.0	0.36	371	$2.5 \times 10^{-18}$
	(ii)	1.72	0.0	0.35	367	$1.2 \times 10^{-19}$
	(iii)	1.11	$8.7 \times 10^{-10}$	$3.1 \times 10^{-3}$	508	1.0
2,2-dimethylpentane T = 42.0 °C FSR = 1000 GHz	(i)	1.80	0.0	0.17	376	$2.8 \times 10^{-22}$
	(ii)	1.90	0.0	0.16	350	0.0
	(iii)	1.05	0.15	0.15	528	1.0
2,3-dimethylpentane T = 12.5 °C FSR = 2000 GHz	(i)	2.40	0.0	0.43	298	0.0
	(ii)	2.50	0.0	0.54	306	0.0
	(iii)	1.05	0.12	0.33	508	1.0
2,2,3-trimethylbutane T = 30 °C FSR = 2000 GHz	(i)	1.70	0.0	0.82	390	$3.4 \times 10^{-14}$
	(ii)	1.81	0.0	0.64	330	$3.0 \times 10^{-17}$
	(iii)	1.04	0.13	0.71	516	1.0

Fitting functions: (i) Single Lorentzian plus flat base, (ii) Single Lorentzian plus exponential base, (iii) Two Lorentzians plus flat base.

However the results of a two Lorentzian fit to the data from 2,3-dimethylpentane are consistent for both FSR's used over a temperature range of 0 °C to approximately 50 °C. Hence both Lorentzian components are well resolved. The decrease of reorientational frequency with increasing temperature above 50 °C at an FSR of 950 GHz is due to the same effects as already discussed for the case of 2,2,4-trimethylpentane.

Shown in Fig 5.2.13 to Fig 5.2.17 are the variations of peak half width with temperature for the second Lorentzian components. Only the results at the larger FSR's, where the signal-to-noise ratio is the largest, are presented. The spread on the data points is large due to effects already discussed. However, the general trend is an increase of peak half width with increasing temperature similar to that found for the isomer 2,2,4-trimethylpentane.

Fig 5.2.13 2-methylhexane. Variation of second Lorentzian peak half width with temperature: FSR = 450 GHz

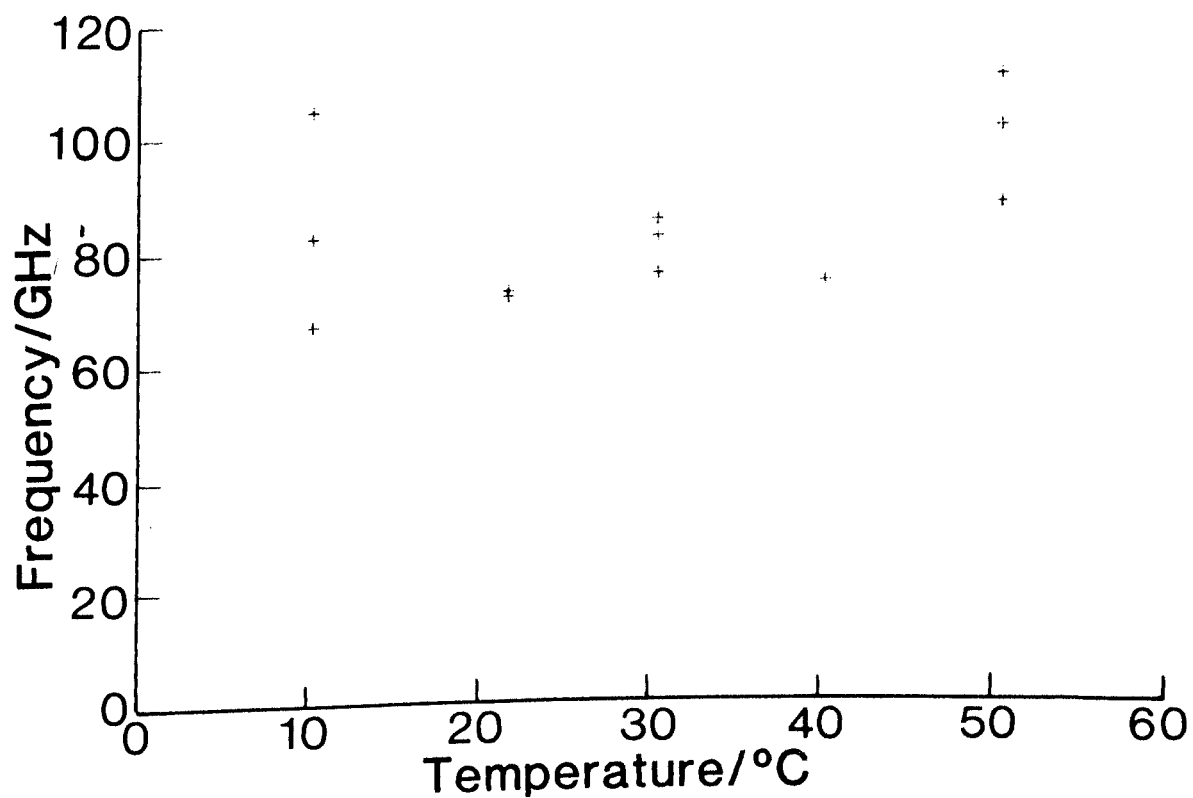


Fig 5.2.14 3-methylhexane. Variation of second Lorentzian peak half width with temperature: FSR = 1250 GHz

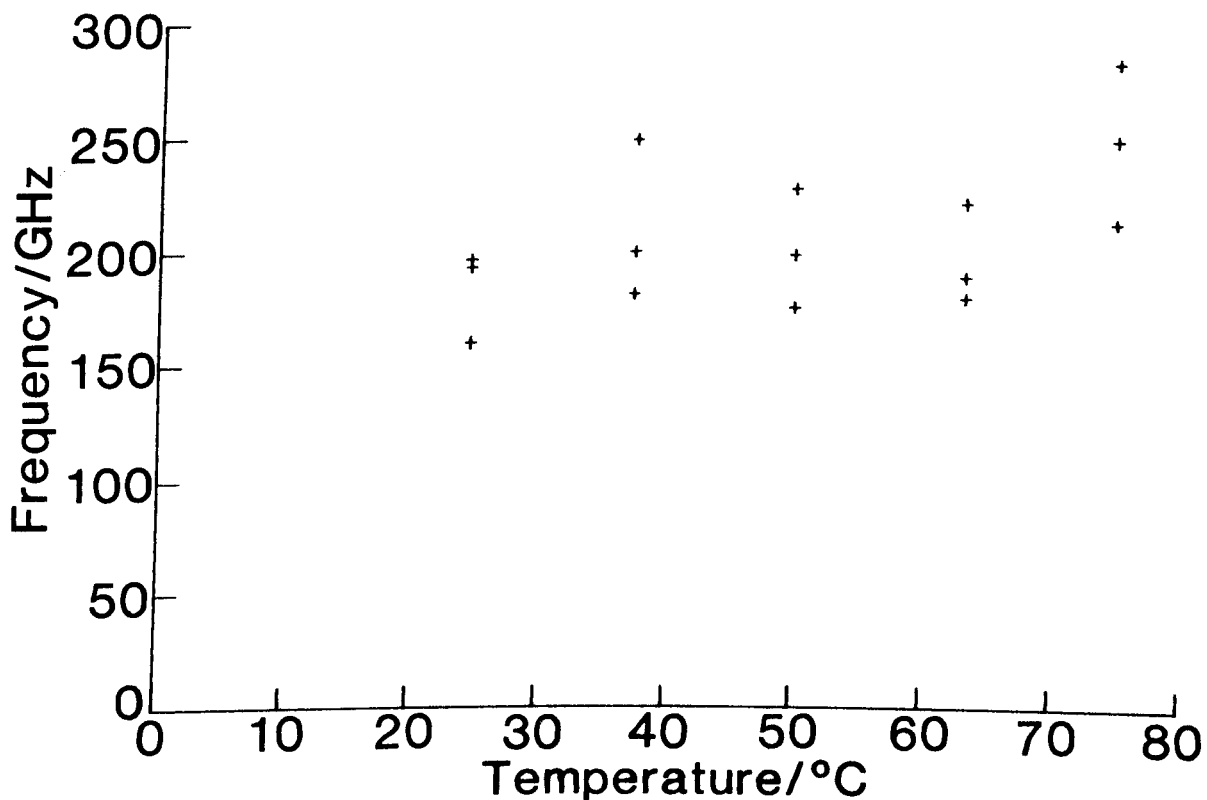


Fig 5.2.15 2,2-dimethylpentane. Variation of second Lorentzian peak half width with temperature: FSR = 1000 GHz

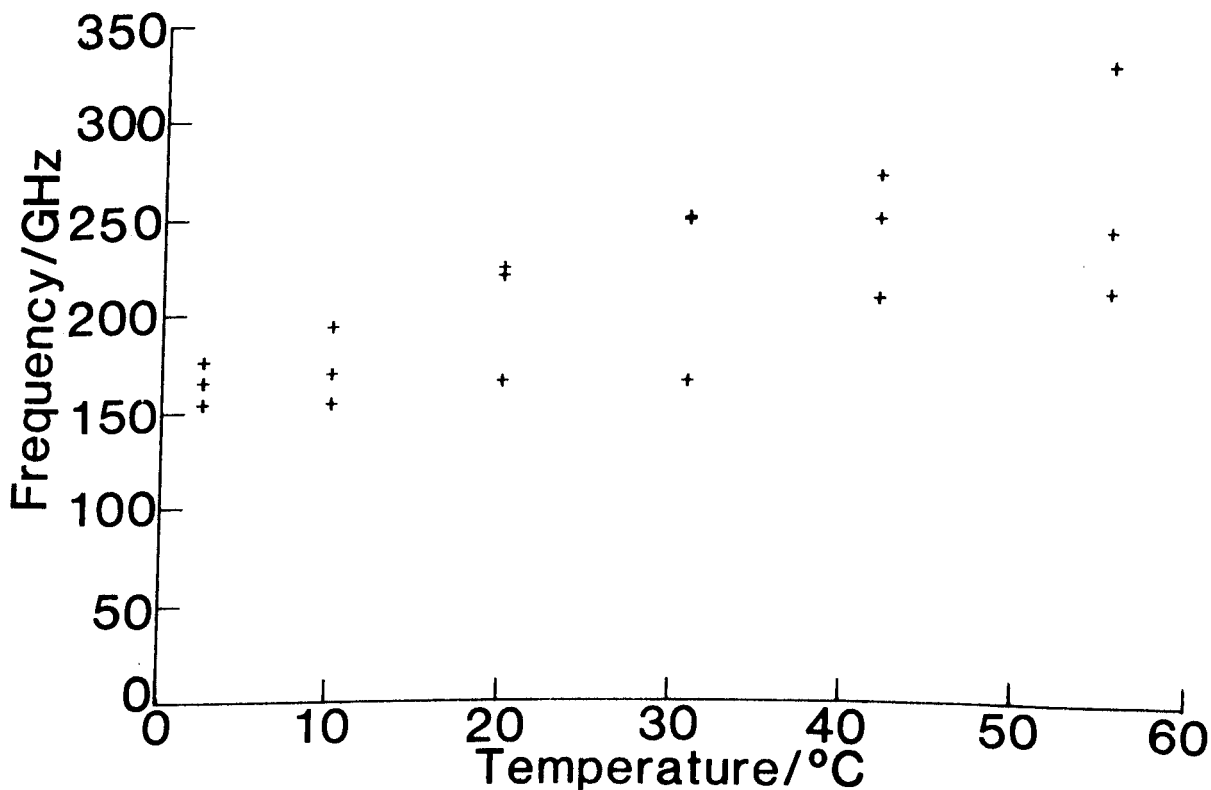


Fig 5.2.16 2,3-dimethylpentane. Variation of second Lorentzian peak half width with temperature: FSR = 2000 GHz

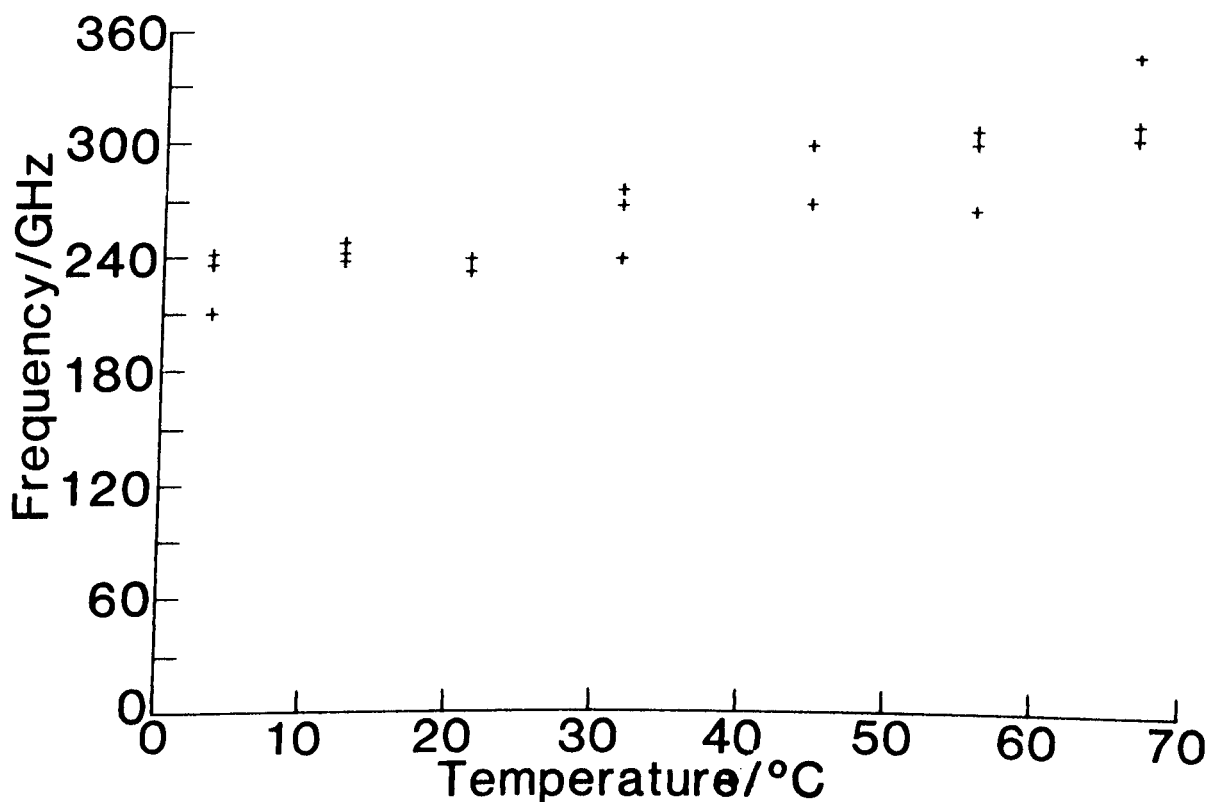
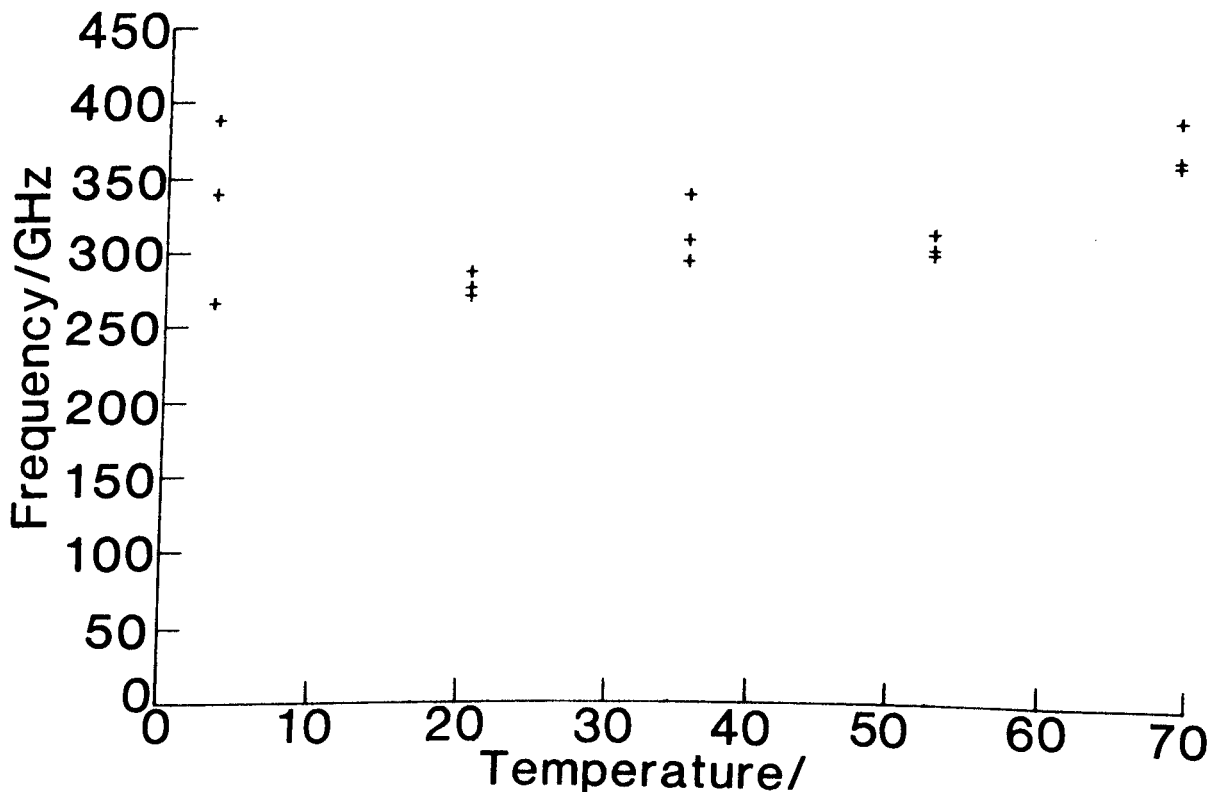


Fig 5.2.17 2,2,3-trimethylbutane. Variation of second Lorentzian peak half width with temperature: FSR = 2000 GHz



### 5.2.3 Isomers of C<sub>6</sub>H<sub>14</sub>

The results of the reorientational frequency as a function of temperature for the isomers n-hexane, 2-methylpentane, 3-methylpentane and 2,2-dimethylbutane are presented in Fig 5.2.18 to Fig 5.2.21. The peak half width increases with increasing temperature for all the isomers.

The spectra obtained from the isomer n-hexane all fitted to a single Lorentzian plus a flat base. The spectra from the isomers 2-methylpentane, 3-methylpentane and 2,2-dimethylbutane all gave improved fits when fitted to two Lorentzian plus a flat base. Table 5.2.4. gives examples of the statistical analysis of the fits to the isomers of C<sub>6</sub>H<sub>14</sub>. It is clearly evident that an exponential base does not improve the fit.

The decrease of reorientational frequency with increasing temperature for the isomer 3-methylpentane when fitted to two Lorentzians, is probably due to the decrease in the signal-to-noise ratio at the higher temperatures.

Shown in Table 5.2.5 is the variation of optical anisotropy for some of the isomers. The isomer 2,2-dimethylbutane has the lowest optical anisotropy of any of the liquids studied. The FSR needed to obtain an adequate resolution of the spectra was very large, of the order 3300 GHz. This corresponds to a Fabry-Perot plate separation of only 0.05 mm. Hence the error in the measured FSR, and consequently the peak-half-widths, is of the order 20%. However spectra were successfully obtained with scan times of approximately 30 minutes.

An example of the quality of the data obtained is shown in Fig 5.2.22.

Fig 5.2.18 n-hexane. Single Lorentzian fit to data: FSR = 450 - 625 GHz

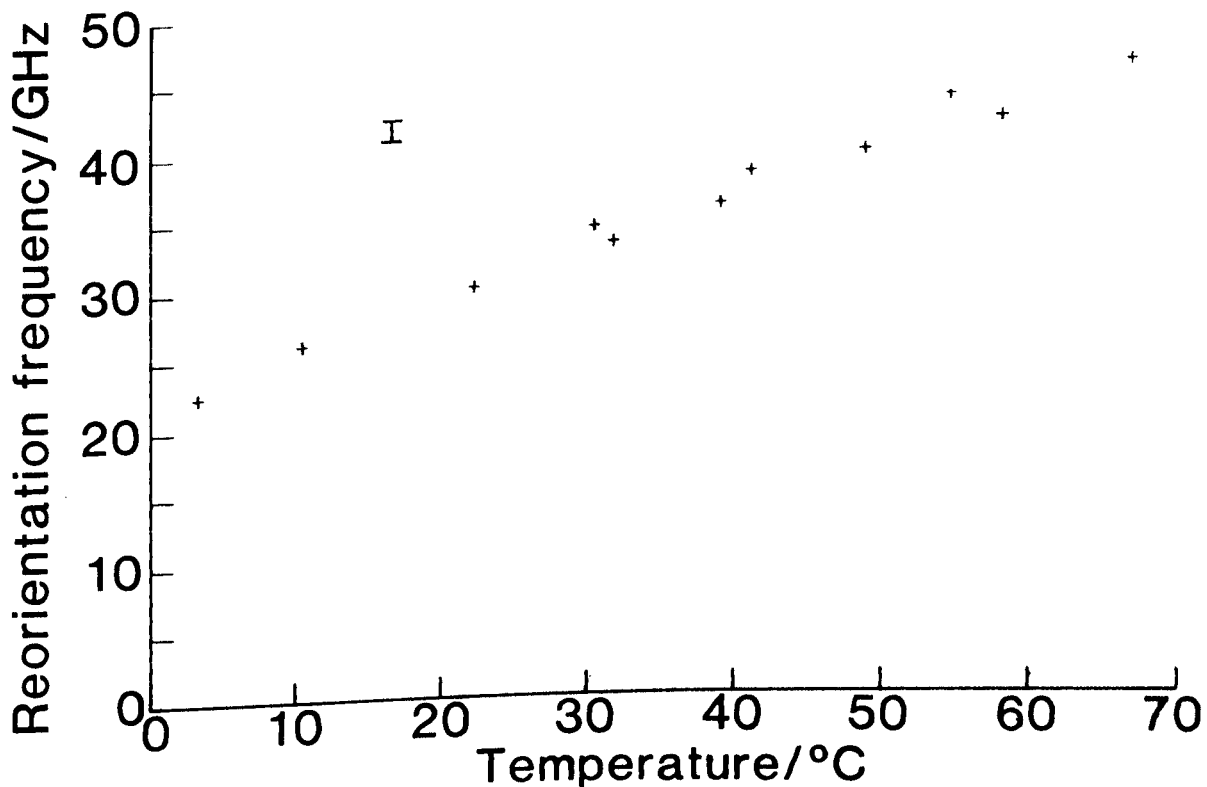


Fig 5.2.19 2-methylpentane.

- (a) Single Lorentzian fit to data: FSR = 1250 GHz
- (b) Single Lorentzian fit to data: FSR = 605 GHz
- (c) Two Lorentzian fit to data: FSR = 1250 GHz

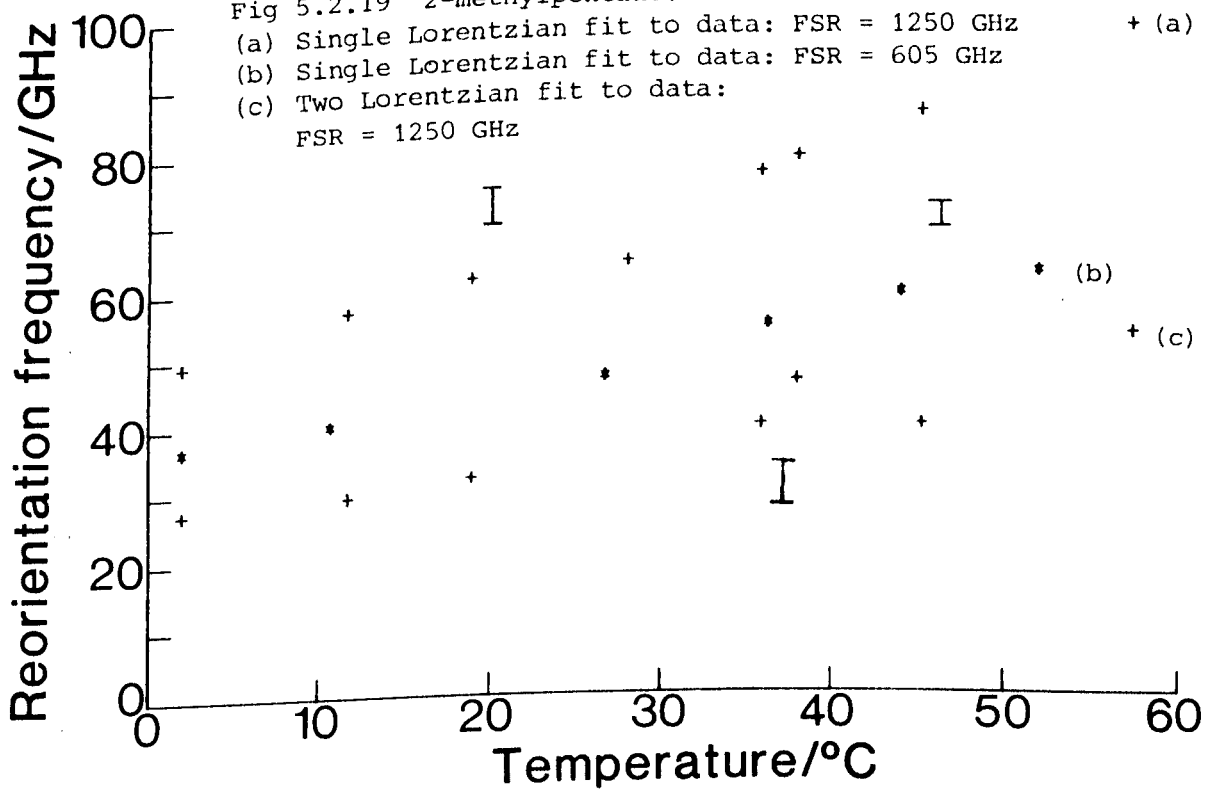


Fig 5.2.20 3-methylpentane.

- (a) Single Lorentzian fit to data: FSR = 1250 GHz
- (b) Single Lorentzian fit to data: FSR = 715 GHz
- (c) Two Lorentzian fit to data: FSR = 1250 GHz

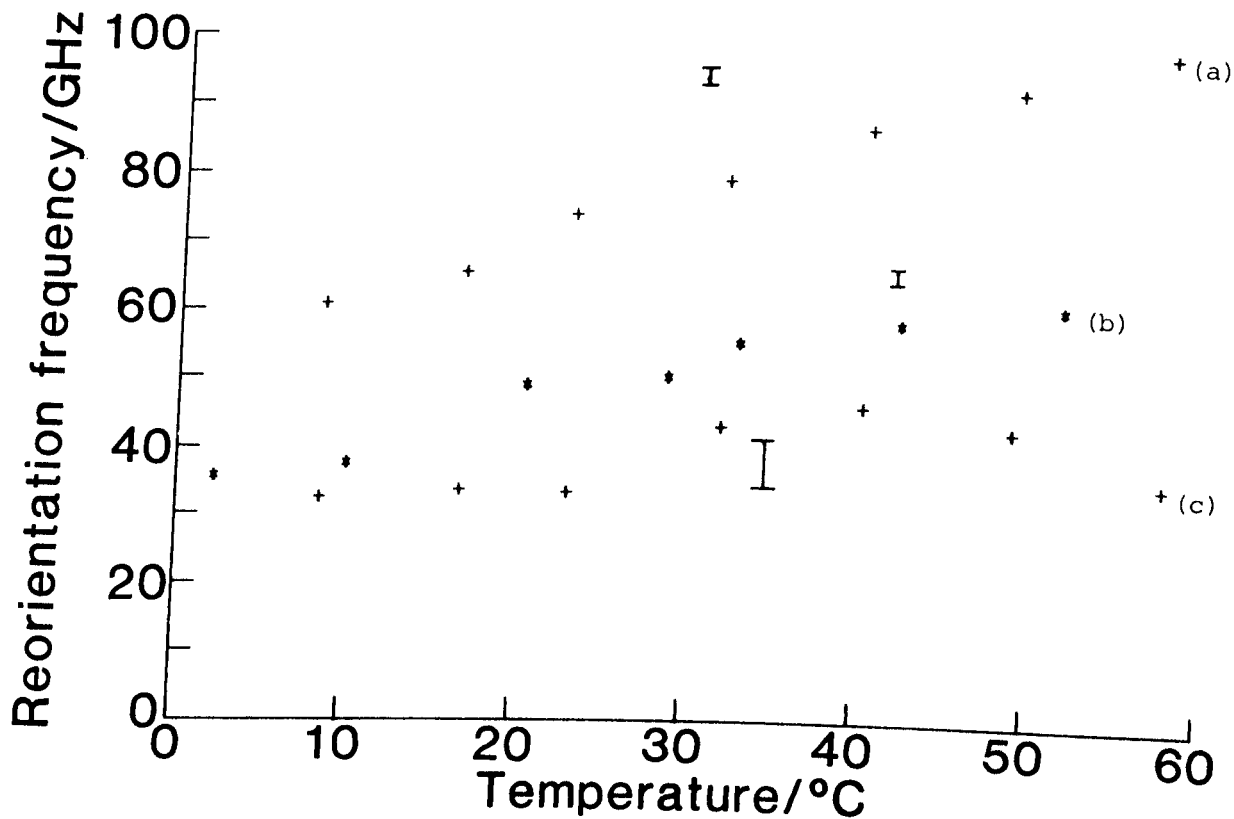


Fig 5.2.21 2,2-dimethylbutane: FSR = 3335 GHz

- (a) Single Lorentzian fit to data
- (b) Two Lorentzian fit to data

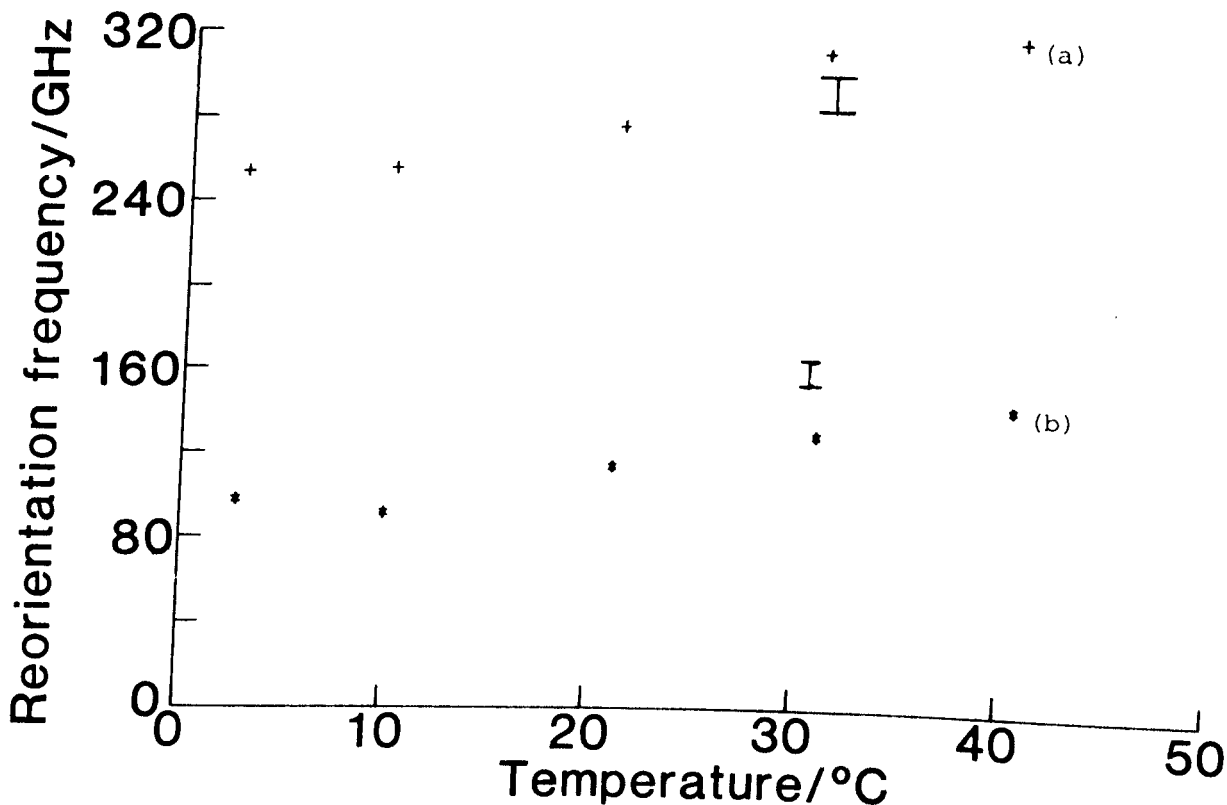


TABLE 5.2.4 COMPARISON OF THE STATISTICAL ANALYSIS OF THE FITTING FUNCTIONS FOR THE ISOMERS OF C<sub>6</sub>H<sub>14</sub>

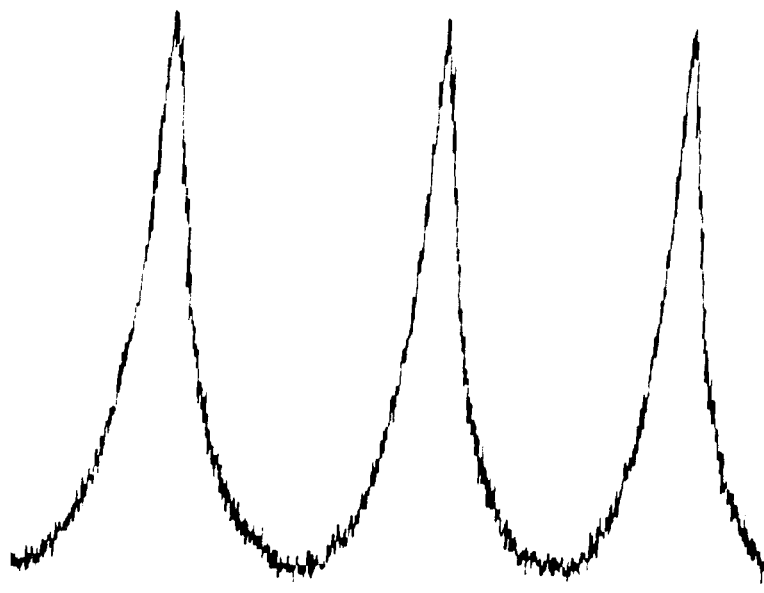
Liquid	Fitting Function	Reduced $\chi^2$	Integral $\chi^2$ Probability	Linear Correlation Test: Probability	One Sample Runs Test	
					Number of Runs ( $n_r$ ) $\mu_r = 512$ $\sigma_r = 16$	Probability of Exceeding $ n_r $
n-hexane T = 40 °C FSR = 450 GHz	(i)	1.10	$1.0 \times 10^{-4}$	0.19	502	1.0
2-methylpentane T = 57.5 °C FSR = 1250 GHz	(i)	1.40	0.0	0.31	441	$8.9 \times 10^{-6}$
	(ii)	1.40	0.0	0.60	449	$1.0 \times 10^{-5}$
	(iii)	1.04	0.11	0.84	519	1.0
3-methylpentane T = 8.5 °C FSR = 1250 GHz	(i)	1.90	0.0	$1.5 \times 10^{-4}$	294	0.0
	(ii)	1.85	0.0	$1.0 \times 10^{-4}$	300	0.0
	(iii)	1.04	0.13	$5.2 \times 10^{-3}$	490	0.11
2,2-dimethylbutane T = 40.5 °C FSR = 3335 GHz	(i)	2.4	0.0	0.26	304	0.0
	(ii)	1.6	0.0	$1.0 \times 10^{-2}$	396	$1.9 \times 10^{-11}$
	(iii)	1.4	0.0	$2.7 \times 10^{-3}$	452	$2.2 \times 10^{-4}$

Fitting functions: (i) Single Lorentzian plus flat base, (ii) Single Lorentzian plus exponential base, (iii) Two Lorentzians plus flat base

TABLE 5.2.5 MOLECULAR OPTICAL ANISOTROPIES

Liquid	$\gamma^2$ (calculated)/Å <sup>6</sup>	$\gamma^2$ (experimental)/Å <sup>6</sup>
n-octane	4.5 [138], 5.41 [137]	6.64 [137]
n-heptane	4.34 [139]	5.38 [137]
n-hexane	3.0 [138], 3.57 [139]	4.1 [137]
2,2-dimethylbutane	2.6 [135]	2.0 [136]
n-pentane	2.1 [138], 2.45 [139]	3.03 [135], 2.93 [137]
2-methylbutane	2.9 [135]	2.6 [136]

Fig 5.2.22 Depolarised Rayleigh-Brillouin Spectra of 2,2-dimethylbutane  
FSR = 3335 GHz; T = 41 °C



With reference to Table 5.2.4 it is evident that although a two Lorentzian fit significantly improved the statistical analysis it is still not the most appropriate fitting function. Due to the very large FSR used it is highly likely that part of the collisional background is being resolved. This was examined by fitting the data to a fitting function that incorporated two Lorentzians plus an exponential base. However, this did not result in an improvement in the statistical analysis. The most probable reason for this is that the exponential base cannot be adequately separated from the second broad Lorentzian due to the FSR used; a larger FSR would enable a separation of the interaction induced component and corresponding improvements in the data analysis however, this would require a monochromator since the Fabry-Perot was set close to its maximum FSR. Since the most appropriate fitting function, of those analysed, consists of two Lorentzians superimposed

on a flat base the analysis is presented on the basis of this fitting function. Although a more appropriate fitting function could result in different peak half-widths for the narrow Lorentzian component the error in assuming the above fitting function should be less than or comparable to the  $\pm 20\%$  uncertainties in measuring the FSR (Section 3.1.2).

The peak half-widths of the second Lorentzian component are shown as a function of temperature in Fig 5.2.23 to Fig 5.2.25. The spread on the fitted values is large. However for the isomers 2-methylpentane and 2,2-dimethylbutane the trend is an increase of peak half-width with increasing temperature. For the isomer 3-methylpentane the values above 40 °C decrease with temperature. However this pattern was also observed in the reorientational peak half-widths (Fig 5.2.20c) and is a result of low signal-to-noise ratio and hence inadequate resolution of the two components. The isomer 2,3-dimethylbutane was also investigated. The sample became contaminated within a few hours and therefore very few results could be obtained. Consequently the results are not presented although the preliminary measurements indicated similar trends to those of 2,2-dimethylbutane.

Fig 5.2.23 2-methylpentane. Variation of second Lorentzian peak half widths with temperature: FSR = 1250 GHz

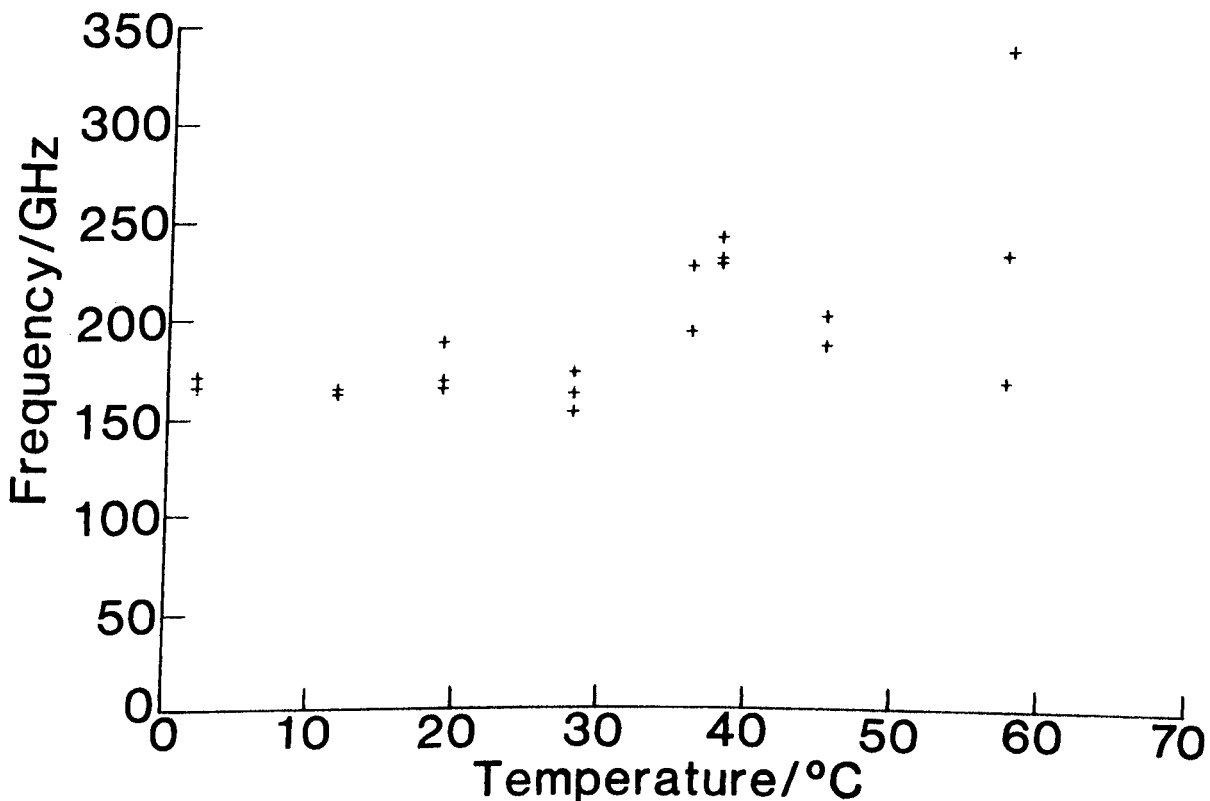


Fig 5.2.24 3-methylpentane. Variation of second Lorentzian peak half widths with temperature: FSR = 1250 GHz

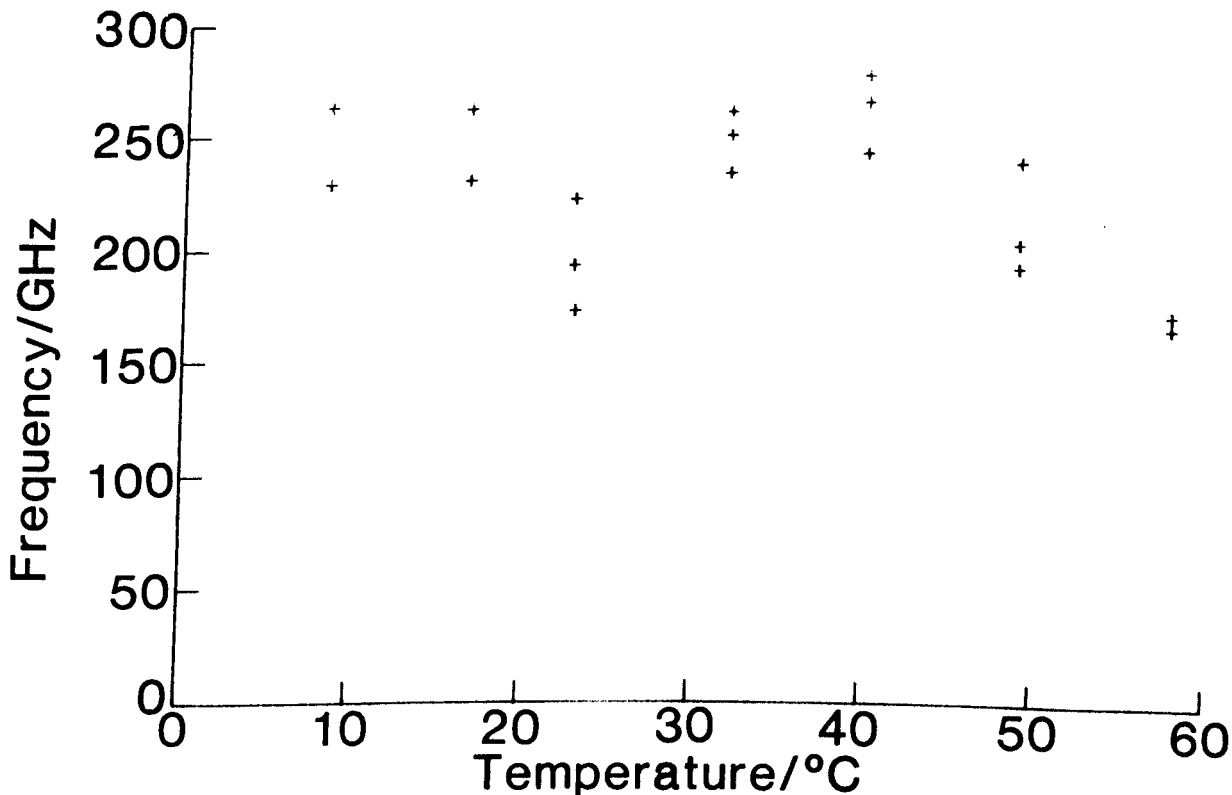
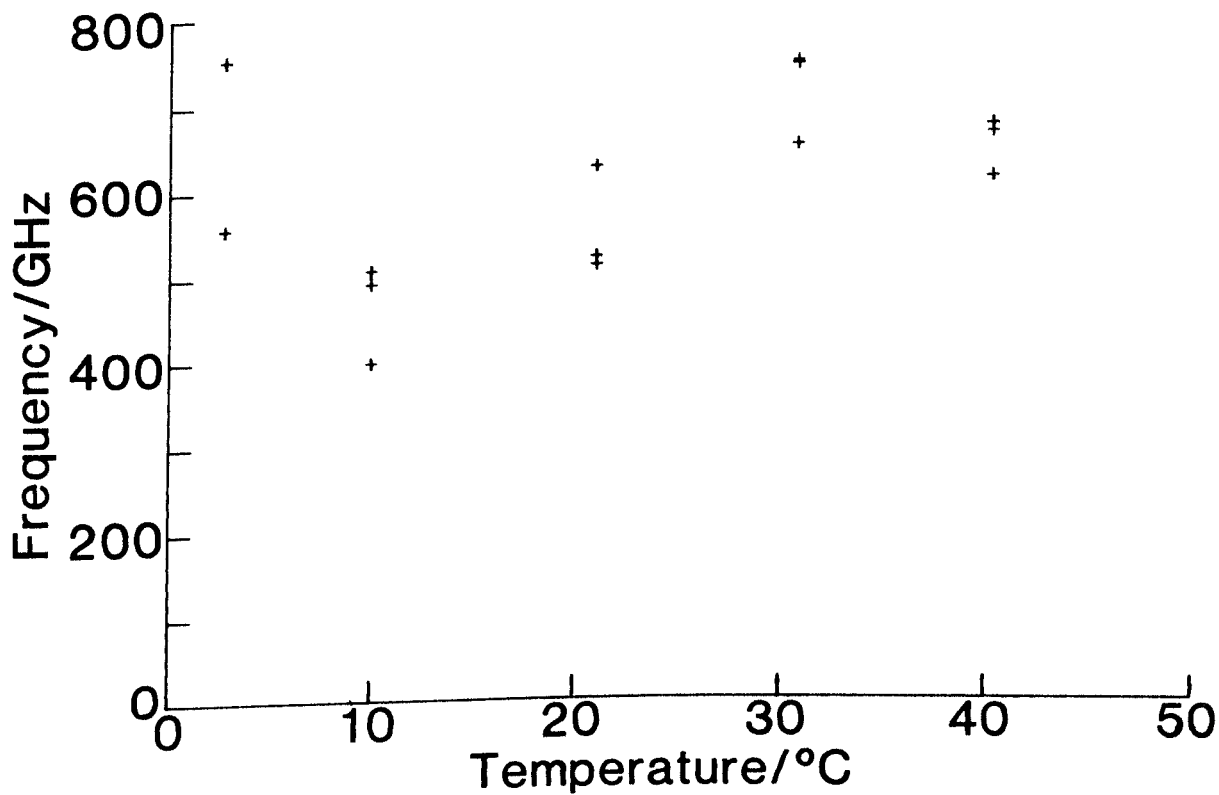


Fig 5.2.25 2,2-dimethylbutane. Variation of second Lorentzian peak half width temperature: FSR = 3335 GHz



#### 5.2.4 Isomers of C<sub>5</sub>H<sub>12</sub>

The peak width variation with temperature for the isomers n-pentane and 2-methylbutane are presented in Fig 5.2.26 and Fig 5.2.27. For both isomers the reorientational frequency increases with increasing temperature. In the case of both isomers the most appropriate fitting function, at the larger FSR for n-pentane, was two Lorentzians superimposed on a flat base. Examples of the statistical analysis of the fit are given in Table 5.2.6.

The variation of the peak half widths with temperature for the second Lorentzian are shown in Fig 5.2.28 and Fig 5.2.29. For both isomers any trend in the second Lorentzian peak half width is masked by the large spread on the fitted values.

Fig 5.2.26 n-pentane

- (a) Single Lorentzian fit to data: FSR = 1320 GHz
- (b) Single Lorentzian fit to data: FSR = 670 GHz
- (c) Two Lorentzian fit to data: FSR = 1320 GHz

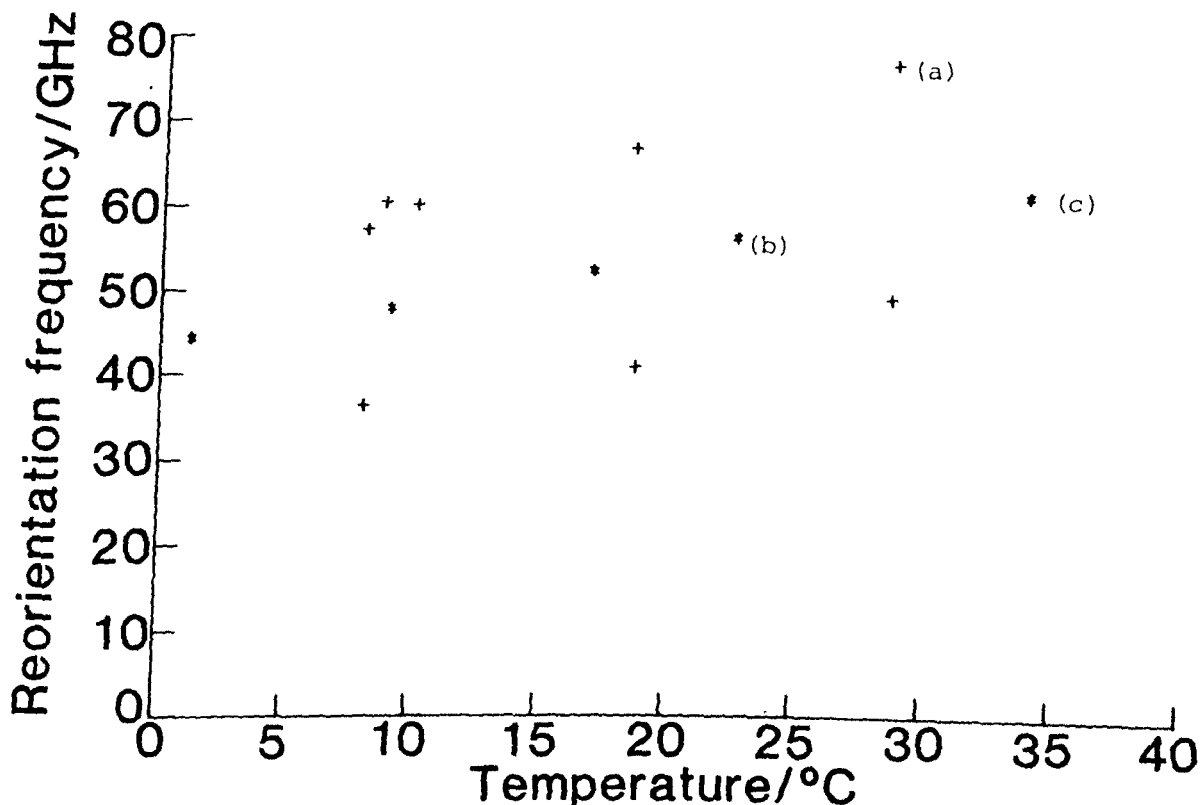


Fig 5.2.27 2-methylbutane: FSR = 2200 GHz

- (a) Single Lorentzian fit to data
- (b) Two Lorentzian fit to data

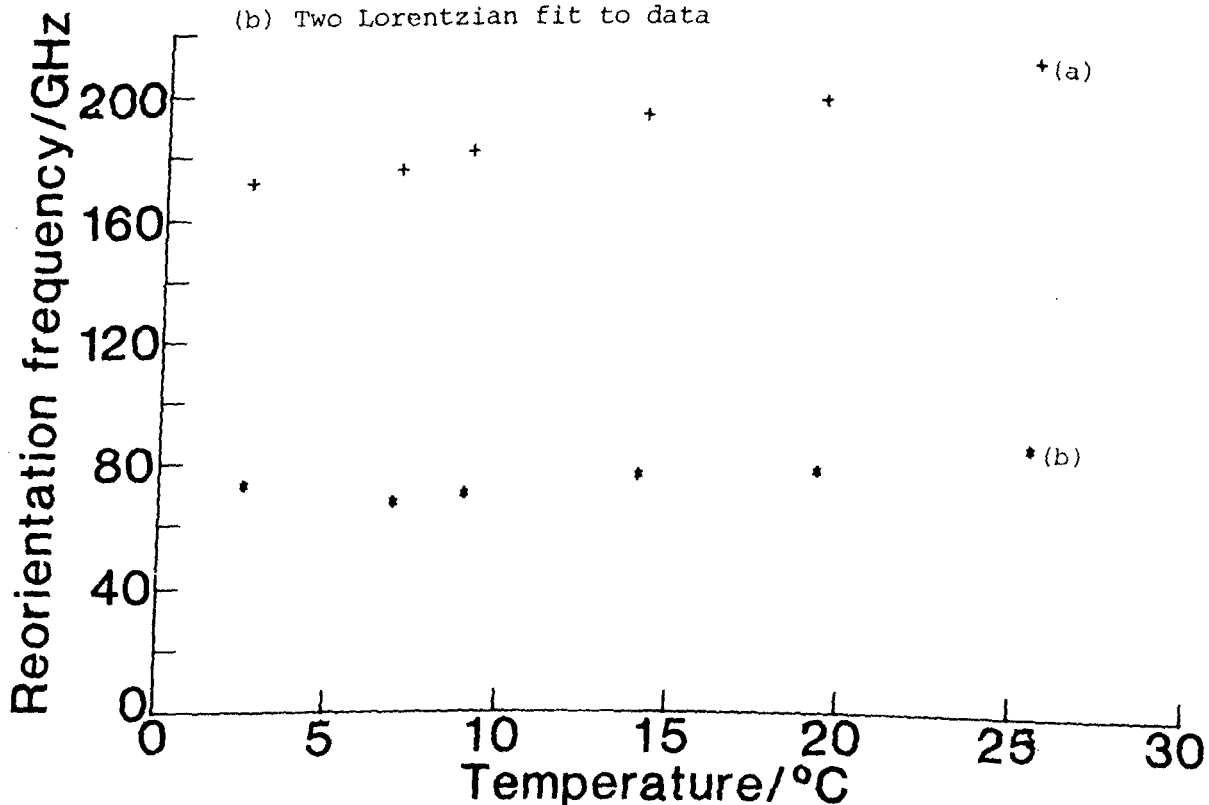


TABLE 5.2.6 EXAMPLES OF THE STATISTICAL ANALYSIS FOR FITS TO THE SPECTRA FROM n-PENTANE AND 2-METHYLBUTANE

Liquid	Fitting Function	Reduced $\chi^2$	Integral $\chi^2$ Probability	Linear Correlation Test: Probability	One Sample Runs Test	
					Number of Runs ( $n_r$ ) $\mu_r = 512$ $\sigma_r = 16$	Probability of Exceeding $ n_r $
n-pentane T = 19 °C FSR = 1320 GHz	(i)	1.4	0.0	$6.8 \times 10^{-4}$	432	$7.3 \times 10^{-7}$
	(ii)	1.2	0.0	$8.7 \times 10^{-4}$	448	$1.2 \times 10^{-4}$
	(iii)	1.05	0.22	$2.1 \times 10^{-4}$	508	1.0
2-methylbutane T = 7.0 °C FSR = 2200 GHz	(i)	1.85	0.0	$2.7 \times 10^{-2}$	382	$3.9 \times 10^{-16}$
	(ii)	2.09	0.0	$3.2 \times 10^{-2}$	338	$4.6 \times 10^{-14}$
	(iii)	1.09	$5.2 \times 10^{-5}$	0.49	508	1.0

Fitting functions: (i) Single Lorentzian plus flat base, (ii) Single Lorentzian plus exponential base, (iii) Two Lorentzians plus flat base.

Fig 5.2.28 n-pentane. Variation of second Lorentzian peak half width with temperature: FSR = 1320 GHz

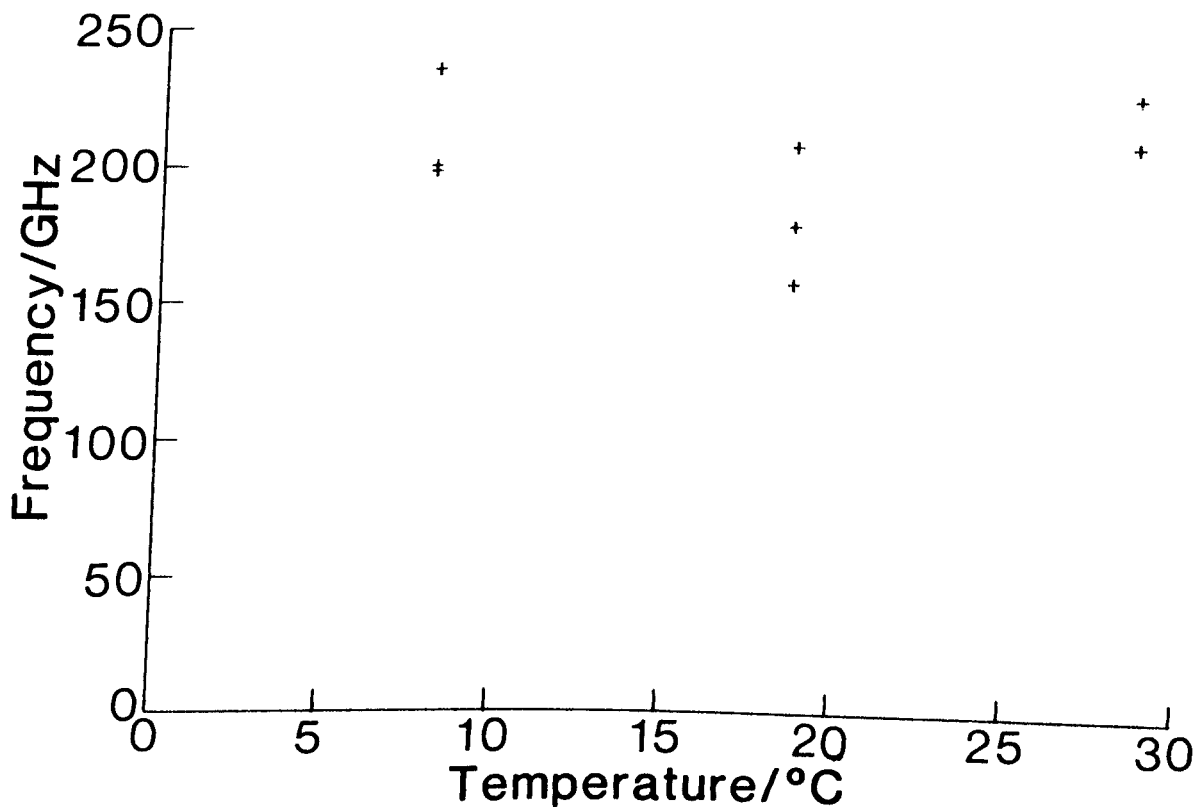
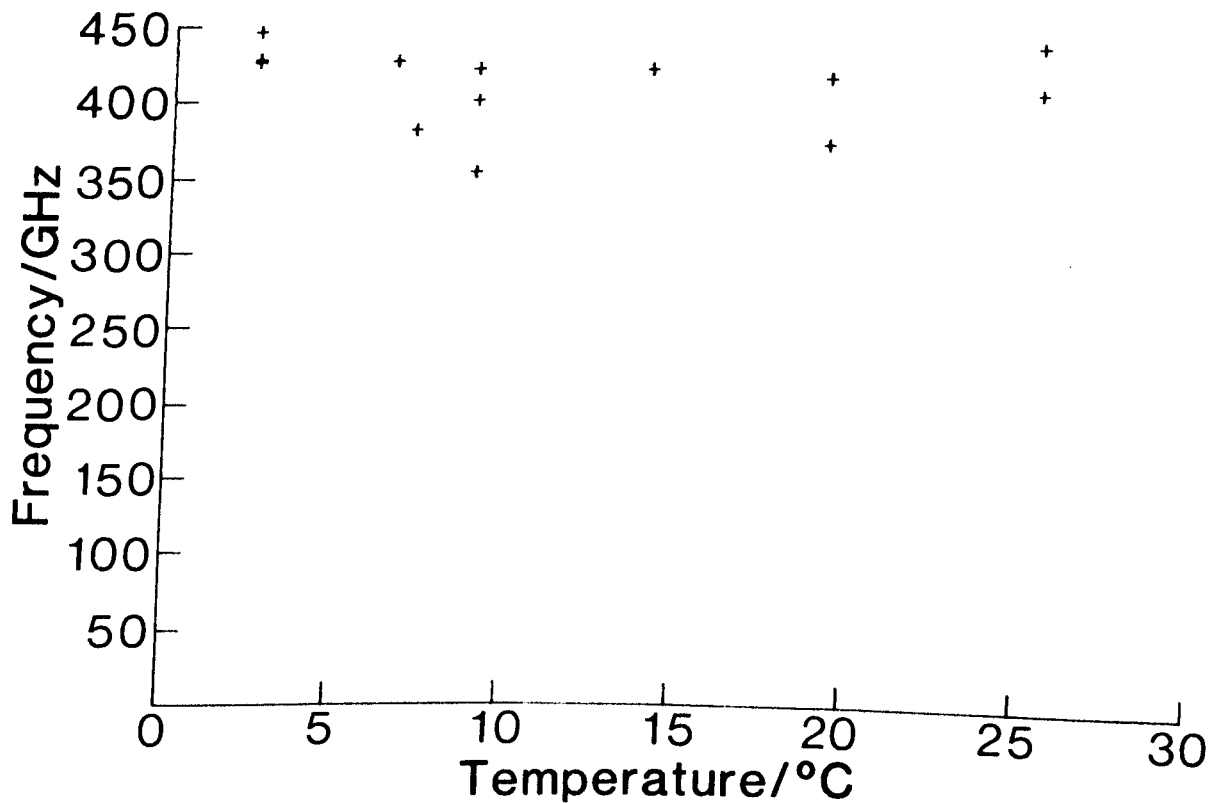


Fig 5.2.29 2-methylbutane. Variation of second Lorentzian peak half width with temperature: FSR = 2200 GHz



### 5.3 Analysis of Spectral Data

#### 5.3.1 The Stokes-Einstein-Debye Relation

The reorientational peak half widths ( $\Gamma_{\text{VH}}$ ) obtained are related to the molecular correlation times ( $\tau_{\text{LS}}$ ) by equation (2.3.1)

$$\tau_{\text{LS}} = \frac{1}{2\pi\Gamma_{\text{VH}}} \quad (2.3.1)$$

The molecular correlation times obtained are analysed in terms of the Stokes-Einstein-Debye relation, given by

$$\tau_{\text{LS}} = \frac{[g_2]^{-1}}{[J_2]^{-1}} \left[ \frac{\alpha P V \eta}{k_B T} + \tau_0 \right] \quad (2.4.14)$$

where: ( $g_2/J_2$ ) is the orientational correlation parameter (Section 2.4.3)

$\alpha$  is the *stick-slip* coefficient (Section 2.4.2)

$P$  is the Perrin factor (Section 2.4.1)

$V$  is the molecular volume

$\eta$  is the macroscopic liquid viscosity

$k_B$  is the Boltzmann constant

$T$  is the absolute temperature

The data is presented by plotting the quantity  $\tau_{\text{LS}}$ , obtained from fits to a single Lorentzian and where appropriate two Lorentzians, against the quantity  $\eta/T$  (Fig 5.3.1 to Fig 5.3.17).

The following observations are made from the straight line fits to the results:

- (i) In all cases the graphs approximate, within the limits of experimental error, to straight lines. The gradient of these graphs can be related to an effective molecular volume by multiplying by Boltzmann's constant and expressing the result in (angstroms)<sup>3</sup>.

Fig 5.3.1 n-octane. Stokes-Einstein-Debye fit to molecular correlation times

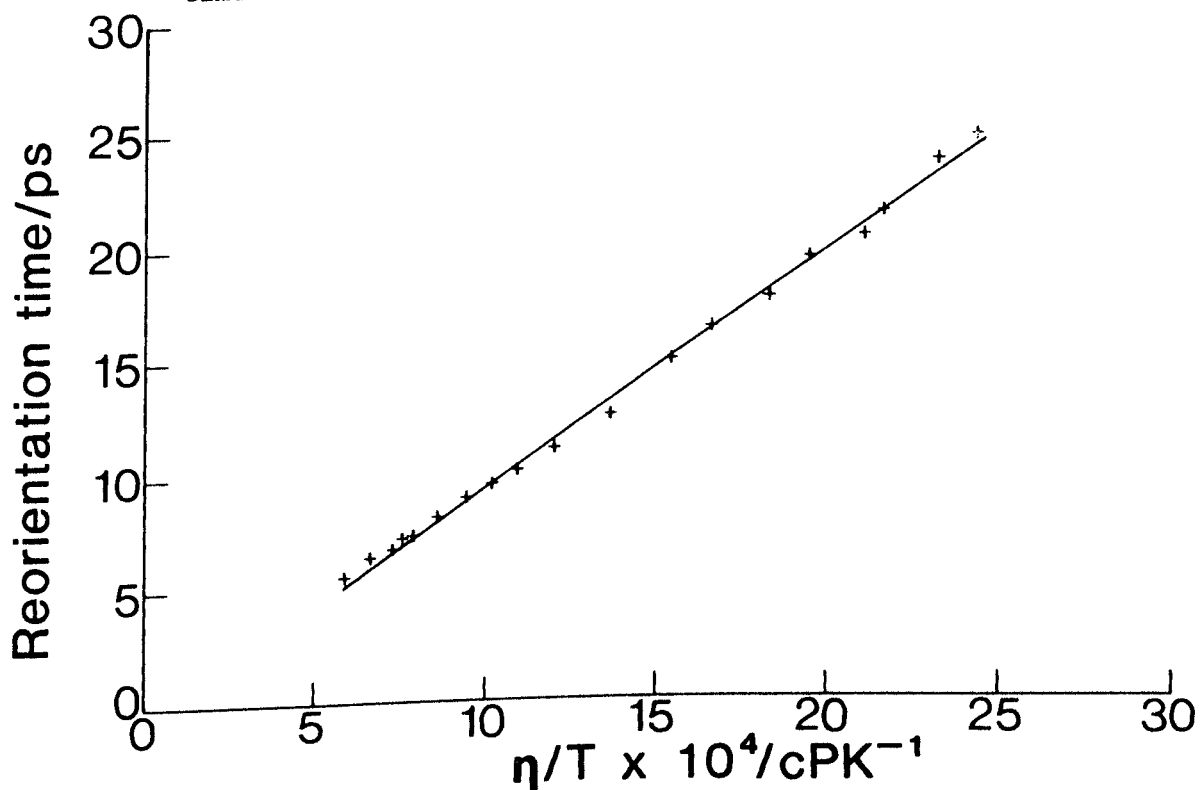


Fig 5.3.2 2-methylheptane. Stokes-Einstein-Debye fit to molecular correlation times

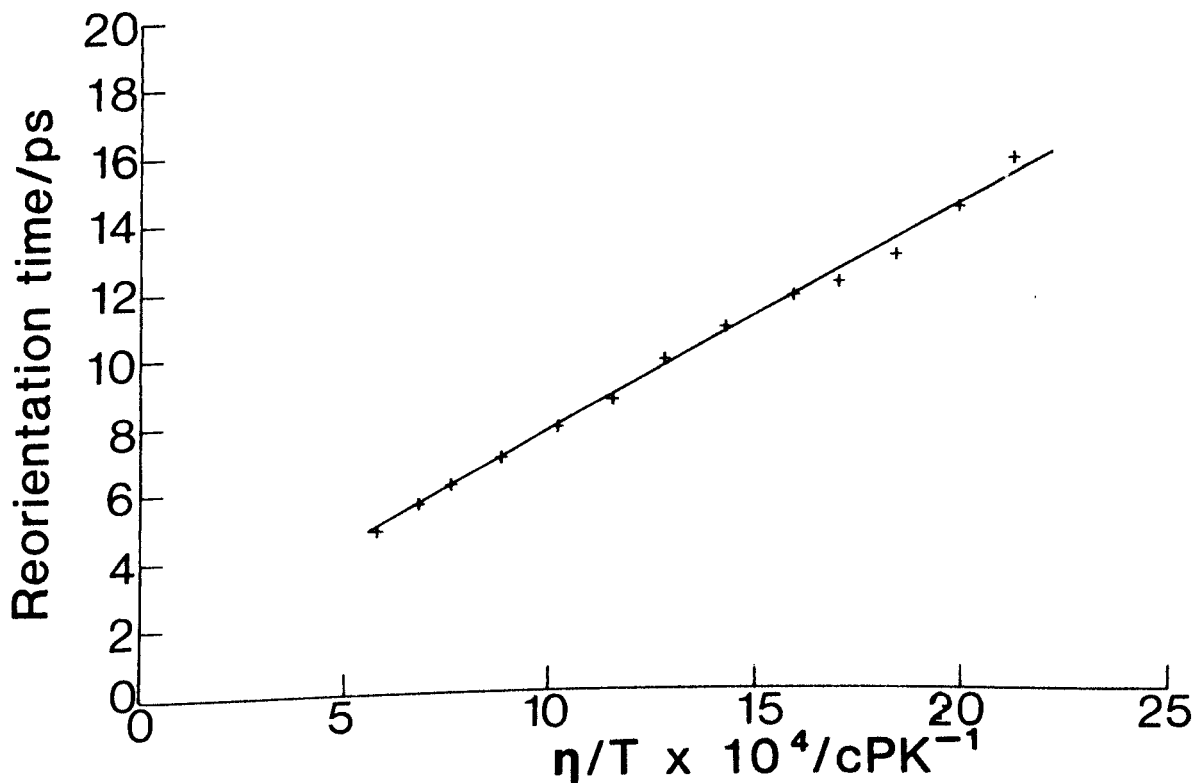


Fig 5.3.3 3-methylheptane. Stokes-Einstein-Debye fit to molecular correlation times

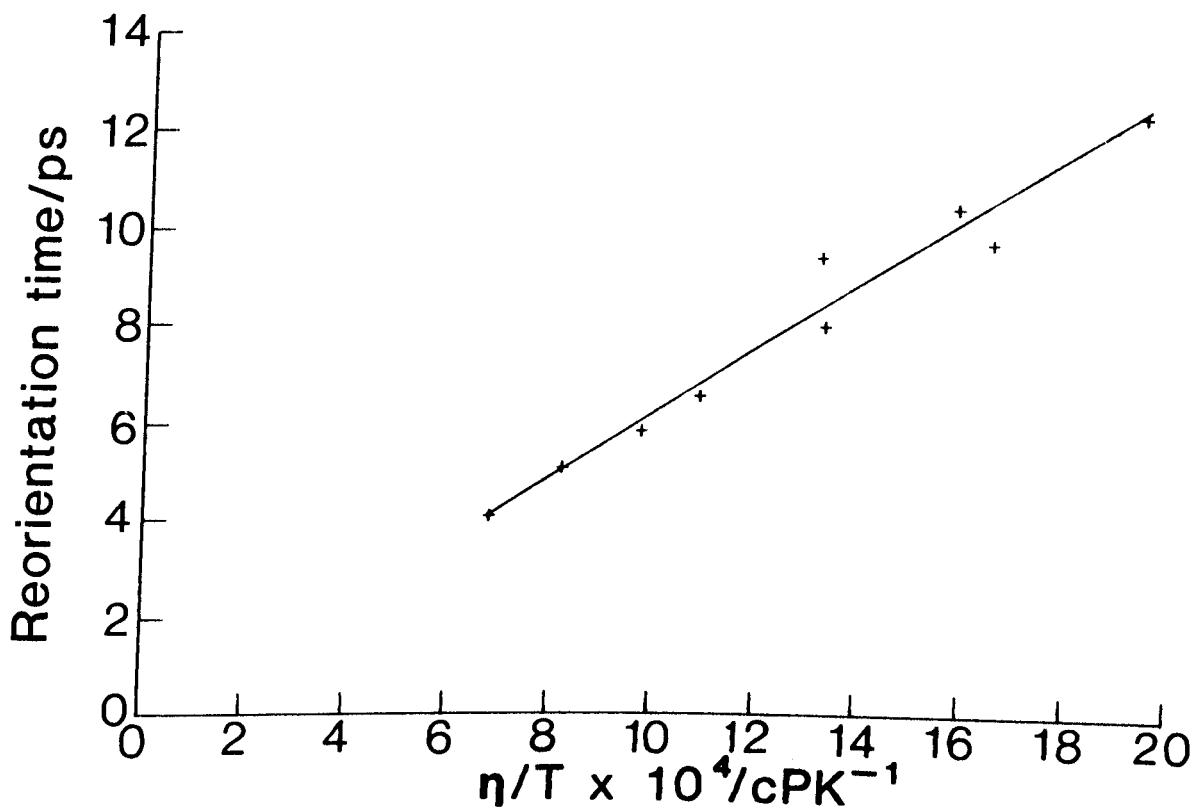


Fig 5.3.4 2,5-dimethylhexane. Stokes-Einstein-Debye fit to molecular correlation times

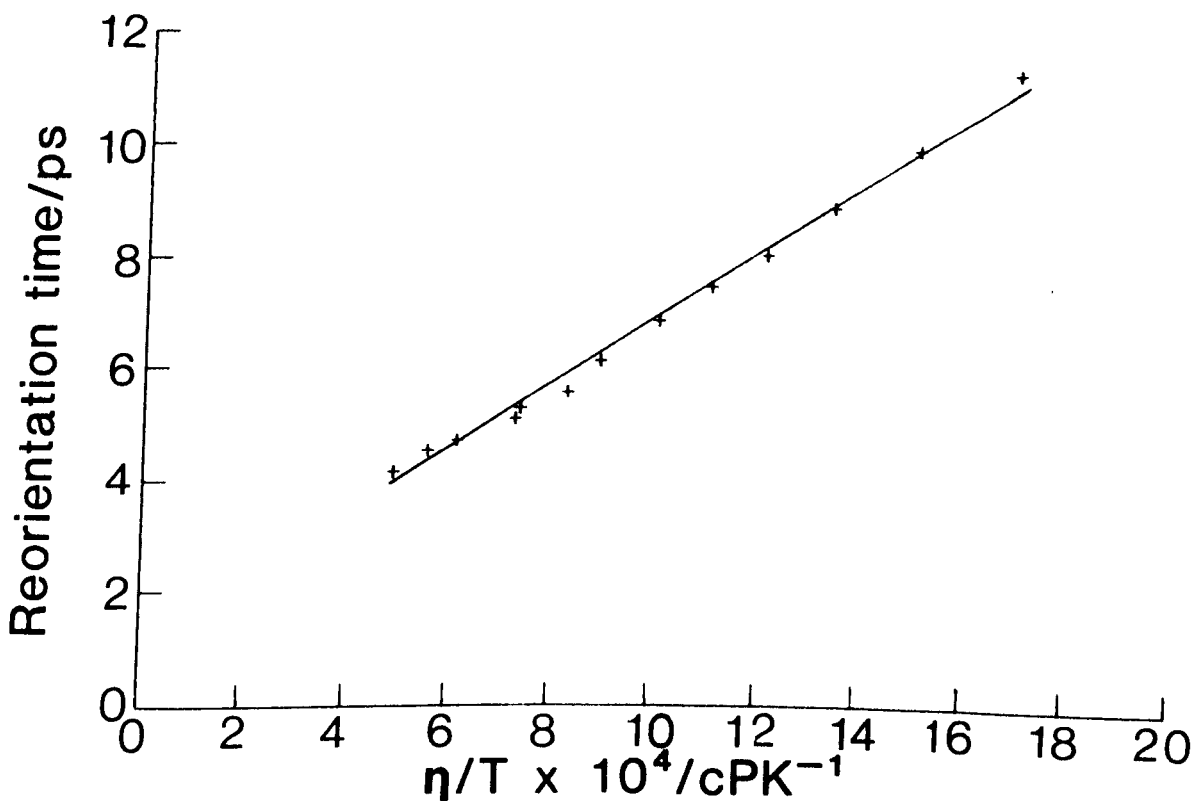
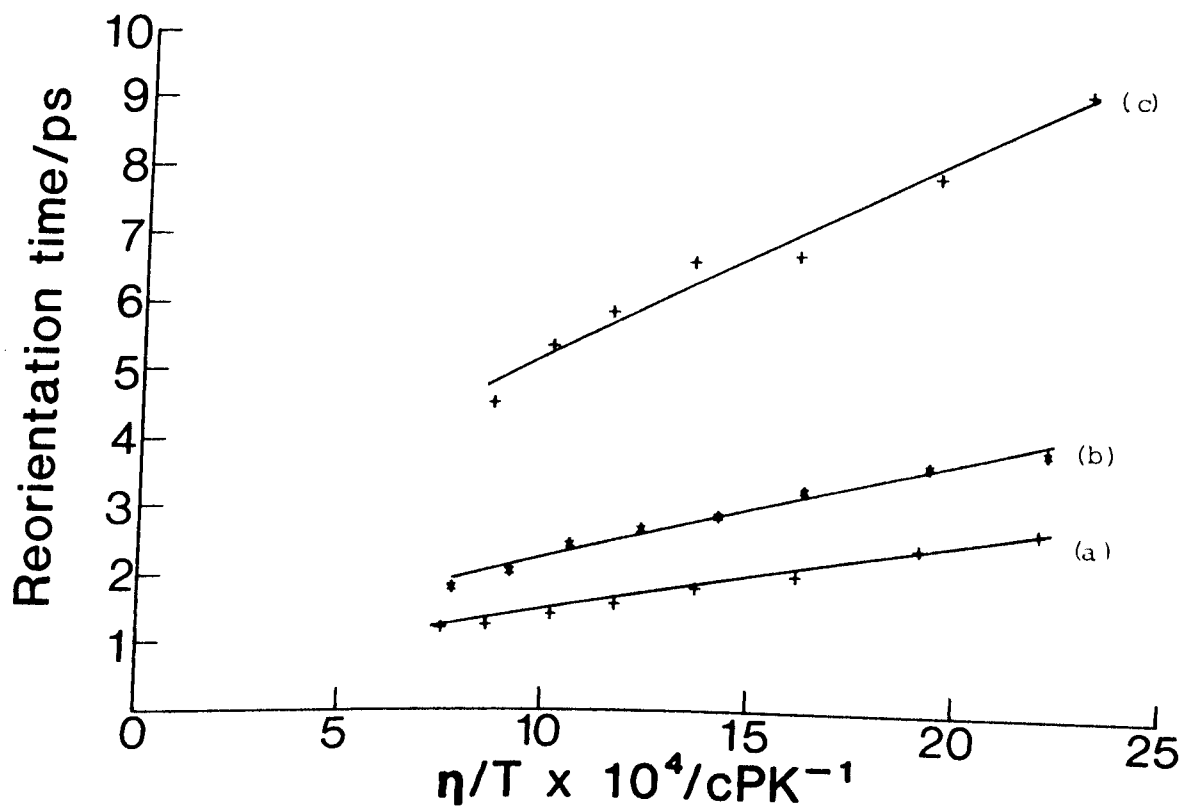


Fig 5.3.5 2,2,4-trimethylpentane. Stokes-Einstein-Debye fit to molecular correlation times



- (a) Single Lorentzian fit to spectra: FSR = 1500 GHz
- (b) Single Lorentzian fit to spectra: FSR = 685 GHz
- (c) Two Lorentzian fit to spectra: FSR = 1500 GHz

Fig 5.3.6 n-heptane. Stokes-Einstein-Debye fit to molecular correlation times

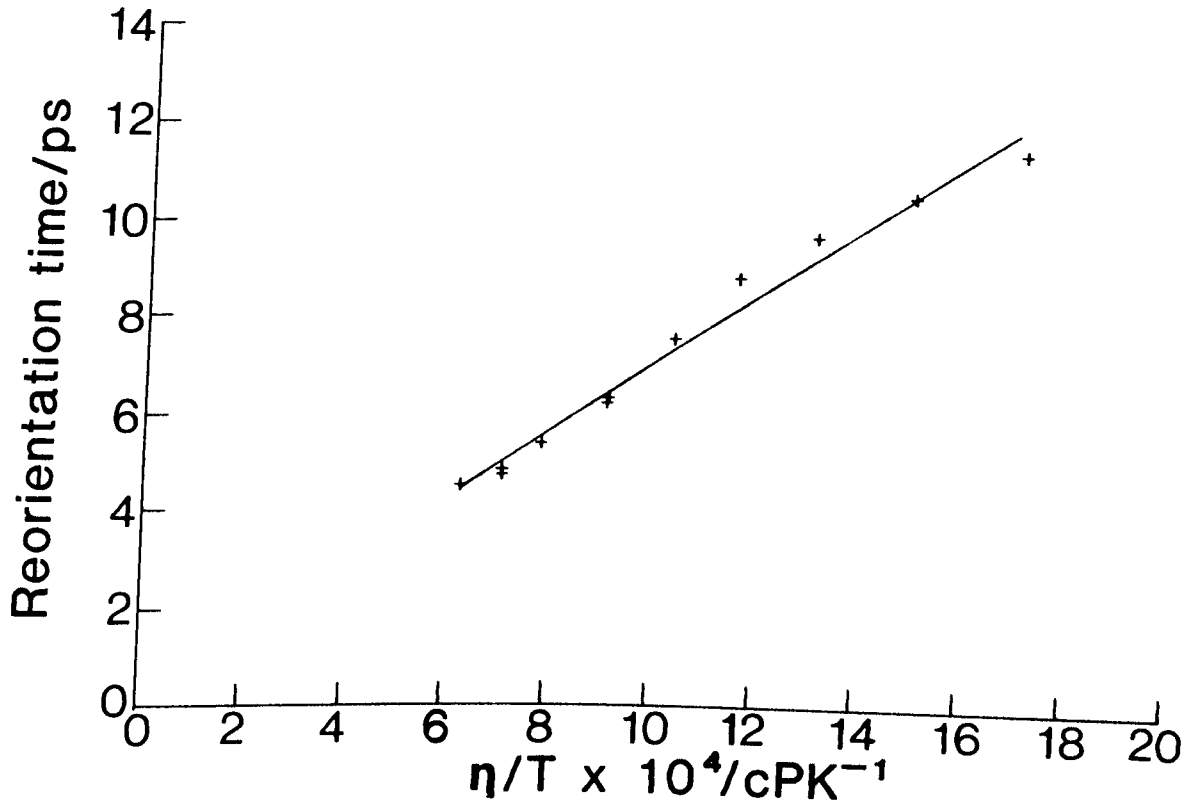


Fig 5.3.7 2-methylhexane. Stokes-Einstein-Debye fit to molecular correlation times: FSR = 450 GHz

- (a) Single Lorentzian fit to data
- (b) Two Lorentzian fit to data

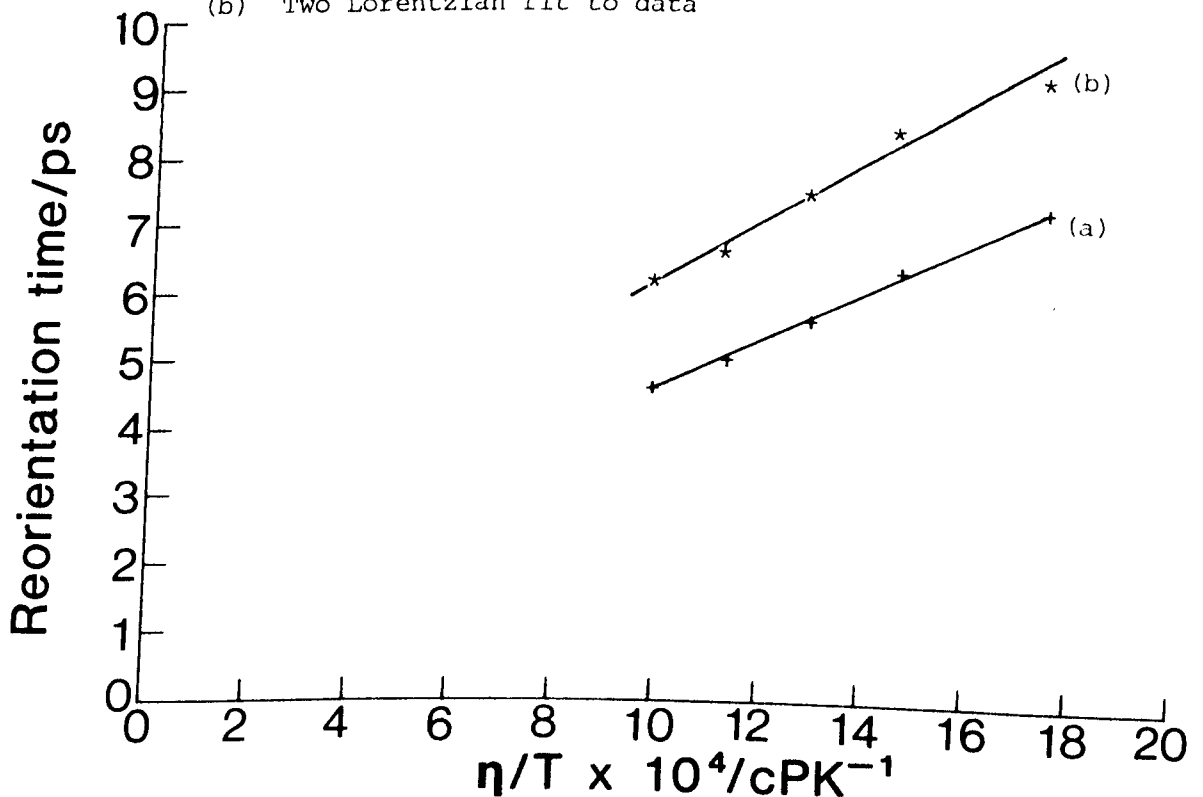


Fig 5.3.8 3-methylhexane. Stokes-Einstein-Debye fit to molecular correlation times

- (a) Single Lorentzian fit to spectra: FSR = 1250 GHz
- (b) Single Lorentzian fit: FSR = 400 - 600 GHz
- (c) Two Lorentzian fit to data: FSR = 1250 GHz

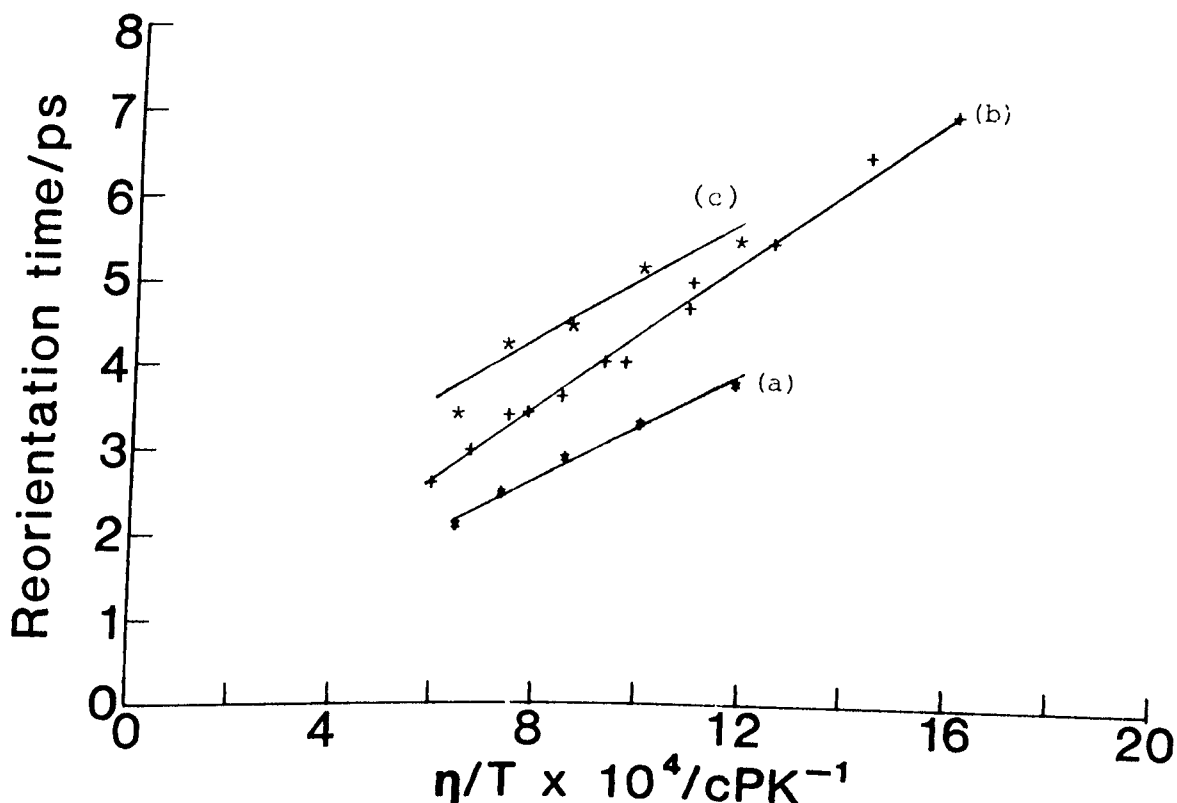


Fig 5.3.9 2,2-dimethylpentane Stokes-Einstein-Debye fit to molecular correlation times: FSR = 1000 GHz

- (a) Single Lorentzian fit to spectra
- (b) Two Lorentzian fit to spectra

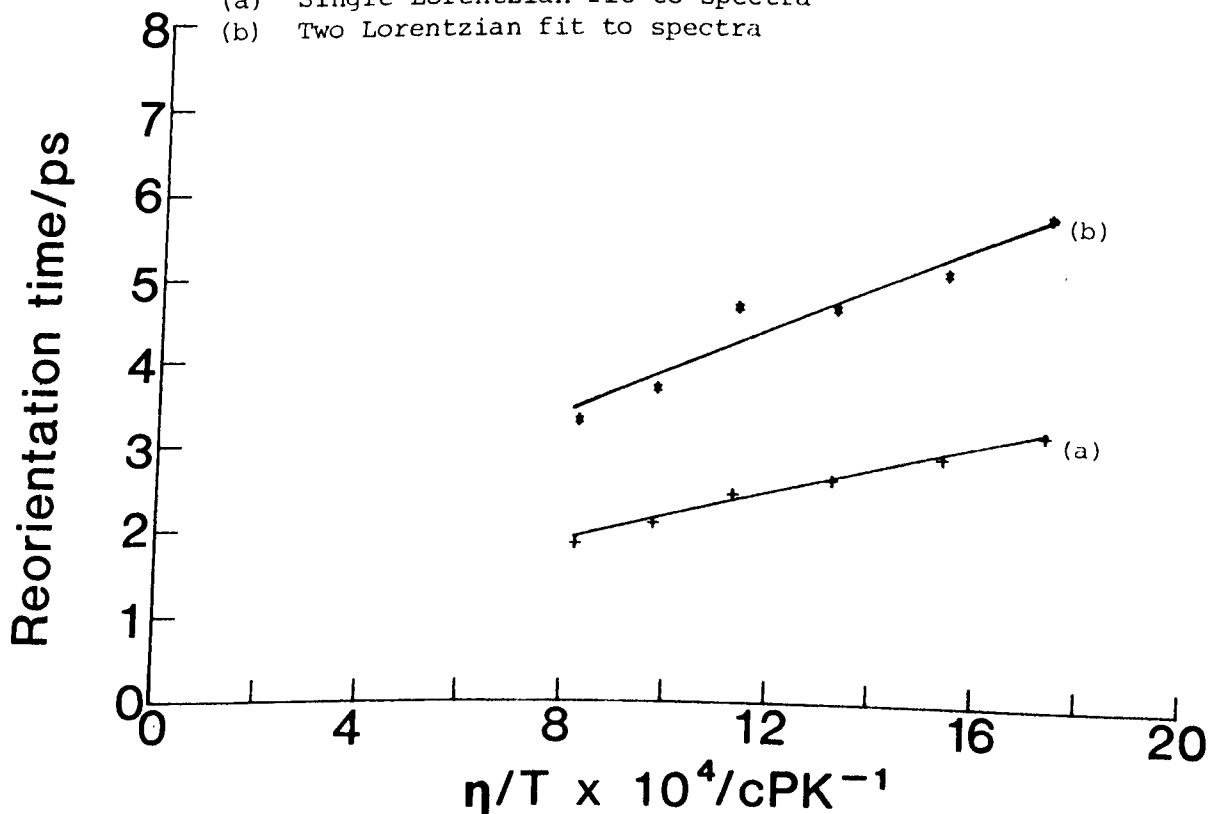


Fig 5.3.10 2,3-dimethylpentane. Stokes-Einstein-Debye fit to molecular correlation times.

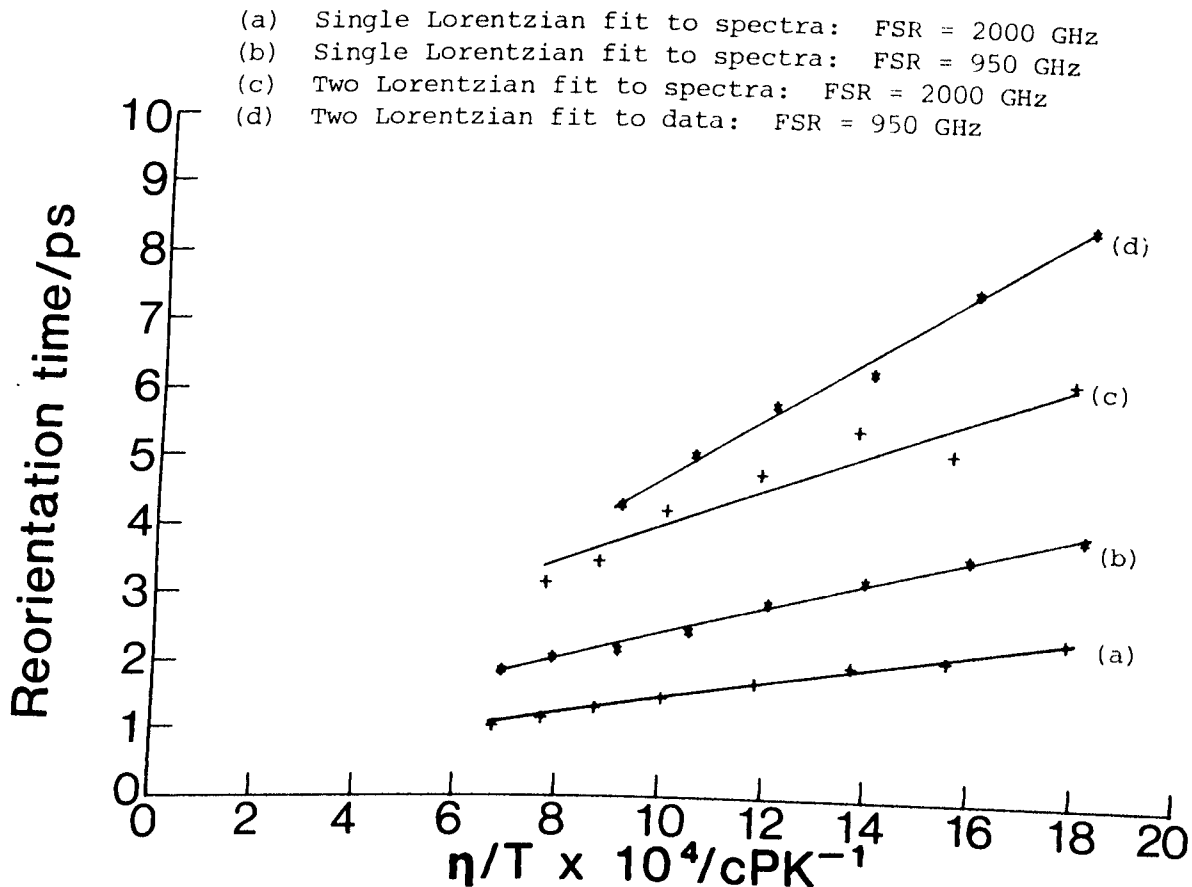


Fig 5.3.11 2,2,3-trimethylbutane. Stokes-Einstein-Debye fit to molecular correlation times: FSR = 2000 GHz

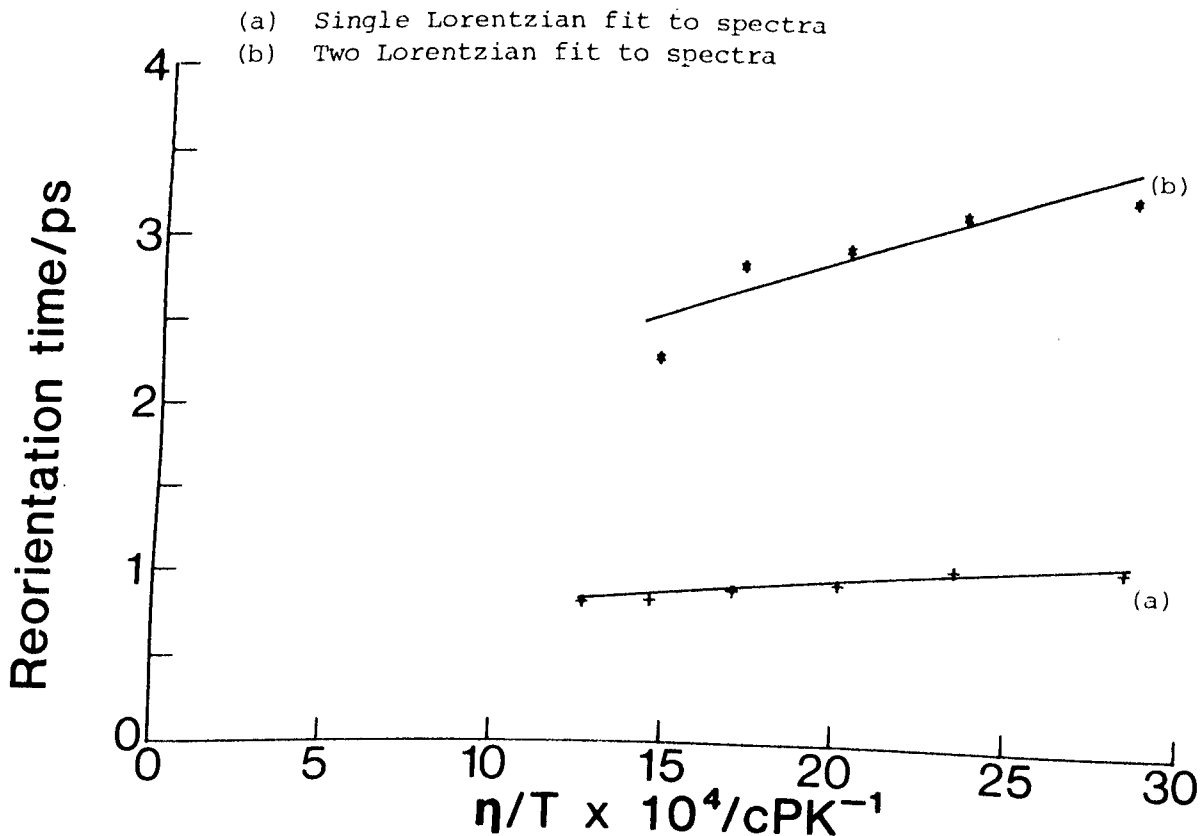


Fig 5.3.12 n-hexane. Stokes-Einstein-Debye fit to molecular correlation times

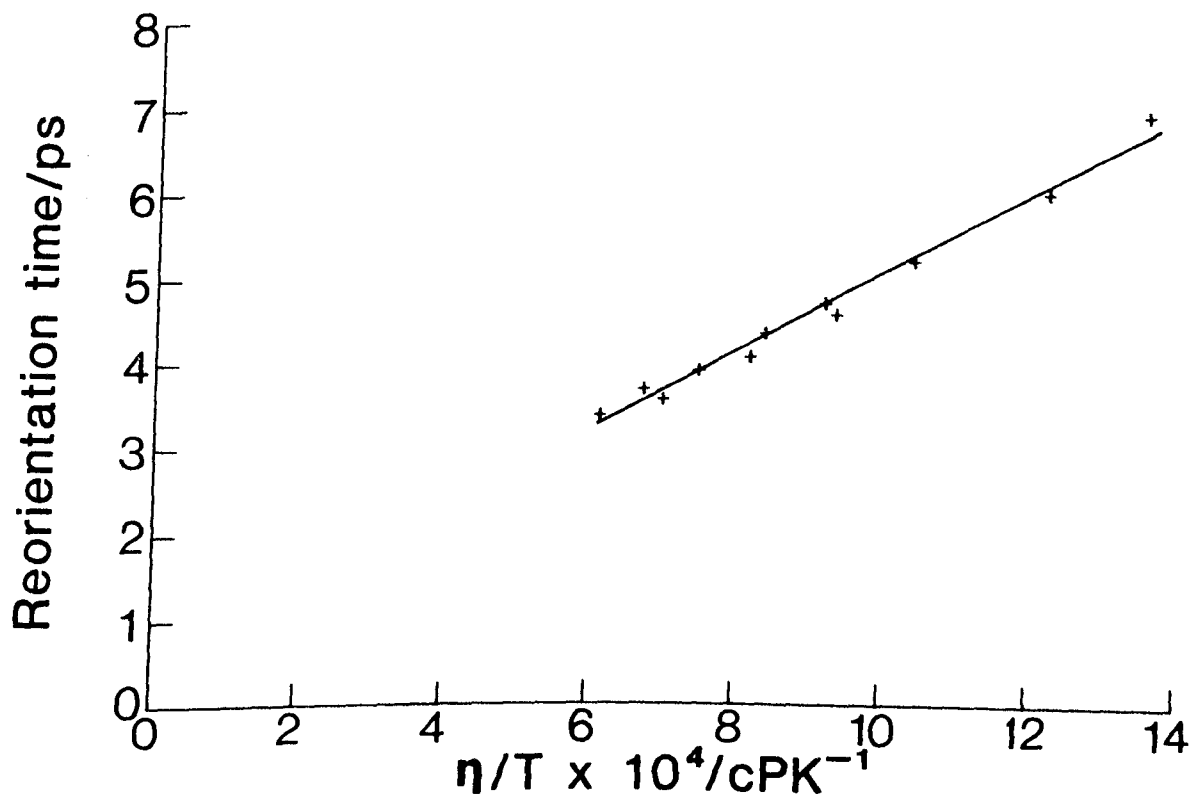


Fig 5.3.13 2-methylpentane. Stokes-Einstein-Debye fits to molecular correlation times

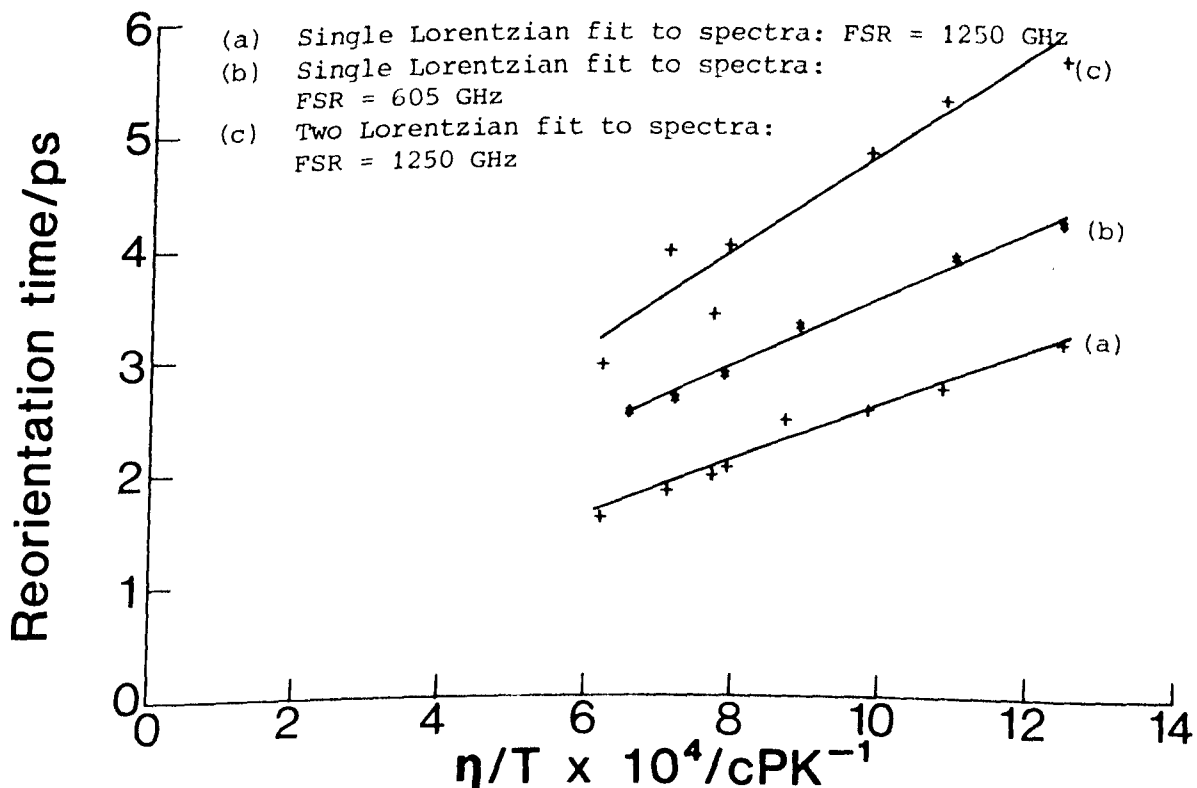


Fig 5.3.14 3-methylpentane. Stokes-Einstein-Debye fit to molecular correlation times

(a) Single Lorentzian fit to spectra: FSR = 1250 GHz

(b) Single Lorentzian fit to spectra: FSR = 715 GHz

(c) Two Lorentzian fit to spectra: FSR = 1250 GHz

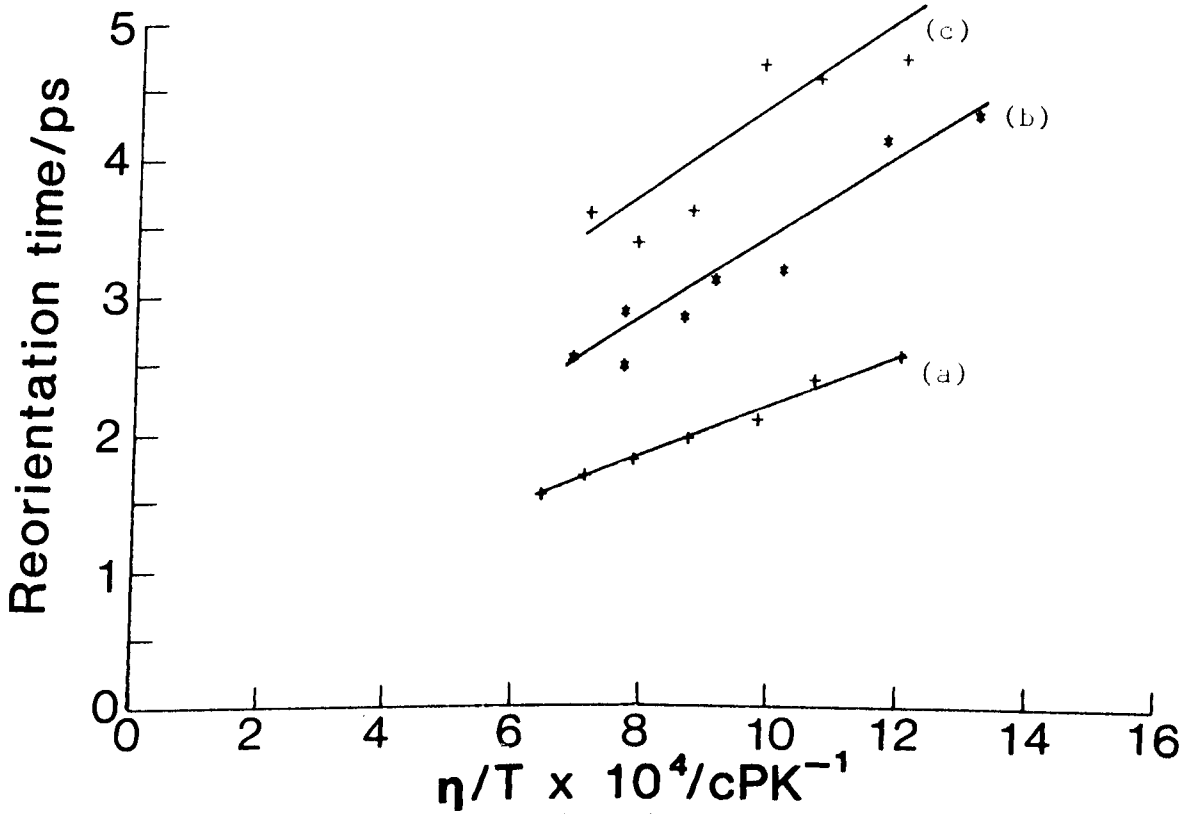


Fig 5.3.15 2,2-dimethylbutane. Stokes-Einstein-Debye fit to molecular correlation times: FSR = 3335 GHz

(a) Single Lorentzian fit to spectra

(b) Two Lorentzian fit to spectra

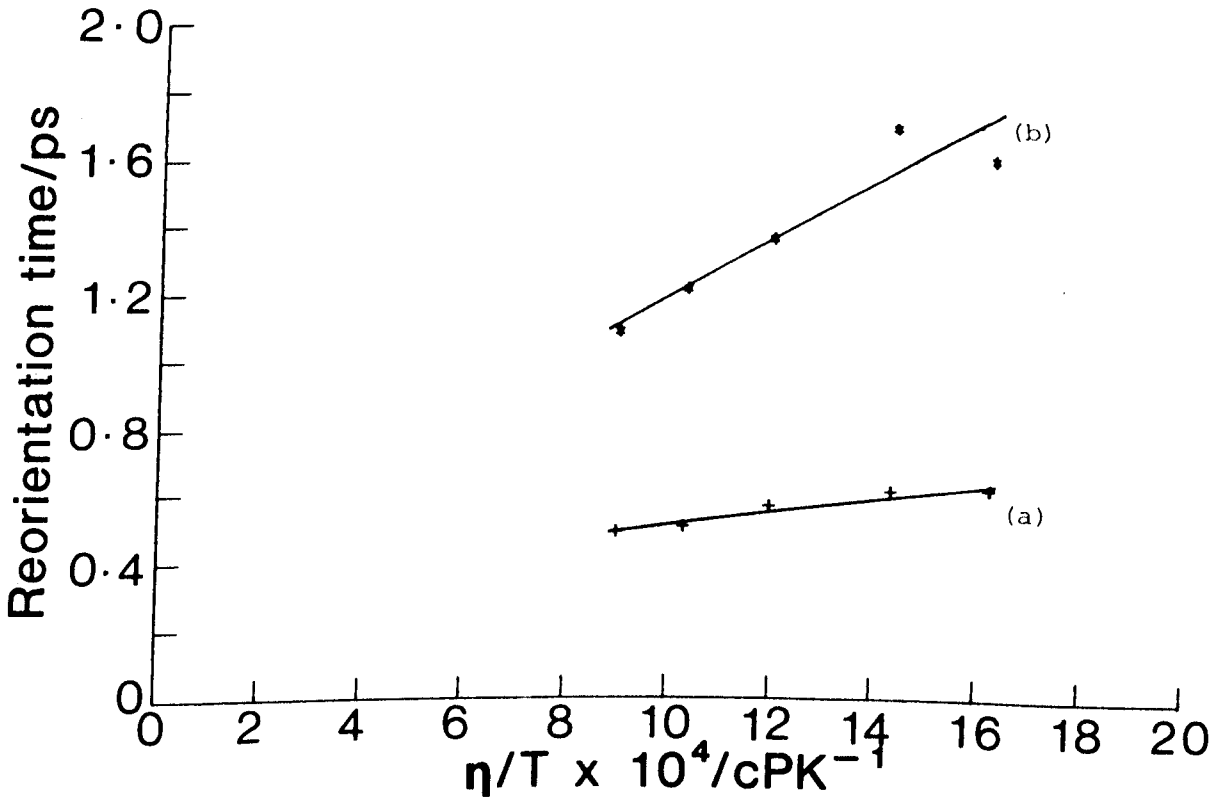


Fig 5.3.16 n-pentane. Stokes-Einstein-Debye fit to molecular correlation times

(a) Single Lorentzian fit to spectra: FSR = 1320 GHz

(b) Single Lorentzian fit to spectra: FSR = 670 GHz

(c) Two Lorentzian fit to spectra: FSR = 1320 GHz

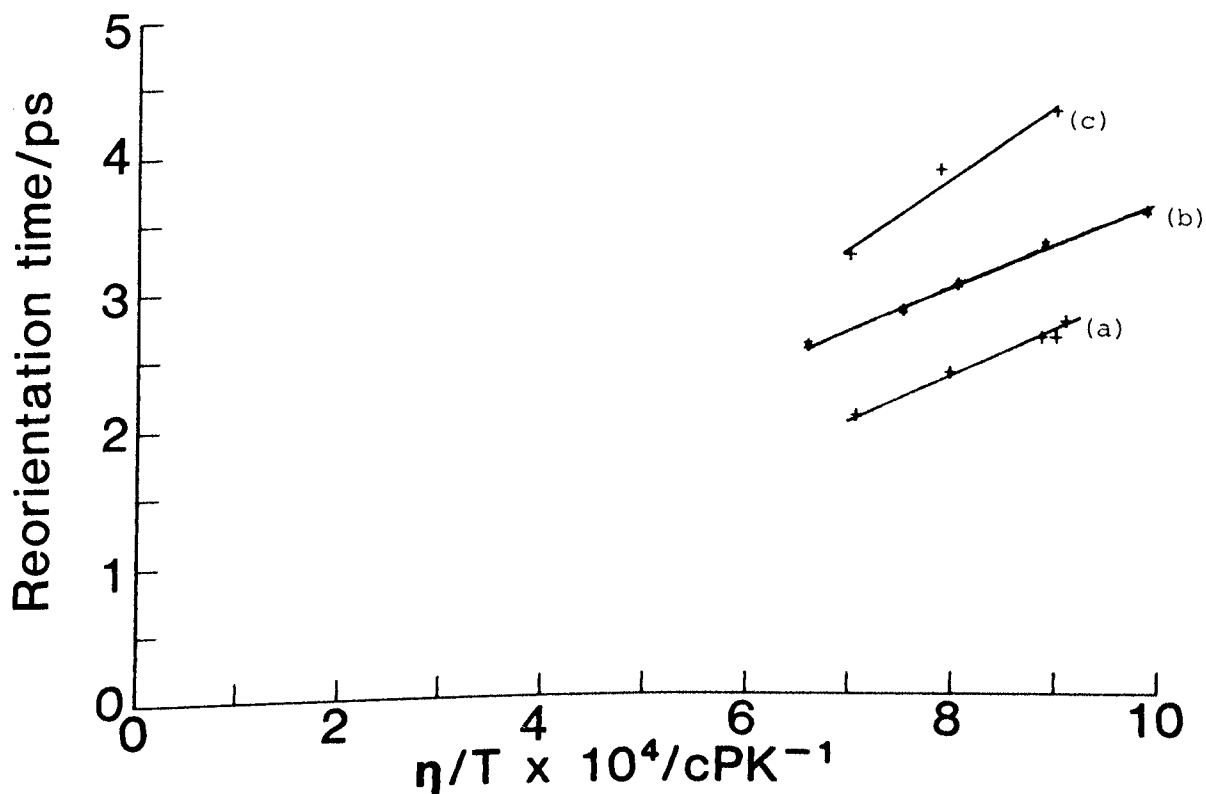
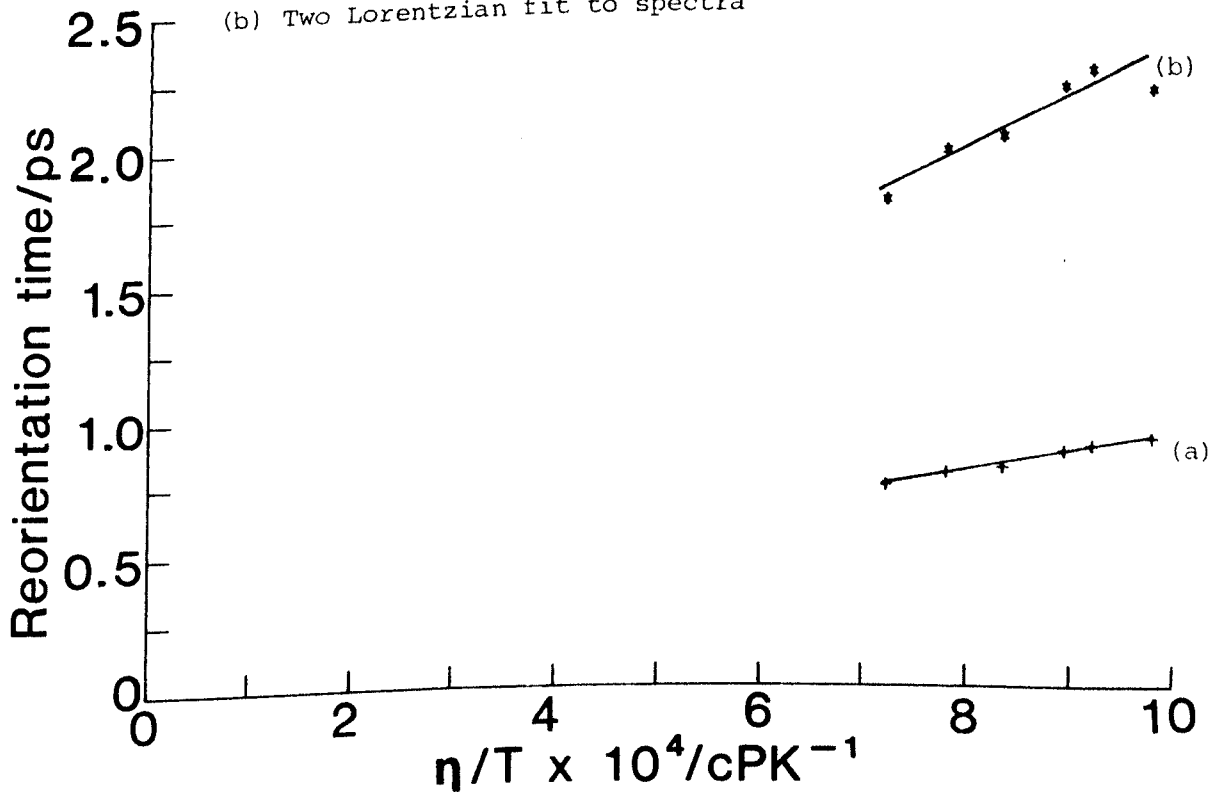


Fig 5.3.17 2-methylbutane. Stokes-Einstein-Debye fit to molecular correlation times: FSR = 2200 GHz

(a) Single Lorentzian fit to spectra

(b) Two Lorentzian fit to spectra



- (ii) Values of the intercept are all within  $\pm 2.5$  ps with the values increasing with increasing branching.

The effective molecular volumes and the intercepts obtained for all the alkanes are presented in Table 5.3.1. Where appropriate the values obtained from a two Lorentzian fit to the spectra are also shown.

A comparison between the Stokes-Einstein-Debye volumes obtained in this work and the results presented recently by Bagshaw<sup>[3]</sup> and Patterson and Carroll<sup>[1]</sup> is made in Table 5.3.2.

There is clearly agreement between the results of Bagshaw and this work for the n-alkanes. However the results of Patterson and Carroll are significantly lower although the trend is similar. The results from the isomer 2,2-dimethylbutane (this work) are compared with those from 2,3-dimethylbutane (ref [1]). This is justified since the molecular conformations are very similar. In addition as already discussed in Section 5.2.2 preliminary results from 2,3-dimethylbutane indicate close agreement with those from 2,2-dimethylbutane. A full discussion of the results from these isomers is presented in Section 5.3.2.

From the Stokes-Einstein-Debye relation (equation 2.4.14) it can be seen that the effective molecular volumes obtained from the gradients are given by the quantity  $(g_2/J_2)PV\alpha$ .  $(g_2/J_2)$  is the orientational correlation parameter,  $\alpha$  is the *stick-slip* coefficient, P is the Perrin factor and V is the molecular volume.

The molecular volume V was determined from the atomic and molecular dimensions measured from a Framework Molecular Model (FMM). The quantities  $(g_2/J_2)$ ,  $\alpha$  and P are determined by the environment of the molecule in the liquid.  $(g_2/J_2)$  is the angular correlation function

TABLE 5.3.1 MOLECULAR VOLUMES CALCULATED FROM STOKES-EINSTEIN-DEBYE FITS TO THE EXPERIMENTALLY OBTAINED CORRELATION TIMES

Liquid	One Lorentzian Fit to Data		Two Lorentzian Fit to Data	
	Effective Molecular Volume/ $\text{\AA}^3$	Intercept/ps	Effective Molecular Volume/ $\text{\AA}^3$	Intercept/ps
n-octane	140.7 ± 5.0	-0.73 ± 0.60		
2-methylheptane	92.0 ± 4.0	1.06 ± 0.43		
3-methylheptane	90.0 ± 7.0	-0.4 ± 0.7		
2,5-dimethylhexane	65.2 ± 4.0	1.03 ± 0.36		
2,2,4-trimethylpentane				
(i) FSR = 685 GHz	18.9 ± 2.5	0.95 ± 0.27	37.1 ± 0.9	2.53 ± 0.11
(ii) FSR = 1500 GHz	14.1 ± 0.6	0.44 ± 0.06	41.3 ± 4.7	2.26 ± 0.52
n-heptane	96.4 ± 9.0	0.05 ± 0.70		
2-methylhexane	50.3 ± 1.5	1.04 ± 0.14	52.9 ± 3.9	2.50 ± 1.0
3-methylhexane				
(i) FSR = 400-600 GHz	60.2 ± 3.8	0.05 ± 0.29		
(ii) FSR = 1250 GHz	42.2 ± 3.0	0.24 ± 0.19	49.7 ± 9.3	1.40 ± 0.61
2,2-dimethylpentane	20.4 ± 1.4	0.71 ± 0.13	35.7 ± 6.4	1.34 ± 0.60
2,3-dimethylpentane				
(i) FSR = 950 GHz	26.5 ± 1.5	0.54 ± 0.14	63.2 ± 3.6	0.46 ± 0.18
(ii) FSR = 2000 GHz	16.8 ± 0.8	0.26 ± 0.07	53.3 ± 3.7	0.23 ± 0.29
2,2,3-trimethylbutane	2.6 ± 0.4	0.59 ± 0.06	9.0 ± 3.0	1.6 ± 0.5
n-hexane	64.8 ± 5.0	0.41 ± 0.35		
2-methylpentane				
(i) FSR = 605 GHz	41.8 ± 3.0	0.54 ± 0.21		
(ii) FSR = 1250 GHz	34.6 ± 3.7	0.10 ± 0.24	58.9 ± 12.0	0.54 ± 0.82
3-methylpentane				
(i) FSR = 720 GHz	42.9 ± 8.0	0.31 ± 0.55		
(ii) FSR = 1250 GHz	26.7 ± 5.8	0.37 ± 0.50	42.9 ± 8.0	1.23 ± 0.90
2,2-dimethylbutane	2.7 ± 0.6	0.33 ± 0.05	11.2 ± 3.0	2.5 ± 1.5
n-pentane				
(i) FSR = 670 GHz	43.0 ± 2.0	0.51 ± 0.13		
(ii) FSR = 1320 GHz	45.4 ± 2.0	-0.26 ± 0.12	65.5 ± 9.5	0.25 ± 0.55
2-methylbutane	9.7 ± 1.0	0.24 ± 0.06	24.7 ± 6.9	0.56 ± 0.43

TABLE 5.3.2 COMPARISON OF STOKES-EINSTEIN-DEBYE VOLUMES MEASURED FROM THIS WORK WITH LITERATURE VALUES

Liquid	Stokes-Einstein-Debye Volume/ $\text{\AA}^3$			Intercept/ps		
	This Work	Bagshaw [ 3 ]	Patterson & Carroll [ 1 ]	This Work	Bagshaw [ 3 ]	Patterson & Carroll [ 1 ]
n-octane	141 ± 5	139 ± 2	106 ± 13	-0.7 ± 0.6	-0.7 ± 0.2	0.3 ± 0.7
n-heptane	96 ± 9	94 ± 3	69 ± 6	0.1 ± 0.7	-0.1 ± 0.2	0.5 ± 0.4
n-hexane	65 ± 5	66 ± 2	52 ± 4	0.4 ± 0.4	0.2 ± 0.1	0.6 ± 0.3
2,2-dimethylbutane	11 ± 3	-	-	0.4 ± 0.3	-	-
2,3-dimethylbutane	-	-	14.5 ± 0.5	-	-	-0.6 ± 0.1
n-pentane	65 ± 10	49 ± 2	40 ± 3	-0.3 ± 0.1	-0.3 ± 0.1	-0.1 ± 0.2
2-methylbutane	25 ± 7	-	42 (2 data points)	0.6 ± 0.4	-	-1.2 (2 data points)

Patterson and Carroll's value of  $42\text{\AA}^3$  for 2-methylbutane is unreliable since it is obtained from only two data points.

and is related to the degree of molecular alignment in the liquid.  $\alpha$  and  $P$  are both related to the hydrodynamics of molecular re-orientation in the liquid.  $\alpha$  is related to the hydrodynamic drag imposed on the molecule by its environment, that is the surrounding molecules.  $P$  is determined exclusively by molecular shape. An oblate or prolate ellipsoid immersed in a continuum undergoes both translational and reorientational diffusion at a slower rate than a sphere of the same volume. Perrin<sup>[68]</sup> calculated the effect of shape, for prolate and oblate ellipsoids, on both the translational and rotational diffusion times. The results are expressed in terms of a Perrin factor  $P$ , discussed in Section 2.4.1, greater than unity. An ellipsoid of volume  $V$  and Perrin factor  $P$  undergoes diffusion processes such that it acts as a sphere with an equivalent volume  $PV$ . The Perrin factor for prolate and oblate ellipsoids is given by equations (2.4.9) to equation (2.4.12).

The liquids investigated are composed of flexible molecules that have time varying conformations, hence the average molecular conformation lies between the all-*trans* configuration, that is with the chain completely extended, and the chain completely coiled such that the molecule approximates to a sphere. Therefore the effective molecular volume,  $PV$ , should lie between the actual molecular volume,  $V$ , and the all-*trans* conformation,  $P_{trans} V$ , where  $P_{trans}$  is the Perrin factor for the all-*trans* molecule.

In Table 5.3.3 a comparison is made between the Stokes-Einstein-Debye volume  $(g_2/J_2) \alpha PV$  and the quantity  $PV$  which may lie within the range of  $V$  and  $P_{trans} V$ . Axial ratios and molecular volumes are calculated from Framework Molecular Models. Where appropriate the comparison is made for Stokes-Einstein-Debye volumes obtained from two Lorentzian fits to the data. All the isomers were modelled as

prolate ellipsoids - except for 2,2,3-trimethylbutane which was modelled as an oblate ellipsoid.

For each set of isomers the general trend is a decrease in the Stokes-Einstein-Debye volume with increasing branching. In addition it appears that the measured Stokes-Einstein-Debye volume is similar for all backbone chains of the same length. For example, for the C<sub>7</sub> backbone the liquids n-heptane, 2-methylheptane and 3-methylheptane have the same effective volume, within two standard deviations. This implies that replacing a hydrogen atom by a methyl group on the backbone chain does not affect the effective molecular volume measured by light scattering. This conclusion is supported by examining space filling models of the all-*trans* configurations of the isomers.

The Stokes-Einstein-Debye volumes shown in Table 5.3.3 are equal to the quantity  $(g_2/J_2) \propto PV$ . Hence maximum and minimum values of the quantity  $(g_2/J_2) \propto$  can be calculated. For example, for the liquid n-octane the range of values which PV can take lies between 163 Å<sup>3</sup> and 443 Å<sup>3</sup>. The experimentally observed Stokes-Einstein-Debye volume for this liquid is 141 Å<sup>3</sup>. From this it can be deduced that the quantity  $(g_2/J_2) \propto$  lies between 0.32 and 0.87.

Table 5.3.4 shows the maximum and minimum values of the quantity  $(g_2/J_2) \propto$  for each liquid. The maximum value would be appropriate if the molecules were completely coiled up in the liquid, whereas the minimum values correspond to a completely extended (all-*trans*) chain. Neither of those extremes is probable, however measurements of infra-red spectra<sup>[121]</sup> have indicated that for the n-alkanes C<sub>8</sub>H<sub>18</sub> and below in the liquid state, the population of *gauche* states is less than that of *trans* states.

TABLE 5.3.3 A COMPARISON OF MOLECULAR VOLUMES

Liquid	Axial Ratio $r$	Molecular Volume $V/\text{\AA}^3$	Perrin Factor Volume: $P_{trans} V/\text{\AA}^3$	Stokes-Einstein-Debye Volume/ $\text{\AA}^3$
n-octane	0.296	163	443	141 ± 5
2-methylheptane	0.441		278	92 ± 4
3-methylheptane	0.441		278	90 ± 7
2,5-dimethylhexane	0.623		204	65 ± 4
2,2,4-trimethylpentane	0.712		187	41 ± 5
n-heptane	0.330	146	346	96 ± 9
2-methylhexane	0.497		221	53 ± 4
3-methylhexane	0.497		221	50 ± 9
2,2-dimethylpentane	0.712		167	36 ± 6
2,3-dimethylpentane	0.712		167	53 ± 4
2,2,3-trimethylbutane	0.832		155	9 ± 3
n-hexane	0.371	130	268	65 ± 5
2-methylpentane	0.568		178	59 ± 12
3-methylpentane	0.568		178	43 ± 8
2,2-dimethylbutane	0.832		142	11 ± 3
n-pentane	0.424	114	203	65 ± 10
2-methylbutane	0.664		136	25 ± 7

TABLE 5.3.4 COMPARISON OF MAXIMUM AND MINIMUM VALUES OF  $(g_2/J_2)_\alpha$

Liquid	Maximum Value of $(g_2/J_2)_\alpha$ - from molecular volume	Minimum Value of $(g_2/J_2)_\alpha$ - from $P_{trans}$ V volume
n-octane	0.865 ± 0.031	0.318 ± 0.011
2-methylheptane	0.564 ± 0.025	0.331 ± 0.014
3-methylheptane	0.552 ± 0.043	0.324 ± 0.025
2,5-dimethylhexane	0.399 ± 0.024	0.319 ± 0.019
2,2,4-trimethylpentane	0.252 ± 0.030	0.220 ± 0.026
n-heptane	0.658 ± 0.061	0.278 ± 0.026
2-methylhexane	0.363 ± 0.027	0.240 ± 0.018
3-methylhexane	0.411 ± 0.027	0.226 ± 0.046
2,2-dimethylpentane	0.247 ± 0.041	0.215 ± 0.043
2,3-dimethylpentane	0.363 ± 0.027	0.317 ± 0.024
2,2,3-trimethylbutane	0.062 ± 0.020	0.058 ± 0.020
n-hexane	0.500 ± 0.039	0.243 ± 0.018
2-methylpentane	0.454 ± 0.085	0.332 ± 0.067
3-methylpentane	0.331 ± 0.061	0.242 ± 0.045
2,2-dimethylbutane	0.082 ± 0.023	0.078 ± 0.021
n-pentane	0.0575 ± 0.033	0.320 ± 0.050
2-methylbutane	0.219 ± 0.062	0.184 ± 0.051

The values of  $(g_2/J_2)\alpha$  are all less than unity with a decrease with increasing branching for each set of isomers.

The quantity  $g_2$  has been measured for a range of n-alkanes by Bothorel et al<sup>[122]</sup>. The results were obtained from the integrated intensities of depolarised light scattering from the neat liquids and solutions in carbon tetrachloride. The measurements indicate that for the n-alkanes  $C_8H_{18}$  to  $C_5H_{12}$  the factor  $g_2$  is approximately equal to unity. As already discussed replacing a hydrogen atom by a methyl group does not appear to significantly change the measured effective volume. Hence the value of  $g_2$  for the isomers of  $C_8H_{18}$  to  $C_5H_{12}$  is also likely to be unity. Assuming the value of  $g_2$  obtained by Bothorel et al is correct then the *slip-stick* coefficient  $\alpha$  can be obtained. From Table 5.3.5 the primary observation is that for all the alkanes  $\alpha$  is less than unity. For the n-alkanes  $\alpha$  decreases with chain length and also decreases with increasing branching for each group of isomers. As the branching increases for each group of isomers the molecule becomes more spherical in shape (Fig 5.1.1a to Fig 5.1.1d) and is thus more likely to rotate within its own cavity in the liquid, interacting less with its neighbours than the hydrodynamic model, which is inherent in the Stokes-Einstein-Debye relation, would suggest. This implies that the process of rotational diffusion approaches the perfect *slip* limit as the molecules becomes more spherical. Similarly the decrease in  $\alpha$  with decreasing chain length for the n-alkanes implies that the shorter an n-alkane molecule the more it approximates to a sphere.

Hu and Zwanig<sup>[69]</sup> performed classical hydrodynamic, Navier-Stokes, calculations of the rotational friction coefficients of rigid prolate and oblate ellipsoids as a function of the axial ratio using *slip* boundary conditions (Section 2.4.2). Table 5.3.5 compares the

TABLE 5.3.5 COMPARISON OF EXPERIMENTAL AND THEORETICAL  $S^1/C^1/K-S^1/H$  COEFFICIENTS

Liquid	$\alpha_{MAX}$	$\alpha_{MIN}$	$\alpha_{HZ}^-$ (Hu & Zwanig [69])
n-octane	0.865 ± 0.031	0.318 ± 0.011	0.508
2-methylheptane	0.564 ± 0.025	0.331 ± 0.014	0.300
3-methylheptane	0.552 ± 0.043	0.324 ± 0.025	0.300
2,5-dimethylhexane	0.399 ± 0.024	0.319 ± 0.019	0.127
2,2,4-trimethylpentane	0.252 ± 0.030	0.220 ± 0.026	0.074
n-heptane	0.658 ± 0.061	0.278 ± 0.026	0.463
2-methylhexane	0.363 ± 0.027	0.240 ± 0.018	0.242
3-methylhexane	0.411 ± 0.027	0.226 ± 0.046	0.242
2,2-dimethylpentane	0.247 ± 0.041	0.215 ± 0.043	0.074
2,3-dimethylpentane	0.363 ± 0.027	0.317 ± 0.024	0.074
2,2,3-trimethylbutane	0.062 ± 0.020	0.058 ± 0.020	0.022
n-hexane	0.500 ± 0.039	0.243 ± 0.018	0.390
2-methylpentane	0.447 ± 0.019	0.332 ± 0.067	0.173
3-methylpentane	0.331 ± 0.067	0.242 ± 0.045	0.173
2,2-dimethylbutane	0.082 ± 0.023	0.078 ± 0.021	0.022
n-pentane	0.575 ± 0.093	0.220 ± 0.050	0.328
2-methylbutane	0.219 ± 0.062	0.184 ± 0.051	0.084

value of  $\alpha_{\text{HZ}}$ , calculated from the results of Hu and Zwanig, to the maximum  $\alpha_{\text{MAX}}$  and minimum  $\alpha_{\text{MIN}}$  values obtained from the Stokes-Einstein-Debye fit to the correlation times. The values of  $\alpha_{\text{HZ}}$  for the n-alkanes lie approximately midway between  $\alpha_{\text{MAX}}$  and  $\alpha_{\text{MIN}}$  indicating that the average conformation of the n-alkanes lies between the straight all-*trans* chain and the coiled sphere.

The monomethylalkanes of the  $\text{C}_8\text{H}_{18}$  and  $\text{C}_7\text{H}_{16}$  groups of isomers have  $\alpha_{\text{MIN}}$  values that are approximately the same as the  $\alpha_{\text{HZ}}$  values. This implies that these longer chain lightly branched alkanes have average conformations that are more spherical than the equivalent length backbone chain n-alkane.

For the rest of the isomers of all the groups the range of values all lie above  $\alpha_{\text{HZ}}$ . Three reasons are possible for this:

- (i) The molecules are influenced more by their neighbours than the Hu and Zwanig model would suggest. On a molecular level the all-*trans* forms of the isomers will appear to have a "rougher" surface than the all-*trans* n-alkanes and hence although *slip* conditions will still apply, a degree of *stick* will be introduced thus increasing  $\alpha$  above  $\alpha_{\text{HZ}}$ .
- (ii) In calculating  $\alpha_{\text{HZ}}$  from the results of Hu and Zwanig estimates were made of the axial ratio. These measurements are readily made for the all-*trans* form of the n-alkanes, however for the branched isomers difficulties are introduced because of the assymetry of the molecules about the longest axis. The smallest axial ratio was measured, that is, the maximum radius of the all-*trans* conformation divided by the length, and this results in the lowest value of  $\alpha_{\text{HZ}}$ . It is possible that because the molecule is not well modelled as an ellipsoid that the values

of  $\alpha_{\text{HZ}}$  should in fact be larger. If this is the case it would indicate that as for the longer chain monomethyl alkanes  $\alpha_{\text{MIN}}$  is approximately equal to  $\alpha_{\text{HZ}}$ .

(iii) It is possible that for the highly spherical molecules molecular reorientation is not the dominant process. Hence a Stokes-Einstein-Debye analysis of the correlation times obtained would not be appropriate. This possibility is further discussed in the following section.

### 5.3.2 Molecular Self-Diffusion

The molecular optical anisotropy correlation time for small molecules is determined principally by the reorientation about the longest axis of the molecule. For a molecule with cylindrical symmetry, reorientation around the long axis does not contribute to the depolarised Rayleigh spectrum. Therefore only reorientation about an axis perpendicular to the long axis contributes to the reorientational degrees of freedom, the spectrum is dominated by the conformations that have the largest optical anisotropy. For example consider the isomers of  $\text{C}_5\text{H}_{14}$ .

The optical anisotropy of the all-*trans* form of 2-methylbutane will be less than that of the all-*trans* form of n-pentane resulting in lower intensities and broader linewidths. This discussion applies to all the groups of isomers, that is, that with increasing branching the molecular optical anisotropy decreases and the correlation times when compared at the same  $\eta/T$  will decrease. This is in fact observed for all the groups of isomers.

However, for the isomer 2,2-dimethylbutane, which has a lower molecular optical anisotropy than 2-methylbutane, the values of the correlation times obtained are shorter than those for

2-methylbutane. The correlation times, when compared at constant  $n/T$ , would be expected to be similar or longer than for 2-methylbutane because of the increase in molecular size. It is possible therefore that molecular reorientation is not the predominant mechanism of optical anisotropy.

In addition to the depolarised Rayleigh scattering due to intermolecular optical anisotropy, there will be scattering due to dipole-induced-dipole interactions between pairs of density fluctuations. Madden<sup>[54]</sup> has calculated the depolarised Rayleigh spectrum from a system of isotropically polarisable molecules. In the central region the spectrum is Lorentzian with a linewidth given by

$$\Gamma_{\text{VH}} \propto 2Dq_0^2 \quad (2.3.6)$$

where:

$D$  is the translational self diffusion coefficient

$q_0$  is the magnitude of the scattering vector at the maximum in the centre of mass structure factor.

This diffusional central feature will be present for all liquids, however, its intensity will be small in comparison to the molecular optical anisotropy.

A comparison between Maddens' theory and the values of the peak half widths obtained for all the isomers from depolarised light scattering is presented.

The values of  $D$  for the n-alkanes have been measured as a function of temperature by Douglass and McCall<sup>[123]</sup> using the NMR spin-echo technique. In a later publication McCall et al<sup>[124]</sup> also measured the self diffusion coefficients for the isomers of  $C_6H_{14}$  using a similar technique.

A structure factor has been determined by electron diffraction from polyethylene melts<sup>[125]</sup>. The data of Voigt-Martin and Mijlhoff<sup>[125]</sup> indicates that the first maximum in the radial distribution function is determined by the interchain distance not by the overall size of the individual molecules. The maximum occurs at  $1.5 \text{ \AA}^{-1}$  which corresponds to an interchain distance of approximately  $5 \text{ \AA}$  which is in agreement with measurements made from molecular models. The value of  $q_0$  for the branched isomers will be less than  $1.5 \text{ \AA}^{-1}$ , that is the interchain distance will be greater because of the methyl side groups. Patterson and Carroll<sup>[1]</sup> assume a value of  $q_0 = 1.3 \text{ \AA}^{-1}$  for the isomer 2,3-dimethylbutane. The value for 2,2-dimethylbutane will be very similar. For the monomethylalkanes the value of  $q_0$  is taken to be  $1.4 \text{ \AA}^{-1}$  since the average interchain distance will be between the values for the n-alkanes and that for 2,2-dimethylbutane.

Table 5.3.6 compares the range of peak half width values predicted by Madden's theory, using values for D obtained from the data in ref [123] and [124] to the experimentally determined peak-half-width values.

It is evident from Table 5.3.6 that, except for the isomers 2,2-dimethylbutane and 2,3-dimethylbutane, the calculated peak-half-widths are very much larger than the experimentally determined ones. Patterson and Carroll conclude that when this large linewidth is coupled with the small intensity associated with this effect, the observed depolarised Rayleigh linewidth for all the alkanes, apart from 2,3-dimethylbutane, is dominated by molecular optical anisotropy relaxation determined by overall reorientation of the molecules. They find for the isomer 2,3-dimethylbutane that their experimental values are in agreement with the values predicted from the Madden theory. However, this conclusion is based on the assumption that

TABLE 5.3.6 COMPARISON OF  $\Gamma_{\text{VH}}$  MEASURED BY DEPOLARISED LIGHT SCATTERING WITH THAT CALCULATED FROM EQUATION (2.3.6)

Liquid	Temperature Range/ $^{\circ}\text{C}$	Range of $D/10^{-9} \text{ m}^2 \text{ s}^{-1}$	Range of $\Gamma_{\text{VH}}/\text{GHz}$ From Equation (2.3.6)	Measured Range of $\Gamma_{\text{VH}}/\text{GHz}$
n-octane $q_{\sigma} = 1.5 \text{ \AA}^{-1}$	0 - 100	1.6 - 5.0 [123]	110 - 360	5 - 25
n-heptane $q_{\sigma} = 1.5 \text{ \AA}^{-1}$	0 - 100	2.0 - 6.0 [123]	140 - 430	15 - 40
n-hexane $q_{\sigma} = 1.5 \text{ \AA}^{-1}$	0 - 60	3.3 - 6.0 [124]	240 - 430	20 - 50
n-pentane $q_{\sigma} = 1.5 \text{ \AA}^{-1}$	0 - 35	4.5 - 6.0 [123]	320 - 430	40 - 60
2-methylpentane $q_{\sigma} = 1.4 \text{ \AA}^{-1}$	0 - 60	3.3 - 5.6 [124]	200 - 350	30 - 60
3-methylpentane $q_{\sigma} = 1.4 \text{ \AA}^{-1}$	0 - 60	2.8 - 5.1 [124]	175 - 320	15 - 50
2,2-dimethylbutane $q_{\sigma} = 1.3 \text{ \AA}^{-1}$	0 - 40	2.4 - 4.0 [124]	130 - 215	100 $\pm$ 20 - 150 $\pm$ 30
2,3-dimethylbutane $q_{\sigma} = 1.3 \text{ \AA}^{-1}$	-10 - 20	1.8 - 3.5 [124]	95 - 190	90 - 200 [1]

the proportionality constant in equation (2.3.6) is equal to unity. (The values tabulated in Table 5.3.6 also assume this.) Patterson and Carroll do not provide any justification for this assumption and it is not clear, at least to this author, why this should be the case. Nevertheless, the proportionality constant is most probably greater than 0.1 since the diffusional central Lorentzian is not found in the spectra from the n-alkanes.

Patterson and Carroll<sup>[1]</sup> do not mention the existence of a second Lorentzian in any of their data. The reason for this is that the fixed FSR of 870 GHz that they used to obtain all their spectra is in general too small to adequately resolve the second Lorentzian component. In addition the FSR used is too large to study the longer chain n-alkanes. It has been demonstrated in this work that in order to obtain high quality spectra that have sufficiently high signal-to-noise ratios to resolve two Lorentzian components the range of FSR's needed is approximately 100 GHz to 3300 GHz. Data that has been collected over only one FSR should be carefully inspected; the line width quoted by Patterson and Carroll for 2,3-dimethylbutane at 20 °C is  $400 \pm 20$  GHz. When overlap from adjacent orders is taken into account this would result in a very low intensity signal-to-noise spectrum from which only very unreliable linewidths could be obtained. It seems fortuitous then that the linewidth measured at 10 °C exactly corresponds to that predicted by the Madden theory assuming a proportionality constant of unity.

However, these reservations aside, the conclusion from this work is that it is possible that for 2,2-dimethylbutane it is dipole-induced-dipole interaction between pairs of density fluctuations that are the predominant mechanism for optical anisotropy. It is also

probable that similar arguments apply for the liquid 2,2,3-trimethylbutane. Unfortunately however, self diffusion data was unavailable to make a direct comparison.

### 5.3.3 Origin of the Second Lorentzian

As discussed in Section 2.3.1 Viovy et al<sup>[49]</sup> have shown that the second broad Lorentzian component present in the depolarised Rayleigh spectra of small rigid molecules is due to a second variable describing local anisotropy. In their three-variable theory the variable associated with the second Lorentzian is the anisotropy in the distribution of the centres of gravity ( $\underline{G}$ ).  $\underline{G}$  is effectively a measure of local translational order. The liquids examined by Viovy et al were composed of very small rigid molecules. The results presented in this thesis are the first to show the existence of a second Lorentzian component in liquids composed of flexible molecules with time varying conformations. An alternative possibility for the occurrence of the second Lorentzian also exists - the possibility of coupling between the reorientational motion and interaction induced effects. For the more spherical rigid molecules the time scale separation between the reorientational and collisional motion is reduced because of two different but related effects - (a) It has been shown recently by Bagshaw<sup>[3]</sup> that the entity involved in collisional processes in n-alkanes is the methyl groups at the chain ends. However, it is far more likely that for the more globular molecules, for example 2,2,4-trimethylpentane, the entity involved in the collisional processes is the entire molecule. This would result in a much narrower interaction induced component because the mass of the colliding unit has greatly increased, that is, from equation (2.3.9)  $1/\omega_0 \propto m^{-\frac{1}{2}}$ , (b) Conversely, the reorientational

portion of the spectrum is much broader because of the spherical shape of the molecule, that is, the molecule can rotate within its own cavity without affecting or being affected to the same extent by surrounding molecules as an n-alkane molecule, thus increasing the reorientation frequency. Bagshaw<sup>[3]</sup> found a value of  $\omega_0$ , the time-scale of the collisional motion, of approximately 900 GHz for the n-alkanes. This corresponds to a mass of 19 amu, the mass of a terminal methyl group. In comparison the peak-half-widths obtained for n-octane are in the range 10 GHz to 30 GHz and hence the time-scale separation between the two processes is approximately 30. Conversely if the entire molecule is involved in the collisional process in the case of 2,2,4-trimethylpentane then  $\omega_0 \approx 390$  GHz. The peak-half-widths are in the range 20 GHz to 50 GHz and the time-scale separation is reduced to approximately 8.

However, it should be noted that in the analysis of the spectral data incorporation of an exponential base into the fitting function was not found to improve the fit. This implies that either, (i) the timescale of the collisional motion is larger than the above discussion would suggest, that is, it is not the complete molecule involved in the collisional process but still only a portion of it or, (ii) that the intensity of the interaction induced component is too small to resolve.

A possible insight into the appropriate mechanism responsible for the second Lorentzian comes from examining the depolarised Rayleigh spectra from 2,2-dimethylbutane. As already discussed, Section 5.3.2, there is evidence that the narrow central Lorentzian component is due to dipole-induced-dipole interactions and not molecular reorientation. This would imply the absence of coupling between the reorientational motion and the interaction induced component and hence that the

theory of Viovy et al is more appropriate.

For all the liquids found to exhibit a second Lorentzian in their depolarised Rayleigh spectra, the scatter on these fitted peak-half-widths is very large thus precluding any quantitative analysis. The results from 2,2,4-trimethylpentane have the lowest scatter and hence it is these that are discussed further.

A Stokes-Einstein-Debye fit to the data is shown in Fig 5.3.18. It is clear that apart from a few points at low  $\eta/T$ , the correlation times do fit to a straight line. In addition, the ratio of the integrated intensities of the second Lorentzian to the total integrated intensity of both Lorentzians was found to be approximately constant over the complete temperature range studied (Fig 5.3.19).

The conclusion from these results is that there is the same temperature dependence for the two mechanisms.

A more detailed discussion is not presented because of the limited amount of data available. However, the existence of this second Lorentzian in the depolarised Rayleigh spectra from short flexible molecules is of fundamental importance to the development of theoretical descriptions of the liquid state.

#### 5.3.4 Comparison of Experimental Molecular Correlation Times with Results from Computer Simulations

In this section a very limited comparison is made between the experimentally obtained molecular correlation times and those obtained from computer simulations by Evans and Knauss<sup>[4]</sup>. Evans and Knauss obtained results for the alkanes n-butane to n-undecane using a Brownian dynamics simulation, discussed in Section 2.4.4. A significant point about these theoretical results is that on changing from one model of torsional motion to another, the values of the correlation times obtained changed significantly. In addition, changing the values of the

Fig 5.3.18 2,2,4-trimethylpentane. Stokes-Einstein-Debye fit to data from second Lorentzian

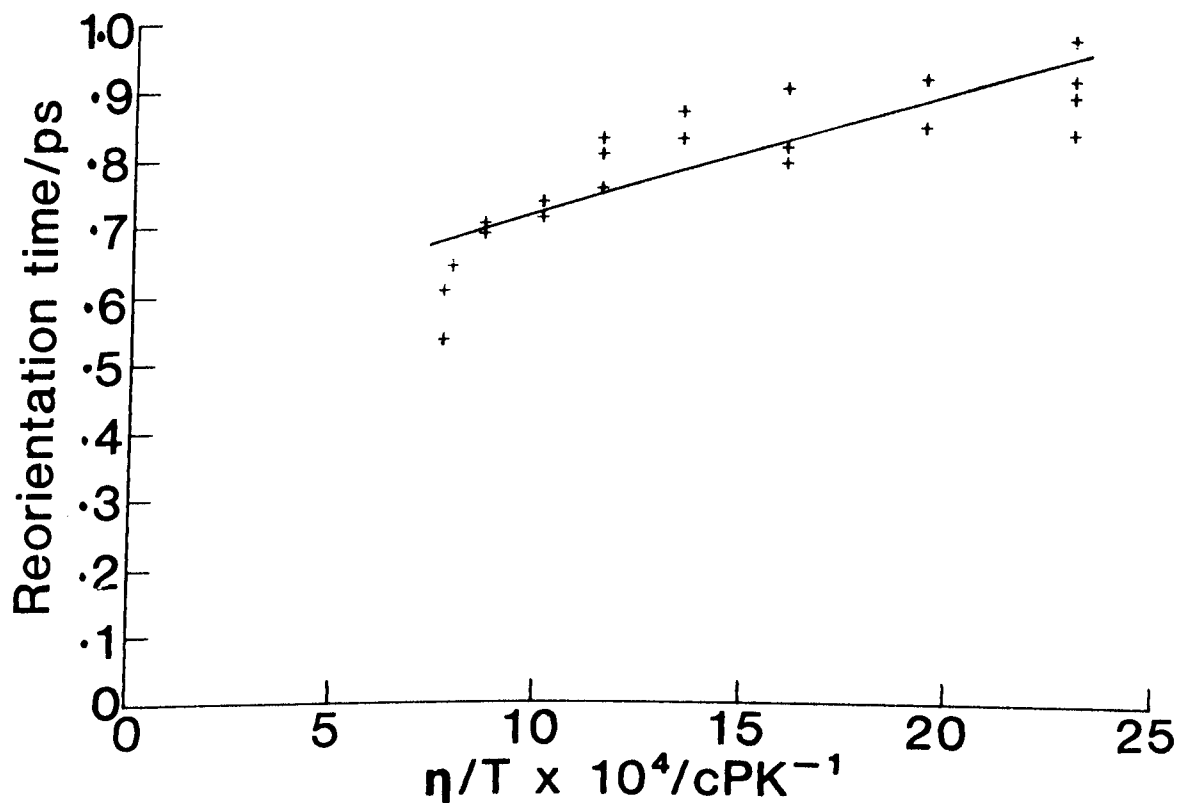
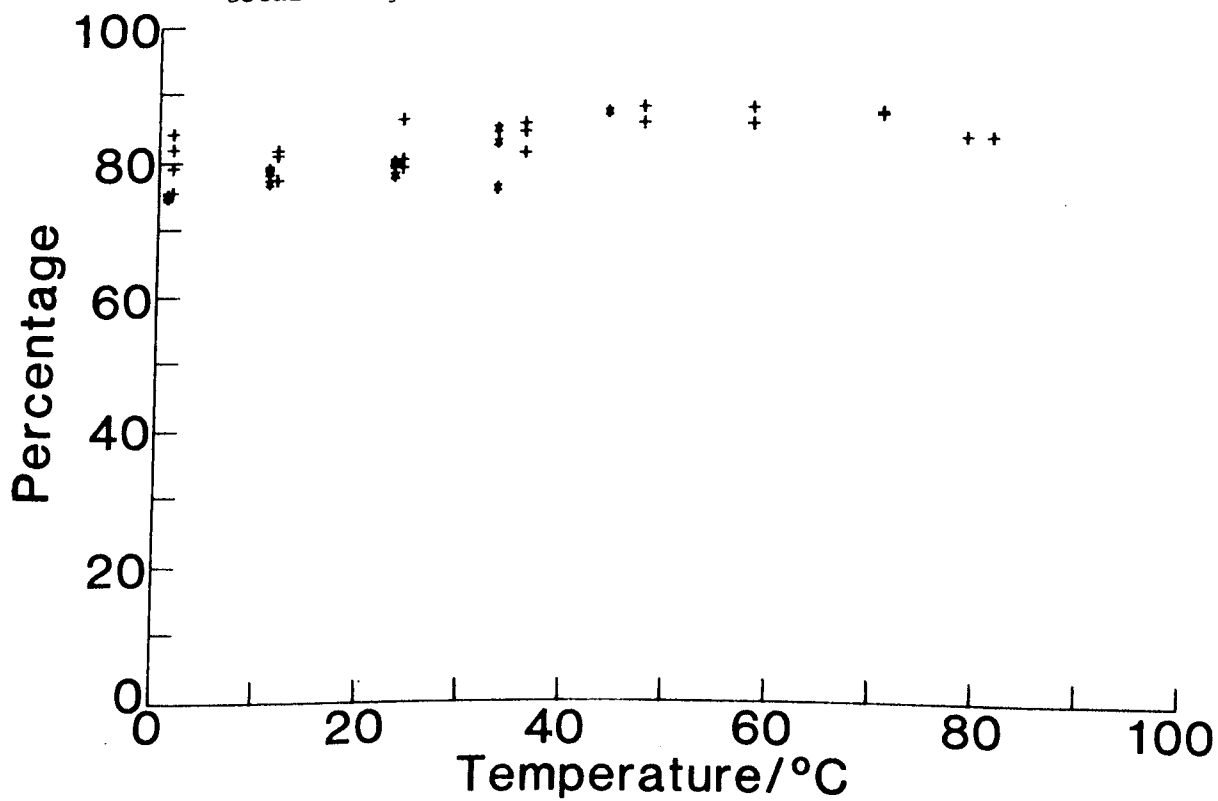


Fig 5.3.19 Ratio of integrated intensity of second Lorentzian to the total integrated intensity of both Lorentzians



torsional potentials significantly changed the correlation times. When the results obtained are so sensitive to the form and detail of so many of the parameters involved in the simulations, one must be confident that the input data selected for the simulation is a reasonable representation of the physical processes involved.

Evans and Knauss identify the  $Q = 1$  mode, first harmonic correlation time, as the closest to molecular reorientation. They propose that the  $U/k_B T = 5$  potential is the most appropriate by comparing their simulation results with those from dielectric relaxation measurements.

In Table 5.3.7 a comparison is made between the Stokes-Einstein-Debye volumes calculated from the results of Evans and Knauss for various potentials and those measured from depolarised Rayleigh scattering.

The simulation results provide only the dynamic quantity, that is, the quantity  $\alpha PV$ , whereas the coherent probe of depolarised light scattering measures the dynamic quantity modified by the orientational correlation, that is,  $(g_2/J_2) \alpha PV$ .

For the isomers n-pentane to n-octane  $g_2$  has been measured to be approximately equal to unity<sup>[122]</sup>. Hence a comparison of the results from the simulations with those from light scattering for the liquids n-pentane to n-heptane indicates that the values of the Stokes-Einstein-Debye volumes from light scattering are approximately half way between the simulation results for  $U/k_B T = 5$  and  $U/k_B T = \infty$  indicating that a torsional potential of  $U/k_B T = 5$ , which Evans and Knauss propose as the most appropriate, is too weak to explain the observed light scattering results.

Due to the limited amount of data available for comparison the only qualitative conclusion is that there is reasonable

TABLE 5.3.7 COMPARISON OF MOLECULAR VOLUMES OBTAINED FROM LIGHT SCATTERING WITH THOSE OBTAINED FROM A COMPUTER SIMULATION [4]

Number of Bonds	Liquid	Stokes-Einstein-Debye Volume from Light Scattering/ $\text{\AA}^3$	Stokes-Einstein-Debye Volume from Simulation/ $\text{\AA}^3$		
			$U/k_B T=0$ Freely Jointed Chain	$U/k_B T=5$	$U/k_B T=\infty$ Rigid Chain
4	$n\text{-C}_5\text{H}_{12}$	$65 \pm 10$	19.3	35.8	55.8
5	$n\text{-C}_6\text{H}_{14}$	$65 \pm 5$	18.9	41.6	82.3
6	$n\text{-C}_7\text{H}_{16}$	$96 \pm 9$	20.3	59.0	115.0

agreement between the simulation and experimental results. However it is worth noting that the model of Evans and Knauss is very simple - rigidly constrained bond lengths and bond angles and *trans* and *gauche* potentials are treated equally. Despite this, the model of Evans and Knauss is the only one that can be compared to experimental results and is thus a useful contribution to the understanding of liquid state dynamics.

CHAPTER 6 - SUMMARY OF CONCLUSIONS AND SUGGESTIONS FOR FUTURE  
INVESTIGATIONS

Contents

6.1 Summary of Conclusions

6.2 Suggestions for Future Investigations

## 6.1 Summary of Conclusions

- (1) The results of an experimental study of the motion of short chain flexible molecules using dynamic light scattering techniques have been described in Chapters 4 and 5.

A comprehensive computer fitting procedure designed to match the experimental data to theoretical spectra has been developed. This program incorporates, in addition to the least squares fitting process, a set of statistical tests designed to detect inadequacies in the theoretical fitting functions. This feature has led to a more rigorous interpretation of the experimental spectra.

Conclusions arising from the experimental work have been drawn in Chapter 4 and Chapter 5. The following paragraphs are a summary of these.

- (ii) The depolarised Rayleigh-Brillouin spectra obtained from the alkanes n-pentane to n-octane and their branched isomers were analysed in terms of the Stokes-Einstein-Debye relation. This provides a useful approach to analysing the data resulting in a quantity, the Stokes-Einstein-Debye volume, that can be interpreted in terms of the dynamic behaviour of the molecules in the liquid. The quantity obtained,  $(g_2/J_2)\alpha PV$ , was successfully separated into the components  $(g_2/J_2)$ ,  $\alpha$ ,  $P$  and  $V$  resulting in values of  $\alpha$ , the *stick-slip* coefficient, that indicate that for the n-alkanes studied the average molecular conformation lies approximately midway between a coiled sphere and an extended chain. These results are in agreement with the comparison made between the experimental Stokes-Einstein-Debye volume and the computer simulation results of Evans and Knauss<sup>[4]</sup>.

(iii) For the first time evidence has been obtained that shows that  $\alpha$ , the *stick-slip* coefficient, decreases as the molecule becomes more rigid and more spherical. This increase in the degree of *slip* with decreasing flexibility is in qualitative agreement with the hydrodynamic calculations of Hu and Zwanig<sup>[69]</sup>.

(iv) Improved experimental techniques and a rigorous data analysis routine have provided evidence for the existence of a second Lorentzian component in the depolarised Rayleigh spectra obtained from small flexible and semi-rigid molecules. Viovy et al<sup>[49]</sup> have shown that the second broad Lorentzian component is due to a second variable describing local anisotropy although an alternative possibility is that it is due to reorientational-collisional coupling that occurs due to the reduced time-scale separations between the two processes.

The contribution to the spectra from the second Lorentzian becomes less dominant as the flexibility increases and hence the shape becomes less spherical.

Future computer simulations of both rigid and flexible small molecules should incorporate the existence of this additional relaxation mechanism.

(v) The spectra obtained from the isomer 2,2-dimethylbutane are also interpreted in terms of a theory proposed by Madden<sup>[54]</sup>; the relaxation of intermolecular optical anisotropy is due to dipole-induced-dipole interactions between pairs of density fluctuations. From the evidence it is not clear that this is the correct interpretation however, it is possible that molecular reorientation is not the predominant relaxation mechanism.

A second Lorentzian component was found in the spectra from 2,2-dimethylbutane. This would suggest, in conjunction with the previous result, that the theory of Viovy et al is correct; the second Lorentzian is due to a second variable describing local order and is not attributable to reorientational coupling.

(vi) *Cis*-9-octadecenoic (oleic) acid was investigated by Rayleigh-Brillouin spectroscopy. The depolarised Rayleigh spectra were found to be too narrow to resolve with a Fabry-Perot interferometer implying a large scale cooperative motion in the liquid. The temperature gradient of the hypersonic frequency shifts and elastic modulus, measured from the polarised spectra, were found to show anomalous behaviour in the range 14 °C to 18 °C. This suggests that oleic acid undergoes a phase transformation to form a locally nematic structure approximately 5 °C above the melting point. Complementary measurements of viscosity, density and refractive index support this interpretation.

## 6.2 Suggestions for Future Investigations

(i) In order to obtain more precise information on the behaviour of the second Lorentzian, in addition to more accurate determination of the linewidth of this profile, the spectra need to be examined over a larger frequency range. This could be accomplished using a monochromator which can resolve the spectra out to frequencies > 10000 GHz.

A monochromator could also be used to examine the time-scale separation between the reorientational and interaction induced motions. This would give an indication as to whether coupling between these two phenomena is likely.

(ii) To obtain further information about the intermediate region between rigid and completely flexible molecules requires a study of a series of molecules that can be changed in flexibility whilst minimising the change in molecular shape. An obvious set of liquids that would satisfy this requirement are the alkenes where extra degrees of rigidity are imposed by the presence of carbon-carbon double bonds. By examining molecules with an increasing number of double bonds whilst keeping the chain length essentially constant the differences between a rigid and flexible chain can be investigated. In the present work, as the flexibility decreased, the value of  $\alpha$  also decreased. However this is also a result of the change in shape of the molecule. With the alkenes it is likely that  $\alpha$  will increase with increasing rigidity since the molecular shape remains essentially linear.

Investigation of the time-scale separation between molecular reorientation and the interaction induced component using a monochromator combined with a study of the behaviour of the second

Lorentzian in the spectra, if it is resolvable, could provide a further insight into the mechanism responsible for this effect.

(iii) Recent theoretical developments of depolarised Rayleigh spectra have concentrated on the low temperature high viscosity ( $\beta \gg 1$ ) regime from rigid symmetric top molecules<sup>[38,41,42,43]</sup>.

A great deal of information could be obtained from low temperature studies of the isomers of the alkanes and the alkenes. The effect on the spectra as the molecules become more flexible should provide a basis for refining present theories and extending them to anisotropic flexible molecules.

There are obviously a number of ways in which this work may develop in the future. It is hoped that the results presented in this thesis will form the basis of both future experimental and theoretical studies leading to a more comprehensive understanding of the behaviour of molecules in the liquid state.

## Figure List

- Figure 1.1 Schematic diagram of light scattering geometry
- Figure 1.2 Polarised Rayleigh-Brillouin spectrum of n-octane
- Figure 1.3 Depolarised Rayleigh-Brillouin spectrum of n-octane
- Figure 2.1.1 Scattering diagram for Rayleigh-Brillouin spectroscopy
- Figure 2.1.2 Scattering geometry
- Figure 2.2.1 Polarised Rayleigh-Brillouin spectrum of octamethylnonane
- Figure 2.2.2 Rayleigh-Brillouin spectrum of supercooled toluene
- Figure 2.3.1 Theoretical depolarised lineshapes
- Figure 3.1.1 Schematic diagram of the light scattering spectrometer
- Figure 3.1.2 Focusing the laser beam
- Figure 3.1.3 Instrumental function
- Figure 3.1.4 Sample cell holder
- Figure 3.1.5 Photograph of the cooling block
- Figure 3.3.1 Flow diagram of analysis program
- Figure 3.3.2 Rayleigh-Brillouin spectra of n-octane
- Figure 3.3.3 Example of misleading interpretation of the chi-square test
- Figure 3.3.4 Experimental data compared with two theoretical functions
- Figure 4.1.1 Configuration of oleic acid
- Figure 4.3.1 Arrhenius plot of the kinematic shear viscosity measurements
- Figure 4.3.2 Density measurements
- Figure 4.3.3 Refractive index measurements
- Figure 4.3.4 Polarised Rayleigh-Brillouin spectrum of the oleic acid solution
- Figure 4.3.5 Measured Brillouin frequency shifts and hypersonic elastic moduli
- Figure 4.3.6 Measured deconvoluted Brillouin linewidths
- Figure 4.4.1 Normalised sum of squares
- Figure 4.5.1 Variation of density and the volume expansion coefficient with temperature
- Figure 4.6.1 All-*trans* configuration of oleic acid
- Figure 4.6.2 Molecular structure of 4-cyano-4'-n-pentylbiphenyl
- Figure 5.1.1 All-*trans* configurations of the alkanes investigated
- Figure 5.2.1 to Figure 5.2.6 Variation of peak half-widths with temperature for the isomers of  $C_8H_{18}$
- Figure 5.2.7 to Figure 5.2.17 Variation of peak half-widths with temperature for the isomers of  $C_7H_{16}$

- Figure 5.2.18 to Figure 5.2.21 Variation of peak half-widths with temperature for the isomers of  $C_6H_{14}$
- Figure 5.2.22 Depolarised Rayleigh-Brillouin spectrum of 2,2-dimethylbutane
- Figure 5.2.23 to Figure 5.2.25 Variation of peak half-widths with temperature for the isomers of  $C_6H_{14}$
- Figure 5.2.26 to Figure 5.2.29 Variation of peak half-widths with temperature for the isomers of  $C_5H_{12}$
- Figure 5.3.1 to Figure 5.3.18 Stokes-Einstein-Debye fits to the data for the isomers of  $C_8H_{18}$  to  $C_5H_{12}$
- Figure 5.3.19 Ratio of integrated intensities for the isomer 2,2,4-trimethylpentane
- Figure A1.2.1 Polarised Rayleigh-Brillouin spectrum of n-octane; original and smoothed data
- Figure A2.1.1 Frequency function for  $\chi^2$  distribution
- Figure A2.2.1 One Sample Runs test
- Figure A2.2.2 Frequency function for a normal distribution
- Figure A2.3.1 Frequency function for linear correlation coefficient

## List of Tables

- Table 3.2.1 List of liquids studied
- Table 3.3.1 Results of statistical analysis for experimental data fitted to different fitting functions
- Table 4.4.1 Results of statistical analysis: oleic acid solution
- Table 4.4.2 Results of statistical analysis: octanoic acid solution
- Table 4.4.3 Transition temperature ( $T_B$ ) and range of  $T_B$  from each experiment: oleic acid solution
- Table 5.2.1 Statistical analysis of the spectra obtained from the isomers of  $C_8H_{18}$
- Table 5.2.2 A comparison of the statistical analysis of various fitting functions for 2,2,4-trimethylpentane
- Table 5.2.3 Statistical analysis of the spectra obtained from the isomers  $C_7H_{16}$
- Table 5.2.4 Statistical analysis of the spectra obtained from the isomers  $C_6H_{14}$
- Table 5.2.5 Molecular optical anisotropies
- Table 5.2.6 Statistical analysis of the spectra obtained from the isomers  $C_5H_{12}$
- Table 5.3.1 Molecular volumes obtained from Stokes-Einstein-Debye fits to the data
- Table 5.3.2 Comparison of molecular volumes from this work with literature values
- Table 5.3.3 A comparison of molecular volumes
- Table 5.3.4 Comparison of maximum and minimum values of  $(g_2/J_2)^\alpha$
- Table 5.3.5 Comparison of experimental and theoretical *stick-slip* coefficients
- Table 5.3.6 Comparison of  $\Gamma_{VH}$  measured from depolarised light scattering with Maddens theory
- Table 5.3.7 Comparison of molecular volumes obtained from light scattering with those from a computer simulation

## REFERENCES

- 1 Patterson G D and Carroll P J, J Chem Phys 76, 4356 (1982).
- 2 Champion J V and Jackson D A, Mol Phys 31, 1169 (1976).
- 3 Bagshaw J M, "An Experimental Investigation of the Motion of Flexible Molecules in the Liquid State by Light Scattering", PhD Thesis, CNA A, 1983.
- 4 Evans G T and Knauss D C, J Chem Phys 72, 1504 (1980).
- 5 Patterson G D, Lindsey C P and Alms G R, J Chem Phys 69, 3250 (1978).
- 6 Stryer L, "Biochemistry", W H Freeman and Co, San Francisco, 1981.
- 7 Lehninger A L, "Biochemistry - The Molecular Basis of Cell Structure and Function", Worth Pub Inc, New York, 1971.
- 8 Einstein A, Ann Phys 33, 1275 (1910).
- 9 Chu B, "Laser Light Scattering", Academic Press, 1974.
- 10 Berne B J and Pecora R, "Dynamic Light Scattering", Wiley-Interscience, New York, 1976.
- 11 Patterson G D, in "Methods of Experimental Physics", 16A, 171, Academic Press, 1980.
- 12 Mountain R D, Rev Mod Phys 38, 205 (1966).
- 13 Keyes T and Kivelson D, J Chem Phys 54, 1786 (1971).
- 14 Levy C and D'Arrigo G, Mol Phys 50, 917 (1983).
- 15 Herzfeld K F and Litovitz T A, "Absorption and Dispersion of Ultrasonic Waves", Academic Press, New York, 1959.
- 16 Mountain R D, J Res Nat Bur Stds 70A, 207 (1966).
- 17 Patterson G D, Ann Rev Mat Sci, 13, 219 (1984).
- 18 Carroll P J and Patterson G D, J Chem Phys 4, 1666 (1984).
- 19 Leontovich M A, Izv Akad Nauk SSR Ser Fiz, 5, 148 (1941) (J Phys USSR, 4, 499 (1941)).
- 20 Rytov S M, Zhur Exsp Teor Fiz, 33, 514 (1957).
- 21 Stegman G I A and Stoicheff B P, Phys Rev A1, 1160 (1973).
- 22 Enright G D, Stegman G I A and Stoicheff B P, J Phys Paris 23, 207 (1972).

- 23 Sixou P, Bezot P and Searby G M, Mol Phys 30, 1149 (1975).
- 24 Volterra V, Phys Rev 180, 156 (1969).
- 25 Chung C H and Yip S, Phys Rev A4, 928 (1971).
- 26 Ailawadi N, Berne J and Forster D, Phys Rev A3, 1462 (1971).
- 27 Ben-Reuven A and Gershon N D, J Chem Phys 54, 1049 (1971).
- 28 Andersen M C and Pecora R, J Chem Phys 54, 2584 (1971).
- 29 Keyes T and Kivelson D, J Chem Phys 56, 1876 (1972).
- 30 Mori H, Prog Theor Phys (Kyoto) 33, 423 (1965).
- 31 Tsay Shyr-Jin and Kivelson D, Mol Phys 29, 1 (1975).
- 32 Searby G M, Bezot P and Sixou P, Faraday Symposium 11, 63 (1977).
- 33 Bezot P, Searby G M and Sixou P, J Chem Phys 62, 3813 (1975).
- 34 Enright G D and Stoicheff B P, J Chem Phys 64, 3658 (1976).
- 35 Wang C H, Mol Phys 41, 541 (1980).
- 36 Lempert W and Wang C H, J Chem Phys 76, 1283 (1982).
- 37 Chappell P J, Allen M P, Hallem R I and Kivelson D, J Chem Phys 74, 5929 (1981).
- 38 Wang C H, Ma R-J, Fytas G and Dorfmueller Th, J Chem Phys 78, 5863 (1983).
- 39 Fytas G, Wang C H, Lilge D and Dorfmueller Th, J Chem Phys 75, 4247 (1981).
- 40 Lempert W and Wang C H, J Chem Phys 72, 2570 (1980).
- 41 Wang C H and Liu Q-L, J Chem Phys 78, 4363 (1983).
- 42 Wang C H, Ma R-J and Liu Q-L, J Chem Phys 80, 617 (1984).
- 43 Wang C H, Samois D and Dorfmueller Th (to be published).
- 44 Chappell P J and Kivelson D, J Chem Phys 76, 1742 (1982).
- 45 Quentrec B, Phys Rev A15, 1304 (1977).
- 46 Quentrec B and Bezot P, Mol Phys 39, 427 (1980).
- 47 MacPhail R A and Kivelson D, J Chem Phys 80, 2102 (1984).
- 48 Viovy J L, Searby G M, Fried F, Vellutini M J and Sixou P, Mol Phys 38, 1275 (1979).
- 49 Viovy J L, Searby G M, Sixou P and Champion J V, Mol Phys 39, 471 (1980).

- 50 Craddock H C, Jackson D A and Powles J G, Mol Phys 14, 373 (1968).
- 51 Jackson D A and Simic-Glavasky B, Mol Phys 18, 393 (1970).
- 52 De Gennes P G, Mol Cryst Liq Cryst 12, 193 (1971).
- 53 Quentrec B, J Phys Paris 37, 1255 (1976).
- 54 Madden P A, Mol Phys 36, 365 (1978).
- 55 Madden P A, Chem Phys Lett 47, 174 (1977).
- 56 Bezot P, Hesse-Bezot N and Quentrec B, Mol Phys 43, 1407 (1981).
- 57 Keyes T, Kivelson D and McTague J P, J Chem Phys 55, 4096 (1971).
- 58 Gelbart W M, Adv Chem Phys 24, 1 (1974).
- 59 Tabisz G C, Mol Spec Chem Soc, 6, 136 (1979).
- 60 Bucaro J A and Litovitz T A, J Chem Phys 54, 3846 (1971).
- 61 Pecora R, J Chem Phys 49, 1036 (1968).
- 62 Kivelson D, Kivelson M G and Oppenheim I, J Chem Phys 52, 1810 (1970).
- 63 Cheung C K, Jones D R and Wang C H, J Chem Phys 64, 3567 (1976).
- 64 Alms G R, Bauer D R, Brauman J I and Pecora R, J Chem Phys 58, 5570 (1973).
- 65 Alms G R, Bauer D R, Brauman J I and Pecora R, J Chem Phys 59, 5310 (1973).
- 66 Bauer D R, Brauman J I and Pecora R, J Chem Phys 63, 53 (1975).
- 67 Alms G R, Bauer D R, Brauman J I and Pecora R, J Chem Phys 59, 5321 (1973).
- 68 Perrin F, J Phys Radium, 5, 33 (1934); J Phys Radium 7, 1 (1936).
- 69 Hu C M and Zwanig R, J Chem Phys 60, 4354 (1974).
- 70 Youngren G K and Acrivos A, J Chem Phys 63, 3846 (1975).
- 71 Kivelson D and Madden P A, Ann Rev Phys Chem 31, 523 (1980).
- 72 Fytas G, J Mol Liq 28, 95 (1984).
- 73 Bauer D R, Brauman J I and Pecora R, J Am Chem Soc 96, 6840 (1974).
- 74 Richardson S J, Fluid Mech 59, 707 (1973).
- 75 Zwanig R, J Chem Phys 68, 4325 (1978).

- 76 Peralta-Fabi R and Zwanig R, J Chem Phys 70, 504 (1979).
- 77 Keyes T and Kivelson D, J Chem Phys 56, 1057 (1972).
- 78 Gierke T D, J Chem Phys 65, 3873 (1976).
- 79 Wolynes P G and Deutch J M, J Chem Phys 67, 733 (1977).
- 80 Battaglia M R, Cox T I and Madden P A, Mol Phys 37, 1413 (1979).
- 81 Cox T I, Battaglia M R and Madden P A, Mol Phys 38, 1539 (1979).
- 82 Patterson G D, Kennedy A P and Latham J P, Macromolecules 10, 667 (1977).
- 83 Bauer D R, Alms G R, Brauman J I and Pecora R, J Chem Phys 61, 2255 (1974).
- 84 Ryckaert J P and Bellemans A, Faraday Disc Chem Soc 66, 95 (1978).
- 85 Rebertus D W, Berne B J and Chandler D, J Chem Phys 70, 3395 (1979).
- 86 Pratt L R, Hsu C S and Chandler D, J Chem Phys 68, 4202 (1978).
- 87 Hsu C S, Pratt L R and Chandler D, J Chem Phys 68, 4213 (1978).
- 88 Weber A, J Chem Phys 69, 2347 (1978).
- 89 Weber A, J Chem Phys 70, 4277 (1979).
- 90 Evans G T, Mol Phys 36, 1199 (1978).
- 91 Evans G T, J Chem Phys 69, 3363 (1978).
- 92 Evans G T and Knauss D C, J Chem Phys 71, 2255 (1979).
- 93 Crossley J, Adv Mol Relax Proc 6, 39 (1974).
- 94 Montgomery J A, Holmgren S L and Chandler D, J Chem Phys 73, 3688 (1980).
- 95 Van Gunsteren W F, Berendsen H J C and Rullman J A C, Mol Phys 44, 69 (1981).
- 96 Evans G T, Cole R G and Hoffman D K, J Chem Phys 77, 3209 (1982).
- 97 Cole R G, Hoffman D K and Evans G T, J Chem Phys 80, 5365 (1984).
- 98 Cole R G, Hoffman D K and Evans G T, J Chem Phys 80, 5375 (1984).
- 99 Kogelnik H and Li, T Appl Opt 5, 1550 (1966).
- 100 Liddel P, "An Investigation of Local Homogeneities in Amorphous Polymers using Light Scattering Techniques", PhD Thesis, CNA, 1979.

- 101 Hecht E and Zajac A, "Optics", Addison Wesley, 4th Edit, 1979.
- 102 Kruger J K, Peetz L and Unruh H G, Colloid and Polymer Sci, 259, 215 (1981).
- 103 Kruger J K, Peetz L, Wildner W and Pietralla M, Polymer 21, 620 (1980).
- 104 Patterson G D, Carroll P J and Pearson D J, J Chem Soc Far Trans 79, 677 (1983).
- 105 Nagle J F and Scott H L, Physics Today, 3138 (1978).
- 106 Trauble H and Hayes D H, Chem Phys Lipids 7, 324 (1971).
- 107 Ranck J L, Maten L, Sadler D M, Tardieu A, Gulik-Kryzwick T and Luzzat V, J Mol Biol 85, 249 (1974).
- 108 Mrcelja S, Nature 241, 451 (1973).
- 109 Phillips M C, Williams R M and Chapman D, Chem Phys Lipids 3, 234 (1969).
- 110 Tables of Physical and Chemical Constants, 14th Edit, Kaye G W C and Laby T H, Longman Group 1973.
- 111 Van Nostrand's Scientific Encyclopedia, 4th Edit, p 1237-1238, D Van Nostrands Co Ltd, 1968.
- 112 Crilly J F and Earnshaw J C in "The Application of Laser Light Scattering to the Study of Biological Motion", NATO, ASI, Eds: Earnshaw J C and Steer M W, Plenum, 1982.
- 113 Crawford G E and Earnshaw J C, European Biophysical J, 11, 25 (1984).
- 114 Pagano R E, Cherry R J and Chapman D, Science 181, 557 (1973).
- 115 White S H, Biophysical J 15, 95 (1975).
- 116 Champion J V and Jackson D A, Mol Phys 31, 1159 (1976).
- 117 Vinogradov G V and Ya Malkin A, "Rheology of Polymers: Viscoelasticity and Flow of Polymers", MIR Publishers, Moscow, 1980.
- 118 Van de Hulst H C, "Light Scattering by Small Particles", Dover Pub Inc, New York, 1981.
- 119 Stevens G C and Richardson M J, Polymer 24, 851 (1983).
- 120 Patterson G D and Alms G R, Macromolecules 10, 1237 (1977).
- 121 Schaufele R F, J Chem Phys 49, 4168 (1968).
- 122 Bothorel P, Such, Clement, J Chime Phys 10, 1453 (1972).

- 123 Douglass D C and McCall D W, J Phys Chem 62, 1102 (1958).
- 124 McCall D W, Douglass D C and Anderson E W, Phys Fluids 2, 87 (1959).
- 125 Voigt-Martin I and Mijlhoff F C, J Appl Phys 46, 1165 (1975).
- 126 Bevington P R, "Data Reduction and Error Analysis for the Physical Sciences", McGraw Hill Pub Co, 1966.
- 127 Jackson D A and Bedborough D S, J Phys E 11, 1121 (1977).
- 128 Van de Hulst H C and Reesnick J J M, Astrophysical J 106, 121 (1947).
- 129 Lipson S G and Lipson H, "Optical Physics", Cambridge University Press, 2nd Edit, 1981.
- 130 Leidecker H W and La Macchia J T, J Acoust Soc Am 43, 143 (1968).
- 131 "Handbook of Mathematical Functions", Eds: Abramovitz M and Stegun I A, Dover Pub Inc, New York, 1965.
- 132 Boas M L, "Mathematical Methods in the Physical Sciences", Wiley and Sons, 1966.
- 133 Mendenhall W, Scheaffer R L and Wackerly D D, "Mathematical Statistics with Applications", Duxbury Press, Boston, 2nd Edit, 1981.
- 134 Pugh E M and Winslow G H, "The Analysis of Physical Measurements", Addison-Wesley, 1966.
- 135 Camail M, Proutiere A and Bodot H, J Phys Chem 82, 2617 (1978).
- 136 Foulani P and Clement C, Bull Soc Chim Fr, 3462 (1969).
- 137 Clement C and Bothorel P, J Chim Phys 61, 878 (1964).
- 138 Bothorel P and Fourche G, J Chem Soc Faraday Trans II 4, 441 (1973).
- 139 Nagai K, J Chem Phys 47, 4690 (1967).

## APPENDIX 1 - DEVELOPMENT OF A DATA ANALYSIS PROGRAM

### Contents

- A1.1        Weighting of the Data Points
  
- A1.2        Initial Estimates of the Fitting Parameters
  
- A1.3        Linearisation of the Data Points
  
- A1.4        Construction of the Fitting Functions
  - A1.4.1    Fitting Functions for Polarised Rayleigh-Brillouin Spectra
  
  - A1.4.2    Fitting Functions for Depolarised Rayleigh-Brillouin Spectra
  
- A1.5        Deconvolution of Instrumental Broadening

## APPENDIX 1 - DEVELOPMENT OF A DATA ANALYSIS PROGRAM

A Numerical Algorithm Group (NAG) routine, EO4GAF, which finds a least-squares solution of M non-linear equations in N variables by the method due to Marquardt<sup>[126]</sup>, was used to fit the experimental data. Subroutines to calculate the residuals (the difference between the object function and the ordinate value at the corresponding abscissae) and the first partial derivatives with respect to each fitting parameter were supplied. Details of these are given in the following sections.

### A1.1 Weighting of the Data Points

Statistical weighting of the data points was required in order to maximise the efficiency of the minimisation routine and to evaluate the integral chi-square probability (Appendix A2.1).

Poisson statistics were used to weight the data points by scaling the output from the transient recorder, ranging from 0 to 255, to the count rate. The count rate required to produce full scale deflection of the transient recorder was found by applying a frequency generator to the rate meter of the photon counting system. Under the experimental conditions used the maximum count rate was found to be approximately 2000.

### A1.2 Initial Estimates of the Fitting Parameters

To ensure that the fitting routine (EO4GAF) finds the global minimum, and to increase computing efficiency, the initial estimates of the fitting parameters should be reasonable estimates of the ultimate values, that is, within a few standard deviations.

In order to calculate the initial estimates the peak position had to be determined as a function of channel number. This was achieved by

numerical differentiation of the data and searching for changes in sign of the first derivative. However, because of the noise on the data (statistical fluctuations), the total number of turning points greatly exceeded the 'true' number. To eliminate the noise the data was smoothed; three successive data points, Y1, Y2 and Y3 were averaged using the relation

$$Y2(\text{NEW}) = (Y1 + 2 * Y2 + Y3) / 4 \quad (\text{A1.2.1})$$

where Y2(NEW) is the new (smoothed) value of Y2. This method ensured that the peak positions were not shifted during the smoothing operation. Initially, 100 smooths were performed. If the number of turning points was outside the required range the data was re-smoothed as appropriate. Only true turning points survived such large scale smoothing. Fig A1.2.1 shows an unsmoothed polarised Rayleigh-Brillouin spectrum of n-octane and the same spectrum after smoothing 250 times.

The Rayleigh peaks contain less data points than the Brillouin peaks and hence on smoothing, the ratio of the Rayleigh/Brillouin height is reduced. In addition, equivalent peaks in successive orders (from left to right) of the smoothed version are also reduced in height. The reason for this is that due to the non-linear scan there are less points per order.

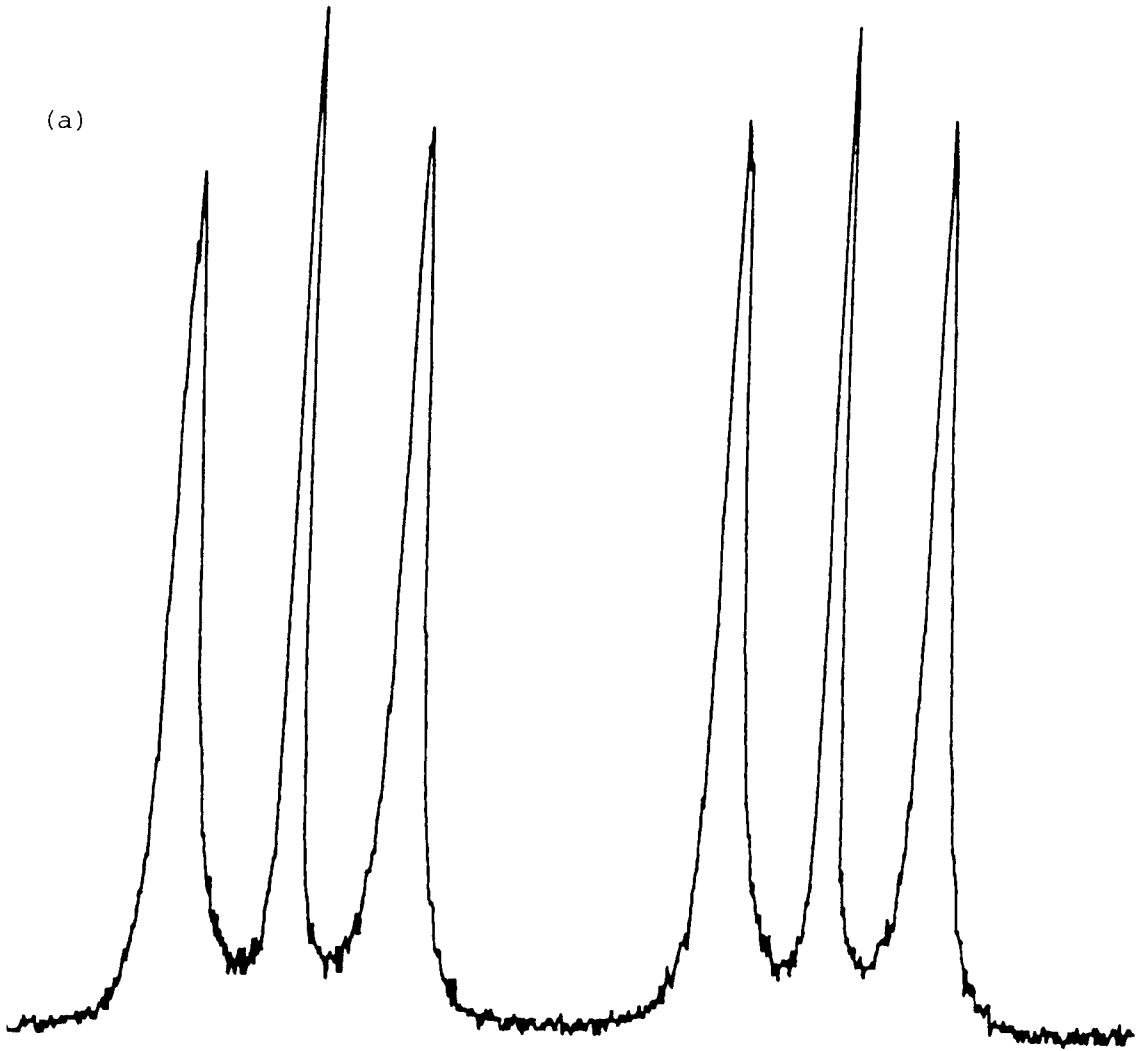
To allow for the possibility of a maximum or minimum at the first turning point, the second derivative at the first data point was examined; a negative value implied a maximum and a positive value a minimum.

Fig A1.2.1 Polarised Rayleigh-Brillouin Spectrum of n-octane

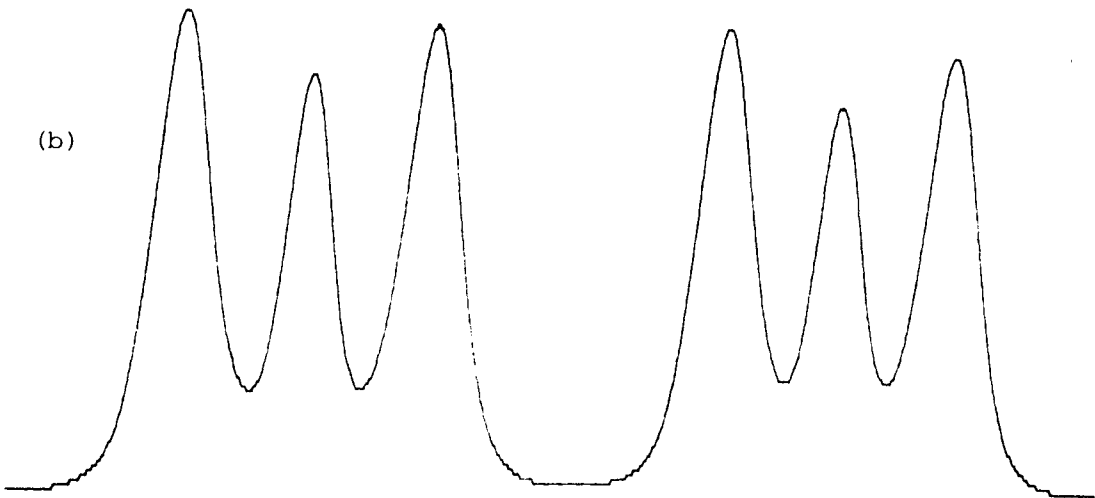
(a) Original (unsmoothed) data

(b) Data smoothed 250 times

(a)



(b)



Once the peak positions had been located the positions of the three Rayleigh peaks were used to linearise the data as discussed in the next section. This manipulation of the data is undertaken only to find the peak positions and hence to linearise the data points. Once this has been accomplished the original unmanipulated data is used in the fitting routine.

### A1.3 Linearisation of the Data Points

The variation of displacement with voltage of the piezoelectric stacks is non-linear. This results in a non-linear scan, the degree of non-linearity depending upon the initial and applied voltages. The result of this non-linearity is that successive Fabry-Perot orders become closer together.

In order to ascertain the most relevant linearisation function the following procedure was adopted. Using the voltage control on the ramp generator it was possible to observe up to six orders in one scan. A colloid was used to produce narrow sharp peaks and the separations of these peaks were determined as the number of points (channels) between them. Each of these peaks was separated by one FSR and hence six data points were available, giving frequency against points (ie voltage). These data were then fitted to the following polynomials

$$\begin{aligned} \text{(i)} \quad Y &= A + BX + CX^2 \\ \text{(ii)} \quad Y &= A + BX^2 \\ \text{(iii)} \quad Y &= A + BX^C \end{aligned} \tag{A1.3.1}$$

The choice of the above functions was governed by two considerations, (i) the variation of the piezoelectric stacks with voltage was

known to vary approximately quadratically<sup>[127]</sup>, and (ii) three orders contained in 1024 points is the optimum number for good resolution of any fine structure within the individual orders. This limited the number of parameters that could be determined from an individual spectrum to three.

Function (i) was found, using the statistical analysis discussed in Section 3.3.2, to give the best fit. It was therefore possible to linearise any experimental spectrum by taking the separations of the Rayleigh peaks as one FSR and performing a least-squares quadratic fit to the 1024 data points.

The initial estimates of the fitting parameters were then found from the linearised data and used in the minimisation routine. The fitting routine returned the final values of the fitted parameters and the chi-square value (Section 3.3.2). The instrumental function was deconvoluted from the fitted variables to obtain the actual spectral widths (Section A1.5). Errors on the fitted parameters were calculated by inverting the curvature matrix using NAG routine FO1ABF.

#### A1.4 Construction of the Fitting Functions

Several different fitting functions were employed in the course of this work to compare the experimental data with theoretical models.

In this section detailed descriptions are given of the fitting functions used to fit data from polarised and depolarised Rayleigh-Brillouin spectra.

##### A1.4.1 Fitting Function for the Polarised Rayleigh-Brillouin Spectra

In Chapter 2 the polarised spectrum from simple liquids was discussed. The unshifted Rayleigh peak and the two symmetrically displaced

Brillouin peaks are described by Lorentzian line shapes. The fitting function is then given by:

$$\begin{aligned}
 Y_i = & A1/((X_i - A2)^2 + (A3/2)^2) \\
 & + A4/((X_i - A2 + A5)^2 + (A6/2)^2) \\
 & + A4/((X_i - A2 - A5)^2 + (A6/2)^2) \\
 & + A1/((X_i - A2 + A8)^2 + (A3/2)^2) \\
 & + A4/((X_i - A2 + A5 + A8)^2 + (A6/2)^2) \\
 & + A4/((X_i - A2 - A5 + A8)^2 + (A6/2)^2) \\
 & + 3 \text{ overlapping orders} \\
 & + A7
 \end{aligned}
 \tag{A1.4.1}$$

where

- A1 = Rayleigh line peak height
- A2 = Starting position for evaluation of  $Y_i$
- A3 = Rayleigh full width at half peak height
- A4 = Brillouin line peak height
- A5 = Brillouin shift
- A6 = Brillouin full width at half peak height
- A7 = Base
- A8 = Free Spectral Range (FSR)

Thus the fitting function allows for overlap from five Fabry-Perot orders. This increases the accuracy with which the Brillouin line-width and shift can be determined.

In addition, for viscoelastic liquids there is the possibility of a Mountain line in the spectrum. The exact shape of the Mountain line is discussed in Section 2.2. However, under the experimental conditions in which the liquids were investigated, the Mountain line can

be described by a Lorentzian lineshape centred on the Rayleigh line.

Adding this additional component into the fitting function increases the number of fitting parameters from eight to ten. A ten parameter fit has several problems. Firstly, the initial estimates need to be relatively close, within a few standard deviation of the actual values, otherwise it is highly likely that a false minimum will be found by the minimisation routine. Secondly, there will be larger errors on the fitted parameters and an increase in the computational time involved. These problems were overcome by replacing the ten parameter fit by two consecutive eight parameter fits.

Initially the data were fitted using equation (A1.4.1) with the initial estimates calculated as described in A1.2. Two of the fitted variables returned, A2 (starting position) and A8 (FSR), are functions only of the particular scan and not the type of spectrum; additional unshifted peaks do not distort the positions of other unshifted peaks although they will distort the linewidths. In addition, the Mountain line will distort both the position and linewidth of the shifted Brillouin peaks.

For the second fit A2 and A8 are held constant and two new variables introduced to describe the Mountain line. The returned values of the fitting parameters for the first fit are used as initial estimates in the second fit. For the Mountain line, the initial value for the linewidth was taken as half the FSR and the peak height as  $0.25 \times$  Rayleigh peak height.

The fitting function now becomes

$$\begin{aligned}
Y_i = & A1/((X_i - C1)^2 + (A3/2)^2) \\
& + A4/((X_i - C1 + A5)^2 + (A6/2)^2) \\
& + A4/((X_i - C1 - A5)^2 + (A6/2)^2) \\
& + A1/((X_i - C1 + C2)^2 + (A3/2)^2) \\
& + A4/((X_i - C1 + A5 + C2)^2 + (A6/2)^2) \\
& + A4/((X_i - C1 - A5 + C2)^2 + (A6/2)^2) \\
& + A2/((X_i - C1)^2 + (A8/2)^2) \\
& + A7 \\
& + 3 \text{ overlapping orders}
\end{aligned} \tag{A1.4.2}$$

where

A2 = Mountain line peak height

A8 = Mountain line full width at half peak height

C1 and C2 are constants from the first fit.

All the other parameters are as given previously. This 'two-fit' approach was found to work faster and with more accuracy than a single ten parameter fit when tested with generated data.

#### A1.4.2 Fitting Function for Depolarised Rayleigh-Brillouin Spectra

In Chapter 2 the theoretical lineshapes of the depolarised spectrum from molecular liquids was discussed. In the limit  $\beta (= q^2 \eta_s / \Gamma) \ll 1$  the low frequency spectrum for many liquids was shown to be described by a single Lorentzian curve.

In this case the fitting function has the form

$$\begin{aligned}
Y_i = & A1/((X_i - A2)^2 + (A3/2)^2) \\
& + A1/((X_i - A2 + A4)^2 + (A3/2)^2) \\
& + A1/((X_i - A2 - A4)^2 + (A3/2)^2) \\
& + 12 \text{ overlapping orders} \\
& + A5
\end{aligned} \tag{A1.4.3}$$

where

A1 = Rayleigh line peak height

A2 = Starting position for evaluation of  $Y_i$

A3 = Rayleigh full width at half peak height

A4 = FSR

A5 = Base

The linewidths in the depolarised spectrum are much broader than those in the polarised spectrum, therefore overlap from many adjacent orders can have a significant effect on the measured linewidths. To allow for this, overlap from 15 adjacent orders was incorporated into the fitting function. A flat base was used since multiple overlapping of the broad collisional induced component appeared as a flat background at the majority of the free spectral ranges used. However, it is possible that for the large free spectral ranges used to study the small branched alkanes the interaction induced contribution to the spectrum can be resolved. This possibility was allowed for by incorporating an exponential base into the fitting function. The fitting function then becomes

$$\begin{aligned} Y_i = & A5 \exp - \left| (X_i - A2) * A6 \right| \\ & + A5 \exp - \left| (X_i - A2 + A4) * A6 \right| \\ & + A5 \exp - \left| (X_i - A2 - A4) * A6 \right| \\ & + 12 \text{ overlapping orders} \\ & + \text{equation (A1.4.3)} \end{aligned} \tag{A1.4.4}$$

where

A5 = Amplitude of the exponential peak

A6 = Width of the exponential peak

All the other terms are as described previously.

The depolarised spectra of many of the branched alkanes investigated in this thesis were found to give significantly improved fits when the objective function was described by two Lorentzians centred on the incident laser frequency. (Section 2.3.1 contains a theoretical discussion of this effect and the experimental development is discussed in Chapter 5.)

The method of incorporating this effect into a fitting function is similar to that of a Mountain line (Section A1.4.1). Initially a fit is performed using equation (A1.4.3). The two parameters A2 and A4 are then held constant for the second fit and two new variables introduced to describe the width and height of the second Lorentzian. The fitting function then has the form

$$\begin{aligned}
 Y_i = & A1/((X_i - C1)^2 + (A3/2)^2) \\
 & + A2/((X_i - C1)^2 + (A4/2)^2) \\
 & + A1/((X_i - C1 + C2)^2 + (A3/2)^2) \\
 & + A2/((X_i - C1 + C2)^2 + (A4/2)^2) \\
 & + 13 \text{ overlapping orders} \\
 & + A5
 \end{aligned}
 \tag{A1.4.5}$$

where

A1 = First Lorentzian peak height

A2 = Second Lorentzian peak height

A3 = First Lorentzian full width at half peak height

A4 = Second Lorentzian full width at half peak height

C1 and C2 are constants from the first fit

A5 = Base

The base can be either flat or represented by an exponential function as in equation (A1.4.4).

For each fitting function examined the first partial derivatives with respect to each fitting parameter were evaluated. For example, from equation (A1.4.1)

$$\frac{\partial Y}{\partial (A1)} = ((X - A2)^2 + (A3/2)^2)^{-1} + ((X - A1 + A8)^2 + (A3/2)^2)^{-1} + \dots \text{ each term in A1}$$

Each objective function and set of partial derivatives was tested by fitting to a spectrum that had been generated from the appropriate objective function. In every case the analysis program returned the values used to generate the spectrum.

### A1.5 Deconvolution of Instrumental Broadening

Linewidth broadening of the power spectrum relative to the theoretical distribution occurs due to effects of Fabry-Perot resolution, finite frequency distribution and finite scattering solid angle<sup>[28]</sup>. The observed spectral profiles must therefore be corrected for instrumental effects.

Mathematically the observed spectrum  $f(\omega)$  consists of the true spectrum  $f'(\omega')$  convolved with an instrumental function  $f''(\omega - \omega')$  which are related by the integral equation

$$f(\omega) = \int_{-\infty}^{\infty} f'(\omega') f''(\omega - \omega') d\omega' \quad (\text{A1.5.1})$$

Numerical methods for solving this integral equation are very laborious<sup>[128]</sup> and in practice  $f'(\omega')$  can only be found if the profiles are known analytically.

By applying the convolution theorem<sup>[129]</sup> to equation (A1.5.1) the integral can be solved by computing the product of the Fourier transforms of the constituent functions. Denoting the Fourier transforms of the spectral distributions  $f(\omega)$ ,  $f'(\omega')$  and  $f''(\omega - \omega')$  by their corresponding capital letters, the observed distribution in the inverse (time) domain becomes

$$F(t) = F'(t) \cdot F''(t) \quad (\text{A1.5.2})$$

The true spectrum  $f'(\omega')$  can be described by analytical functions (Chapter 2) and it is therefore the form of the instrumental function that has to be determined.

The generally accepted form of the Fabry-Perot instrumental function is a Voigt function<sup>[130]</sup>. A Voigt function refers to a family of distribution the exact type depending upon one parameter,  $a$ <sup>[128]</sup>. They include Gaussian ( $a = 0$ ) and Lorentzian ( $a = \infty$ ) functions as special cases.

In general, the Voigt function will have the form

$$h(\omega) = C \int_{-\infty}^{\infty} \left[ \frac{\beta_1}{\beta_1^2 + (\omega' - \omega_0)^2} \right] \cdot \left[ \frac{1}{\beta_2} \exp \left( -\left( \frac{\omega - \omega'}{\beta_2} \right)^2 \right) \right] d\omega' \quad (\text{A1.5.3})$$

where  $\beta_1 = \Gamma/2$ ,  $\Gamma$  being the full width at half maximum height of the Lorentzian peak.  $\beta_2^2 = 2\sigma^2$ ,  $\sigma^2$  being the variance of the Gaussian function and  $C$  is a constant.

The exact shape of the resulting function depends on the values of the Voigt parameters  $\beta_1$  and  $\beta_2$ .

These parameters were determined for the light scattering system by Fourier transforming the instrumental data, obtained using a colloid as an elastic scatterer, using the NAG routine C06FCF and thereby converting convolution into simple multiplication of the transformed functions. The resulting data was fitted to a function of the form

$$H(t) = A \exp(-\beta_2^2 t^2 / 4 - \beta_1 t) \quad (\text{A1.5.4})$$

where A is an amplitude factor.

The parameter 'a' which determines the exact form of the Voigt function,  $h(\omega)$ , is defined by

$$a = \beta_1 / \beta_2 \quad (\text{A1.5.5})$$

where  $\beta_1$  and  $\beta_2$  are referred to as the Voigt parameters of the function with parameter 'a'.

Typical values of 'a' were found to be of the order  $10^5$ , implying that the frequency domain instrumental function was predominantly Lorentzian.

The same data were also fitted to a Gaussian and Lorentzian profile. The statistical analysis of the fit (Section 3.4.7) indicated that the Lorentzian was the most appropriate form for the Fabry-Perot instrumental function, in agreement with the value of the Voigt parameter 'a'.

In Chapter 2 the lineshapes of the polarised and depolarised spectra were shown to approximate very closely to Lorentzian profiles. Hence, both  $f'(\omega')$  and  $f''(\omega - \omega')$  in equation (A1.5.1) are described by Lorentzian distributions. These functions have the property that  $f(\omega)$  is also described by a function of this type.

The parameters  $\beta_1$  are connected by the relation<sup>[128]</sup>

$$\beta_1 = \beta_1' + \beta_1'' \quad (\text{A1.5.6})$$

Therefore the linewidth ( $\beta_1'$ ) of the true spectrum  $f'(\omega')$  is simply the subtraction of the instrumental linewidth ( $\beta_1''$ ) from the observed linewidth ( $\beta_1$ ).

## APPENDIX 2 - STATISTICAL TESTS

### Contents

- A2.1        The Chi-Square Test
  
- A2.2        The One-Sample Runs Test
  
- A2.3        The Linear Correlation Test

## APPENDIX 2 - STATISTICAL TESTS

### A2.1 The Chi-Square ( $\chi^2$ ) Test

The chi-square test<sup>[126]</sup> can be used to test the validity of the object function (eg Lorentzian or Gaussian) as representative of the experimental data.

$\chi^2$  is defined as

$$\chi^2 = \sum_{i=1}^N \frac{(Y_i - F_i)^2}{\sigma_i^2} \quad (\text{A2.1.1})$$

where  $\sigma_i^2$  are the variances on the experimental points  $Y_i$ , and  $F_i$  are the theoretical values. The reduced chi-square is defined as  $\chi^2/n$  where  $n$  is the number of degrees of freedom, that is, the number of data points ( $N$ ) minus the number of parameters of the distribution determined from the  $N$  data points. For example, for an eight parameter fit to 1024 data points,  $n = 1016$ .

Although the  $\chi^2$  test is a reliable indicator of goodness-of-fit it is not as meaningful statistically as the Cumulative Distribution Function or Integral chi-square probability for a  $\chi^2$  distribution.

#### $\chi^2$ Distribution

The probability density function (or frequency function) for  $\chi^2$  with  $n$  degrees of freedom is given by<sup>[13]</sup>

$$f_n(\chi^2) = \frac{(\chi^2)^{(n-2)/2} \cdot \exp(-\chi^2/2)}{2^{n/2} \Gamma(n/2)} \quad (\text{A2.1.2})$$

valid for  $0 \leq \chi^2 < \infty$

where  $\Gamma(n/2)$  is the gamma function.

Physically, the important statistic is the probability of obtaining a particular value of  $\chi^2$  for a given number of degrees of freedom assuming normal statistics hold.

$$\begin{aligned}
 P(\chi^2 | n) &= \int_0^{\chi_n^2} f_n(\chi^2) d\chi^2 \\
 &= (2^{n/2} \Gamma(n/2))^{-1} \cdot \int_0^{\chi_n^2} (\chi^2)^{(n-2)/2} \exp(-\chi^2/2) d\chi^2 \quad (\text{A2.1.3})
 \end{aligned}$$

and gives the probability of obtaining a  $\chi^2$  less than or equal to the  $\chi^2$  obtained ( $\chi_n^2$ ), that is,  $P(\chi^2 | n) = \text{Pr}[\chi^2 \leq \chi_n^2]$ .

The complementary probability  $Q(\chi^2 | n)$  is simply

$$Q(\chi^2 | n) = 1 - P(\chi^2 | n) \quad (\text{A2.1.4})$$

and gives the probability of obtaining a  $\chi^2$  value greater than or equal to  $\chi_n^2$ . (See Fig A2.1.1)

The procedure used to calculate  $P(\chi^2 | n)$  was complicated because of the large  $\chi^2$  and  $n$  used;  $\chi^2 \approx 1016$  and  $n \approx 1016$ .

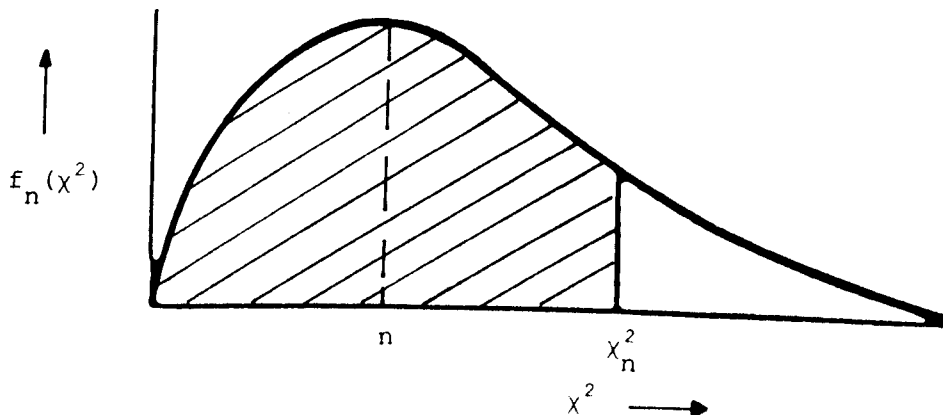


Fig A2.1.1 - Frequency function for  $\chi^2$  distribution centred on the number of degrees of freedom ( $n$ ). The shaded area is  $P(\chi^2 | n)$ .

There are several types of functions that can be used to calculate  $P(\chi^2 | n)$ . Examples are given below<sup>[131]</sup>.

(1) Series Expansions

$$(a) P(\chi^2 | n) = \left(\Gamma\left(\frac{n}{2}\right)\right)^{-1} \cdot \sum_{j=0}^{\infty} \frac{(-1)^j (\chi^2/2)^{n/2+j}}{j! \left(\frac{n}{2} + j\right)} \quad (A2.1.5)$$

$$(b) Q(\chi^2 | n) = \frac{(\chi^2/2)^{n/2}}{\Gamma\left(\frac{n+2}{2}\right)} \exp(-\chi^2/2) \cdot \left[ 1 + \sum_{j=1}^{\infty} \frac{(\chi^2)^j}{(n+2)(n+4)\dots(n+2j)} \right] \quad (A2.1.6)$$

(2) Asymptotic Expansion for Large  $\chi^2$

$$Q(\chi^2 | n) \sim \frac{(\chi^2)^{n/2 - 1}}{2^{n/2} \Gamma(n/2)} \cdot \exp(-\chi^2/2) \cdot \sum_{j=0}^{\infty} (-1)^j \frac{\Gamma(1 - n/2 + j) 2^{j+1}}{\Gamma(1 - n/2) (\chi^2)^j} \quad (A2.1.7)$$

(3) Asymptotic Distribution for Large  $n$

$$P(\chi^2 | n) \sim P(x)$$

$$\text{where } x = \frac{\chi^2 - n}{(2n)^{1/2}} \text{ and } P(x) = \frac{1}{(2\pi)^{1/2}} \int_{-\infty}^x \exp(-t^2/2) dt \quad (A2.1.8)$$

$P(x)$  is the Normal (Gaussian) probability function with zero mean and unit variance.

Computational problems were encountered when  $P(\chi^2 | n)$  was evaluated using either equation (1) or (2). The problem was an overflow due to the very large numbers evaluated by  $\Gamma(n/2)$  and/or  $(\chi^2)^{n/2}$  and consequent non-evaluation of  $P(\chi^2 | n)$ .

The problem was overcome by casting equation (3) (Asymptotic approximation) in the form of the error function erf(x) for which approximations exist for the ranges  $x \leq 2$  and  $x \geq 2.5$ .

$$\text{erf}(x) = \frac{2}{(\pi)^{\frac{1}{2}}} \int_0^x \exp(-t^2) dt \quad (\text{A2.1.9})$$

The error function is directly related to  $P(x)$  using the substitution  $t = \frac{x}{(2)^{\frac{1}{2}}}$ .  $P(\chi^2 | n)$  is then given by

$$P(\chi^2 | n) \sim \left(\frac{2}{\pi}\right)^{\frac{1}{2}} \int_0^{(2)^{\frac{1}{2}} \cdot t} \exp(-x^2/2) dx \quad (\text{A2.1.10})$$

$P(\chi^2 | n)$  is then evaluated using the expansion<sup>[132]</sup> appropriate to the required ranges.

For  $x \leq 2$

$$P(\chi^2 | n) = \left(\frac{2}{\pi}\right)^{\frac{1}{2}} \left[ x - \frac{x^3}{3} + \frac{x^5}{5 \cdot 2!} - \dots \right] \quad (\text{A2.1.11})$$

For large  $x$ ,  $x > 2$ , erf(x) has the same value as for erf( $\infty$ ). An asymptotic series is then used to evaluate  $P(\chi^2 | n)$ .

$$P(\chi^2 | n) \sim 1 - \frac{\exp(-x^2/2)}{x(\pi)^{\frac{1}{2}}} \left[ 1 - \frac{1}{2x^2} + \frac{1 \cdot 3}{(2x^2)^2} - \frac{1 \cdot 3 \cdot 5}{(2x^2)^3} + \dots \right]$$

(A2.1.12)

The subtraction of the series from unity results from the series evaluating erf(x) from  $x$  to  $\infty$ . It should be noted that equation (A2.1.12) is a divergent series. This is accommodated for in the computer program by truncating the series when the term in brackets is sufficiently small not to significantly affect the value of  $P(\chi^2 | n)$ .



For example in Fig A2.2.1 the number of positive residuals (pluses) is  $n_1 = 8$ , and the number of negative residuals (minuses) is  $n_2 = 6$ . The total number of runs is  $n_r = 7$ .

The total number of runs in a sample of any given size gives an indication of whether or not the sample is random. If very few runs occur, a time trend or some bunching due to lack of independence is suggested. If too many runs occur, systematic short-period cyclical fluctuations could be influencing the data.

For large  $n_1$  and/or  $n_2$  a good approximation<sup>[132]</sup> to the sampling distribution of  $n_r$  is the normal distribution with

$$\text{mean} = \mu_r = \frac{2n_1n_2}{n_1 + n_2} + 1 \quad (\text{A2.2.2})$$

and Standard Deviation

$$\sigma_r = \left[ \frac{2n_1n_2(2n_1n_2 - n_1 - n_2)}{(n_1 + n_2)^2(n_1 + n_2 - 1)} \right] \quad (\text{A2.2.3})$$

The standardised normal variable is then given by

$$x = \frac{n_r - \mu_r}{\sigma_r} \quad (\text{A2.2.4})$$

The probability is then calculated using the normal probability distribution function.

$$P(x) = \frac{1}{(2\pi)^{\frac{1}{2}}} \int_{-\infty}^x \exp(-t^2/2) dt \quad (\text{A2.2.5})$$

In fact the computer program calculates  $Q(x) = 1 - P(x)$  using the

following asymptotic approximation<sup>[131]</sup>

$$Q(x) \sim \frac{\exp(-x^2/2)}{(2\pi)^{1/2} \cdot x} \left\{ 1 - \frac{1}{x^2} + \frac{1.3}{x^4} + \dots \right. \\ \left. + \frac{(-1)^n 1.3 \dots (2n-1)}{x^{2n}} \right\} + R_n \quad (\text{A2.2.6})$$

where  $R_n$  is a remainder and is less in absolute value than the first neglected term.

This is a two-tailed distribution and calculates the probability of obtaining  $n_r$ , greater than or equal to  $\mu_r + n_r$  and less than or equal to  $\mu_r - n_r$ .

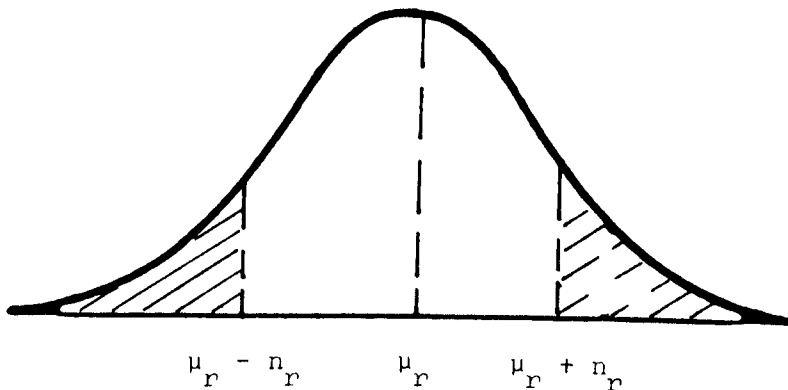


Fig A2.2.2 Frequency function for a normal distribution centred on  $\mu_r$ .

The shaded area is  $Q(x)$ .

For example, with our data  $\mu_r = 512$ ,  $\sigma_r \cong 16$  and  $Q(x)$  should then be very close to 1.0 ie the probability of obtaining either above or below  $n_r$  should be equal.

### A2.3 The Linear Correlation Test

The Correlation Test indicates whether or not there exists a relationship between the variables  $x$  and  $y$ , that is, whether or not the variations in the observed values of one quantity  $y$  are correlated with the variations in the observed values of the other quantity  $x$ .

A linear-correlation coefficient can be defined<sup>[126]</sup>

$$r = \frac{N\sum x_i y_i - \sum x_i \sum y_i}{\left[ N\sum x_i^2 - (\sum x_i)^2 \right]^{\frac{1}{2}} \cdot \left[ N\sum y_i^2 - (\sum y_i)^2 \right]^{\frac{1}{2}}} \quad (\text{A2.3.1})$$

If there is no correlation  $r = 0$ , and if there is complete correlation  $|r| = 1$ .

Clearly, because of random fluctuations  $r \neq 0$ , even if there is no real connection between  $x$  and  $y$ , and conversely, if a linear relationship exists  $r$  will not be exactly equal to one. Hence, the correlation coefficient cannot be used directly to indicate the degree of correlation.

A common test of  $r$  is to compare its value with the probability distribution for a parent population which is completely uncorrelated. Such a comparison will test the hypothesis that the data points could represent a sample derived from uncorrelated parent populations. The frequency function for a random sample of uncorrelated experimental data points which would yield an experimental linear-correlation coefficient equal to  $r$  is given by<sup>[134]</sup>

$$f_n(r) = \frac{1}{(\pi)^{\frac{1}{2}}} \frac{\Gamma[(n+1)/2]}{\Gamma(n/2)} (1-r^2)^{(n-2)/2} \quad (\text{A2.3.2})$$

where  $n = N - 2$  is the number of degrees of freedom for  $N$  data points.

The integral probability  $P(r|n)$  is the probability that a random sample of  $N$  uncorrelated experimental data points would yield an experimental linear-correlation coefficient as large as or larger than the observed value of  $|r|$ .

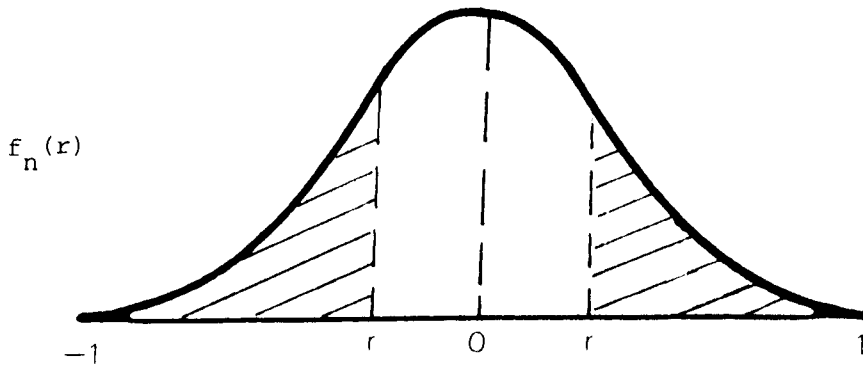


Fig A2.3.1 Frequency function  $f_n(r)$ . The shaded area is  $P(r|n)$ .

$$P(r|n) = 2 \int_{|r|}^1 f_n(r) \, dp \quad (\text{A2.3.3})$$

With this definition,  $P(r|n)$  indicates the probability that the observed data could have come from an uncorrelated ( $r = 0$ ) parent populations.

$P(r|n)$  can be evaluated by expanding the integral. For even values of  $n$  the exponent is an integer and the binomial expansion can be used to expand the argument of the integral.

$$P(r|n) = 1 - \frac{2}{(\pi)^{\frac{1}{2}}} \frac{\Gamma[(n+1)/2]}{\Gamma(n/2)} \sum_{i=0}^I \left[ \frac{(-1)^i}{(I-i)!} \frac{|r|^{2i+1}}{2i+1} \right] \quad (\text{A2.3.4})$$

For odd values of n,

$$P(r|n) = 1 - \frac{1}{(\pi)^{\frac{1}{2}}} \left[ \sin^{-1}(|r|) + |r| \sum_{i=\frac{1}{2}}^{\frac{1}{2}} \left[ (1 - r^2)^i \frac{(2i - 1)!!}{2i!!} \right] \right]$$

where  $x!! = x(x - 2)(x - 4) \dots (3)(1)$  for  $x$  odd

(4)(2) for  $x$  even.

A probability of 1.0 is returned if the two variables are uncorrelated and 0.0 if there is complete correlation.

## Evidence for a Thermotropic Phase Transition in Oleic Acid

John V. Champion\*, James F. Crilly and Ralph P. Tatam

Physics Department, City of London Polytechnic, 31 Jewry Street, London EC3N 2EY

Oleic acid has been investigated by Rayleigh-Brillouin spectroscopy. The temperature gradient of the hypersonic frequency shift and elastic stiffness constant show anomalous behaviour in the range 14–18 °C. This suggests that oleic acid undergoes a change of phase to form a locally nematic structure *ca.* 5 °C above the melting point. Complementary measurements of viscosity, density and refractive index support this interpretation.

Recent Brillouin spectroscopy experiments have provided considerable evidence for the existence of a phase transformation in the melts of various *n*-alkanes.<sup>1,2</sup> It is believed that the transition involves the formation of a mesomorphic structure in the melt, occurring at a particular temperature. This temperature is above the melting point and depends on the molecular weight of the alkane homologue. As this transition is characterized by a change in the hypersonic attenuation properties it has become known as the  $T_{ii}$  phenomenon. The results of Brillouin scattering measurements have been corroborated by a variety of experimental techniques including densitometry, viscometry and ultrasonic attenuation measurements. In spite of much experimental evidence the existence of the phenomenon in the higher *n*-alkanes continues to be the subject of controversy.<sup>3</sup>

Previous authors have associated the  $T_{ii}$  phenomenon with the isotropic–nematic transition of low molecular weight liquid crystals.<sup>1,4</sup> Unfortunately, Brillouin scattering measurements on liquid crystals close to the transition temperature have been inconclusive.<sup>1</sup> It is pertinent therefore to investigate substances other than the *n*-alkanes which are known to have definite liquid crystalline properties at accessible temperatures.

Whilst the work of Kruger *et al.*<sup>1,2</sup> concentrates on the *n*-alkane melts, many substances, such as lipids or fatty acids, comprise hydrocarbon chains in their molecular structure. It is known that some of these do not undergo a direct thermal transition from an isotropic liquid phase to the gel or crystalline state. An intermediate or mesomorphic state exists below a well defined characteristic transition temperature. The lipids of some biomembranes show this thermotropic behaviour. The nature of lipid transitions has been the object of intensive research over the past 20 years.<sup>5</sup> Extensive theoretical and experimental research has shown that the transition has its origin in the conformational changes in the lipid alkyl chain.<sup>6–8</sup> In membranes the effect is cooperative and consequently influences the intramolecular forces leading to a change in the macroscopic properties of the system.<sup>9</sup> The idea of mesophases resulting from changes in the configuration of the saturated hydrocarbon chains of lipids is clearly relevant to the thermotropic behaviour of *n*-alkanes.<sup>6,9</sup>

Oleic (*cis*-9-octadecenoic) acid is an important structural component of certain biopolymers, *e.g.* sphingomyelin. It occurs in most natural fats in the form of the glyceride and it is believed that lipids with oleyl chains are preferentially synthesised in biomembranes to maintain fluidity below physiological temperatures. At room temperature oleic acid is an oily liquid and freezes to a white opaque wax at *ca.* 13 °C. There is some evidence for the existence of a thermotropic mesophase in the melt of oleic acid: prior to freezing, colourless needles form in the melt which become visually evident below *ca.* 14 °C. The appearance of such structures suggests that oleic acid in the higher

temperature liquid state has some degree of short-range order which increases as the temperature is reduced towards the melting point. Above a certain intermediate temperature the melt may be considered an isotropic liquid. The range in the published values of its melting point suggests that oleic acid freezes continuously over the range 13.6–16.4 °C.<sup>10, 11</sup> This gives tentative support to the idea of an intermediate phase between the isotropic liquid and solid.

Light scattering<sup>12, 13</sup> and other measurements<sup>14, 15</sup> on membranes composed of the monoglyceride ester of oleic acid (glycerol monooleate) have provided evidence of a thermotropic structural transformation within the range 15–18 °C. There is clearly some overlap between this temperature range and that of the freezing range of oleic acid. The structural similarity, *i.e.* the oleyl chain between these substances implies a concomitance possible in their thermotropic behaviour.

This work is primarily concerned with following the thermotropic behaviour of oleic acid and the techniques used are suited to measuring changes in, rather than absolute values of the physical properties of the solution studied. Results of Brillouin scattering experiments on oleic acid solutions complemented by measurements of density, viscosity and refractive index are presented and detailed description is given of the rigorous statistical tests which were applied to all the data.

## Experimental

### Materials and Methods

In its low-temperature state oleic acid is a white, opaque wax having a melting transition at *ca.* 13.0 °C. To separate the structural transition from the melting transition a small quantity of a non-perturbing (inert) solvent was added to the oleic acid to depress the freezing point and assist in the elucidation of the transitions. All the light-scattering data were collected above the freezing point.

The addition of CCl<sub>4</sub> depressed the melting transition to *ca.* 9.0 °C; separating the freezing point from the temperature of the mesomorphic phase transition by some 7 °C. However, the solution properties are still dominated by the oleic acid. In the light-scattering experiments the refractive indices of the components matched to better than 0.3%, and were not complicated by concentration fluctuations. In the viscometric measurements, the temperature coefficient of viscosity for CCl<sub>4</sub> is 0.011 cP K<sup>-1</sup> *c.f.*, 0.89 cP K<sup>-1</sup> for oleic acid and the solution measurements paralleled those of oleic acid.

Sample preparation was carried out in a clean-air cabinet to minimise dust contamination. CCl<sub>4</sub> (spectroscopic grade) was added to oleic acid (>92% purity by assay) to obtain a 10% solution by volume. Both chemicals were obtained from B.D.H. Chemicals Ltd. The solution was then filtered, using a Millipore filtration unit with a 0.22 μm filter, into a fused-quartz light-scattering cell. This stoppered rectangular cell had a light path of 1.0 cm and was supplied by Helma GmbH and Co.

### Brillouin Scattering

A schematic diagram of the light scattering system is shown in fig. 1. A Spectra-Physics model 165 argon-ion laser operating in a single longitudinal mode at 488.0 nm was used as a source. The scattered light was monitored at 90° by a piezo-electrically scanned Fabry-Perot interferometer. The free spectral range was adjusted to *ca.* 15.0 GHz and the finesse of the system was always greater than 40.

The interference pattern produced by the interferometer was focused onto an EMI 9789B photomultiplier tube using a lens of 1.33 m focal length. The photomultiplier tube output was fed directly into a photon counting system and subsequently to a 1024 channel data store. The data were then transferred to a microcomputer and stored on floppy disc for subsequent processing on the mainframe computer.

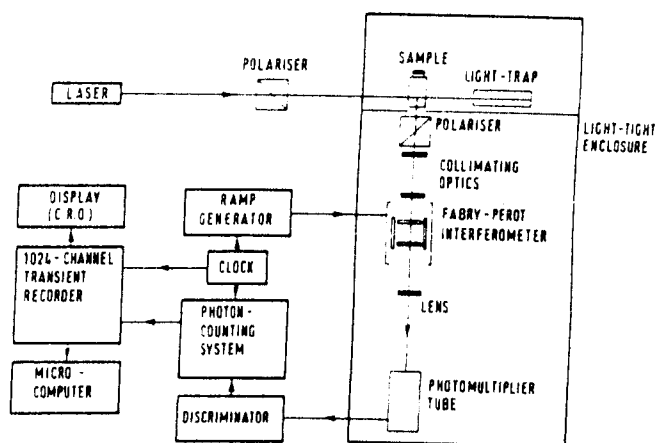


Fig. 1. Schematic diagram of the light-scattering spectrometer.

The sample cell was held in a thermostatically controlled brass block. Cooling was provided by circulating water from a large thermostatted water bath through a base mounted on the brass heating block. The brass block was protected from pump vibrations by a hydraulic damper in the pump line and by several metres of silicone rubber tubing. The water bath was held at a constant temperature of *ca.* 5 °C, and the fine temperature control was provided by heating coils inside the brass block. The complete cell holder, base and block, were enclosed in an insulated box to avoid condensation forming on the cell walls. The sample temperature was monitored with a digital thermometer and was stable to within 0.1 °C over the temperature range studied.

### Kinematic Viscosity, Density and Refractive Index

The kinematic viscosity was measured using a Ubbelohde viscometer immersed in a water bath thermostatically controlled to 0.1 °C. The viscosity of the solution can be described by the Arrhenius–Frenkel–Eyring (AFE) eqn<sup>16</sup>

$$\eta = \left[ \frac{hN}{V} \exp(-\Delta S^*/R) \right] \exp(\Delta H^*/RT) \quad (1)$$

where  $h$  is Planck's constant,  $N$  is the Avogadro number,  $V$  is the molar volume,  $\Delta S^*$  and  $\Delta H^*$  are, respectively, the entropy and enthalpy of activation of the process of viscous flow,  $R$  is the gas constant and  $T$  is the absolute temperature.

The corresponding kinematic viscosity is given by

$$\eta^* = \eta/\rho = [(h/m) \exp(-\Delta S^*/R)] \exp(\Delta H^*/RT) \quad (2)$$

where  $m$  is the molar mass and  $\rho$  the density.

In the viscosity measurements the maximum velocity occurring in the isotropic solution was of the order of 200 s<sup>-1</sup>. This decreased with the increasing viscosity as the transition was approached, and hence the occurrence of non-Newtonian behaviour is unlikely to be detectable in this system.

Density measurements over the temperature range 10–40 °C were made using a Paar DMA40 density meter and refractive indices were measured using a Bellingham and Stanley Abbe refractometer. Both systems were thermostatically controlled to within 0.1 °C.

## Results

### Density, Viscosity, Refractive Index

Fig. 2(a) shows the results of density measurements. The individual data points were measured with an accuracy of  $10^{-4}$  g cm $^{-3}$ . It is apparent that the dependence of density on temperature is nearly linear, except for a distinct change in gradient between 17 and 14 °C.

The corresponding kinematic viscosity measurements are shown in fig. 2(b). The results are presented in the form of an Arrhenius plot. There is a well defined discontinuous change in slope which occurs at a temperature of *ca.* 18.5 °C. According to eqn (1) the change in slope is indicative of an increase in the activation energy associated with viscous flow between the high and low temperature ranges. The decrease in the corresponding intercept implies an overall increase in the entropy. A further quantitative analysis of these results is presented in a later section.

The refractive index measurements are shown in fig. 2(c). The accuracy was estimated to be  $5 \times 10^{-4}$ . Clearly, a point of inflexion occurs at a temperature similar to that found for the change in slope of both the density and viscosity.

### Brillouin Scattering

Brillouin scattering occurs as the result of photon-phonon interactions; thermally induced density fluctuations give rise to propagating longitudinal modes (phonons) from which inelastic light scattering occurs. The Brillouin doublet, shifted in frequency by  $\nu_B$  and disposed symmetrically about the Rayleigh line, is due to the inelastic scattering from the longitudinal phonons. The scattering from the heavily damped transverse phonons is normally not observed. Entropy, or heat fluctuations, give rise to the elastically scattered Rayleigh component.<sup>17</sup>

The velocity of the longitudinal phonons,  $V_s$ , is proportional to the frequency shift ( $\nu_B$ ), typically of the order of a few GHz for 90° scattering, and can be determined from the expression<sup>18</sup>

$$V_s = \nu_B \lambda_i / [2n_i \sin(\theta/2)] \quad (3)$$

where  $\lambda_i$  is the free space wavelength of the incident radiation,  $\theta$  the scattering angle and  $n_i$  is the liquid refractive index at the incident frequency. Hence from measurements of the Brillouin shifts an estimate of the elastic stiffness constant ( $K$ ) may be evaluated from the relationship

$$K = \rho V_s^2 \quad (4)$$

The frequency half-width at half maximum height of the Brillouin line  $\Delta\nu_B$  is related to the shear and volume viscosities of the liquid.

In order to determine the phonon frequency shift and Brillouin linewidth, three orders of a Fabry-Perot spectrum were analysed using a non-linear least-squares fitting procedure. Overlap from five adjacent orders was taken into account in the analysis.

To obtain the actual Brillouin linewidth the observed spectrum was deconvoluted from the instrumental profile. The instrumental profile of the light-scattering system was Lorentzian, hence the corresponding width was subtracted from the observed Brillouin widths.

The possibility of the occurrence of a Mountain line<sup>19</sup> in the Brillouin spectra, *i.e.* the coupling of intramolecular relaxations to translational motion, was included in the data fitting. The statistical analysis showed a lower sum of squares and the removal of cyclical deviations when this effect was included in the data analysis (see section on statistical analysis). Fig. 3 shows a Rayleigh-Brillouin spectrum of oleic acid/CCl $_4$  at 12 °C. Only two orders of the spectrum are shown for clarity.

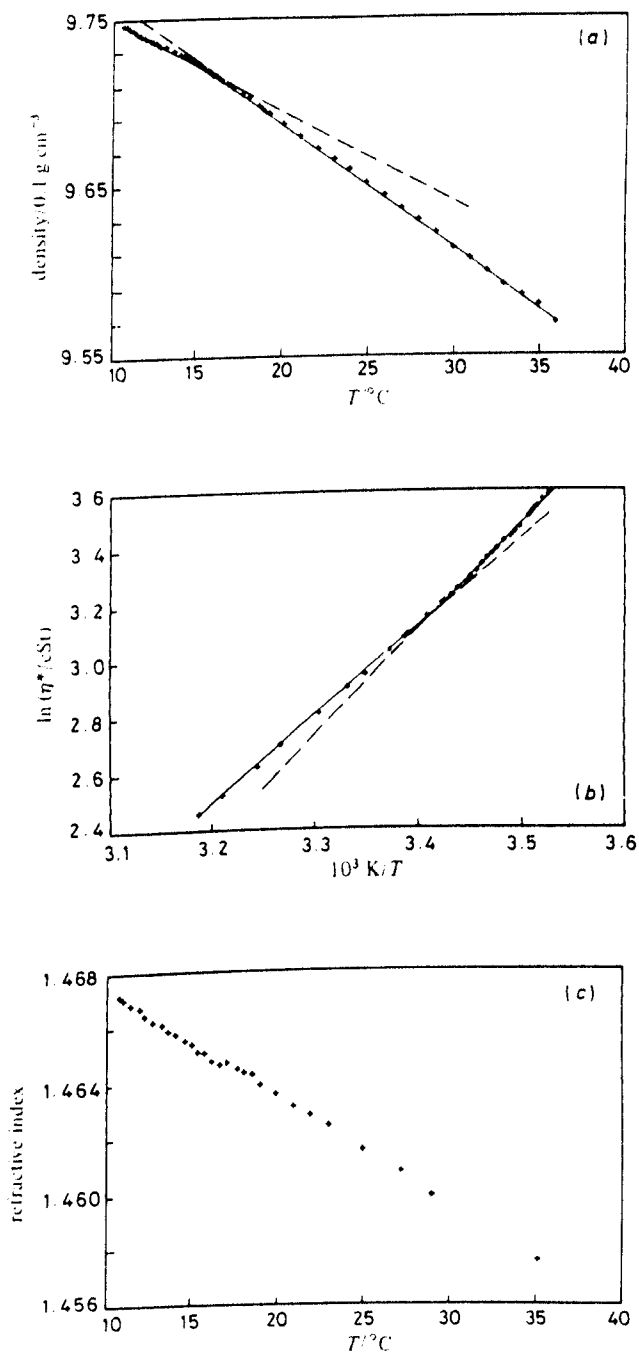


**Fig. 2.** (a) Density measurements for oleic acid showing the two best fit straight lines. (b) Arrhenius plot of the kinematic viscosity  $\eta^*$  for oleic acid showing the two best fit straight lines. (c) Refractive index measurements for oleic acid at 488.0 nm. The point of inflexion at  $T \approx 16^\circ\text{C}$  is clearly evident.

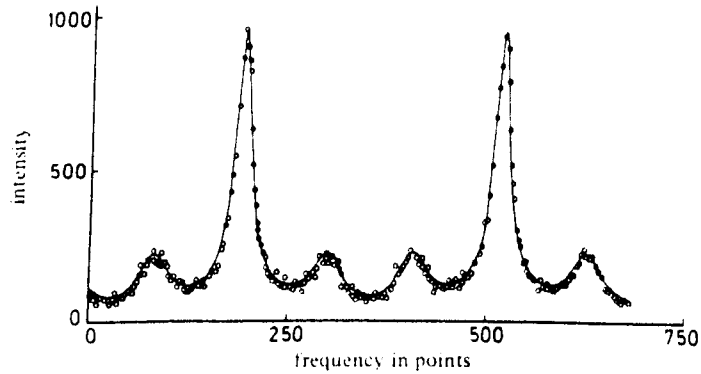


**Fig. 3.** Experimental Rayleigh-Brillouin spectrum of oleic acid at 11.6 °C showing two Fabry-Perot orders. The solid line indicates the theoretical fit incorporating a Mountain line and every fourth data point by a  $\circ$ .

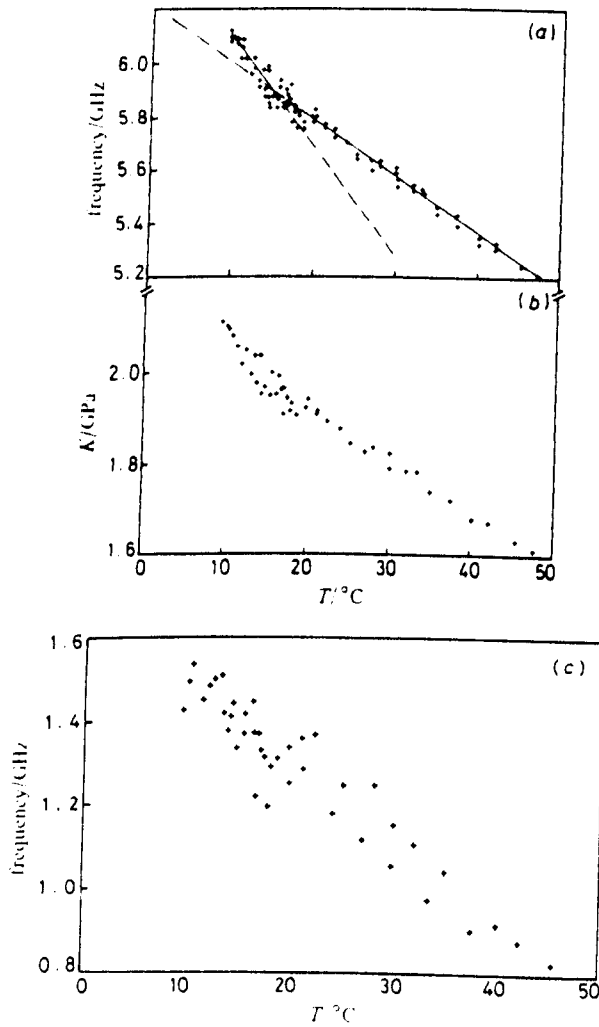


**Fig. 4.** (a) Measured Brillouin shifts plotted against temperature. (b) Calculated hypersonic elastic stiffness constant plotted against temperature. (c) Measured deconvoluted Brillouin linewidths for oleic acid plotted against temperature.

The Brillouin frequency shift as a function of temperature is shown in fig. 4(a). This quantity appears to vary linearly with temperature outside a narrow temperature range centred on 16.5 °C. The elastic stiffness constant ( $K$ ) is plotted in fig. 4(b) for comparison and shows a similar variation indicating that the anomaly is not only a consequence of density. The linear dependence of Brillouin shift on temperature is typical, and has been found for a wide range of polymer melts.<sup>20</sup> It is evident that there is considerably more spread on the data points within the transition region than outside it. This increased scatter has been found in other light scattering experiments on lipid phase transitions.<sup>13</sup> Two straight lines describe this behaviour most closely, intersecting at a temperature of 16.2 °C with a marked change in slope of *ca.* 50% (fig. 4).

The full-width at half maximum height (f.w.h.m.) of the Brillouin linewidths show no discernible anomaly in the variation with temperature. The scatter on the Brillouin linewidth data is considerably larger than that on the shift measurements. A discontinuity in the slope of the Brillouin linewidth with change in temperature may indeed exist, but even if this is the case it is smaller than that for the shift and masked by the large scatter on the original data. However, the f.w.h.m. tends to increase with decreasing temperature.

The results for the temperature dependent kinematic viscosity agree with those found by other workers for a variety of polymer melts.<sup>1</sup> The Arrhenius plot consists of two straight lines with a break point at 18.5 °C. The slope in the  $T < 18.5$  °C range is greater than that in the  $T > 18.5$  °C, the converse is true for the corresponding intercepts. The thermodynamic parameters that describe viscous flow by the AFE rate theory are the activation energy  $\Delta H^*$  and the entropy of activation  $\Delta S^*$  which appear in eqn (1).

The activation energy increases from the high temperature to the low temperature state from 26.04–32.15 kJ mol<sup>-1</sup>. The intercept for the high temperature state exceeds that for the low temperature state, indicating a change in entropy at the transition temperature. This result implies that the transition involves an increase in the local order of the fluid.

### Statistical Analysis of the Results

Three independent statistical methods were employed to ascertain the optimum choice of fitting function for the results. In addition to the usual least-squares criteria a linear correlation test and the one-sample runs test were used. The correlation test indicates the interdependence of two variables. If two variables are statistically independent a correlation coefficient of zero is expected. However, any long range trends will increase the result of the test. In addition, the one-sample runs test<sup>21</sup> examines the order in which the residuals occur. It is very sensitive to systematic deviations in the data sample. The results were fitted to two straight lines. For comparison the results were also fitted to a single straight line and an exponential.

For the case of two straight lines it was necessary to determine a statistically significant break point between the high and low temperature regions. This was achieved by making the break point a variable parameter of the fitting procedure. The optimum value of the break point ( $T_b$ ) is that which corresponded to a global minimum in the sum of squares and maximised the runs test probability.

The statistical analysis of the data is shown in table 1. It is apparent that two straight lines intersecting at a unique temperature best describe the viscosity data of fig. 2(b) and the density data of fig. 2(a). On the basis of the one-sample runs test, two straight lines were found to be preferable to the other functions because the systematic deviations were less pronounced. Moreover, the standard deviations on the fitted variables were lower. The results of the statistical analysis for the Brillouin measurements are also presented in table 1. As with the foregoing results the variation of frequency shift with temperature is best described by two straight lines.

The results for the f.w.h.m. of the Brillouin lines indicate that there is no preferred

Table 1. Results of statistical tests

fitting function	experimental results	sum of squares	runs test probability	linear correlation test probability	line 1 ( $T \leq T_0$ )		line 2 ( $T > T_0$ )	
					A(1) (s.d.)	A(2) (s.d.)	A(1) (s.d.)	A(2) (s.d.)
one straight line	$v_B$	$1.4 \times 10^{-3}$	0.1	1.0	6.25 (0.05)	-0.022 (0.002)		
	f.w.h.m. <sup>b</sup>	$3.5 \times 10^{-2}$	0.1	1.0	1.69 (0.10)	-0.019 (0.004)		
	$\eta^{*c}$	$2.0 \times 10^{-4}$	$5.5 \times 10^{-6}$	1.0	-8.19 (0.36)	3.33 (0.11)		
	$\rho^d$	$8.2 \times 10^{-8}$	$1.0 \times 10^{-10}$	1.0	0.9827 (0.0028)	-0.0007 (0.0001)		
two straight lines	$v_B^d$	$4.9 \times 10^{-4}$	1.0	1.0	6.49 (0.13)	-0.040 (0.009)	6.21 (0.04)	-0.021 (0.001)
	f.w.h.m. <sup>b</sup>	$3.1 \times 10^{-3}$	1.0	1.0	1.82 (0.24)	-0.029 (0.017)	1.71 (0.127)	-0.020 (0.004)
	$\eta^{*c}$	$2.0 \times 10^{-2}$	$2.1 \times 10^{-2}$	1.0	-7.53 (0.18)	3.13 (0.05)	-0.63 (0.32)	3.75 (0.09)
	$\rho^d$	$8.5 \times 10^{-2}$	$1.3 \times 10^{-2}$	1.0	0.9804 (0.0004)	-0.0005 (0.0000)	0.9836 (0.0039)	-0.0007 (0.0002)
one exponential curve	$v_B^d$	$3.5 \times 10^{-3}$	$9.1 \times 10^{-2}$	1.0	6.28 (0.01)	-0.004 (0.000)		
	f.w.h.m. <sup>b</sup>	$2.2 \times 10^{-3}$	1.0	1.0	1.81 (0.08)	-0.017 (0.003)		
	$\eta^{*c}$	$2.4 \times 10^{-6}$	$2.4 \times 10^{-4}$	1.0	0.07 (0.04)	1.10 (0.01)		
	$\rho^d$	$2.0 \times 10^{-6}$	$8.2 \times 10^{-8}$	1.0	0.9831 (0.0030)	-0.0007 (0.0001)		

<sup>a</sup> Brillouin shift. <sup>b</sup> Brillouin f.w.h.m. <sup>c</sup> Kinematic viscosity. <sup>d</sup> Density. A(1) and A(2) are the fitted parameters from fits to:  $F(X) = A(1) + A(2)X$ , and  $F(X) = A(1) \exp[-A(2)X]$ . Standard deviations (s.d.) are also shown.

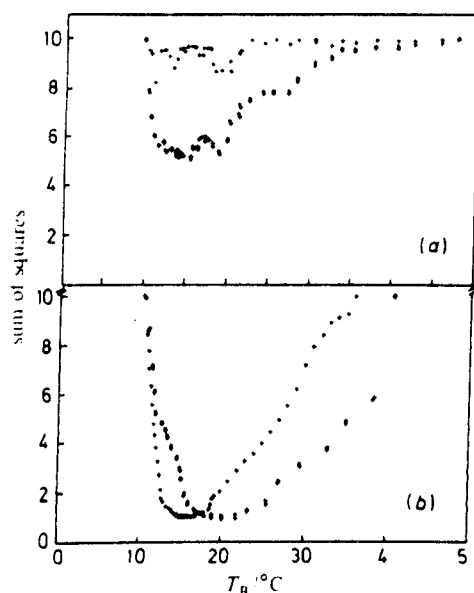


**Fig. 5.** Normalised sum of squares plotted against break-point temperature  $T_B$ . (a) Brillouin line widths (+); Brillouin shifts (‡). (b) Density (+); Kinematic viscosity (‡).

**Table 2.** Transition temperature ( $T_B$ ) and range of  $T_B$  from each experiment

experiment	$T_B / ^\circ\text{C}$	range of $T_B / ^\circ\text{C}$
Brillouin shift	16.2	14.0-18.0
Brillouin f.w.h.m.	18.0	14.5-20.0
viscosity	18.5	18.0-20.0
density	16.0	15.4-17.6

functional description. This is not surprising in view of the characteristically large scatter on the data.

In fig. 5 the sum of squares corresponding to each selected break point for all the results is depicted. The sum of squares is weighted to that of a single straight line fit, *i.e.* the sum of squares for a single straight line fit is 10. In all cases there is a clear optimum range of values over which the sum of squares varies very little from its minimum value. This was also found to be the case for the runs test probability. The ranges shown in table 2 are those for which the transition temperature is nearly equiprobable.

The transition temperatures ( $T_B$ ) found for each experimental set are shown in table 2. The correlation test returned a probability of 1.0 for all the functional forms investigated, indicating that none of the fitting functions investigated was preferred. They were, therefore, not useful in distinguishing the appropriate function.

The general concurrence of the statistical tests demonstrates that in all cases, except that of the Brillouin widths, the data are best represented by two intersecting straight lines in agreement with previous results.<sup>1,2</sup>

### Discussion

A rigorous statistical analysis of all the results shows that the change in the properties of the oleic acid/ $\text{CCl}_4$  solutions between 15 and 18 °C can be best described as being discontinuous. The increase of activation energy is consistent with this model.

The density variation with temperature shows the same behaviour as the Arrhenius plot of the viscosity. The low-temperature state has a smaller expansion coefficient than the high temperature state.

From the various measurements described above, it appears that oleic acid exhibits anomalous behaviour in the temperature variation of the physical properties investigated. In separate measurements of density, viscosity and refractive index for a single sample of oleic acid, distinct changes in the temperature coefficients of these quantities were observed. This behaviour is also reflected in the hypersonic propagation over the same temperature range. As mentioned above there is an increase in scatter on the data points within the transition region. This transition region involves a change of phase analogous to that of the glass-to-rubber transition that occurs in amorphous polymers. The glass-to-rubber transition has been found to be rate dependent.<sup>22</sup> It is likely, therefore, that the  $T_u$  phenomenon is also a rate dependent process accounting for the increased spread on the data.

The important fact that different physical properties of oleic acid show anomalous behaviour within the same narrow temperature range (14–18 °C) implicates a change of structure. This range compares with that found in some biological membranes containing fatty acid alkyl chains of which oleic acid is a fundamental constituent. This suggests that the thermotropic phase transformations seen in these systems can be associated with the  $T_u$  phenomenon occurring in the oleyl chain.

Depolarised Rayleigh scattering can also be used to study molecular motion in liquids. The depolarised spectrum monitors fluctuations in the anisotropy tensor associated with molecular reorientation. This spectrum would be very sensitive to any mesomorphic ordering in the liquid. The depolarised (VH) spectrum of oleic acid/ $\text{CCl}_4$  was examined, but the width of the Lorentzian peak obtained was found to be too narrow to resolve with the Fabry-Perot interferometer. This implies that the multiparticle correlation time is very long and that there is large scale cooperative motion. Future studies will require the use of light-beating spectroscopy to adequately resolve the central component.

### References

- 1 J. K. Kruger, L. Peetz and H. G. Unruh, *Colloid Polym. Sci.*, 1981, **259**, 215.
- 2 J. K. Kruger, L. Peetz, W. Wildner and M. Pietralla, *Polymer*, 1980, **21**, 620.
- 3 G. D. Patterson, P. J. Carroll and D. S. Pearson, *J. Chem. Soc., Faraday Trans. 2*, 1983, **79**, 677.
- 4 P. D. De Gannes, *Mol. Cryst. Liq. Cryst.*, 1971, **12**, 193.
- 5 J. F. Nagle and H. L. Scott, *Physics Today*, 1978, 38.
- 6 H. Trauble and D. H. Haynes, *Chem. Phys. Lipids*, 1971, **7**, 324.
- 7 J. L. Ranck, L. Maten, D. M. Sadler, A. Tardieu, T. Gulik-Kryzwick and V. Luzzat, *J. Mol. Biol.*, 1974, **85**, 249.
- 8 S. Morcelja, *Nature (London)*, 1973, **241**, 451.
- 9 M. C. Phillips, R. M. Williams and D. Chapman, *Chem. Phys. Lipids*, 1969, **3**, 234.
- 10 *Table of Physical and Chemical Constants*, G. W. C. Kaye and T. H. Laby (Longmans, London, 1973), 14th edn.
- 11 *Van Nostrand's Scientific Encyclopedia* (Van Nostrand, Place, 1973), 4th edn.
- 12 J. E. Crilly and J. C. Earnshaw, *The Application of Laser Light Scattering to the Study of Biological Motion*, NATO, ASI (Plenum Press, New York, 1982).
- 13 G. E. Crawford and J. C. Earnshaw, *Eur. Biophys. J.*, 1984, **11**, 25.
- 14 R. E. Pagano, R. J. Cherry and D. Chapman, *Science*, 1973, **181**, 557.
- 15 S. H. White, *Biophys. J.*, 1975, **15**, 95.
- 16 G. V. Vinogradov and Ya. Malkin, *Rheology of Polymers: Viscoelasticity and Flow of Polymers* (MIR Publishers, Moscow, 1980).

- 17 B. J. Berne and R. Pecora, *Dynamic Light Scattering* (Wiley, New York, 1976).
- 18 B. Chu, *Laser Light Scattering* (Academic Press, London, 1974).
- 19 R. D. Mountain, *J. Res. Nat. Bur. Stand.*, 1966, **70A**, 207.
- 20 J. V. Champion and D. A. Jackson, *Mol. Phys.*, 1976, **31**, 1159.
- 21 C. A. Bennett and N. L. Franklin, *Statistical Analysis in Chemistry and the Chemical Industry* (Wiley, Chichester, 1966), 4th edn.
- 22 G. C. Stevens and M. J. Richardson, *Polymer*, 1983, **24**, 851.

*Paper S/571: Received 3rd April, 1985*